APPROXIMATING MANY-BODY INDUCTION TO EFFICIENTLY DESCRIBE MOLECULAR LIQUIDS AND CLUSTERS WITH IMPROVED ACCURACY

THESIS

Presented in Partial Fulfillment of the Requirements for
the Degree Doctor of Philosophy in the Graduate
School of The Ohio State University

By

Leif David Jacobson, B.S.
Graduate Program In Chemistry
The Ohio State University

2011

Thesis Committee:

John M. Herbert, Adviser
Sherwin J. Singer
Anne B. McCoy

ABSTRACT

Construction of accurate potential energy (PE) surfaces for molecular systems is one of the primary tasks performed by theoretical physical chemists. Once in hand, these PE functions can be used to study the dynamics and spectroscopies, as well as the structures and properties of molecular systems. This study focuses on approximating many-body electronic induction in order to improve the accuracy of existing potentials and improve the efficiency of *ab initio* methods in order to allow “on-the-fly” energy and force evaluations in dynamical calculations.

The majority of the work reported here focuses on the solvated electron. We initiate a study aimed at understanding the effects of explicitly including the (ultrafast) electron–solvent electronic induction, or polarization. We construct a single electron potential in which the coarse grained electronic degrees of freedom of the solvent are treated self-consistently along with the electronic wave function. Predictions of the binding energy of an excess electron in water clusters obtained using this potential compare well to *ab initio* electronic structure theories. Subsequently, this potential was used to investigate the behavior of the excess electron in liquid water. The explicit treatment of induction appears to have a minimal impact on the structure and solvation dynamics of the excess electron (in the ground state) but does have a large impact on the vertical detachment energy and the optical absorption spectrum. In

these latter cases there is an abrupt change in the charge distribution of the excess electron. In such cases the electronic response from the solvent can be large and should be taken into account.

The electronic response of the solvent occurs on the time scale of electronic excitation. This introduces technical complications when solving for orthogonal eigenstates of this system since the model Hamiltonian is state dependent. We describe a simple method of solving this problem and discuss the possibility of generalizing this scheme to many-electron theories (such and density functional and Hartree-Fock theories). This procedure may potentially enable the study of non-adiabatic excited state relaxation dynamics including the electronic response of the solvent.

Construction of empirical potential energy surfaces, such as the one developed here, is a time intensive process and one questions whether or not they have found the optimal set of parameters. We would prefer to use accurate electronic structure theories to compute energies and forces. Of particular interest is the use of *ab initio* methods which offer a systematically improvable route to the exact energy. Currently this is only feasible for small systems and short time scales. A class of algorithms called fragment methods are currently being developed to extend these approaches to condensed phase environments. Our strategy has been to efficiently approximate electronic induction and fold this into the description of the single molecular fragments. The fragments are then coupled to one another through a version of symmetry adapted perturbation theory. This yields an accurate and efficient method that scales linearly in the large system limit.

To Jamie Valentine, without whose unconditional and undying support I would have not succeeded.

ACKNOWLEDGMENTS

I gratefully acknowledge support from Chris F. Williams, Mary A. Rohrdanz, Adrian "Bill Angel" Lange and the rest of the Herbert group, continued support from my parents, Sheryl K. and Charles D. Jacobson and my sister Juliet E. Jacobson. I would like to acknowledge support from the Presidential Fellowship from Ohio State University. Insightful discussions about the hydrated electron with James Coe and many random discussions with members of the Singer research group such as Ali Hassanali and Corey Beck are gratefully acknowledged. I would like to thank Sherwin J. Singer for letting me bug him on a sometimes frequent basis and setting me straight on a number of issues. I owe many thanks to my advisor, John M. Herbert, for continued counseling on all things scientific and some extracurricular discussions. I also would like to thank John for encouraging me to pursue the XPol/SAPT project, during which I learned a great deal about modern electronic structure theory. Finally I owe uncountable thanks to Jamie Valentine, mainly for putting up with me and somehow being willing to leave Bellingham Washington in favor of an uncertain future in Columbus Ohio and beyond.

VITA

1978	Born, Puyallup Washington
1997	Puyallup Senior High School
2002	B.S. Chemistry, Central Washington University
2005	Western Washington University
2006-2008	Graduate Teaching Associate, The Ohio State University
2009-2010	Graduate Research Associate, The Ohio State University
2011-present	Presidential Fellow, The Ohio State University

PUBLICATIONS

(11) L. D. Jacobson and J. M. Herbert *"Combining the Explicit Polarization potential (XPol) with Many-Body, Symmetry-Adapted Perturbation Theory (SAPT): Reformulation of Theory and Three-Body Induction" in preparation*

(10) L. D. Jacobson and J. M. Herbert, *"Simulation of Four Isomer Types in Anionic Water Clusters using a Polarizable Electron Water Potential" in preparation*

(9) J. M. Herbert and L. D. Jacobson, *"Assessment of one-electron pseudopotential models for the aqueous electron: Comparison to experimental data and time-dependent density functional theory."* Journal of Physical Chemistry, A *submitted*

(8) L. D. Jacobson and J. M. Herbert, *"A Simple Algorithm for Determining Orthogonal, Self-Consistent Excited–State Wave Functions For a State–Specific Hamiltonian:*

Application to the Optical Spectrum of the Aqueous electron." Journal of Chemical Theory and Computation (2011), 7 2085

(7) L. D. Jacobson and J. M. Herbert, *"Comment on 'Does the Hydrated Electron Occupy a Cavity?' "* Science (2011), 331 1387

(6) L. D. Jacobson and J. M. Herbert, *"An Efficient, Fragment-Based Electronic Structure Method for Molecular Systems: Self-Consistent Polarization With Perturbative Two-Body Exchange and Dispersion."* Journal of Chemical Physics (2011), 134 094118

(5) J. M. Herbert and L. D. Jacobson, *"Nature's Most Squishy Ion: The Important Role of Solvent Polarization in the Description of the Hydrated Electron."* International Reviews of Physical Chemistry (2011), 30 1

(4) L. D. Jacobson and J. M. Herbert, *"A One-Electron Model for the Aqueous Electron that Includes Many-Body Polarization: Bulk Equilibrium Structure, Vertical Electron Binding Energy, and Optical Absorption Spectrum."* Journal of Chemical Physics (2010), 133 154506

(3) L. D. Jacobson and J. M. Herbert, *'Polarization-Bound Quasi-Continuum States Are Responsible for the 'Blue Tail' in the Optical Absorption Spectrum of the Aqueous Electron."* Journal of the American Chemical Society (2010), 132 10000

(2) L. D. Jacobson, C. F. Williams and J. M. Herbert, *"The Static Exchange Electron–Water Pseudopotential, in Conjunction with a Polarizable Water Model: A New Hamiltonian for Hydrated-Electron Simulations."* (2009), 130, 124115

(1) J. M. Herbert, L. D. Jacobson and C. F. Williams, *"The Role of the Neutral Water Potential in Determining the Properties of Anionic Water Clusters."*
In Molecular Potential Energy Surfaces in Many Dimensions ed. by M. M. Law and A. Ernesti, Collaborative Computational Project on Molecular Quantum Dynamics (CCP6) , Daresury, United Kingdom (2009).

FIELDS OF STUDY

Major Field: Chemistry, Theoretical Physical Chemistry

Table of Contents

APPENDICES

List of Figures

List of Tables

TABLE PAGE

CHAPTER 1

Introduction

In 1927 Max Born and Robert Oppenheimer published a paper that would forever influence the way physical chemists think about processes such as chemical reactions, solvation and isomerization.[10] This approximation defines what is meant by a potential energy surface. A surface that, if we treat nuclei as classical point particles as we shall in this work, guides the dynamics of the system. This idea of nuclear motion following a potential energy landscape that is determined by the average positions, momenta and sometimes dynamics of the electrons is fundamental and will be our starting point. We will then proceed by discussing, in general terms, how one attempts to solve the electronic Schrödinger equation, which will be defined below. We will use this discussion to set up a bottom up approach to describe what is meant by electronic polarization, which we may also have occasion to refer to as induction. As an alternative viewpoint we will briefly touch on a top down approach to describing these inductive intermolecular interactions. A very brief introduction to the hydrated electron will be given, as well as an introduction to fragment methods.

1.1 Defining a Potential Energy Surface

The fundamental equation of quantum mechanics is the time-dependent Schrödinger equation (TDSE),[11]

$$i|\dot{\Psi}\rangle = \hat{H}|\Psi\rangle, \tag{1.1}$$

where $|\dot{\Psi}\rangle$ is the time derivative of the state vector $|\Psi\rangle$, $\hat{H}$ is the Hamiltonian and atomic units will be used throughout this work unless otherwise specified. We will work with a standard molecular Hamiltonian,

$$\hat{H} = \sum_I \frac{\hat{p}_I^2}{2M_I} + \hat{H}_{elec} \ , \tag{1.2}$$

which is the sum of nuclear kinetic energy and an electronic Hamiltonian defined as

$$\hat{H}_{elec} = \sum_i \frac{\hat{p}_i^2}{2} + \frac{1}{2}\sum_i \sum_{j\neq i} \frac{1}{|\vec{r}_i - \vec{r}_j|} - \sum_I \sum_i \frac{Z_I}{|\vec{r}_i - \vec{R}_I|} + \frac{1}{2}\sum_I \sum_{J\neq I} \frac{Z_I Z_J}{|\vec{R}_I - \vec{R}_J|} \ . \tag{1.3}$$

The notation here is standard, $\vec{r}_i$ is the position of electron i, $\vec{R}_I$ is the position of nuclei I, Z_I is its charge and $\hat{p}_i = -i\hat{\nabla}_i$ is the momentum operator. The index i should not be confused with the imaginary number and $\hat{\nabla}_i$ is the vector derivative operator for particle i.

In the basis of eigenfunctions of the Hamiltonian, the time evolution of the state vector is trivial, therefore we concentrate not on Eq. (1.1) but the time-*independent* Schrödinger equation (TISE),

$$\hat{H}|\Psi\rangle = E|\Psi\rangle \ . \tag{1.4}$$

Suppose we have a set of eigenfunctions of the *electronic* Hamiltonian, Eq. (1.3), which we denote as the set $\{|\Phi_\mu\rangle\}$ with corresponding eigenvalues $\{\epsilon_\mu\}$. We note that the positions of the nuclei, $\{\vec{R}_I\}$, appear as parameters in the electronic Schrödinger equation [trivially defined as Eq. (1.4) with the electronic Hamiltonian replacing the total Hamiltonian] implying that the eigenfunctions and eigenvalues are parametrically dependent on the nuclear positions. We proceed by assuming we can write the total wave function as [11]

$$|\Psi\rangle = \sum_{\mu\nu} C_{\mu\nu} |\Phi_\mu\rangle |\chi_\nu^\mu\rangle \tag{1.5}$$

where $C_{\mu\nu}$ are expansion coefficients and the nuclear functions $|\chi_\nu^\mu\rangle$ have one index that associates with them an electronic state, and a second index whose meaning will become clear shortly. We are interested in the nature of TISE in this basis so we begin by writing

$$\left(\sum_I \frac{\hat{p}_I^2}{2M_I} + \hat{H}_{elec}\right) \sum_{\mu\nu} C_{\mu\nu} |\Phi_\mu\rangle |\chi_\nu^\mu\rangle = E \sum_{\mu\nu} C_{\mu\nu} |\Phi_\mu\rangle |\chi_\nu^\mu\rangle. \tag{1.6}$$

Next, let us apply $\langle\Phi_\lambda|$ to yield

$$\begin{aligned} &\sum_{\mu\nu} \sum_I C_{\mu\nu} \frac{1}{2M_I} \left(|\chi_\nu^\mu\rangle \langle\Phi_\lambda|\hat{p}_I^2|\Phi_\mu\rangle + \langle\Phi_\lambda|\hat{p}_I|\Phi_\mu\rangle \hat{p}_I |\chi_\nu^\mu\rangle \right) \\ &+ C_{\lambda\nu} \sum_I \frac{\hat{p}_I^2}{2M_I} |\chi_\nu^\lambda\rangle + C_{\lambda\nu}\epsilon_\lambda |\chi_\nu^\lambda\rangle = E C_{\lambda\nu} |\chi_\nu^\lambda\rangle \ , \end{aligned} \tag{1.7}$$

we have used the fact that the set $\{|\Phi_\mu\rangle\}$ are eigenfunctions of the electronic Hamiltonian and form an orthonormal set. The two terms in parenthesis are the so-called derivative couplings [11] and will be briefly discussed below. Neglecting these terms is the Born-Oppenheimer approximation, this yields

$$\left(\sum_I \frac{\hat{p}_I}{2M_I} + \epsilon_\lambda(\mathbf{R})\right) |\chi_\nu^\lambda\rangle = E |\chi_\nu^\lambda\rangle \ . \tag{1.8}$$

In Eq. 1.8 which we have made the parametric dependence of the electronic eigenvalues on nuclear coordinates explicit. In this chapter we use arrows over variables to indicate three dimensional cartesian vectors whereas bold symbols signify higher dimensional objects such as matrices. In Eq. 1.8 $\mathbf{R}$ represents all of the coordinates of the system.

The Born-Oppenheimer approximation states that in the absence of derivative, or non-adiabatic coupling, the eigenvalues of the electronic Hamiltonian define a potential energy function that can be used to compute nuclear vibrational eigenstates. In this approximation the nuclear and electronic degrees of freedom cannot exchange energy and are said to be adiabatically separated. So long as the electronic eigenfunctions are slowly varying functions of the *nuclear* coordinates, the approximation is robust. This fails when two eigenfunctions of the electronic Hamiltonian approach degeneracy as a function of the nuclear positions.

In this work we make an additional approximation. We assume that the motion of the nuclei can be treated classically. We suggest that the potential energy surface, given by $\epsilon_\mu(R)$, exerts a force on the I^{th} nucleus equal to

$$\vec{F}_I = -\frac{\partial \epsilon_\mu(\boldsymbol{R})}{\partial \vec{R}_I} \ . \tag{1.9}$$

The motion of the nuclei remains adiabatically separated from the electronic degrees of freedom. This being said, it is important to understand where the idea of potential energy surfaces arises from and bear in mind that it is an approximation, though a very good one for many applications.

1.2 Solving the Electronic Schrödinger Equation

Finding eigenfunctions of the electronic Hamiltonian is a nontrivial task and at first glance it is not even clear where to begin. In what follows we only consider attempts at finding the ground state eigenvector, $|\Phi_0\rangle$. The electronic Hamiltonian can be written as a sum of zero, one and two electron operators,

$$\hat{H}_{elec} = \sum_i \hat{h}(\vec{r}_i) + \frac{1}{2}\sum_i \sum_{j \neq i} \frac{1}{|\vec{r}_i - \vec{r}_j|} + \frac{1}{2}\sum_I \sum_{J \neq I} \frac{Z_I Z_J}{|\vec{R}_I - \vec{R}_J|} \ , \tag{1.10}$$

where $\hat{h}(\vec{r}_i)$ collects the electronic kinetic energy and electron-nuclear attraction for electron i. If electrons were non-interacting, i.e. if the second term in Eq. (1.10) were zero, the eigenfunctions could be written as direct products of single-particle functions which would be eigenfunctions of the single particle operator $\hat{h}$. This is called a Hartree product.[12] The problem with this Hartree product (other than the fact that electrons do indeed interact) is that it does not satisfy the Pauli principle, the notion that no two fermions can occupy the same state simultaneously. To satisfy the Pauli principle we form a Slater determinant [12] of N electrons in N spin-orbitals (single particle functions),

$$|\Phi_0\rangle = \frac{1}{\sqrt{N!}} \begin{vmatrix} \phi_1(1) & \phi_2(1) & \cdots & \phi_N(1) \\ \phi_1(2) & \phi_2(2) & \cdots & \phi_N(2) \\ \vdots & & & \vdots \\ \phi_1(N) & \phi_2(N) & \cdots & \phi_N(N) \end{vmatrix} \ . \tag{1.11}$$

Another way to define the Slater determinant, which we we will encounter in chapter 7, is by the use of the antisymmetrizer, $\hat{\mathcal{A}}$. The action of $\hat{\mathcal{A}}$ on a Hartree product of spin orbitals produces an antisymmetrized product of spin-orbitals,

$$|\Phi_0\rangle = \hat{\mathcal{A}}\left(\phi_1(1)\phi_2(2)\cdots\phi_N(N)\right) \ . \tag{1.12}$$

In these expressions we have used the simplifying notation $\phi_i(\vec{r}_i) \equiv \phi_i(i)$.

In Hartree-Fock theory (HF) we use a single Slater determinant to represent the wave function,[12] this is the simplest wave function possible that satisfies the Pauli principle. The form of this wave function is correct in the limit that electrons are non-interacting. In this non-interacting case the spin-orbitals are the set of eigenfunctions of the single particle operators in Eq. (1.10), each of these N single particle operators is identical. That is, we only have to solve

$$\hat{h}(1)\phi_i(1) = \epsilon_i \phi_i(1) \ , \tag{1.13}$$

then construct the total (ground state) wave function with the N lowest energy spin-orbitals. The total energy, defined as the expectation value of the Hamiltonian, is just the sum of these single particle energies. Once we allow the electrons to interact we have to face the question of how to define the single particle levels, $\{\phi_i\}$. The answer is simple, we appeal to the variational principle. We require that the expectation value of the true Hamiltonian, using the HF *ansatz* for the wave function, be a minimum in energy with respect to variations in the spin-orbitals,[12]

$$E_{HF} = \min_{\{\phi_i\}} \left(\langle \Phi_0 | \hat{H}_{elec} | \Phi_0 \rangle - \sum_{ij} \epsilon_{ij} (S_{ji} - \delta_{ji}) \right) \ . \tag{1.14}$$

For convenience we also require that the spin-orbitals be orthonormal by using a set of Lagrange multipliers, $\{\epsilon_{ij}\}$. S_{ij} is the overlap integral of spin-orbitals i and j while δ_{ij} is the kronecker delta. We take the spin-orbitals to be a product of a spatial function and a spin function. In what follows we have integrated over the spin variables so that the resulting equations are only for the spatial part. We work in the restricted formalism [12] where the alpha and beta spatial orbitals are identical (accurate for closed shell systems) and we wish to find these spatial orbitals.

The spatial orbitals that minimize the HF energy satisfy the Hartree-Fock equations,

$$\hat{f}(1)\phi_i(1) = \epsilon_i \phi_i(1) \tag{1.15}$$

where ϵ_i is a diagonal element of the Lagrange multiplier matrix and the single-particle Fock operator is

$$\hat{f}(1) = \hat{h}(1) + 2\hat{J}(1) - \hat{K}(1) \ . \tag{1.16}$$

The coulomb ($\hat{J}$) and exchange ($\hat{K}$) operators are defined by their action on a spatial orbital, also known as molecular orbital (MO),

$$\langle \phi_j(1)|\hat{J}(1)|\phi_i(1)\rangle = \sum_k (ji|kk) \tag{1.17}$$

$$\langle \phi_j(1)|\hat{K}(1)|\phi_i(1)\rangle = \sum_k (jk|ki) \ . \tag{1.18}$$

The sums run over the alpha-spin occupied orbitals (the $N/2$ lowest in energy) and the four index integrals are written in the chemists notation, [12] defined by

$$(ij|kl) = \int dr_1 \int dr_2 \phi_i^*(1)\phi_j(1) \frac{1}{|\vec{r}_1 - \vec{r}_2|} \phi_k^*(2)\phi_l(2) \ . \tag{1.19}$$

It is important to note that the one-electron density for a single slater determinant is given by the sum, of products of occupied MOs,

$$\rho(\vec{r}) = \int d\vec{r}_2 d\vec{r}_3 \cdots d\vec{r}_N \Phi_0^*(\vec{r}_1, \vec{r}_2, \cdots, \vec{r}_N)\Phi_0(\vec{r}_1, \vec{r}_2, \cdots, \vec{r}_N) = \sum_i \phi_i^*(\vec{r})\phi_i(\vec{r}) \ . \tag{1.20}$$

From this it is clear that a diagonal matrix element of the coulomb operator (say $\mathbf{J}_{ii}$) represents the coulomb interaction of the single-particle density of an electron inhabiting orbital i with the full system density (including the self-interaction). The presence of the exchange operator is a direct consequence of the Pauli principle and exactly corrects for the self-interaction present in $\mathbf{J}_{ii}$. The HF equations are solved by expanding the MOs in some basis set. In this work we use gaussian orbitals centered on atoms, which we will refer to as atomic orbitals (AOs), though other choices are possible. The HF equations then take the form [12]

$$\mathbf{FC} = \mathbf{SC}\boldsymbol{\epsilon} \ , \tag{1.21}$$

where $\mathbf{C}$ is the matrix of expansion coefficients that we are solving for, $\mathbf{S}$ is the overlap matrix in the AO basis, $\boldsymbol{\epsilon}$ is the matrix of Lagrange multipliers and the Fock matrix in the AO basis takes the form

$$F_{\mu\nu} = h_{\mu\nu} + \sum_{\lambda\sigma} P_{\lambda\sigma} \left((\mu\nu|\lambda\sigma) - \frac{1}{2}(\mu\sigma|\lambda\nu) \right) \ . \tag{1.22}$$

$\mathbf{P} = 2\mathbf{C}\mathbf{C}^{\dagger}$ is the density matrix in the AO basis. Diagonalization of $\boldsymbol{\epsilon} = \mathbf{C}^{\dagger}\mathbf{F}\mathbf{C}$ yields the eigenvalues of Eq. (1.15) in a finite basis set. Solving these AO basis equations is iterative and proceeds in three basic steps, forming $\mathbf{F}$ from $\mathbf{P}$ which nominally scales as $\mathcal{O}(N_{basis}^4)$, diagonalizing $\mathbf{F}$ to get $\mathbf{C}$ which scales as $\mathcal{O}(N_{basis}^3)$ and constructing $\mathbf{P}$ which is also a cubic operation.

HF theory is a mean field theory in which electrons interact with the average field of all of the other electrons.[12] It contains no electron correlation, that is, the motions of the electrons within the electron density are not correlated, as they should be. [1.1] This leads to small errors, but errors that are large on the energy scale that chemists care about. For example, the HF energy of the water dimer is roughly 152 Hartree, a simple estimate of the correlation energy (defined as the difference between the HF energy and the correct energy) is ~ 0.5 Hartree, clearly a small fraction of the total energy. However, the binding energy of the water dimer is less than 0.01 Hartree. If we are to calculate energy differences on this scale we need to improve upon HF theory (and probably also rely on a cancellation of errors).

To proceed from our mean field theory we can use HF theory as a starting point and the HF determinant $|\Phi_0\rangle$ as the "reference". The HF reference determinant is a single Slater determinant built from the N canonical HF MOs (solutions of Eq. (1.21)) that have the lowest eigenvalues. In any reasonable basis set the number of MOs (equal to the number of basis functions) greatly exceeds the number of occupied MOs, the remaining unoccupied MOs are referred to as virtual orbitals. We can make a large number of Slater determinants by replacing one or more occupied orbitals with one or more virtual orbitals. For example, the set of determinants in which we replace one occupied orbital i with virtual a will be denoted as $|\Phi_i^a\rangle$, these are singly excited determinants.

The true wave function is not a single determinant wave function. [1.2] However,

---

[1.1] Actually, inspection of the two-particle density reveals that HF theory accounts for same-spin correlation while the spatial distribution of opposite spin electrons is completely uncorrelated.

[1.2] This can be easily seen if one inspects the so-called normal ordered Hamiltonian [13], which is well beyond the scope of this introductory discussion.

the set of all replacement determinants (singles, doubles, triples ...) approaches completeness as the single particle basis approaches completeness. Therefore, one can expand the exact electronic wave function in this basis. The form of the expansion leads to different electronic structure methods such as configuration interaction, coupled cluster theory and Møller-Plesset perturbation theory.[12, 13] We will refer to these methods as wave function methods. This approach offers a systematic route to the exact answer from HF theory since one can truncate the wave function expansion at some arbitrary level.

1.3 Electronic Polarization: A Microscopic Viewpoint

We will use the tools developed in the previous section to provide a description of electronic polarization and make a connection to the formulas used in the context of polarizable force fields, such as AMOEBA.[14] Let us start by considering a system in which we have a molecule centered at $\vec{R}_m$ for which we have solved the HF equations. For simplicity we assume it is a closed shell molecule and we work in the restricted formalism. At some other point $\vec{R}_a$ we place a point charge q and investigate the changes this brings about to the wave function, the dipole and the energy. Fig. 1.1 pictorially shows the system and coordinates. We write the Hamiltonian as the sum of the Fock operator, the fluctuation operator ($\hat{W}$) and the interaction with the point charge ($\hat{V}$) as

$$\hat{H} = \sum_i \hat{f}(i) + \chi\hat{W} + \zeta\hat{V} \ , \tag{1.23}$$

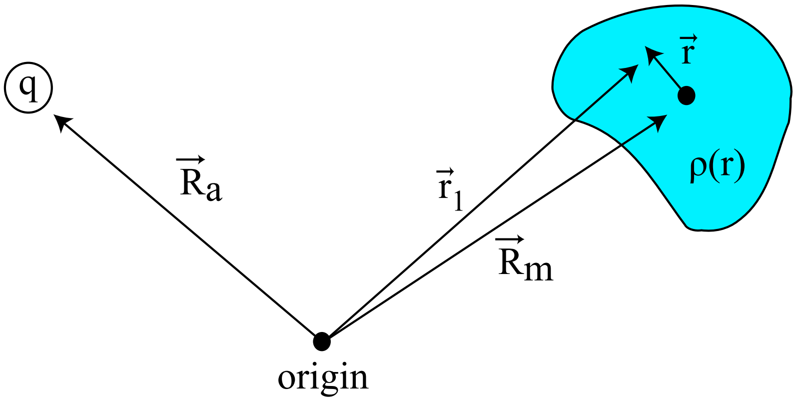

Figure 1.1: Coordinate System for a simple model of electronic polarization.

χ and ζ serve as perturbation parameters and we are only interested in expanding with respect to ζ. The fluctuation operator is simply the difference between the molecular Hamiltonian and the molecular Fock operator.[12] The perturbation $\hat{V}$ is explicitly given by

$$\hat{V} = -\sum_i \frac{q}{|\vec{r}_i - \vec{R}_a|}, \tag{1.24}$$

i indexes electrons. The first order correction to the energy is just the expectation value of the perturbation, the HF density interacts with the point charge. The first order corrected wave function is more interesting,

$$|\Phi\rangle = |\Phi_0\rangle + 2\sum_{ia} \frac{\langle\Phi_i^a|\hat{V}|\Psi_0\rangle}{\epsilon_i - \epsilon_a}|\Phi_i^a\rangle \ , \tag{1.25}$$

where the factor of two is from the restricted formalism.

The matrix element appearing in Eq. (1.25) is easily evaluated with the Slater-Condon rules [12] to give

$$\langle \Phi_i^a | \hat{V} | \Phi_0 \rangle = -q \int d\vec{r}_1 \frac{\phi_i(\vec{r}_1 - \vec{R}_m)\phi_a(\vec{r}_1 - \vec{R}_m)}{|\vec{r}_1 - \vec{R}_a|} \tag{1.26}$$

where we have shown explicitly that the MOs are localized on the molecule at $\vec{R}_m$. Referring to Fig. 1.1 we can now make the replacement $\vec{r}_1 = \vec{r} + \vec{R}_m$ and expand $1/|\vec{r} + \vec{R}_m - \vec{R}_a|$ about $\vec{r} = 0$ to give

$$\langle \Phi_i^a | \hat{V} | \Psi_0 \rangle = -q \int d\vec{r} \phi_i(\vec{r}) \phi_a(\vec{r}) \left[\frac{1}{|\vec{R}_m - \vec{R}_a|} + \left(\hat{\nabla}_{R_m} \frac{1}{|\vec{R}_m - \vec{R}_a|} \right) \cdot \vec{r} + ... \right] . \tag{1.27}$$

The first term in Eq. (1.27) is zero by orthogonality, the second term can be written as

$$\langle \Phi_i^a | \hat{V} | \Psi_0 \rangle = -\vec{F}(\vec{R}_m) \cdot \vec{\mu}_{ia} \tag{1.28}$$

by recognizing the electric field (due to the point charge) at the center of the molecule as $\vec{F}(\vec{R}_m) = -q\hat{\nabla}_{R_m} 1/|R_m - R_a|$ and a dipole moment matrix element. This expression is expected to be accurate when the point charge at $\vec{R}_a$ is well separated from the molecule. Let us now use this wave function correction to calculate the dipole moment of the molecule up to linear order in the field.

$$\vec{\mu} = \sum_I Z_I \vec{R}_I - \langle \Phi_0 | \vec{r} | \Phi_0 \rangle + 2 \sum_{ia} \langle \Phi_0 | \vec{r} | \Phi_i^a \rangle \frac{\vec{F} \cdot \vec{\mu}_{ia}}{\epsilon_i - \epsilon_a} + 2 \sum_{ia} \langle \Phi_i^a | \vec{r} | \Phi_0 \rangle \frac{\vec{F} \cdot \vec{\mu}_{ai}}{\epsilon_i - \epsilon_a} + \mathcal{O}(\vec{F}^2) \tag{1.29}$$

$$\vec{\mu} = \vec{\mu}_0 - 4 \sum_{ia} \frac{\vec{F} \cdot \vec{\mu}_{ia}}{\epsilon_i - \epsilon_a} \vec{\mu}_{ai} + \mathcal{O}(\vec{F}^2)$$

where we have assumed that the MOs are real and have written the dipole moment in the absence of the field as $\vec{\mu}_0$. Eq. 1.29 can be simplified even further by defining the polarizability tensor,

$$\alpha_{xy} = -\sum_{ia} 4\frac{(\vec{\mu}_{ai})_x(\vec{\mu}_{ia})_y}{\epsilon_i - \epsilon_a} \tag{1.30}$$

so that the dipole is

$$\vec{\mu} = \vec{\mu}_0 + \boldsymbol{\alpha} \cdot \vec{F} + \mathcal{O}(F^2) \ . \tag{1.31}$$

This is the usual expression relating the induced dipole to the polarizability of the molecule and the electric field.[15, 16] The electric field causes single excitations which allow the zeroth order density to deform slightly and, as we shall see below, lowers the energy of the system. Finally lets go back and calculate the second order energy correction,

$$E^{(2)} = 2\sum_{ia} \frac{\langle \Psi_0|\hat{V}|\Phi_i^a\rangle\langle\Phi_i^a|\hat{V}|\Phi_0\rangle}{\epsilon_i - \epsilon_a} \ . \tag{1.32}$$

Inserting Eq. (1.28) yields

$$E^{(2)} = 2\sum_{ia} \frac{\vec{F}\cdot\vec{\mu}_{ai}\vec{F}\cdot\vec{\mu}_{ia}}{\epsilon_i - \epsilon_a} \tag{1.33}$$

$$E^{(2)} = -\frac{1}{2}\vec{F}\cdot\boldsymbol{\alpha}\cdot\vec{F} \tag{1.34}$$

$$E^{(2)} = -\frac{1}{2}\vec{\mu}_{ind}\cdot\vec{F} \ . \tag{1.35}$$

The result in Eq. 1.28 is to be compared to the usual expression for an electric dipole interacting with an electric field $E = -\vec{\mu}\cdot\vec{F}$.[16] Evidently, half of the stabilization energy of a dipole lined up with the field has gone missing. This missing energy will be discussed below, first, we would like to analyze the polarizability and the sign of the interaction. The xy^{th} element of the polarizability tensor tells us the magnitude of a dipole induced in the x direction if we apply a small electric field in the y direction. We intuitively expect that the diagonal elements will be much larger than the off diagonal elements, in fact if the MOs are real $\boldsymbol{\alpha}$ is symmetric and we can find some axis system in which it is diagonal. Eq. (1.30) indicates that the diagonal elements of $\boldsymbol{\alpha}$ are positive in an arbitrary axis system, therefore, the polarizability tensor is positive definite. This fact, together with Eq. (1.28) indicate that this effect, which we refer to as electronic polarization, is a stabilizing effect.

We have just demonstrated that if we place a small point charge some distance away from a molecule this charge induces an excess dipole in the molecule which then interacts with the point charge, and that this is a stabilizing effect. Eq. (1.28) indicates that the interaction of this induced dipole with the point charge is only half of the magnitude of a permanent dipole of the same size and direction interacting with the same point charge, why is this so? The answer is that some work must be done to induce the dipole and this work is apparently equal to $\vec{\mu}_{ind} \cdot \vec{F}/2$. This is called the work of polarization,[17, 18] or sometimes the self energy. [19] To understand this recall that prior to the placement of the point charge, the (unperturbed) molecule has associated with it a wave function that produces an energy that is a minimum (variational principle). When we place the point charge near the molecule, the wave function is perturbed to produce an induced dipole that interacts with this charge, lowering the interaction energy. However, if we computed the energy of the molecule with this new, perturbed wave function, it is necessarily higher than it was prior to the perturbation. Evidently, this energy is precisely $\vec{\mu}_{ind} \cdot \vec{F}/2$. We will come back to this in the next section.

The development above was overly simplistic and should be extended to many molecules. It is clear that one could consider a perturbative approach similar to that above, but extended to many molecules. In this approach one would obtain pairwise terms that would describe the polarization or induction effects of these molecules in a pairwise form. At higher orders there would be three- and higher-body terms that describe “higher order” induction effects. All orders of this perturbation can be captured in a self-consistent treatment (such as HF theory).[20] Suppose we have three molecules, the first molecule polarizes the first and the second. These polarized molecules then “back polarize” the first molecule. All of this very complicated mutual polarization occurs very rapidly until the total system wave function finds a minimum of energy. This is a many-body effect (body being molecule) and cannot be computed to high accuracy using a pairwise approximation. It is the hypothesis of this thesis that this many-body polarization is the most important many-body effect in molecular systems.

1.4 Electronic Polarization: A Macroscopic Viewpoint

To gain additional insight into the process of electronic polarization we will appeal to a macroscopic viewpoint. This will also allow us to discuss, in the context of common formulas such as Eq. (1.31), the connection between molecular properties and bulk electrostatic properties. This discussion closely follows Nitzan.[11] We consider matter that consists of neutral molecules that move as net neutral objects and possibly

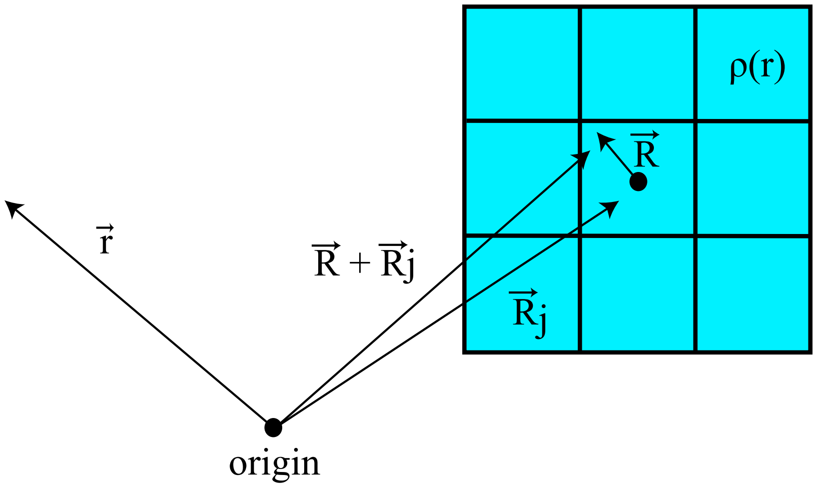

Figure 1.2: Coordinate System for a simple model of dielectric matter.

some mobile charges in the form of ions. Consider an infinite environment of such (dielectric) matter. We divide this matter into non-overlapping regions of space, each with volume $\mathcal{V}$. This volume is much larger than the size of the molecules composing the matter. Our system and coordinates are shown in Fig. 1.2. The electrostatic potential at point $\vec{r}$ is

$$\Phi(\vec{r}) = \sum_j \int_{\mathcal{V}} d\vec{R} \frac{\rho(\vec{R} - \vec{R}_j)}{|\vec{r} - (\vec{R} + \vec{R}_j)|} \ , \tag{1.36}$$

where $\rho(\vec{r})$ is the charge density and the sum is over the infinite number of non-overlapping regions, each integrated over their own volume. We now expand each term in the sum about $\vec{R}_j$

$$\Phi(\vec{r}) = \sum_j \int_{\mathcal{V}} d\vec{R} \ \rho(\vec{R} - \vec{R}_j) \left(\frac{1}{|\vec{r} - \vec{R}_j|} - \left(\hat{\nabla}_r \frac{1}{|\vec{r} - \vec{R}_j|} \right) \cdot \vec{R} \right) \tag{1.37}$$

which can be simplified by performing the integration to give the total charge (q_j) and dipole (d_j) of region j,

$$\Phi(\vec{r}) = \sum_j \left(\frac{q_j}{|\vec{r} - \vec{R}_j|} - \left(\hat{\nabla}_r \frac{1}{|\vec{r} - \vec{R}_j|} \right) \cdot \vec{d}_j \right) \ . \tag{1.38}$$

We choose not to use the symbol μ_j to denote a dipole because it is not a molecular dipole. We now introduce the coarse grained charge and dipole densities defined by

$$q_j = \rho(\vec{R}_j)\mathcal{V} \tag{1.39}$$

$$\vec{d}_j = \vec{P}(\vec{R}_j)\mathcal{V} \ , \tag{1.40}$$

$\vec{P}$ is also known as the polarization. In the macroscopic limit we replace the sum over regions by an integral [11]

$$\Phi(\vec{r}) = \int d\vec{R} \left(\frac{\rho(\vec{R})}{|\vec{r} - \vec{R}|} - \left(\hat{\nabla}_r \frac{1}{|\vec{r} - \vec{R}|} \right) \cdot \vec{P}(\vec{R}) \right) \ . \tag{1.41}$$

Next we use the identity $\hat{\nabla}_r(1/|\vec{r} - \vec{R}|) = -\hat{\nabla}_R(1/|\vec{r} - \vec{R}|)$ and integrate the second term in Eq. (1.41) by parts to obtain

$$\Phi(\vec{r}) = \int d\vec{R} \frac{1}{|\vec{r} - \vec{R}|} \left(\rho(\vec{R}) - \hat{\nabla}_R \cdot \vec{P}(\vec{R}) \right) \ . \tag{1.42}$$

This result states that the electrostatic potential arises from two types of density. The "free" charge density $\rho(r)$ and a "bound" charge density, the latter of which is proportional to the divergence of the dipole density. In a solution with no ions, the free charge is zero. Classical electrostatics only rigorously applies to *static* systems [16] so the charge density of matter is viewed in a macroscopic and time averaged sense.

Let us write the Poisson equation [16] for the bound plus free charge system,

$$\hat{\nabla} \cdot \vec{F} = 4\pi(\rho_f + \rho_b) = 4\pi(\rho_f - \hat{\nabla} \cdot \vec{P}) \ . \tag{1.43}$$

A standard procedure at this point is to define a the displacement field ($\vec{\mathcal{D}}$), which satisfies Poisson's equation for the free charge density, that is

$$\hat{\nabla} \cdot \vec{\mathcal{D}} = 4\pi\rho_f \ . \tag{1.44}$$

It is simple to work out that

$$\vec{\mathcal{D}} = \vec{F} + 4\pi\vec{P} \ . \tag{1.45}$$

In a system lacking free charge density (ions in a solution or electrons in a conductor) the displacement field represents any applied field and the polarization (dipole density) represents the response to this field. A linear dielectric is defined as a material that responds linearly with the applied field,

$$\vec{P}(\vec{r}, t) = \int d\vec{R} \int dt' \beta(\vec{r} - \vec{R}, t - t')\vec{\mathcal{D}}(\vec{R}, t'), \tag{1.46}$$

where β is the macroscopic polarizability and we have assumed that the response only depends on time differences and distances (the dielectric is homogenous spatially and temporally). Eq. (1.46) allows the dielectric to respond on different time and length scales and can be Fourier transformed using the convolution theorem to yield

$$\vec{P}(\vec{k}, \omega) = \beta(\vec{k}, \omega)\vec{\mathcal{D}}(\vec{k}, \omega) \tag{1.47}$$

in which the quantities of interest are functions of wave vector and frequency. For now, we assume that the response is local in space and time, dropping the dependence on $\vec{k}$

and ω. Using Eq. (1.45) in combination with Eq. (1.47) we can relate the displacement and electric fields

$$\vec{F} = (1 - 4\pi\beta)\vec{\mathcal{D}} = \frac{1}{\epsilon}\vec{\mathcal{D}} \tag{1.48}$$

which defines the dielectric constant ϵ and tells us that external electric fields are "screened" by the dielectric. We can also relate the polarization to the total electric field

$$\vec{P} = \left(\frac{\epsilon - 1}{4\pi}\right)\vec{F} = \chi\vec{F} \tag{1.49}$$

which defines the linear susceptibility.

As in the previous section we are primarily interested in the response of the dielectric material to the presence of some solute, for example, a point charge immersed in the dielectric. Eq. (1.46) tells us that the response to this point charge would be to induce a dipole density, it is the macroscopic analogue of $\mu_{ind} = \boldsymbol{\alpha} \cdot \vec{F}$. Eq. (1.46) states that the response can occur on several length and timescales. Let us assume that the response is local in space and can be characterized by two timescales, nuclear and electronic, and write the polarization as

$$\vec{P} = \beta_{tot}\vec{\mathcal{D}} = (\beta_e + \beta_n)\vec{\mathcal{D}} \tag{1.50}$$

where β_e and β_n represent the electronic and nuclear responses, respectively. These responses can be observed experimentally. Consider switching on a homogeneous electric field at some time t_0, at this time we assume the locally averaged dipole density is zero. At some later time, long compared to τ_e but short compared to τ_n, which are characteristic timescales of the electronic and nuclear responses, the dipole density becomes $\vec{P} = \beta_e \vec{\mathcal{D}}$. At much later times, long compared to τ_n, the polarization becomes $\vec{P} = \beta_{tot} \vec{\mathcal{D}}$. These responses are more commonly defined in terms of two dielectric constants, the electronic response can be characterized by

$$\vec{P}_e = \frac{1}{4\pi}\left(1 - \frac{1}{\epsilon_e}\right)\vec{\mathcal{D}}\ . \tag{1.51}$$

The *total* response is characterized by a similar equation,

$$\vec{P}_{tot} = \frac{1}{4\pi}\left(1 - \frac{1}{\epsilon_{tot}}\right)\vec{\mathcal{D}}\ . \tag{1.52}$$

Using these definitions it follows that the nuclear response is characterized by

$$\vec{P}_n = \vec{P}_{tot} - \vec{P}_e = \frac{1}{4\pi}\left(\frac{1}{\epsilon_e} - \frac{1}{\epsilon_{tot}}\right)\vec{\mathcal{D}}\ . \tag{1.53}$$

The term in parenthesis in Eq. (1.53) is known as the Pekar factor.[11] It is important to note that the dielectric "constant" is not simply a sum of electronic and nuclear components but that these two constants represent an extremely coarse grained dielectric function. ϵ_e is typically taken to be the "optical" dielectric constant, ϵ_∞ that represents the infinite frequency response of the electronic degrees of freedom of the material. In this thesis we take this definition, i.e., electronic responses are instantaneous. The constant ϵ_{tot} is often referred to as the static dielectric constant, it is the other limit, the zero frequency limit.

In this thesis we do not often rely on dielectric theory though it is useful to have this alternative view of matter. In short, we treat the ultrafast electronic induction approximately, but explicitly. The nuclear response is modeled by propagating the classical equations of motion forward in time, therefore, the nuclear component of the dielectric response is modeled accurately, within the approximations of whatever potential is being used. In the case of the hydrated electron this means that the motion of the nuclei is driven by the pseudopotential developed in this work together with a polarizable force field that models the electronic response of the solvent (dielectric) by the use of atom centered “linear response” dipoles similar to those discussed in the previous section. In the latter chapters of this thesis we discuss a fragment method whose goal it is to apply wave function theory to on-the-fly calculations of potential energies and there derivatives in order to propagate classical nuclear dynamics. In this treatment it is necessary to efficiently approximate the many-body components of the ultrafast dielectric response.

Before moving on we would like to use dielectric theory to compute the classical work of polarization and show that the result is the same as that of the previous section, even though the description of matter is quite different. The total energy stored in a continuous charge distribution can be written as [16]

$$W = \frac{1}{2} \int d\vec{r} \rho(\vec{r}) \Phi(\vec{r}) \ . \tag{1.54}$$

We can use Poisson’s equation in combination with integration by parts to show that this can be re-written in a convenient form,

$$W = \frac{1}{8\pi} \int d\vec{r} \vec{F}(\vec{r}) \cdot \vec{F}(\vec{r}) \ . \tag{1.55}$$

This equation expresses the total energy stored in a continuous charge distribution as a functional of the electric field. This is the energy required to construct a charge distribution by taking all charges from infinity and placing them in their *final* location, it does not contain the work of polarization.[16] To include this work we must consider a dielectric fixed in space and evaluate the *change* in work when we add some amount of free charge, this change in work is given by

$$\delta W = \int d\vec{r}\delta\rho_f(\vec{r})\Phi(\vec{r}) \ . \tag{1.56}$$

The change in free charge satisfies Poisson's equation using the displacement field, $\nabla \cdot \delta\vec{D} = 4\pi\delta\rho_f$, inserting this into Eq. (1.56) and integrating by parts gives

$$\begin{aligned} \delta W &= \frac{1}{4\pi}\int d\vec{r}\vec{F}(\vec{r}) \cdot \delta\vec{\mathcal{D}}(\vec{r}) && (1.57) \\ \delta W &= \frac{1}{2}\delta\left(\frac{1}{4\pi}\int d\vec{r}\vec{F}(\vec{r}) \cdot \vec{\mathcal{D}}(\vec{r})\right) \\ W &= \frac{1}{8\pi}\int d\vec{r}\vec{F}(\vec{r}) \cdot \vec{\mathcal{D}}(\vec{r}) \ . && (1.58) \end{aligned}$$

In the second line we have used the fact that $\vec{\mathcal{D}} = \epsilon\vec{F}$ to rewrite the infinitesimal and in the final line we have simply recognized the total work. This energy expression contains all of the terms in Eq. (1.54) plus the work required to distort the dielectric, the work of polarization. By subtracting Eq. (1.55) from the final line of Eq. (1.58) and inserting Eq. (1.45) for $\vec{\mathcal{D}}$ we find that the polarization work is

$$W_{pol} = \frac{1}{2}\int d\vec{r}\vec{P}(\vec{r}) \cdot \vec{F}(\vec{r}) \ . \tag{1.59}$$

This result states that the work of polarization is the integral, over all space, of the dipole density dotted into the total electric field. This is the macroscopic version of the work of polarization of a single dipole, such as that discussed in the microscopic version of the theory. It is important to recognize that this work depends on the total electric field, not just that associated with the free charge. That is, the free charge induces some dipole density in the dielectric which contributes to the total field. If we were to consider some small patch of dielectric, the dipole density in this patch would depend on the free charge density as well as the dipole density in the immediately surrounding vicinity. The dipole densities of many patches would equilibrate and would be a many-body process, where in this case body is a patch. From this treatment it should be clear that this many-body induction process is a mean field effect (as opposed to a correlation effect) and therefore can be included in a self-consistent procedure. This is the approach taken in this thesis.

1.5 A Short Introduction To the Hydrated Electron

The notion of a solvated electron was first invoked by Charles A. Kraus in 1908 in an article reporting experiments concerning electrical currents in solutions of alkali metals dissolved in liquid ammonia.[21] The first *observation* of the solvated electron in ammonia was probably much earlier, as it had been known for some time that solutions of alkali metals in ammonia produced a blue color, now attributed to the solvated electron. The fact that this blue color (and absorption maximum) arose from the solvated electron was first pointed out by Gibson and Argo in 1918.[22] While the solvated electron in ammonia is quite long lived, the aqueous electron has a lifetime on the order of microseconds.[23] For this reason, the absorption spectrum was not recorded until 1962, by Hart and Boag.[24] It is now known that the hydrated electron (e^-_{aq}) is one of the primary products in the radiolysis of water and because of this, understanding this species is important to fields as disparate as radiation biology and nuclear waste management.[25–27]

A single water molecule does not bind an excess electron while the water dimer supports a dipole-bound anionic state.[28] In this sense, the existence of bound states of the excess electron is a many-body effect and hence all properties of this species are solvent effects. This is a unique aspect of this highly quantum mechanical solute. Direct experimental observation of the structure, relaxation dynamics and energetics of this species in the liquid phase is complicated due to the difficulty of producing samples with high concentrations of hydrated electrons and contamination from a large number of other species formed in pulse radiolysis experiments.[25, 29] For this reason studies on finite-sized cluster analogues of the hydrated electron have been used to estimate the bulk binding energy as well as to investigate the non-adiabatic relaxation dynamics.[29, 30] Extrapolation of the cluster properties to the bulk limit has been called into question due to a controversy over whether the clusters observed by photoelectron spectroscopy correspond to electrons solvated on the surface of the cluster, or internally.[30–35] This debate is what initially interested us in this problem and we will use this controversy to motivate our work.

Finite-sized anionic water clusters were first observed by Haberland and co-workers in the 1980s by mass spectrometry.[36, 37] A fews year later Barnett *et al.* used path integral monte-carlo simulations to study these clusters and suggested that the excess electron could either bind to the surface or the interior of the cluster. The internal states were seen to have binding energies which scaled with cluster size as $N^{-1/3}$, where N is the number of water molecules.[31, 38, 39] Shortly afterword Coe *et al.*

reported photoelectron spectra of anionic water clusters up to $N = 69$ and found a linear trend in the binding energy, when plotted against $N^{-1/3}$,[30] these data were extrapolated to a bulk vertical binding energy of 3.3 eV. Interestingly, the surface isomer binding energies predicted by Barnett *et al.* were in better absolute agreement with the photoelectron data than the internalized states.[31] Barnett, Landman, Makov and Nitzan later observed, using both simulation and dielectric theory, that the optical absorption spectra of internally bound states were converged to the bulk value at small cluster size while surface states exhibited a slow convergence.[40] In 1994 Makov and Nitzan pointed out that, according to dielectric theory, both surface and internally bound electrons have binding energies that scale with cluster size as $N^{-1/3}$, this scaling law is insufficient to definitively assign an isomer class as surface or internal.[9]

In 1997 Ayotte and Johnson measured the absorption spectra of anionic water clusters from $N = 6 - 50$ and found that these spectra are strongly red-shifted compared to the bulk (1.72 eV) and blue-shift with increasing clusters size.[41] In 2005 Verlet *et al.* demonstrated that by varying the source conditions in the gas expansion, one could form three isomer classes, the populations of which could be continuously modified.[34] Around this same time Turi *et al.* used a mixed quantum/classical simulation approach (similar to that used in this thesis) and found that internally bound clusters were not stable up to $N > 100$ and may only be kinetically stable in that range. They observed that the absorption maxima of the surface bound isomers blue-shifted with cluster size but that the maxima of internally bound electronic "states" did not.[42] Turi *et al.* made the rather bold claim that all experimental observations reported thus far were consistent with surface isomers.[42] This point was immediately questioned in the literature.[33, 35] In their comment, Verlet *et al.* pointed out that the binding energies of the internally bound isomers were actually in much better agreement with the photoelectron data for the strongest binding isomer than the surface isomers were.[35]

It is not surprising that comparisons between experiment and theory have not been quantitative. Accurate computational prediction of vertical electron binding energies (VEBE), sometimes referred to as vertical detachement energies (VDE), is a demanding task. This is because local minima on the anionic potential energy surface tend to be located in regions of configuration space that are high in energy on the neutral potential energy surface.[43] This is no different in the case of a "classical" ion such as Iodine. What is different is the fact that one cannot instantaneously remove an Iodine ion, but one can (essentially instantaneously) promote an electron to a vacuum level. In fact, the VDE measured by photoelectron spectroscopy serves as a primary experimental observable in the study of anionic water clusters. This means that an adequate description of local minima on the anion potential energy surface is as important as an adequate description of unfavorable configurations on the neutral potential energy surface, we hope that a "polarizable" water model (one that treats many-body induction explicitly) is more accurate near these points than one that is not. Additionally, and more importantly, is the observation that the electrostatic environment immediately before and after an electron ejection event is dramatically different (charged versus neutral). This is also true in the case of optical absorption spectra. We presume that in these cases, the electronic response of the water molecules is large. If we wish to *directly* compare predicted to experimentally observed binding energies, the electronic response of the solvent molecules should be explicitly included. However, since the size of systems we are interested in studying is large, we must include this response approximately. This is the approach we have taken in constructing and applying an electron-water potential.

Our potential is initially developed in chapter 2 with promising results as compared to *ab initio* predictions. This potential yielded poor results when applied to the bulk hydrated electron, as discussed in Ref. [43], and so was re-parameterized. This is discussed in chapter 3, along with application to the liquid phase. This chapter highlights the important effects of including electronic polarization in this system. Chapter 4 provides a comment on a recent pseudopotential constructed by Larsen, Glover and Schwartz.[44] This work underscores the difficulty in constructing such potentials and the need for efficient, on-the-fly, *ab initio* molecular dynamics techniques. The optical absorption spectrum, initially discussed in chapter 3, is studied further in chapter 5. The fact that the electronic response of the solvent is included in a self-consistent treatment of the electron leads to a state specific Hamiltonian, in turn, leading to non-orthogonal solutions. This is discussed in chapter 6, along with a simple algorithm for finding strictly orthogonal eigenstates for this state specific Hamiltonian.

1.6 A Brief Introduction to Fragment Methods

Post-HF schemes, such as Møller-Plesset perturbation theory (MP), configuration interaction (CI) and coupled cluster theory (CC), seek to improve the description of the wave function and provide a systematically improvable route to accurate energetics.[12, 13] These wave function methods also scale poorly with system size which prevents them from being useful in condensed phase applications.[45] Wave function methods improve upon HF theory by treating electron correlation (absent in the mean-field treatment). Electrons are only correlated at short range which implies that these methods scale unphysically with system size.[46] In order to apply these accurate methods to molecular interactions in condensed environments one must exploit locality, that is, one must understand the length-scale over which particular interactions persist and utilize distance-based cutoffs to improve asymptotic computational scaling.[47]

One way to reduce the cost of electronic structure calculations [including HF and density functional theory (DFT)] is to employ some sort of fragmentation scheme. Consider the matrix representation of a Hamiltonian for a system containing four molecules (which we will refer to as fragments) in a basis that is constructed from functions that are localized on these fragments. For example, an atom-centered Gaussian basis set. We can schematically think about this matrix as being composed of molecular blocks and there couplings,

$$\mathbf{H} = \begin{pmatrix} H_{11} & H_{12} & H_{13} & H_{14} \\ H_{21} & H_{22} & H_{23} & H_{24} \\ H_{31} & H_{32} & H_{33} & H_{34} \\ H_{41} & H_{42} & H_{43} & H_{44} \end{pmatrix} \tag{1.60}$$

where the diagonal blocks represent intramolecular interactions and the off-diagonal blocks represent intermolecular interactions. If we neglect the off-diagonal blocks we can diagonalize the molecular (diagonal) blocks separately, instead of diagonalizing the full matrix. This leads to a block diagonal density matrix; the eigenfunctions of the molecular blocks are expanded only in terms of basis functions local to that molecule. This procedure also leads to a potentially significant computational savings since we replace a diagonalization step which scales as $\mathcal{O}((N_{basis}^{tot})^3)$ with four steps that scale as $\mathcal{O}((N_{basis}^{frag})^3)$, where N_{basis}^{frag} is the number of basis functions on a fragment and N_{basis}^{tot} is the total number of basis functions. We have neglected interactions in the Hamiltonian that couple the molecules and so we must find a way to include these. If we can find an efficient and accurate way to do this we would have an efficient and accurate method. There are many ways to include these interactions and correspondingly many fragment methods, a small number of which we will mention only to illustrate the different approaches and motivate our own.

The most conceptually straightforward fragment method is the SCF for molecular interactions (SCF-MI) method originally developed by Stoll, Wagenblast and Prueß [48] and recently revisited by Khaliullin, Head-Gordon and Bell.[49] This is an approach to efficiently approximate the HF SCF energy while simultaneously eliminating basis set superposition error (BSSE). The MOs belonging to a particular fragment (molecule) are expanded only in terms of AOs localized on that fragment, Khaliullin *et al.* term these absolutely localized molecular orbitals (ALMOs).[49] The ALMOs on one fragment are not required to be orthogonal to ALMOs on another fragment. The full Fock matrix in this basis is projected onto molecular blocks, which are then diagonalized. This yields a new density matrix which is used to reconstruct the Fock matrix. In this approach, the intermolecular interactions are not made any more approximate than the underlying HF theory so SCF-MI requires construction of the Fock matrix in the full basis set, an expensive step. The projection of the full Fock matrix onto molecular blocks makes clear that one can *implicitly* include the effect of the molecular coupling in the monomer matrices. One potential difficulty with this approach is that it is difficult to describe charge-transfer interactions in the ALMO basis.[49, 50]

A popular approach to reproducing the super-system energy of a model chemistry (such as MP2 or CCSD) by fragmentation is the many-body expansion. In this approach one writes the total energy of a system composed of many molecules as

$$\begin{aligned} E_{tot} = & \sum_i E_i^{(1)} + \sum_i \sum_{j>i} \left(E_{ij}^{(2)} - E_i^{(1)} - E_j^{(1)} \right) \\ & + \sum_i \sum_{j>i} \sum_{k>j} \left(E_{ijk}^{(3)} - E_{ij}^{(2)} - E_{ik}^{(2)} - E_{jk}^{(2)} - E_i^{(1)} - E_j^{(1)} - E_k^{(1)} \right) + \ldots \end{aligned} \tag{1.61}$$

where $E_i^{(1)}$ is the energy of monomer i, $E_{ij}^{(2)}$ is the energy of the ij dimer, etc. The first term in Eq. 1.61 is the sum of monomer energies, the second term is the sum of dimer *interaction* energies, the third, trimer interaction energies and so on. For a system of N monomers this expansion is exact if one retains terms up to $E^{(N)}$, it is also more expensive than the super-system (N-body) calculation. However, if one can accurately truncate the expansion at low order significant computational savings can be made. Dahlke *et al.* have demonstrated that if one embeds the monomer, dimer, trimer, etc. calculations in the approximate electrostatic potential of the other monomers by way of point charges, the many-body expansion is essentially converged at three-body terms.[51–54] Dahlke *et al.* have also shown that if one performs a HF super-system calculation, the many-body expansion of the MP2 correlation energy (again using electrostatic embedding) is convergent with only two-body terms.[53] Beran has extended this line of thinking by evaluating the many-body interactions with the use of a force field that explicitly treats many-body induction, followed by a many-body expansion of the MP2 energy keeping only two body terms.[55, 56] The work of Dahlke *et al.* indicates that a full many-body description is important at the mean field level while correlation can be treated fairly accurately in a pairwise manner. The work of Beran has demonstrated that by many-body, we mean to say many-body induction. If one can include this many-body induction into the description of the monomers, correlation can be treated as a pairwise sum.

Of interest to us is the explicit polarization (X-Pol) potential, developed by Gao and co-workers.[57–59] This is an approach that is not intended to reproduce any particular model chemistry, but is intended as a "next-generation" force field.[60] X-Pol utilizes the ALMO *ansatz* and fragments interact via approximate electrostatics (this approach will be described in detail in chapter 7). X-Pol neglects exchange repulsion, a result of the fact that the X-Pol wave function does not satisfy the Pauli principle.

For this reason, the X-Pol energy is supplemented with a Lennard-Jones (LJ) empirical potential energy function to describe both exchange repulsion and dispersion interactions.[58] The X-Pol procedure is very efficient because one only constructs and diagonalizes fragment Fock matrices, nothing is done in the full basis. The X-Pol potential describes intramolecular interactions from first principles and approximates electrostatic interactions. It is iterative and as such, should describe many-body induction effects, albeit approximately. We were interested in this procedure but wanted to eliminate the need for LJ parameters. Our idea was to obtain exchange repulsion and dispersion by a perturbative procedure after the SCF iterations were complete. During the perturbative procedure we would also correct for inaccuracies in the approximate electrostatics. We assume that the many-body interactions present in the SCF iterations are reasonably accurate so that the perturbative scheme can be applied in a pairwise fashion. This procedure is described in detail in chapter 7.

CHAPTER 2

The static-exchange electron–water pseudopotential, in conjunction with a polarizable water model: A new Hamiltonian for hydrated-electron simulations [2.1]

2.1 Introduction

The chemical physics literature is replete with electron–water interaction potentials,[38, 39, 61–71] which have long been used (in conjunction with various methods of one-electron quantum mechanics) to examine the nature of the hydrated electron.[31, 38, 39, 42, 61–83] As such, a person might reasonably question whether the chemical physics community genuinely needs yet another hydrated-electron model, especially in view of a study by Turi *et al.*[66] that seems to validate certain assumptions that were made previously in the course of constructing electron–water pseudopotentials, for example, the use of a local potential to model the exchange interaction. We note, however, that the pseudopotential of Turi and Borgis (TB),[67] which was parameterized based on the work of Turi *et al.*,[66] has fueled[34, 35, 42] (rather than

---

[2.1] This chapter appeared as an article in the *Journal of Chemical Physics* in 2009, volume 130, page 124115.

settled) the old controversy regarding the nature and evolution of the electron binding motifs in finite $(H_2O)_n^-$ clusters, and whether photoelectron spectroscopy experiments in such clusters probe surface-bound or cavity-bound states of the unpaired electron.[30, 31, 34, 35, 42, 84–87]

At a phenomenological level, there are at least two important features missing from the TB hydrated-electron model that one might reasonably expect to be qualitatively important. The first of these is the absence of any dynamical correlation between the unpaired electron and the charge distributions of the classical water molecules, *i.e.*, the absence of electron–water dispersion interactions. *Ab initio* electronic structure calculations suggest that such interactions are significantly larger for cavity-bound electrons than they are for surface-bound electrons.[1] Jordan and co-workers[68–70, 77–79] address this deficiency using a quantum-mechanical Drude oscillator for each H_2O molecule;[68, 69] for prediction of vertical electron binding energies (VEBEs), this appears to be the most accurate model currently available, short of *ab initio* quantum chemistry. For an $(H_2O)_n^-$ cluster, however, this model involves not a one-particle quantum mechanics problem but rather an $(n+1)$-particle problem. Although the Drude model is still substantially cheaper than *ab initio* calculations, exhaustive simulations have so far been reported only for $(H_2O)_{13}^-$ and smaller clusters.[69, 70, 79]

A second potential deficiency of the TB model is its use of a fairly crude water–water interaction potential, namely, the simple point charge (SPC) model.[88, 89]

Electrostatic interactions are represented in the SPC model by means of fixed, atom-centered point charges, and we will demonstrate that this potential is rather inaccurate for predicting conformational energies of neutral water clusters. Meanwhile, considerable evidence points to the fact that the neutral water potential is often more important in determining VEBEs than is the electron–water potential,[90, 91] because the electron–water interaction stabilizes water networks that are extremely high in energy (and far from any stationary point) on the neutral water potential surface. Neutral water potentials, however, are rarely parameterized using such high-energy structures, and simple functional forms are not flexible enough to describe structures that are far from any local minimum for neutral water. As detailed in Refs. [90] and [91], one consequence in the context of $(H_2O)_n^-$ is that small differences in the cluster geometry, which scarcely affect the total electron–water interaction energy, often substantially modify the water–water interaction and hence the VEBE, defined as

$$\mathrm{VEBE} = E_{\mathrm{neutral}} - E_{\mathrm{anion}} \ . \tag{2.1}$$

Changes in the underlying water potential have been shown, for example, to produce qualitatively different isomer distributions for $(H_2O)_6^-$ in finite-temperature Monte Carlo simulations.[79]

At present, the manner in which these facets of the TB model manifest as observables remains unknown. As a first step toward investigating this issue, we report a re-parameterization of the electron–water interaction potential, following the TB procedure but using the polarizable AMOEBA water model,[14] which is known to perform well (compared to *ab initio* calculations) for structures and conformational energies of neutral water clusters.[14, 92] The result is a one-electron model Hamiltonian for $(H_2O)_n^-$ in which the one-electron wave function and the water molecules polarize one another self-consistently. An electron–water polarization potential thus arises in a natural way, via induced dipoles on the water molecules, and does not need to be tacked on in an *ad hoc* fashion, as it is in the TB model. (The form of the TB polarization potential can be recovered as a well-defined approximation to the polarization potential arising from our model.)

We calculate eigenstates of the resulting one-electron Hamiltonian on a three-dimensional real-space grid, using a modified Davidson algorithm that is considerably simpler than the Lanczos-based algorithm often used in hydrated-electron simulations.[93] Based on comparisons to *ab initio* electronic structure calculations in $(H_2O)_n^-$ clusters ($n = 2$–33), the new model appears to be significantly more accurate than the TB model, for both relative conformational energies and VEBEs.

2.2 Background

2.2.1 Pseudopotential theory

To date, most electron-water pseudopotentials have been based upon the so-called static-exchange (SE) approximation.[39, 64, 66, 94] Within this approximation, one considers the interaction of the excess electron with the ground-state wave function of the isolated molecule, in our case H_2O. The system wave function is taken as an antisymmetrized product of the excess electron orbital and the frozen ground state wave function of the target molecule (itself an antisymmetrized product of spin–orbitals) which leads to a one-electron eigenvalue equation for the excess electron:[64, 66, 94]

$$\hat{H}_{\mathrm{SE}}|\Psi\rangle = (\hat{T} + V_n + V_c + \hat{V}_x)|\Psi\rangle = \varepsilon\,|\Psi\rangle\ . \tag{2.2}$$

Here, $\hat{T}$ is the one-electron kinetic energy operator, V_n is the electron–nuclear interaction, V_c is the electronic Coulomb energy, and $\hat{V}_x$ is the (nonlocal) exchange operator. The quantities V_c and $\hat{V}_x$ are identical to the Coulomb and exchange operators in a Hartree–Fock calculation of the isolated neutral molecule, so the lowest energy solutions of Eq. (2.2) are the doubly-occupied molecular orbitals (MOs) of the neutral H_2O, followed by the ground–state excess electron orbital. The highest occupied MO (HOMO) in the SE approximation is the lowest unoccupied MO (LUMO) in the Hartree–Fock calculation.

Although Eq. (2.2) is a one-electron eigenvalue equation, construction of $\hat{H}_{\mathrm{SE}}$ requires the H_2O MOs. Our goal is to remove this dependence, so that we can define a local potential $V(\vec{r})$ that can be readily evaluated and fit to some analytical expression, thus converting Eq (2.2) into a relatively simply one-electron eigenvalue equation $(\hat{T} + V)|\Psi\rangle = \varepsilon|\Psi\rangle$.

To motivate this approximation, consider the two reasons why Eq. (2.2) is not already such an equation: first, the nonlocality of $\hat{V}_x$ means that the exchange interaction depends on the core MOs; and second, the MOs must remain orthogonal (which prevents the excess electron from penetrating significantly into the core molecular region). It is common to approximate the exchange interaction with some local functional of the density, as in the electron-gas (or local-density) approximation,[95] which affords an attractive potential near the core region. In order to avoid collapse of the one-electron wave function into the molecule, a repulsive potential must be added. Early pseudopotentials[39, 62, 63] used a simple exponential for the repulsive potential, a functional form that can be motivated based on density-functional considerations of the change in kinetic energy upon assembling the system (*e.g.*, H_2O^-) from its constituents ($H_2O + e^-$).[96] As an alternative, we employ a repulsive potential derived from an approximate version[64] of Philips-Kleinman (PK) theory.[97] This repulsive potential has the form

$$V_{rep}(\vec{r}\,) = -\sum_{\alpha} \varepsilon_\alpha \, \psi_\alpha(\vec{r}\,) \int d\vec{r}\,' \; \psi_\alpha(\vec{r}\,') \; , \tag{2.3}$$

where the ψ_α are the MOs of neutral H_2O, with orbital energies ε_α.

The repulsive potential in Eq. (2.3) was derived from exact PK theory by Schnitker and Rossky[64] by expressing the wave function of the excess electron as a sum of a nodeless pseudo-wave function and a linear combination of the MOs for neutral H_2O. By subtracting out the core oscillations, one obtains a Hamiltonian that is (by construction) written for a nodeless wave function. Simplification of this Hamiltonian to yield the repulsive potential in Eq. (2.3) involves two assumptions:[64] first, that the excess electronic eigenvalue is much less than that of the core MOs (which is validated by Hartree Fock calculations); and second, that the pseudo-wave function is constant in the core region. Although the second approximation is less well-grounded than the first, it was later validated by Turi and Borgis.[67]

The repulsive potential can be included in the SE Hamiltonian to obtain a Hamiltonian that contains a local pseudopotential that is easily evaluated:

$$\hat{H}_{\mathrm{SE}}(\vec{r}\,) = \hat{T} + V_n(\vec{r}\,) + V_c(\vec{r}\,) + V_x[\rho(\vec{r}\,)] + V_{rep}(\vec{r}\,)\ . \tag{2.4}$$

Since the core MOs used to construct these local potentials are frozen, polarization is not included in the SE treatment. Previous workers[39, 64, 67] have dealt with this deficiency by grafting an *ad hoc* polarization potential onto an otherwise nonpolarizable model, as detailed in the next section. We will instead use a polarizable water potential, from which an electron–water polarization potential arises in a natural way. Our approach is described in Section 2.3.

2.2.2 Turi–Borgis (TB) model

In the model potential given by TB,[67] the interaction between the unpaired electron and a given atomic site (oxygen or hydrogen) has a very simple functional form, expressed in terms of three error functions:

$$V^{TB}_{es/rep} = \frac{1}{r_i}\Big\{-q^i\ \mathrm{erf}(A^i_1\, r_i) + B^i_1\left[\mathrm{erf}(B^i_2\, r_i) - \mathrm{erf}(B^i_3\, r_i)\right]\Big\}\ , \tag{2.5}$$

which incorporates both repulsion (rep), in the sense discussed in the previous section, as well as electrostatics (es). Beginning with Eq. (2.5), summation over repeated indices is implied; atomic units are used throughout. The quantity r_i represents the distance between the electron and the ith nucleus, q^i are the point charges of the SPC water model, and the A^i_j and B^i_j are empirical parameters. These parameters were not fit to reproduce the various components (*i.e.*, the local potentials) of the pseudopotential derived from the SE approximation, but rather to reproduce the eigenvalue and density of the excess electron obtained by solution of Eq. (2.2). It is clear, however, that the first term in Eq. (2.5) is a damped Coulomb interaction, while the second and third terms together represent a repulsive interaction. It is important to damp the Coulomb potential to avoid singularities at the atomic sites.

TB suggest that the ability of their potential to predict the bulk optical absorption spectrum with reasonable accuracy is due to the fact that the potential in Eq. (2.5) is much less repulsive at the molecular core than previous potentials.[67] The spectrum obtained with their potential is redshifted from previous potentials, an effect that is suggested to arise from electron penetration into the core molecular region.

The polarization potential used by TB is taken from Barnett *et al*:[39]

$$V_{pol}^{TB} = -\frac{\alpha}{2(r_{oxy}^2 + C_{oxy}^2)^2} \ , \tag{2.6}$$

where α is the isotropic polarizability of H_2O, r_{oxy} is the electron–oxygen distance [with an implied summation over oxygen sites in Eq. (2.6)], and C_{oxy} is a parameter that is fit to give the correct ground-state eigenvalue of the bulk aqueous electron. This potential is spherically symmetric and has the proper asymptotic distance dependence, but the presence of the electron has no effect on the water–water interactions defined by the SPC water model. In this way, one might consider the TB potential to be a truly adiabatic surface, *i.e.*, the electron–water and water–water potentials are coupled only through geometry.

Our implementation of the TB model employs the harmonic version of the flexible SPC potential,[89] as we experienced difficulties using the Morse version of the stretching potential; see Ref. [91] for a detailed discussion. The SPC water model consists simply of a Coulomb interaction between point charges located at the oxygen and hydrogen sites, a 12-6 Lennard-Jones potential between the oxygen sites, and intramolecular interactions that are quadratic in the atomic displacements.

2.3 New electron–water pseudopotential

Our new electron–water model is based upon the polarizable water model known as AMOEBA (Atomic Multipole Optimized Energetics for Biomolecular Applications), which is part of a more general polarizable molecular mechanics force field developed by Ren and Ponder.[14] In order to establish our notation, and to lay the groundwork for our model, we briefly review AMOEBA's electrostatic and polarization potentials in Section 2.3.1. (For complete details, see Ref. [14].) Following this, our electron–water model is introduced in Section 2.3.2.

2.3.1 AMOEBA water potential

Electric multipole moments through the quadrupole are obtained from a distributed multipole analysis[98, 99] of gas-phase H_2O at the MP2/aug-cc-pVTZ level of theory, where MP2 denotes second-order Møller–Plesset perturbation theory. The quadrupole moments of the water monomer were adjusted by scaling the gas-phase moments by a factor of 0.73 in order to reproduce the "flap-angle" of the dimer, as compared to *ab initio* results.

Using the notation of Applequist,[18, 100] we may collect the electrical moments at site i into a “polytensor”

$$\mathbf{M}_i = [q^i,\, \vec{\mu}^{\,i},\, \mathbf{Q}^i]^\top \tag{2.7}$$

consisting of the monopole, dipole, and cartesian quadrupole moments, respectively. We use cartesian multipole moments[100] in the equations to follow, but note that AMOEBA uses traceless quadrupole moments,[14] which differ by a factor of 3 from the cartesian moments. (The trace of $\mathbf{Q}^i$ is not unique, and our convention differs from that in Ref. [14], but either formulation yields exactly the same electrostatic energy.[15]) Define the interaction tensor elements as

$$t^{ij} = \frac{1}{r_{ij}}\ , \tag{2.8a}$$

$$t^{ij}_{\alpha} = \hat{\nabla}^i_{\alpha}\, \frac{1}{r_{ij}}\ , \tag{2.8b}$$

and

$$t^{ij}_{\alpha\beta} = \hat{\nabla}^i_{\alpha} \hat{\nabla}^i_{\beta}\, \frac{1}{r_{ij}}\ , \tag{2.8c}$$

where i and j index atomic sites, $\alpha, \beta \in \{x, y, z\}$, and $r_{ij} = |\vec{r}_j - \vec{r}_i|$. From this we can construct an interaction polytensor

$$\mathbf{T}_{ij} = \begin{pmatrix} t^{ij} & t^{ij}_{\alpha} & t^{ij}_{\alpha\beta} \\ -t^{ij}_{\alpha} & -t^{ij}_{\alpha\beta} & -t^{ij}_{\alpha\beta\gamma} \\ t^{ij}_{\alpha\beta} & t^{ij}_{\alpha\beta\gamma} & t^{ij}_{\alpha\beta\gamma\epsilon} \end{pmatrix}\ , \tag{2.9}$$

where the negative signs in alternating rows arise from the identity

$$\hat{\nabla}^i\, \frac{1}{r_{ij}} = -\hat{\nabla}^j\, \frac{1}{r_{ij}}\ . \tag{2.10}$$

This allows us to write the full electrostatic potential in a simple, compact form:

$$V_{es} = \tfrac{1}{2}\, \mathbf{M}_i^\top\, \mathbf{T}_{ij}\, \mathbf{M}_j. \tag{2.11}$$

Equation (2.11) is merely a compact notation for the double Taylor series expansion of the Coulomb potential between two charge distributions; the multipole moments are the coefficients of this expansion.

In AMOEBA, polarization is represented by induced dipoles at each atomic site,

$$\vec{\mu}^{\,i}_{ind} = \alpha_i \, \vec{F}_i \; , \tag{2.12}$$

or in polytensor notation

$$\mathbf{M}_i^{ind} = \alpha_i [0, \, \vec{F}_i \, , \, 0]^\top = \alpha_i \, \mathcal{F}_i \; , \tag{2.13}$$

where $\vec{F}_i$ is the electric field due to all other sites, α_i is the isotropic polarizability at the ith site, and $\mathcal{F}_i = [0, \vec{F}_i \, , 0]^\top$ is defined for convenience. Since $i \in \{1, 2, \ldots, 3N\}$ for an N-atom system, Eq. (2.12) constitutes a set of $3N$ linear equations that must be solved self-consistently, since the induced dipoles themselves contribute to the electric field.

If we write the full multipole polytensor as the sum of permanent and induced terms, keeping in mind that only dipoles are treated as polarizable within the AMOEBA model, then Eq. (2.11) may be partitioned according to

$$V_{es} = V_{es}^{perm} + V_{pol} \; , \tag{2.14}$$

where

$$V_{es}^{perm} = \tfrac{1}{2} \, (\mathbf{M}_i^{perm})^\top \, \mathbf{T}_{ij} \, \mathbf{M}_j^{perm} \tag{2.15}$$

is the electrostatic interaction arising from the permanent multipoles and

$$V_{pol} = (\mathbf{M}_i^{perm})^\top \, \mathbf{T}_{ij} \, \mathbf{M}_j^{ind} + \tfrac{1}{2} \, (\mathbf{M}_i^{ind})^\top \, \mathbf{T}_{ij} \, \mathbf{M}_j^{ind} \tag{2.16}$$

is a polarization potential, defined as the sum of all electrostatic terms involving induced dipoles. It should also be clear that the electric field at site i can be generated by a polytensor $\mathcal{E}_i$, where

$$\mathcal{E}_i = [\phi_i,\, \vec{F}_i,\, \mathbf{G}_i]^\top = -\mathbf{T}_{ij}(\mathbf{M}_j^{perm} + \mathbf{M}_j^{ind}) \; . \tag{2.17}$$

The quantities ϕ_i, $\vec{F}_i$ and $\mathbf{G}_i$ are, respectively, the electric potential, electric field, and electric field gradient at the ith site.

The final term that defines the electrostatics is the "self-energy",[19] *i.e.*, the work required to distort a charge distribution from its equilibrium state (an isolated molecule) to its final state in the supramolecular system. In the case of the linear response dipoles in Eq. (2.12), this work is given by[17, 18]

$$W_{pol} = \frac{(\mathbf{M}_i^{ind})^\top \mathbf{M}_i^{ind}}{2\,\alpha_i} \; . \tag{2.18}$$

Using Eqs. (2.13) and (2.17) to simplify, and noting that $\mathcal{F}_i^\top \mathbf{M}_i^{ind} = \mathcal{E}_i^\top \mathbf{M}_i^{ind}$ when only the dipoles are polarizable, the final expression for the electrostatic contribution to the AMOEBA water potential is

$$\begin{aligned} V_{tot} &= V_{es}^{perm} + V_{pol} + W_{pol} \qquad (2.19) \\ &= \tfrac{1}{2}\,(\mathbf{M}_i^{perm})^\top\, \mathbf{T}_{ij}\, \mathbf{M}_j^{perm} + \tfrac{1}{2}\,(\mathbf{M}_i^{perm})^\top\, \mathbf{T}_{ij}\, \mathbf{M}_j^{ind} \; , \end{aligned}$$

where the second equality reflects how the potential in AMOEBA is actually implemented. It should be noted that the electric field due to all atomic-site multipoles is damped using a Thole-type scheme,[101] in which dipole interactions are attenuated by replacing one of the point dipoles by a smeared charge distribution. Interaction elements analogous to those found in Eqs. (2.8) are obtained by differentiation. This procedure is used to avoid the so-called polarization catastrophe, in which the electric field diverges as any site–site distance approaches zero.

Dispersion and exchange repulsion are modeled in AMOEBA using a buffered 14-7 potential. Unlike SPC, AMOEBA uses pairwise van der Waals interactions at every site in the system. DeFusco *et al.*[102] point out the necessity of including repulsive interactions between all atomic sites in order to describe the potential energy surface of the water dimer at oxygen–oxygen distances shorter than about 2.65 Å.

2.3.2 Electron–water model

We are now prepared to describe the components of our electron–water potential and the fitting procedure used to parameterize it. To avoid singularities arising from the electron–water Coulomb interaction, electrostatic interactions between the electron and the water molecules must be damped, while the electric field due to the electron (which is used to induce the water dipoles) must also be damped, in order to avoid polarization catastrophes of the sort described above. The damping of both interactions is done in the same manner. In the spirit of the TB potential, we define a damped Coulomb potential

$$t'_{elec,j} = \frac{1}{r_{elec,j}} \, \mathrm{erf}(a_j \, r_{elec,j}) \; , \tag{2.20}$$

where a_j is one of two damping parameters (one for oxygen and one for hydrogen), and the subscript *elec* is a special case of the subscript j that indexes all multipole centers in the system. Higher-order interaction elements are derived by replacing the

Coulomb potential in Eqs. (2.8) and (2.9) by the damped form in Eq. (2.20). The electric field is computed by integrating the damped analogue of Eq. (2.8b) over the coordinates of the electron, weighted by the one-electron density $|\Psi(\vec{r})|^2$.

The electron–water electrostatic interaction is

$$V_{es}^{elec} = (\mathbf{M}_{elec})^\top \, \mathbf{T}'_{elec,j} \, \mathbf{M}_j^{perm} \ , \tag{2.21}$$

where the prime indicates that the interaction matrix elements are generated from the damped Coulomb potential, Eq. (2.20). The polytensor $\mathbf{M}_{elec}$ for the electron contains only a negative point charge (*i.e.*, the dipole and quadrupole moments are set to zero), and the implied sum over j in Eq. (2.21) runs over all molecular mechanics (MM) atoms. By defining a damped Coulomb potential, polarization from the quantum-mechanical (QM) region (*i.e.*, the electron) arises in a natural way and does not require additional consideration. We simply add the electric field due to the electron to that of the MM region when solving for induced dipoles.

In order to compute the polarization work, we separate the contributions due to the MM and QM regions,

$$\begin{aligned} W_{pol} &= \frac{(\mathbf{M}_i^{ind})^\top \, \mathbf{M}_i^{ind}}{2\,\alpha_i} \\ &= \tfrac{1}{2}\,(\mathcal{F}_i^{\mathrm{MM}} + \mathcal{F}_i^{elec})^\top \, \mathbf{M}_i^{ind} \ , \end{aligned} \tag{2.22}$$

where $\mathcal{F}_i^{\mathrm{MM}}$ contains the electric field ($\vec{F}_i^{\mathrm{MM}}$) at site i arising from both the permanent and induced multipoles of the MM region, while $\mathcal{F}_i^{elec}$ contains the electron's contribution to the electric field ($\vec{F}_i^{elec}$) at the same site. We define the final term in

Eq. (2.22) to be the polarization work done by the electron,

$$W_{pol}^{elec} = \tfrac{1}{2}\,\mathcal{F}_i^{elec}\,\mathbf{M}_i^{ind}\ . \tag{2.23}$$

Note, however, that while W_{pol} is strictly positive, W_{pol}^{elec} need not be. This can be understood by imagining a system in which a large electric field in the MM region effectively "wins out" over $\vec{F}_i^{elec}$, polarizing a dipole nearby the excess electron in a such a way that this dipole has a positive (destabilizing) interaction with the electron. In such a case, $W_{pol}^{elec} < 0$ and represents a stabilizing or restoring force that would re-orient the nearby dipole, in the absence of the MM electric field.

Following TB, we employ a repulsive potential of the form given in Eq. (2.3). This potential was computed using Hartree–Fock/aug-cc-pV6Z+diff MOs and eigenvalues for H_2O, at the Hartree–Fock geometry. (The "diff" designation in the basis set indicates the addition of two extra s-type diffuse functions on the hydrogen atoms, with exponents of 0.001 and 0.006 a.u., and also the fact that we have removed all g-type and higher angular momentum functions.) The integrals appearing in Eq. (2.3) were evaluated analytically and $V_{rep}(\vec{r}\,)$ was calculated on a grid. These numerical data were then fit to a linear combination of four gaussian functions placed at the center of mass of the H_2O molecule.

Denoting AMOEBA's van der Waals terms and valence (intramolecular) terms as V_{disp} and V_{val}, respectively, the full electron–water potential for our new model is

$$\begin{aligned} V^{elec-water} = {} & V_{val}^{\mathrm{MM}} + V_{disp}^{\mathrm{MM}} + V_{es}^{\mathrm{MM}} + V_{pol}^{\mathrm{MM}} + W_{pol}^{\mathrm{MM}} \\ & + V_{es}^{elec} + V_{pol}^{elec} + W_{pol}^{elec} + V_{rep}^{elec}\ . \end{aligned} \tag{2.24}$$

Writing out the electrostatic and repulsive terms explicitly, the potential is given by

$$\begin{aligned} V^{elec-water} = V_{val}^{\mathrm{MM}} + V_{disp}^{\mathrm{MM}} &+ \tfrac{1}{2}\,(\mathbf{M}_i^{perm})^\top\,\mathbf{T}_{ij}\,\mathbf{M}_j^{perm} \\ &+ \tfrac{1}{2}\,(\mathbf{M}_i^{perm})^\top\,\mathbf{T}_{ij}\,\mathbf{M}_j^{ind} + (\mathbf{M}_{elec})^\top\,\mathbf{T}'_{elec,j}\,\mathbf{M}_j^{perm} \\ &+ (\mathbf{M}_{elec})^\top\,\mathbf{T}'_{elec,j}\,\mathbf{M}_j^{ind} + \tfrac{1}{2}\,\mathbf{M}_i^{ind}\,\mathcal{F}_i^{elec} \\ &+ \sum_{\mathrm{H_2O}}\sum_{n=1}^{4} C_n \exp(-z_n\, r_{elec,com}^2). \end{aligned} \tag{2.25}$$

The final term represents the repulsive potential, and involves a sum over each water molecule and a second sum over four gaussians centered at that water molecule's center of mass, as discussed above.

Unlike the *ad hoc* treatment of polarization within the TB model, the new potential $V^{elec-water}$ includes a polarization potential, $V_{pol}^{elec} + W_{pol}^{elec}$, that arises in a natural way. It is not immediately obvious how (or even if) this potential is related to empirical polarization potential defined in Eq. (2.6) and used in most previous studies, but Eq. (2.6) can in fact be recovered as a well-defined approximation to $V_{pol}^{elec} + W_{pol}^{elec}$.

To see this, consider a model in which the polarization of a given water molecule is represented by a single, isotropic inducible dipole, and where we furthermore insist that the value of this dipole be induced solely by a point charge located at some other site that we label "*elec*". The component of the jth dipole in the cartesian direction x is then given by

$$\mu_{ind}^{j,x} = -\alpha\, q^{elec}\, t_x^{j,elec} = \alpha\, q^{elec}\, t_x^{elec,j}\ . \tag{2.26}$$

As we imagine the charge at site *elec* to be the unpaired electron, this equation *does not* contain an implicit sum over the "*elec*" index, nor does Eq. (2.27) that follows.

We next substitute the induced dipole in Eq. (2.26) into the polarization potential $V_{pol}^{elec} + W_{pol}^{elec}$ to obtain

$$\begin{aligned} V_{pol}^{elec} + W_{pol}^{elec} &= -\tfrac{1}{2}\,\alpha\,(q^{elec}\,t_x^{elec,j})(q^l\,t_x^{elec,j}) \\ &= -\frac{\alpha}{2\,r_{elec,j}^4}\;. \end{aligned} \tag{2.27}$$

Note that we have not damped the interaction elements in the final equality of Eq. (2.27). Our polarization potential thus recovers the r^{-4} distance dependence of the empirical polarization potential. By replacing $r_{elec,j}^2$ in Eq. (2.27) with $r_{elec,j}^2 + C$, we recover the empirical polarization potential in Eq. (2.6). This substitution has the effect of damping the "direct" polarization interaction in Eq. (2.27), and we expect that this damping will mimic the effect of allowing the rest of the system to polarize the water molecule. (The bath will tend to induce dipoles in directions dissimilar to those induced by the point charge, thus reducing the polarization of the water dipole due to the presence of the point charge, compared to what it would be in the absence of other water molecules.) The damping parameter C also avoids a singularity as the electron–water distance approaches zero.

The new electron–water potential contains no explicit exchange potential. Attempts to fit exchange were unsuccessful, as described below (Section 2.5.2); similar difficulties were noted by TB.[67] Instead, we adjusted the two damping parameters (a_{O} and a_{H}) and an overall scaling factor for the repulsive potential, in order to reproduce the VEBE of $(\mathrm{H_2O})_2^-$. The value that we obtain from the model, 24 meV, is essentially the same as the MP2/6-31(1+,3+)G* value (26 meV),[103] which is underbound only by ∼10 meV compared to higher-level *ab initio* estimates, and by about

Table 2.1: Parameters that determine the electron–water potential developed in this work.

Parameter	Value/a.u.
a_{O}	0.38
a_{H}	0.72
z_1	1.5
z_2	0.5
z_3	0.1
z_4	0.01
C_1	−0.0144
C_2	0.2170
C_3	0.0453
C_4	−0.0110

20 meV relative to experiment. We consider this level of accuracy acceptable. In performing the fit, we attempted to maintain the two damping parameters at similar values, in order to obtain an even-tempered electrostatic potential. The final fitted parameters are collected in Table 2.1.

Energy gradients of the electron–water potential are formally simple due to the fact that the total energy is minimized with respect to all parameters in the Hamiltonian, namely, the induced dipoles for the MM atoms, and the expansion coefficients of the one-electron wave function (grid amplitudes, in our implementation, though they could be expansion coefficients in some other basis). Stationarity with respect to the latter is obvious, since the wave function is determined by solving the time-independent Schrödinger equation, but the induced dipoles are determined by solution of coupled linear equations [see Eq. (2.12)], and it is not immediately obvious that these parameters are indeed variational. This we now demonstrate, following the proof outlined in Ref. [104].

One may imagine determining the one-electron wave function via a minimization carried out in two separate steps: first, we fix the induced dipoles and minimize the expectation value of the Hamiltonian with respect to linear expansion coefficients of the wave function. This minimization is equivalent to solving the Schrödinger equation and yields a new one-electron density and hence a new electric field $\vec{F}_i^{elec}$ at each MM site. This electric field, together with that of the water molecules, is used to compute the induced dipoles, and the energy (at fixed values of the wave function coefficients) may be expressed as a function of these dipoles:

$$E(\mathbf{M}^{ind}) = \tfrac{1}{2}\,\mathbf{M}_i^\top\,\mathbf{T}_{ij}\,\mathbf{M}_j + \big\langle\Psi\big|\,(\mathbf{M}_{elec})^\top\,\mathbf{T}_{elec,j}\,\mathbf{M}_j^{ind}\,\big|\Psi\big\rangle + \frac{(\mathbf{M}_i^{ind})^\top\,\mathbf{M}_i^{ind}}{2\,\alpha_i}\ . \tag{2.28}$$

Taking the derivative of the energy with respect to the induced dipole on the kth site, $\partial E/\partial\vec{\mu}_{ind}^{k}$, and equating the result to zero, one obtains

$$\begin{aligned} 0 &= \mathbf{T}_{ki}\,\mathbf{M}_i + \big\langle\Psi\big|\,\mathbf{T}_{k,elec}\,\mathbf{M}_{elec}\,\big|\Psi\big\rangle + \frac{\mathbf{M}_k}{\alpha_k} \\ &= -\mathcal{E}_k^{\mathrm{MM}} - \mathcal{E}_k^{elec} + \frac{\mathbf{M}_k^{ind}}{\alpha_k}\ . \end{aligned} \tag{2.29}$$

We only allow the dipoles to be flexible and so this last expression simplifies to

$$0 = -\vec{F}_k^{\mathrm{MM}} - \vec{F}_k^{elec} + \frac{\vec{\mu}_{ind}^{k}}{\alpha_k}\ , \tag{2.30}$$

which shows that the variational condition $\partial E/\partial\vec{\mu}_{ind}^{k} = 0$ is equivalent to Eq. (2.12), the equation that determines the linear-response dipoles. Thus, gradients of the energy require only direct differentiation of the Hamiltonian, *i.e.*, Hellman-Feynman forces, with no response terms.

2.4 Simulation algorithm

In this section we describe the algorithm used to calculate eigenstates of the model Hamiltonian

$$\hat{H} = \hat{T} + V^{elec-water} + V^{AMOEBA} \,. \tag{2.31}$$

In view of the easy availability of analytic energy gradients, this algorithm may equally well be used to perform quantum/classical molecular dynamics simulations, in which classical molecular dynamics for the water molecules is propagated on the adiabatic potential energy surface corresponding to an eigenvalue of $\hat{H}$ (but always with self-consistent polarization of the wave function and the water molecules).

2.4.1 Description of the algorithm

We calculate the lowest few eigenstates of $\hat{H}$ on an evenly-spaced cartesian grid in three dimensions,[105, 106] via an iterative technique, then calculate forces on the atoms via the Hellmann–Feynman theorem, $\partial E/\partial x = \langle\Psi|\partial V/\partial x|\Psi\rangle$. Regarding iterative eigensolvers, Webster *et al.*[93] have noted that Lanczos-type methods are problematic for hydrated-electron models, due to the high spectral density of $\hat{H}$. In our hands, we are consistently able to converge the ground state, and occasionally one or two excited states, using a standard block-Lanczos procedure, but we are unable to converge all of the excited states that have significant oscillator strength out of the ground state.

To overcome this problem, Webster *et al.*[93] employ a two-step procedure that involves first using Lanczos iteration to determine eigenpairs of the operator

$$\hat{\mathcal{W}} = \exp(-\beta\,V/2)\ \exp(-\beta\,\hat{T})\ \exp(-\beta\,V/2)\ , \tag{2.32}$$

where $\hat{H} = \hat{T} + V$ is the original Hamiltonian. If the parameter $\beta > 0$ is sufficiently large, then the spectrum of $\hat{\mathcal{W}}$ will be much less dense than that of $\hat{H}$, making the former amenable to Lanczos iteration. A second Lanczos procedure is then used to correct for the fact that the eigenstates of $\hat{\mathcal{W}}$ are not eigenstates of $\hat{H}$. When using this technique, one must take steps to detect and remove spurious eigenvalues.[93, 107]

As an alternative to this rather complicated prescription (which appears still to be in widespread use[42, 67, 108]), we calculate eigenstates of $\hat{H}$ via block-Davidson iteration,[109] a procedure that is known to work well for diagonally-dominant matrices. When represented on a real-space grid, the matrix of V is strictly diagonal, while the matrix representation of $\hat{T}$ has its largest elements along the diagonal, with off-diagonal elements T_{ij} that decay like $\sim (i-j)^{-2}$ (see Ref. [106]).

For fixed-charge potentials (*e.g.*, the TB model), we employ a standard version of the Davidson algorithm (as described, for example, in the Appendix to Ref. [110]). All subspace vectors $\mathbf{v}_1, \mathbf{v}_2, \ldots, \mathbf{v}_n$ are stored in core memory, as are the vectors $\mathbf{w}_i = \mathbf{H}\mathbf{v}_i$ generated by the action of Hamiltonian matrix. Some limited testing led us to cap the number of subspace vectors at $n \sim 200$ to avoid a diagonalization bottleneck; if the subspace size reaches this limit, it is collapsed down to one vector per root. We employ a "locking" procedure, whereby only the unconverged roots are used to generate new subspace vectors.[110]

Comparison to exact diagonalization indicates that this procedure consistently determines as many eigenpairs of $\hat{H}$ as desired, to arbitrary accuracy and without spurious eigenvalues. Starting from guess vectors with random entries, with a limit of $n = 200$ subspace vectors and a very stringent convergence criterion ($||(\hat{H} - E)\Psi|| < 1.0 \,\mathrm{x}\, 10^{-8}$ a.u.), the subspace must be collapsed two or three times in order to calculate the lowest five eigenstates of a $(H_2O)_{216}^-$ cluster in which the electron is contained within a cavity. (For the TB model, these five states account for $\gtrsim 90\%$ of the oscillator strength out of the ground state.) For geometry optimizations and molecular dynamics simulations, where converged eigenvectors from a previous step are available as an initial guess, the same calculation requires only 15–25 subspace vectors per root, for molecular dynamics, and significantly fewer than that for geometry optimizations. In fact, for geometry optimizations it is often the case that *zero* additional subspace vectors are required, *i.e.*, it is only necessary to diagonalize the new Hamiltonian in the very small basis of converged eigenvectors from the previous geometry. (To some extent, this is a consequence of the fact that we optimize in cartesian coordinates, where the step sizes are necessarily small.)

The simple block-Davidson procedure must be modified for polarizable water models, because in this case $\hat{H}$ depends upon the values of the induced dipoles, and these in turn depend upon the one-electron density, $|\Psi(\vec{r})|^2$. Hence $\hat{H}$ is a functional of its own eigenvectors. Strictly speaking, in such cases the vectors $\mathbf{w}_i$ become out-of-date every time one adds a new subspace vector, because each new subspace vector modifies the approximate eigenvectors (Ritz vectors), thus altering the density $|\Psi(\vec{r})|^2$ that is used to polarize the water molecules, and consequently modifying the Hamiltonian itself. However, the difference in $\mathbf{w}_i = \mathbf{H}\mathbf{v}_i$ is likely to be small from one iteration to the next, especially in the later iterations.

The procedure that we adopt is to update the subspace matrix after the error (measured by the norm of the residual vector) decreases by a factor of 2–5. We store the potential each time we polarize the water with the electron density; once we decide to update, we re-polarize the solvent bath, compute the change ΔV in the potential energy at each grid point, and finally update the matrix–vector products $\mathbf{w}_i$ using ΔV. This procedure is very efficient for smaller clusters with highly diffuse, surface-bound electrons, where a large grid is required but where the potential and linear response equations [Eq. (2.12)] are inexpensive to compute. All results presented here utilize this algorithm.

Preliminary calculations on larger clusters [*e.g.*, $(H_2O)_{216}^-$] exhibiting cavity-bound electrons indicate that high accuracy can be achieved using much smaller grids, since the electron is highly localized, but that evaluation of the potential and self-consistent iteration for the induced dipoles are the bottleneck steps. (In smaller clusters with large grids, repeated formation of matrix–vector products is the most expensive step.) For these larger clusters, it is advantageous to converge all eigenvectors of interest between each update of the dipoles. Overall convergence is then achieved when the difference in energy between updates of the dipoles is smaller than some threshold, for each eigenvalue of interest. This typically requires 3–5 updates of the dipoles.

2.4.2 Computational Details

All eigenpairs were converged to a precision $||(\hat{H}-E)\Psi|| < 10^{-6}$ a.u. Our calculations employ a 60 Å × 60 Å × 60 Å cartesian grid with a spacing of 1 Å, except in the case of $(H_2O)_2^-$, where an 80 Å wide cubic grid (with the same grid spacing) is necessary to converge the ground-state eigenvalue with respect to the grid parameters. A grid spacing of Δx implies that the maximum momentum component in the x direction is $\hbar\pi/\Delta x$.[111] A wave function represented on a uniform grid in three dimensions may therefore possess a kinetic energy no greater than $(3/2m)(\hbar\pi/\Delta x)^2$, and values for $\langle\hat{T}\rangle$ in our calculations are well below this limit. Furthermore, numerical tests reveal that VEBEs obtained using the aforementioned grids are converged to within 0.01–0.02 eV with respect to decrease of Δx. Such differences are smaller than the intrinsic accuracy of the calculated VEBEs themselves.

These grid-based calculations were performed with our home-built code, Furry (ver. A). This code employs a locally-modified version of the Tinker[112] MM package to evaluate the AMOEBA water potential, solve for the induced dipoles, and evaluate the electron–water potential.

In Section 2.5, we assess our new model and the TB model against benchmark *ab initio* calculations. For VEBEs, we benchmark against MP2/6-31(1+,3+)G* calculations, which have been shown to provide reasonable accuracy for VEBEs[103, 113] (as quantified in Section 2.5) yet can be applied to medium-sized water clusters. A library of $(H_2O)_n^-$ clusters isomers, ranging from $n = 2$ to $n = 33$, was obtained from Ref. [1]. All *ab initio* calculations reported here utilize these geometries.

While the MP2/6-31(1+,3+)G* method affords accurate VEBEs (due largely to a lack of strong correlation effects and absence of significant orbital relaxation upon electron detachment[113]), accurate benchmarks for relative conformational energies demand a higher level of theory, and for these energies we employ complete basis set (CBS) MP2 benchmarks. MP2/CBS energies were determined by separate extrapolation of the Hartree–Fock energy and the MP2 correlation energy, using the aug-cc-pVXZ+diff sequence of basis sets, where $X = 2, 3$, or 4 (*i.e.*, D, T, or Q). The "+diff" signifies that we have added an additional diffuse s function on each hydrogen (with an exponent of 3.72 x 10^{-2} a.u.) as well as a diffuse s function and a set of diffuse p functions on each oxygen (with exponents of 9.87 x 10^{-2} and 8.57 x 10^{-2} a.u., respectively). In Ref. [114], these diffuse functions were shown to perform adequately for small $(H_2O)_n^-$ clusters. The Hartree–Fock CBS energy was estimated using a three-point fit to the *ansatz*[115]

$$E(X) = E(\infty) + a\, e^{-bX} \; , \tag{2.33}$$

where a and b are fitting parameters. The MP2 correlation energy was extrapolated using a two-point fit ($X = 3$ and 4) to the expression[116]

$$E(\infty) = E(X) + c\, X^{-3} \; , \tag{2.34}$$

where c is a fitting parameter.

All *ab initio* calculations were performed using Q-Chem.[117] The Visual Molecular Dynamics program[118] was used for visualization.

2.5 Analysis of the new model

We now turn our attention from the development and technical description of the model to the analysis of its properties. We first verify, by comparison to *ab initio* benchmarks, that the new model is indeed more accurate than the TB model We then make a detailed analysis of the potential itself, in order to compare and contrast it with the TB potential. In this work, we consider only the ground state of the model potentials.

2.5.1 Comparison to *ab initio* results

Figure 2.1 compares VEBEs computed at the MP2/6-31(1+,3+)G* level to those obtained from our new model Hamiltonian and the TB model Hamiltonian. The 76 $(H_2O)_n^-$ cluster isomers in our data set range from $n = 2$ to $n = 33$ and include both surface and cavity binding motifs. This diverse database poses a challenging test to a model's ability to predict VEBEs across the $(H_2O)_n^-$ potential surface (for a given n), and for a wide range of cluster sizes. Relative to the MP2 benchmarks, our new model outperforms the TB model, reducing the mean absolute deviation from 0.185 eV (for the TB model) to 0.089 eV (for the new model). The maximum deviation is also reduced, from 0.623 eV (TB model) to 0.339 eV (this work). We emphasize that our model is fit exclusively to the VEBE of $(H_2O)_2^-$, so we regard the rather small errors in VEBEs as evidence that our model contains *most* of the correct physics for $(H_2O)_n^-$. (As discussed below, a QM treatment of electron–water dispersion, which is absent or at best implicit in our model, affords further improvement to VEBEs.)

The mean accuracy of the TB model for VEBEs (0.185 eV) is comparable to that reported previously by Turi *et al.*[80] based on MP2/6-31(1+,3+)G* benchmarks for a set of $(H_2O)_{12}^-$ isomers. However, whereas in that study all of the VEBEs obtained from the TB model were offset by an essentially constant amount relative to MP2 results, our results demonstrate that a constant offset cannot be expected across a more diverse set of cluster isomers.

For cluster isomers with very small VEBEs, the MP2/6-31(1+,3+)G* level of theory underbinds the excess electron by $\sim$0.03 eV.[103] If we adjust the MP2 VEBE benchmarks upward by 0.03 eV for all structures whose VEBEs are less than 0.5 eV, and use these modified values as benchmarks, then our new model underestimates the VEBEs of these weak-binding clusters by only 0.06 eV, as compared to 0.10 eV for the TB model. For strongly-bound isomers, VEBEs computed at the MP2/6-31(1+,3+)G* level are estimated to be about 7% too small,[113] and our model is underbound relative to these MP2 values by roughly another 8% (versus 22% for TB). Our new model is thus nearly quantitative in its prediction of VEBEs, whereas the TB model is only qualitative. It is significant that our model underbinds the electron in nearly all cases, since we have neglected a QM treatment of electron–water dispersion, which should increase the VEBE. Using a Drude model to incorporate this interaction, Wang and Jordan[68] report errors of less than 0.005 eV in small-cluster VEBEs ($n \leq 4$), relative to high-level coupled-cluster benchmarks. Thus, we have a hierarchy of model Hamiltonians of increasing complexity, expense, and accuracy. A point-charge water model combined with an *ad hoc* polarization potential suffices to

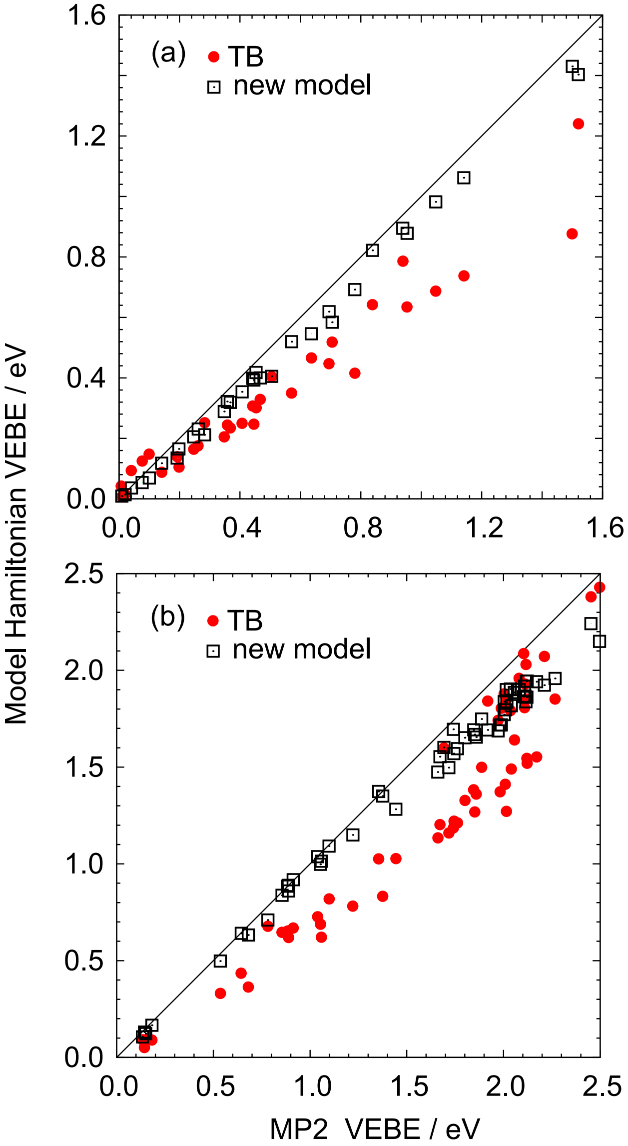

Figure 2.1: Comparison of VEBEs computed at the MP2/6-31(1+,3+)G* level of theory to VEBEs predicted using model Hamiltonians, for a library of $(H_2O)_n^-$ isomers ranging from $n = 2$ to $n = 33$. The diagonal line indicates where the model Hamiltonian and MP2 predications are identical.

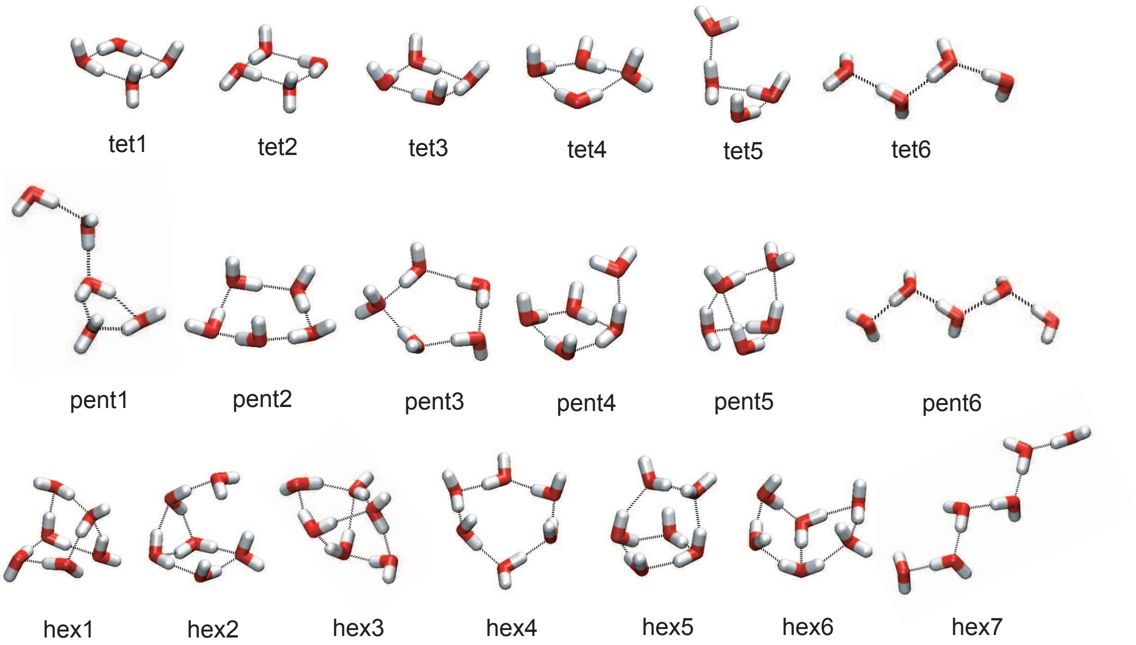

Figure 2.2: Structures of $(H_2O)_4^-$, $(H_2O)_5^-$, and $(H_2O)_6^-$ isomers used to benchmark relative conformational energies. Each cluster is a stationary point at the B3LYP/6-31(1+,3+)G* level.

predict VEBEs within ~ 0.2 eV, while a more accurate, self-consistent treatment of polarization decreases this error to less than 0.1 eV. A QM description of dispersion reduces the error even further, albeit at significantly greater expense.

Another important test of a model potential is its ability to predict relative conformational energies of cluster isomers. In the case of $(H_2O)_n^-$ clusters, molecular beam experiments appear to sample preferentially those isomers with the largest VEBEs,[119] which tend to be fairly *high*-energy local minima on the anion potential energy surface.[90] For this reason, we desire a model that can predict relative conformation energies, for both $(H_2O)_n$ and $(H_2O)_n^-$ cluster isomers, at energies well above the global minimum. Thus, we next compare the relative conformational energies predicted by the model Hamiltonians to those obtained at the MP2/CBS level, for a set of $(H_2O)_4^-$, $(H_2O)_5^-$, and $(H_2O)_6^-$ cluster isomers whose structures are depicted in Fig. 2.2. Each of these isomers is a stationary point at the B3LYP/6-31(1+,3+)G* level of theory. In what follows, we discuss relative conformational energies not only for these anionic clusters, but also for the corresponding neutral cluster isomers at the same geometries.

Figure 2.3 compares the relative conformational energies for the tetrameric clusters. Five of the six structures exhibit the well-known “double acceptor” or “AA” structural motif,[120] in which one water molecule accepts two hydrogen bonds and donates none, leaving it with two dangling hydrogen atoms. The excess-electron wave function (or singly-occupied MO, in the case of *ab initio* calculations) is largely localized around this AA water molecule. Among these six cluster isomers, the only non-AA isomer is the cyclic structure tet3 (see Fig. 2.2), and it is the lowest in energy on both the anionic and the neutral potential energy surfaces. [In view of the extensive *ab initio* calculations available for this isomer,[90, 121] it seems safe to conclude that tet3 is the global minimum of $(H_2O)_4^-$. This isomer is structurally similar to the $(H_2O)_4$ global minimum.[90]] The AA isomers, although they are far more prominent in the experimental photoelectron spectrum of $(H_2O)_4^-$,[122] each lie at least 4 kcal/mol above tet3; upon detachment of the excess electron, these AA structures

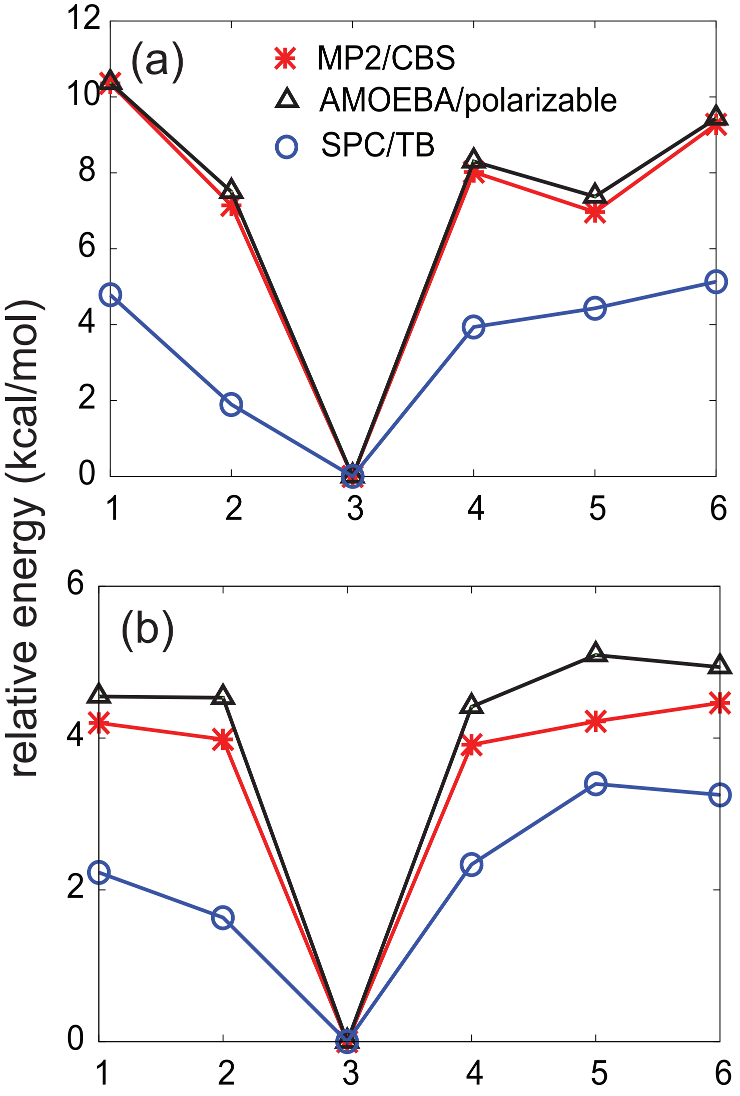

Figure 2.3: Energies of tetrameric clusters on (a) the $(H_2O)_4$ potential surface and (b) the $(H_2O)_4^-$ potential surface. Note that the two panels use different energy scales. The structure of each isomer is depicted in Fig. 2.2.

lie at least 8 kcal/mol above the neutral tet3 isomer.

The SPC water model and the TB model fail badly at describing the relative energies of the $(H_2O)_4$ and $(H_2O)_4^-$ isomers, respectively. This is mostly a reflection of the fact that the SPC model significantly underestimates the energy difference between tet3, which is the most neutral-like isomer, and the rest of the structures. This is in keeping with our expectations that simple water models cannot provide consistent accuracy across the potential energy surface. The AMOEBA potential, in contrast, almost exactly reproduces the MP2/CBS results for $(H_2O)_4$, and the hydrated-electron model built upon this potential also performs well for the $(H_2O)_4^-$ isomers.

Like the tetramers, the pentameric structures are mostly AA-type binding motifs, the exception being the neutral-like pent2 isomer. Relative energies of these isomers are depicted in Fig. 2.4, and once again the non-AA isomer is the lowest-energy structure on both the neutral and the anionic potential surface. The SPC potential significantly underestimates the energy difference between pent2 and the rest of the structures, except for structure pent4, where the energy difference is approximately correct. Looking at the $(H_2O)_5^-$ relative energies, the largest differences between the MP2/CBS and the TB results occur for isomers pent3 and pent5, coinciding with the largest differences between SPC and MP2/CBS for the neutral pentamers. Clearly, the SPC model plays a leading role in the success or failure of the TB model.

The TB model erroneously places $(H_2O)_5^-$ isomer pent5 below the true minimum-energy structure. We note that pent5 is a compact structure possessing more hydrogen

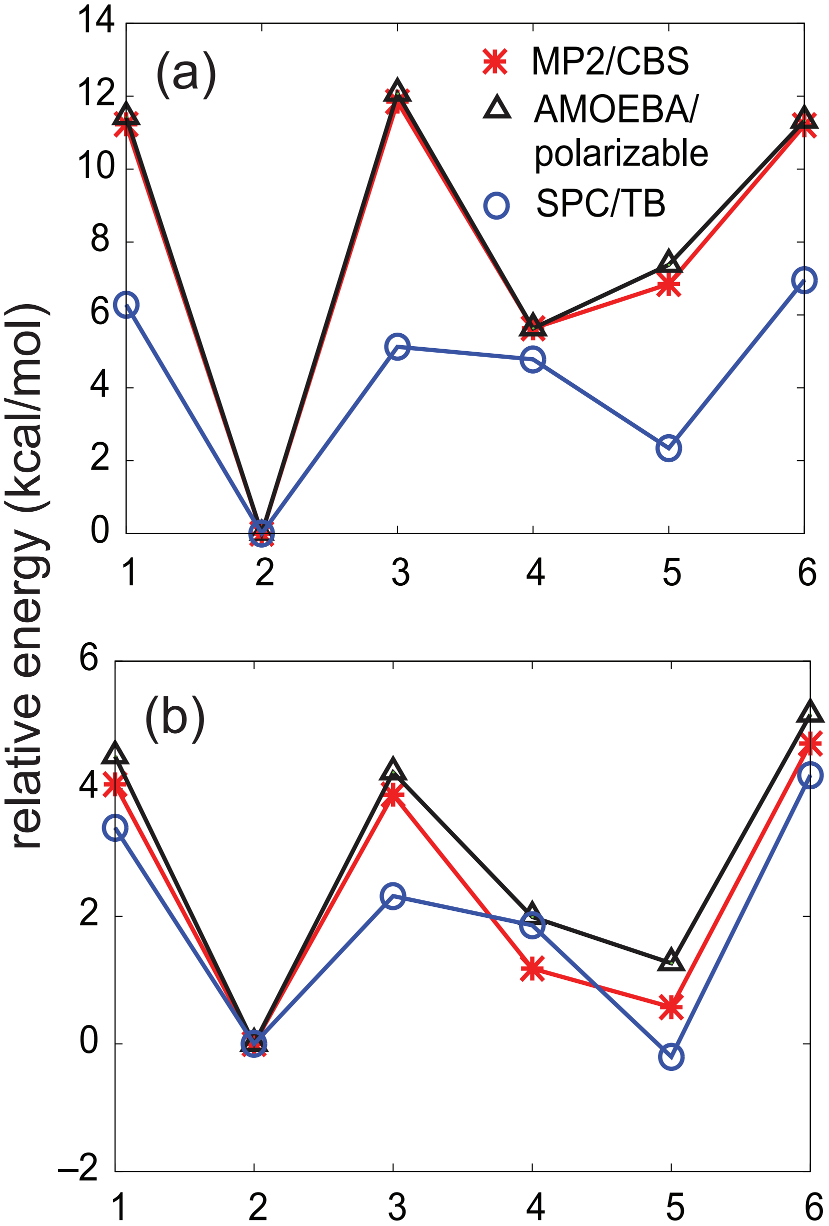

Figure 2.4: Energies of pentameric clusters on (a) the $(H_2O)_5$ potential surface and (b) the $(H_2O)_5^-$ potential surface. Note that the two panels use different energy scales. The structure of each isomer is depicted in Fig. 2.2.

bonds than any of the other pentameric isomers, despite the presence of one AA water molecule. This suggests a bias in the TB model toward neutral-like structures that maximize the number of water–water hydrogen bonds. The fact that pent5 is *not* the lowest neutral pentamer suggests that SPC does impose some additional penalty against water molecules in the AA configuration (beyond simply the loss of hydrogen bonds), but that the strong electron–AA interaction more than compensates for this penalty in anionic clusters.

The AMOEBA water model once again agrees *quantitatively* with MP2/CBS results for the neutral structures. Relative energies of $(H_2O)_5^-$ isomers, as predicted by our new model, agree with MP2/CBS results to within 1 kcal/mol.

Relative energies for the hexameric clusters are depicted in Fig. 2.5. For the neutral hexamers, the performance of SPC is not quite as poor as was observed for the tetrameric and pentameric clusters, perhaps because most of the hexameric clusters are much more compact than the smaller clusters, but AMOEBA is quantitative yet again. For the anions, the TB model again yields an incorrect minimum-energy structure, placing two non-AA isomers (hex1 and hex3) below the correct minimum-energy structure, the AA isomer hex5. The maximum error in the new model occurs for hex2 and is only slightly greater than 1 kcal/mol.

2.5.2 Comparison to the TB potential

A direct comparison between the TB potential and our new potential is made in Fig. 2.6. The origin of the plots is the center of mass of oxygen in all plots other than Fig. 2.6(d), where the oxygen atom is the origin. As it would be difficult to visualize

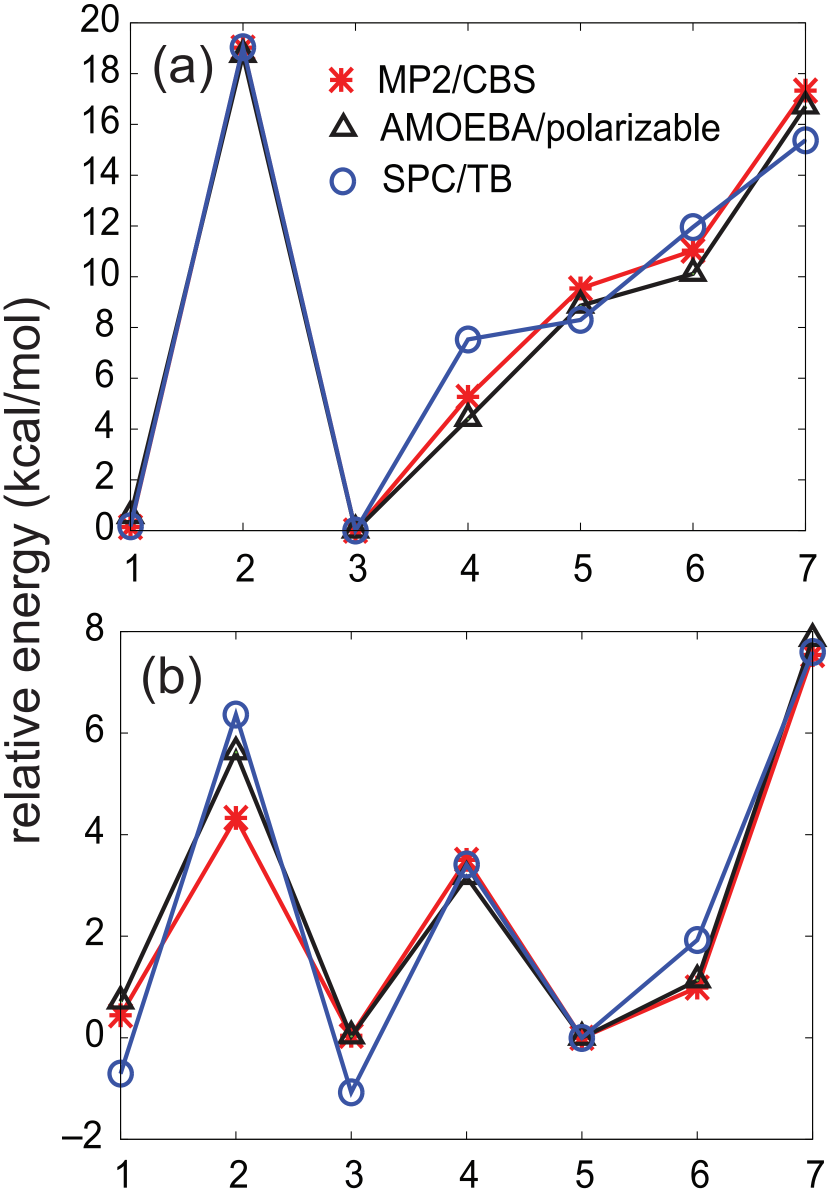

Figure 2.5: Energies of hexameric clusters on (a) the $(H_2O)_6$ potential surface and (b) the $(H_2O)_6^-$ potential surface. Note that the two panels use different energy scales. The structure of each isomer is depicted in Fig. 2.2.

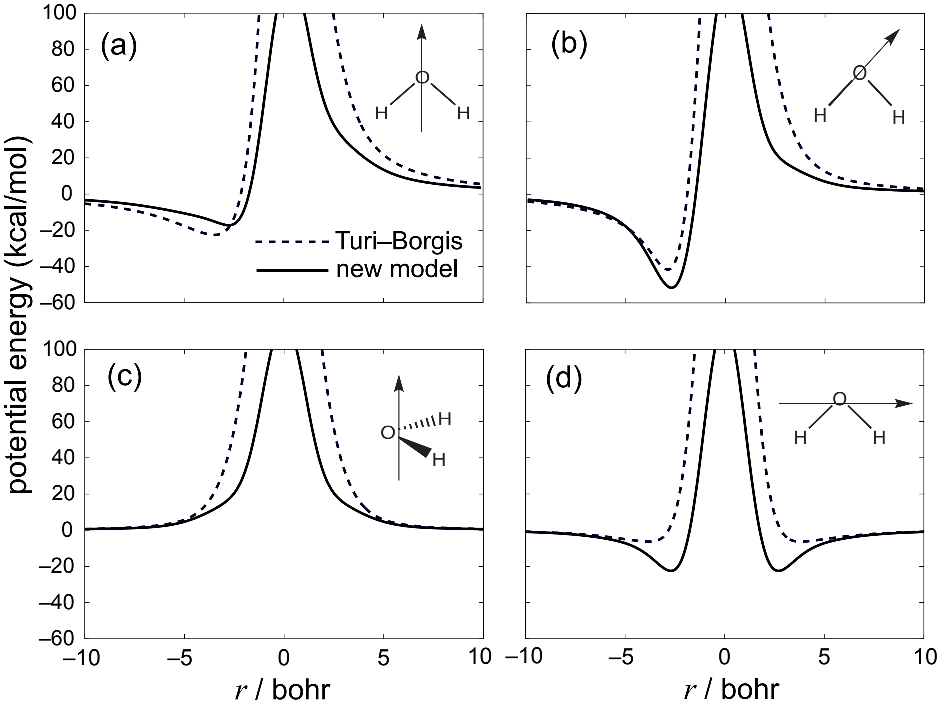

Figure 2.6: Comparison of the TB model (dashed curves) and the new potential (solid curves) for H_2O^-, in four one dimensional slices. Both potentials are shown without polarization. In (a)–(c), $r = 0$ represents the H_2O center of mass, whereas in (d), $r = 0$ at the oxygen atom.

the polarization potential of our model, we plot both potentials sans polarization potential, that is, we omit Eq. (2.6) from the TB potential and set all induced dipoles to zero in our model. Our potential is much softer around the oxygen atom and is largely attractive along the in-plane axis perpendicular to the molecular C_2 axis [see Fig. 2.6(d)].

The attractive regions about the oxygen atom [Fig. 2.6(d)] is an indication that the exchange interaction is included implicitly in the fit. TB showed[66] that a Slater-type (or Xα-type)[95] exchange potential

$$V_{X\alpha}(\vec{r}\,) = -\frac{2}{\pi}\, k_F(\vec{r}\,) = -\frac{2}{\pi}\left[3\pi^2\rho(\vec{r}\,)\right]^{1/3}, \tag{2.35}$$

in which $\rho(\vec{r}\,)$ is the neutral water electron density, reproduces the eigenvalue of the excess electron in the SE approximation. The collection of constants in Eq. (2.35) corresponds to a Slater-exchange α value (not to be confused with a polarizability) of $\alpha \approx 1.33$. This is larger than the values typically employed in atomic Xα calculations,[95] but consistent with variationally-optimized α values determined recently for small molecules.[123]

Figure 2.7 depicts the pseudopotential energy surface for H_2O^- from using the exchange potential in Eq. (2.35) scaled by a constant C_x, with $0 \leq C_x \leq 1$. Increasing C_x deepens the potential wells—especially around the oxygen atom—and narrows the repulsive part of the potential. Also note that the difference in well depth between the bisector coordinate in Fig. 2.7(a) and the bond coordinate in Fig. 2.7(b) increases with increasing exchange. Although we attempted to adjust the parameters in our potential to fit the numerical surface directly, the results were unsatisfactory; while we were able to reproduce the VEBE of $(H_2O)_2^-$, we were not able to reproduce the VEBE of even a small number of other structures, based on comparison to MP2 benchmarks.[1, 103, 113] TB were similarly unable to achieve a satisfactory direct fit of the pseudopotential energy surface,[67] which may indicate an inadequacy in the simple local exchange functional of Eq. (2.35).

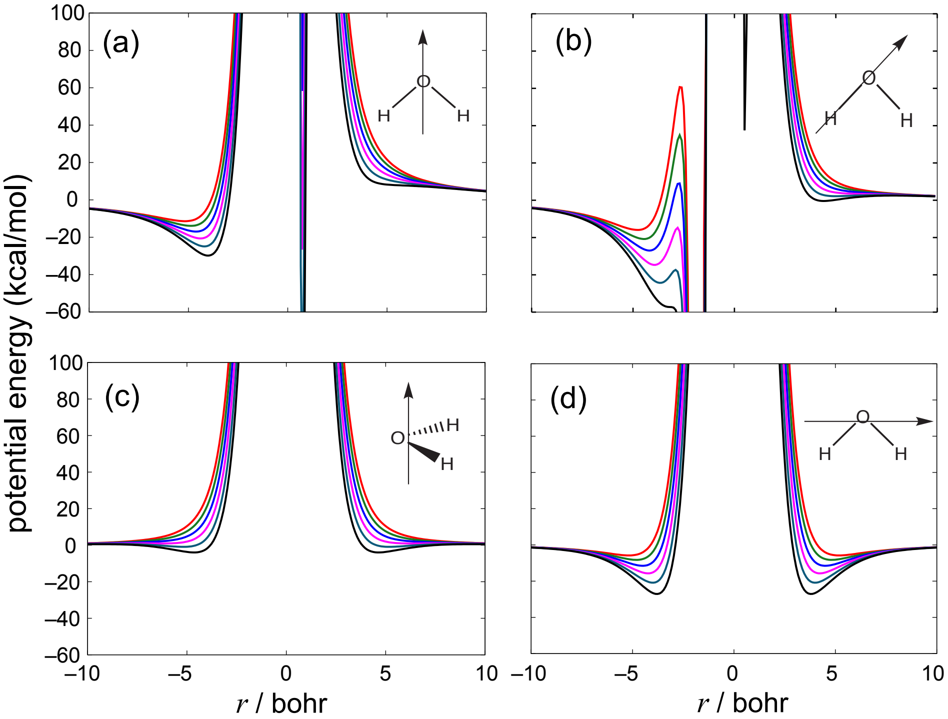

Figure 2.7: Plots of the pseudopotential for H_2O^- using various Xα-type exchange potentials of the form $V_x(\vec{r}) = C_x\, V_{X\alpha}(\vec{r})$. Values of the scaling parameter C_x range from $C_x = 0$ (the top curve, in red, which is least attractive) to $C_x = 1$ (the bottom curve, in black, which is most attractive), in increments of 0.2. In (a)–(c), $r = 0$ represents the H_2O center of mass, whereas in (d), $r = 0$ at the oxygen atom.

Our new potential model is more attractive along the O–H bond than is the TB model [Fig. 2.6(b)], but equally less attractive along the H–O–H bisector coordinate [Fig. 2.6(a)]. Perhaps most importantly, we observe that our potential decays more rapidly that that of Turi and Borgis [Figs. 2.6(c) and 2.6(d)]. This is due to the fact that at long range the monopole term dominates the electrostatic expansion, and the exaggerated point charges of the SPC model ($q^{\mathrm{O}} = -0.82$, $q^{\mathrm{H}} = 0.41$) provide a more attractive potential than those of AMOEBA ($q^{\mathrm{O}} = -0.51966$, $q^{\mathrm{H}} = 0.25983$). This is significant because the hydrated electron is quite diffuse, and the long range part of the potential is thus sampled extensively.

2.5.3 Expectation values of the model potential

In an effort to understand why our new potential is less repulsive than the TB potential, and also to evaluate which $(\mathrm{H_2O})_n^-$ structures are most affected by polarization, we have calculated expectation values of various components of the electron–water interaction potential, for the library of $(\mathrm{H_2O})_n^-$ isomers that was used to evaluate VEBEs (Fig. 2.1). Recall that this library consists of 76 different clusters ranging in size from $n = 2$ to $n = 33$, including both surface states and cavity states. Figures 2.8–2.12 show histograms of various expectation values, binned over this library of structures. For ease of analysis, we have sub-divided the database into AA-type isomers, non-AA surface states (called simply "surface states" in the discussion that follows), and cavity states.

The histogram in Fig. 2.8 shows the distribution of values for $\langle V_{rep} \rangle$, the expectation value of the repulsive potential, for both the new model and the TB model. This

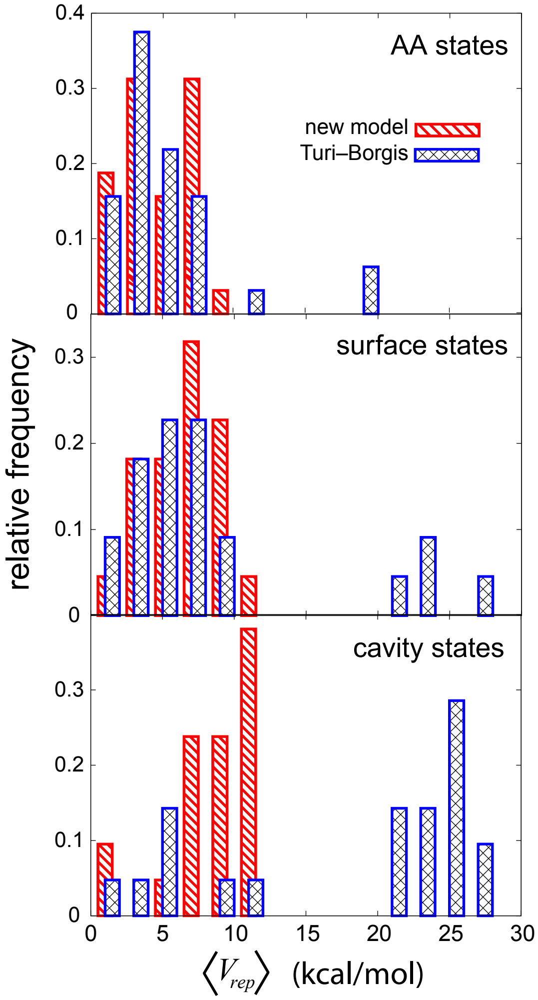

Figure 2.8: Histograms of $\langle V_{rep} \rangle$ for a library of $(H_2O)_n^-$ isomers.

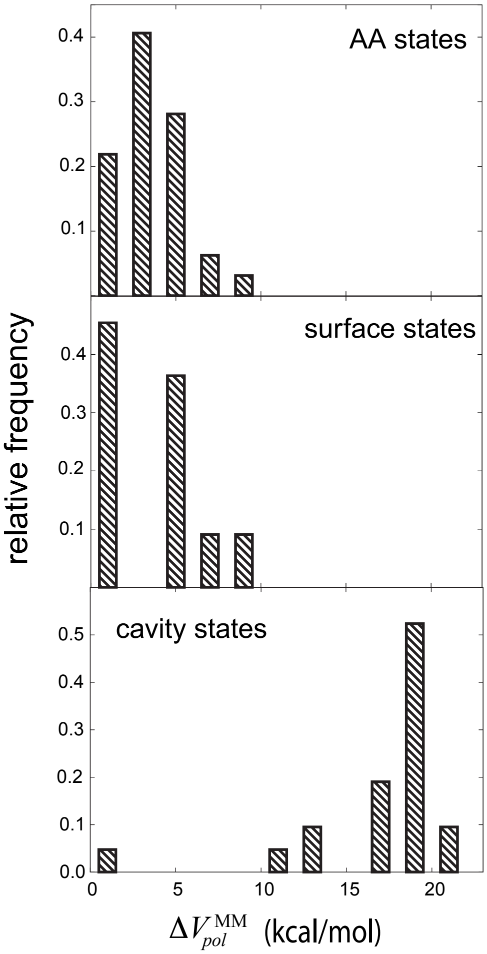

Figure 2.9: Histograms illustrating the change in the polarization energy of the water molecules, V_{pol}^{MM}, upon electron attachment. The expectation value of V_{pol}^{MM} is binned over a library of $(\mathrm{H_2O})_n^-$ isomers, for the polarizable model potential developed in this work.

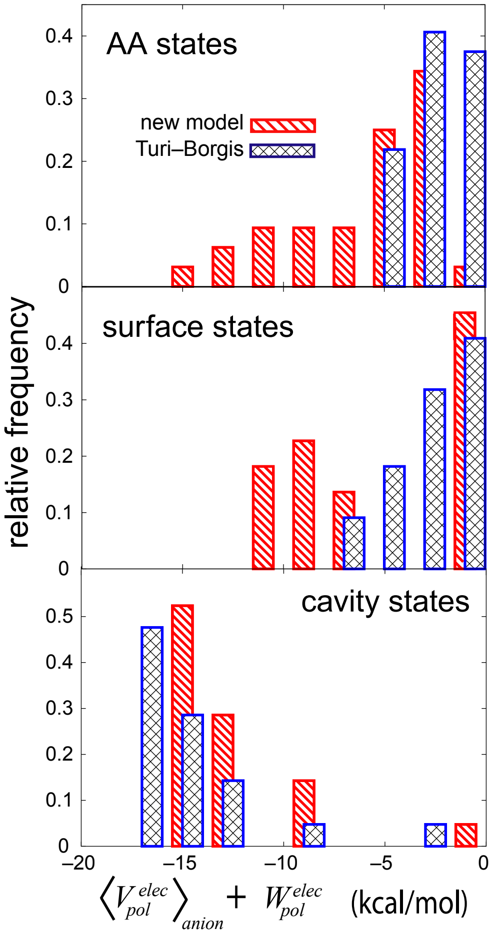

Figure 2.10: Histogram of the expectation value of the total polarization energy (including the self-energy, in the case of our new model), binned over a library of $(H_2O)_n^-$ isomers.

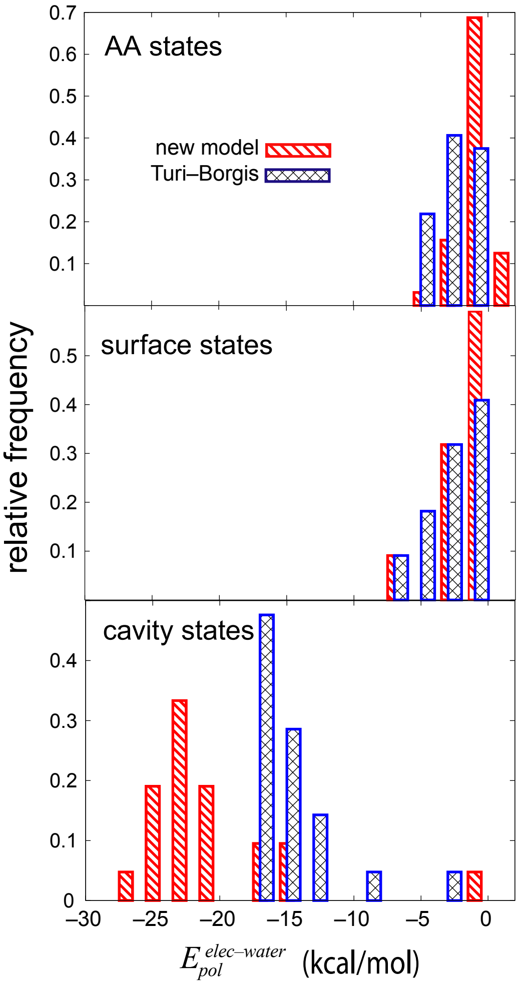

Figure 2.11: Histogram of expectation values of the electron–water polarization potential, including the self-energy, binned over a library of $(H_2O)_n^-$ isomers.

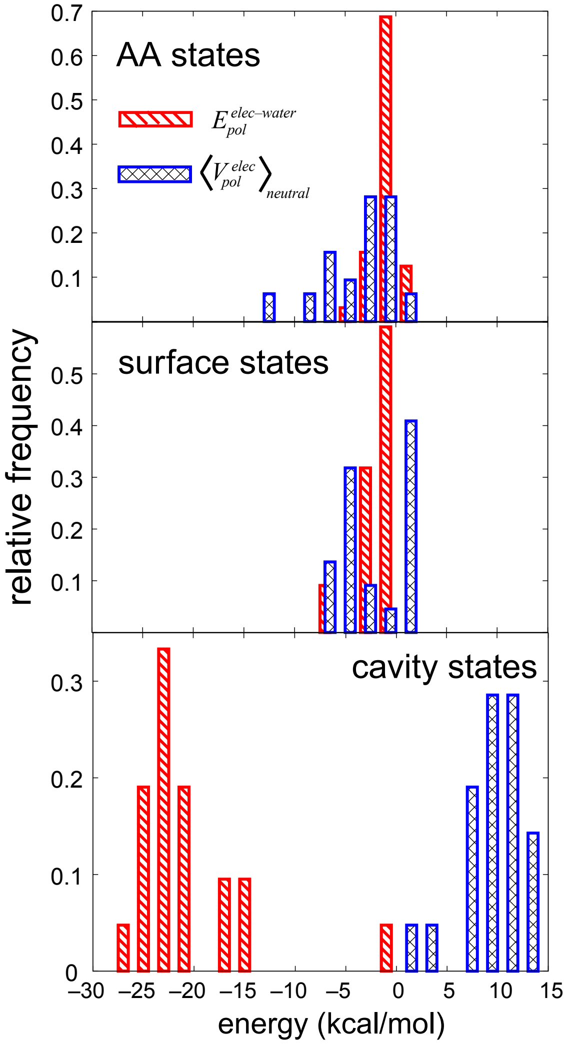

Figure 2.12: Histogram of the components of Eq. (2.36), binned over a library of $(H_2O)_n^-$ isomers.

quantity is smallest, on average, for AA isomers and largest for cavity states. This indicates that electron penetration into the molecular core is greatest for cavity states, whereas for AA isomers the excess electron resides largely outside of the cluster and does not sample the repulsive potential. The most noticeable difference between our new model and the TB model is that the latter predicts much larger values of $\langle V_{rep} \rangle$ in the case of cavity-bound electrons. According to our model, $\langle V_{rep} \rangle < 12$ kcal/mol for all of the structures in the data set, whereas the TB model affords $\langle V_{rep} \rangle > 20$ kcal/mol for most cavity states.

Because both models exhibit qualitatively similar VEBEs, in the case of cavity states there must be some other component of the TB potential that is more negative than the corresponding component of our model. Polarization energy is an obvious candidate, and the histograms in Fig. 2.9 identify the precise culprit, namely, the change in the water–water polarization energy upon electron attachment. (Specifically, these histograms show the difference between the water–water part of the potential when the dipoles are converged for the neutral system versus when they are converged in the anion, including the self-energy due to the electron in the latter case.) For cavity states described using our potential, there is a significant increase in the water–water potential upon electron attachment, due to re-polarization of the water molecules by the electron. This increase compensates for a comparatively small repulsive potential. This effect, which is missing from the TB potential, seems qualitatively correct—the induced dipoles computed in the neutral system minimize the total potential energy of the water cluster, so introduction of the electron *must* lead to an increase in the water–water part of the potential. Apparently, this increase is much larger for cavity states than it is for either AA or surface states, a point to which we shall return. We re-iterate that our potential is fit exclusively to the VEBE of $(H_2O)_2^-$—a far cry from any cavity state—so these results cannot simply be dismissed as some obvious artifact of the fit.

The TB model contains a pairwise polarization potential between the electron and the water molecules that simulates the effect of the electron polarizing the water molecules, but omits water–water polarization. Polarization in our model is a many-body effect, so in order to isolate the electron–water polarization in our model, and thus facilitate detailed comparison to the TB model we must separate out the water–water contribution to the polarization energy in our model. To this end, we define (for our model only) an electron–water polarization energy $\langle V_{pol}^{elec} \rangle_{elec} + W_{pol}^{elec}$ according to

$$\langle V_{pol}^{elec} \rangle_{elec} + W_{pol}^{elec} = \langle V_{pol}^{elec} \rangle_{anion} + W_{pol}^{elec} - \langle V_{pol}^{elec} \rangle_{neutral} \, . \tag{2.36}$$

The subscripts $\langle \cdots \rangle_{anion}$ and $\langle \cdots \rangle_{neutral}$ in this equation indicate whether the dipoles used to evaluate $V_{pol}^{elec} = (\mathbf{M}_{elec})^{\top} \, \mathbf{T}'_{elec,j} \, \mathbf{M}_j^{ind}$ are induced in the electric field of the neutral or anionic cluster. In this notation, $\langle V_{pol}^{elec} \rangle_{anion} + W_{pol}^{elec}$ is the expectation value of the *total* polarization potential (as defined in Section 2.3.2), which includes contributions from water–water polarization. The total polarization potential is strictly negative, since polarization is variational in our formalism, although the electron–water polarization potential defined in Eq. (2.36) may have either sign.

Figures 2.10 and 2.11 show the total polarization energy and the electron–water polarization energy, respectively. Compared to TB, our model tends toward larger values of the total polarization energy for both AA and surface states, with results comparable to TB for cavity states. In contrast, when we isolate the polarization energy due to the electron, the two models yield similar results for AA and surface states but our model gives a much larger polarization energy for cavity states (see Fig. 2.11). For water networks that afford surface-bound or AA isomers of $(\mathrm{H_2O})_n^-$, the dipoles are oriented in essentially the same way in both the neutral and the anionic cluster, whereas in cavity-type geometries, the dipoles change qualitatively upon electron attachment. Thus, while polarization may certainly amplify electron binding in the AA and surface isomers, it does not qualitatively change the electrostatic environment of these clusters. In contrast, the excess electron qualitatively alters the electrostatics of cavity-type geometries.

Figure 2.12 supports this conclusion by comparing the polarization energy in the field of the neutral dipoles, $\langle V_{pol}^{elec} \rangle_{neutral}$, with the electron–water polarization potential $\langle V_{pol}^{elec} \rangle_{elec} + W_{pol}^{elec}$. [The sum of these two quantities equals the total polarization energy plus the self energy; see Eq. (2.36)]. For AA and surface states, the interaction of the electron with the induced dipoles is nearly the same when the dipoles come from the neutral water calculation as it is when the dipoles are self-consistently converged for the anion. For cavity states on the other hand, the electron–water polarization energy (with dipoles converged self-consistently for the anion) is large in magnitude and negative in sign, whereas $\langle V_{pol}^{elec} \rangle_{neutral}$ is equally large but positive, indicating a qualitative change in the electrostatic environment upon electron attachment.

It is perhaps counter-intuitive that the electron–water polarization energy should be so much more stabilizing in cavity-type isomers than it is in AA isomers, since the latter are characterized by an unpaired electron that is strongly localized around the AA water molecule. In small AA isomers, the AA water molecule is effectively "buried" within the excess-electron wave function; see the figures in Refs. [90], [119] or [120], for example. This observation is rather revealing, however. It seems that AA and surface states owe their existence to the fact that the water cluster is oriented in such a way that the electron simply attaches to the positive end of an extant dipole moment, and this dipole moment essentially determines the VEBE of anionic cluster. The stability of surface states, including AA isomers, is thus largely dictated by the electrostatic environment of the *neutral* water cluster, which is only mildly perturbed by the presence of the electron. This is clearly *not* the case for the cavity-type isomers, for which we observe a significant re-polarization due to the electron. We speculate that this might be a consequence of the more diffuse nature of surface-bound (as compared to cavity-bound) electrons. While permanent electrostatics may suffice to describe surface states, a non-polarizable model may not be able to offer a *balanced* description of both surface and cavity isomers.

2.6 Conclusions

We have developed a new electron–water pseudopotential, using a sophisticated, polarizable water model, from which an electron–water polarization potential arises in a natural fashion and need not be grafted onto the model *a posteriori*. Notably, our model incorporates the fact that introduction of an excess electron must increase the water–water potential energy (even when the anion is bound). This effect is absent in previous hydrated-electron models.

Our model is fit only to the VEBE of $(H_2O)_2^-$, and it is impressive that both VEBEs, as well as relative conformational energies, are reproduced across a diverse set of $(H_2O)_n^-$ cluster isomers. In particular, our model significantly outperforms a similar model[67] that is based upon a non-polarizable force field for water. Comparisons to this fixed-charge model reveal that polarization is especially important for cavity states, for which the induced dipoles are qualitatively altered by the presence of the electron. In the case of surface states (including so-called “AA” isomers), the excess electron simply attaches to the positive end of an existing dipole moment.

The close agreement between our model and *ab initio* calculations suggests to us that our model incorporates most of the relevant physics, and in particular, that the majority of what might be considered (in *ab initio* language) as electron correlation is really just polarization. While QM treatments of electron–water dispersion (via Drude models) achieve somewhat greater accuracy in VEBEs, especially for very weakly-bound anions, they do so at considerably greater expense, and it is not clear whether such a treatment is necessary for larger, strongly-bound anions.

CHAPTER 3

A one-electron model for the aqueous electron that includes many-body electron–water polarization: Bulk equilibrium structure, vertical electron binding energy, and optical absorption spectrum [3.1]

3.1 Introduction

Since its absorption spectrum was first observed in 1962,[124, 125] there have been numerous experimental[4–7, 30, 34, 41, 119, 120, 126–146] and theoretical studies[31, 32, 38, 44, 62, 63, 65, 67, 70, 72–74, 77, 80–83, 90, 108, 147–160] focused on elucidating the structure, dynamics, and spectroscopy of the aqueous electron (e^-_{aq}) in bulk water, as well as finite $(H_2O)_n^-$ cluster anions. The hydrated electron is a prototypical system for studying the interplay between quantum mechanics, which is required to describe the unpaired electron, and classical mechanics, which is necessary to sample over solvent configurations or cluster morphologies. Despite extensive study, however, agreement between theory and experiment—regarding some of the most basic structural and spectroscopic properties of these systems—is still lacking.

[3.1] This chapter appeared as an article in the *Journal of Chemical Physics* in 2010, volume 133, page 154506.

Extrapolation of the vertical electron binding energies (VEBEs) for $(H_2O)_n^-$ cluster anions suggests a value of ≈ 3.4 eV for the VEBE of the aqueous electron,[2, 30] consistent with several recent direct measurements of the VEBE for e_{aq}^- using liquid microjets.[5–7] However, recent simulations using one-electron pseudopotential models suggest that the cluster photo-electron experiments do not actually probe "internal" (cavity-bound) states of the excess electron, but rather surface-bound states with no bulk analogue.[32, 153] This interpretation remains controversial,[33, 35, 86] and the cluster size at which the electron internalizes remains a topic of contemporary interest.

The optical absorption spectrum is the primary experimental handle for e_{aq}^- in bulk solution, yet quantitative reproduction of this spectrum by theoretical means has proven elusive. Simulations based on a one-electron pseudopotential model developed recently by Turi and Borgis[67] (TB) reproduce the absorption maximum to within ~ 0.2 eV,[67, 160] but so far none of the different one-electron models that have been developed over the years[67, 72, 147, 148, 152, 154] reproduces the asymmetric Lorentzian tail that is observed on the blue edge of the spectrum.[2, 26, 161–163]

The solvation environment of the bulk species is also under discussion. Long ago, Kevan[126, 127] proposed a hexavalent coordination motif, based upon spin echo measurements in aqueous glasses at $T = 77$ K. Shkrob[157] has recently provided theoretical support for this interpretation, based upon *ab initio* calculations of hyperfine coupling constants in small $(H_2O)_n^-$ clusters. However, the aforementioned TB model potential affords a tetravalent structure at $T = 300$ K.[67] Very recently, Larsen *et al.*[44] have suggested, based upon a different one-electron model, that the e^-_{aq} wavefunction is not really “coordinated” in the same sense as atomic ions such as Br^- or I^-, but is instead delocalized over a large number of water molecules, on which it exerts only a weak orientational influence. Further complicating the matter are vibrational spectra of $(\mathrm{H_2O})_n^-$ clusters that suggest the presence of a so-called double acceptor (“AA”) electron electron binding motif[119, 120, 137] in clusters as large as $n = 50$,[141] whereas resonance Raman spectra of the bulk species are interpreted as arising from a coordination motif that involves only one hydrogen atom per water molecule.[136]

Motivated by these outstanding issues, we decided to revisit the most basic structural, spectroscopic, and dynamical aspects of the hydrated electron, using a one-electron model that is built upon a sophisticated and accurate water force field. In practice, this means a polarizable force field, whereas most previous one-electron models for e^-_{aq} have employed fairly rudimentary water models, such as the “simple point charge” (SPC) model.[88, 89] We expect that a polarizable model will better describe the relative energies of distorted hydrogen-bonding networks that are stabilized by the excess electron, but are highly unfavorable in neutral water.[43, 91] In addition, we wish to determine the extent to which a self-consistent treatment of many-body electron–water polarization is qualitatively important. Along these lines, we note that cavity-bound $(\mathrm{H_2O})_n^-$ isomers are characterized by a much larger number of significant electron–$\mathrm{H_2O}$ interactions, as compared to surface-bound isomers.[1] As such, one might expect very different polarization energies for surface- versus cavity-bound electrons.

In chapter 2 we reported an electron–water pseudopotential designed for use with the "AMOEBA" polarizable water model.[14, 164] In the discussion that follows, this one-electron model for e^-_{aq} is termed "polarizable electron–water potential #1" (PEWP-1). Compared to the non-polarizable TB model,[67] which has been used extensively in recent simulations,[32, 67, 80–83, 153, 159] PEWP-1 affords significantly better agreement with *ab initio* benchmarks for both VEBEs and relative isomer energies of $(H_2O)^-_n$ clusters.[3] When used to simulate e^-_{aq} in bulk solution, however, we found that PEWP-1 predicts a diffuse ground-state electronic wavefunction that penetrates throughout the water network, rather than forming a proper cavity.[43] As a result, PEWP-1 predicts an unrealistically fast diffusion coefficient of $\gtrsim 1.0$ Å^2/ps at 300 K, as compared to an experimental value of 0.51 Å^2/ps.[129] Given the compelling experimental evidence for electron localization in polar fluids,[126, 127, 165] plus the fact that *ab initio* calculations strongly suggest cavity formation in hydrated-electron systems,[103, 155, 160] we rejected this model and decided to revisit the parameterization of the electron–water pseudopotential. The largest difference between our previous parameterization and the one reported here, the latter of which we shall call PEWP-2, is that the new potential is much more repulsive in the core molecular region. This difference alone facilities cavity formation.

In this work we re-parameterize our model on the basis of the static exchange (SE) approximation.[39, 64, 66, 94] Unlike previous SE treatments, however, we use density functional theory (DFT) to provide an electron–water exchange-correlation potential, rather than relying on Hartree-Fock theory for this purpose. After construction of an exchange-correlation potential, we fit a repulsive potential in order to reproduce the density maximum of the lowest unoccupied molecular orbital (LUMO) near the core molecular region. As compared to the original parameterization (PEWP-1), this new model (PEWP-2) affords even better agreement with *ab initio* benchmarks for $(H_2O)_n^-$ clusters. Application of PEWP-2 to the bulk aqueous electron reveals that the description of electronic relaxation upon electron detachment is crucial for obtaining a reasonable bulk binding energy. Most interestingly, the inclusion of electron–water polarization not only provides an accurate prediction of the optical absorption maximum, but for the first time affords a significant "blue tail" in the spectrum, vastly improving the agreement with the experimental line shape, as compared to all previous one-electron models.

3.2 Re-parameterization of the model potential

3.2.1 Motivation

In order to construct a scalar potential for the electron–water interaction, we follow the procedure of Smallwood *et al.*,[166] which provides a computationally exact way to solve for the Phillips-Kleinman[97] pseudo-wavefunction. Although this procedure was developed in the context of Hartree-Fock (HF) theory, one can easily replace the HF exchange operator with the exchange-correlation operator defined by any Kohn-Sham density functional, and thereby obtain a potential that includes dynamical correlation, provided that one accepts that the Kohn-Sham MOs are suitable replacements for the HF MOs. The problem with using traditional DFT for the hydrated electron is that self-interaction error causes widely-used functionals such as B3LYP and BLYP to overbind the unpaired electron by a significant amount.[103] Recently-developed "long-range corrected" (LRC) density functionals, however, are asymptotically free of self-interaction error, and the LRC-μBOP functional[167, 168] has recently been shown to provide extremely accurate VEBEs in $(\mathrm{H_2O})_n^-$ clusters.[3, 114] Presumably, this is because the singly-occupied MO (SOMO) mostly occupies a region of space apart from the valence MOs, and the LRC procedure therefore eliminates self-interaction error associated with the SOMO.

At the outset, we should clarify that we expect any pseudopotential to be semi-quantitative at best, due to a neglect of many-electron contributions to the wavefunction, which appear to be necessary in order to explain certain aspects of the spectroscopy of e_{aq}^-. All-electron calculations in $(\mathrm{H_2O})_n^-$ clusters indicate that ~ 10–20% of the spin density resides on $\mathrm{H_2O}$ molecules, which provides an explanation for observed vibrational red shifts[156] and hyperfine coupling constants.[157] In addition, the total oscillator strength associated with the optical spectrum of e_{aq}^- is ~ 1.1,[146] indicating that the electronic excitations contain a small amount of many-electron character. (Because the excited states obtained from time-dependent DFT calculations clearly resemble particle-in-a-box eigenstates,[160] we expect that many-electron character plays only a minor role in the excitation spectrum.)

In view of these facts, our main aim is to study the extent to which polarization is qualitatively important in describing the features of $(\mathrm{H_2O})_n^-$ clusters and bulk e_{aq}^-, using a model that is tractable enough to facilitate adequate statistical sampling. At the same time, we do wish to make contact with photo-electron data and to infer relationships between cluster spectroscopy and bulk measurements, both of which demand an accurate treatment of VEBEs. Furthermore, the ongoing debate regarding surface states versus cavity states in $(\mathrm{H_2O})_n^-$ clusters is, at its core, a debate over extrapolations to the bulk limit, so we desire a model that can also reproduce bulk properties.

The model constructed herein is empirical in nature; we use the SE approximation as a guide to constructing a potential, but not to *derive* quantitative interaction terms. That said, we do not fit this model directly to any measured or computed observables, so to the extent that the model successfully reproduces observables, it is reasonable to conclude that much of the basic physics has been described successfully.

3.2.2 The static-exchange approximation

To date, most electron–water pseudopotentials are either extremely heuristic in nature, which is inconsistent with our goal of achieving at least a semi-quantitative description of e_{aq}^- and $(\mathrm{H_2O})_n^-$ spectroscopy, or else are based upon the SE approximation.[39, 64, 66, 94] Within this approximation, one considers the interaction of an excess electron with the ground-state wavefunction of an isolated molecule, in our case, $\mathrm{H_2O}$. The $\mathrm{H_2O^-}$ wavefunction, $|\Psi\rangle$, is taken to be an antisymmetrized product of the excess-electron orbital, $|\psi\rangle$, and the frozen MOs from a (neutral) $\mathrm{H_2O}$ calculation, $|\psi_i\rangle$. This leads to a one-electron eigenvalue equation for the excess electron:[64, 66, 94]

$$\hat{H}_{\mathrm{SE}}|\Psi\rangle = (\hat{T} + V_n + V_H + \hat{V}_{xc})|\Psi\rangle = \varepsilon\,|\Psi\rangle\ . \tag{3.1}$$

Here, $\hat{T}$ is the kinetic energy operator, V_n is the electron–nuclear Coulomb interaction, V_H is the electronic Coulomb (Hartree) energy, and $\hat{V}_{xc}$ is the (nonlocal) exchange-correlation operator. The quantities V_H and $\hat{V}_{xc}$ are identical to the Coulomb and exchange (or exchange-correlation) operators in a HF (or Kohn-Sham DFT) calculation of H_2O, hence the highest occupied MO (HOMO) in the SE approximation is the LUMO in the HF or DFT calculation. Inclusion of a DFT exchange-correlation component in Eq. (3.1) is a novel feature of the present treatment.

Although Eq. (3.1) is a one-electron eigenvalue equation, construction of $\hat{H}_{\mathrm{SE}}$ requires the H_2O MOs. This dependence must be removed in order to obtain a scalar potential, $V(\vec{r})$, that can be readily evaluated and fit to some analytical expression, thus converting Eq. (3.1) into a simple one-electron eigenvalue equation, $(\hat{T}+V)|\Psi\rangle = \varepsilon|\Psi\rangle$.

Following Schnitker and Rossky,[64] we write the actual SE wavefunction, $|\psi\rangle$, as a linear combination of a nodeless wavefunction, $|\phi\rangle$, that is asymptotically correct but lacks oscillations in the core molecular region, along with a residual that is expanded in terms of the MOs, $|\psi_i\rangle$, from a calculation on an isolated H_2O molecule:

$$|\psi\rangle = |\phi\rangle + \sum_{i}^{N_{occ}} c_i|\psi_i\rangle\ . \tag{3.2}$$

Inserting Eq. (3.2) into Eq. (3.1) affords an eigenvalue equation for the nodeless wavefunction,[64]

$$\left(\hat{H}_{SE} + \sum_{i}^{N_{occ}} (\varepsilon - \varepsilon_i)|\psi_i\rangle\langle\psi_i|\right)|\phi\rangle = \varepsilon|\phi\rangle \ . \tag{3.3}$$

The second term in parenthesis in Eq. (3.3) is an operator that forces $|\phi\rangle$ to remain outside of the core (H_2O) region, preventing variational collapse. One may express the action of this operator on $|\phi\rangle$ using a (scalar) repulsive potential

$$V_{rep}(\vec{r}) = \sum_{i}^{N_{occ}} \frac{(\varepsilon - \varepsilon_i)\, \psi_i(\vec{r})\langle\psi_i|\phi\rangle}{\phi(\vec{r})} \ , \tag{3.4}$$

but this potential then depends upon the nodeless pseudo-wavefunction itself.

To eliminate this dependence, Schnitker and Rossky make two subsequent approximations:[64] first, that the excess electron is weakly-bound ($|\varepsilon| \ll |\varepsilon_i|$), and second, that the nodeless function $|\phi\rangle$ is not only smooth but is constant in the core region. Although the latter assumption is somewhat dubious, without it the nodeless function is not uniquely defined by Eq. (3.3).[166] Recently, Smallwood *et al.*[166] have shown that this ambiguity can be removed (and the assumption that $|\phi\rangle$ is constant in the core region can be avoided) by supplying an additional constraint. Following those authors, we choose this constraint to be that $\langle\phi|\hat{T}|\phi\rangle$ should be minimized. This requirement leads to an iterative recipe for calculating the nodeless pseudo-wavefunction:[166]

$$|\phi\rangle = |\psi\rangle + \sum_{i}^{N_{occ}} \frac{\langle\psi_i|\hat{T}|\phi\rangle}{\langle\phi|\hat{T}|\phi\rangle}|\psi_i\rangle \ . \tag{3.5}$$

Once $|\phi\rangle$ is known, one can always define an orbital-dependent scalar potential

$$v[\phi](\vec{r}) = \frac{\langle\vec{r}|\hat{v}|\phi\rangle}{\phi(\vec{r})} \tag{3.6}$$

for any operator $\hat{v}$. [In fact, Eq. (3.4) is just a special case of Eq. (3.6).] Construction of this potential requires the H_2O MOs, but once $v[\phi](\vec{r})$ is determined, it can be fit to some analytic form for convenient evaluation. In practice, we will use Eq. (3.6) to obtain a local potential for exchange and correlation ($\hat{v} = \hat{V}_{xc}$). Note also that since the MOs $|\psi_i\rangle$ used to construct this potential are frozen, polarization is not included in this potential. Polarization is sometimes grafted onto the SE approximation, in the form of a two-body polarization potential of the form

$$V_{pol}(r) = -\frac{\alpha}{2(r^2 + C)^2} \ , \tag{3.7}$$

where α is the isotropic polarizability of H_2O and C is a constant.[39, 62, 64, 67] In the present work, *many-body* polarization is incorporated self-consistently, via a polarizable water potential from which an electron–water polarization potential arises in a natural way, and from which the two-body potential in Eq. (3.7) can be obtained based on well-defined approximations.[3]

Electrostatic interactions between the electron and the water molecules are destined to be replaced by electron–multipole interactions, where the multipoles come from the water force field. Inclusion of the exact SE potentials V_n and V_H from Eq. (3.1) would double-count these interactions, thus we allow the force field alone to represent the electrostatic parts of the electron–water interaction. The non-electrostatic components of the interaction, which include Pauli repulsion and exchange-correlation effects, are represented in the form of a potential $V_{rep} + V_{xc}$, where V_{xc} comes from Eq. (3.6) as described above, and V_{rep} is a repulsive potential that prevents collapse of the wavefunction. Fundamentally, V_{rep} arises from orthogonality; its construction is discussed in Section 3.2.4.

3.2.3 Electrostatic interactions

Electrostatics and polarization are handled in the same way as in our earlier work,[3] to which the reader is referred for details. The essential features are summarized in this section. Let V^{MM} denote all of the intramolecular and water–water interaction terms contained within the AMOEBA force field. Within AMOEBA, electrostatic interactions are represented in terms of permanent charges, dipoles, and quadrupoles, along with inducible dipoles, and we denote the electron's interactions with the permanent and the induced multipoles as $V_{perm}^{elec-water}$ and $V_{pol}^{elec-water}$, respectively. The full interaction potential is then

$$\begin{aligned} V^{elec-water} = V^{\mathrm{MM}} &+ V_{perm}^{elec-water} + V_{pol}^{elec-water} \\ &+ V_{xc}^{elec-water} + V_{rep}^{elec-water} \ , \end{aligned} \tag{3.8}$$

where the final two terms come from the pseudopotential. (Fitting of these two terms is discussed in the next section.) Induced dipoles on the water molecules are determined using the total electric field, which contains contributions from the water molecules and from the wavefunction.[3]

Polarizable force fields based upon induced dipoles must utilize a damped Coulomb operator that is finite as $r \rightarrow 0$, in order to avoid a "polarization catastrophe".[101] The water–water interactions within AMOEBA already employ such an operator,[14] which we do not modify here. For the electron–water electrostatic interactions, we use the modified Coulomb potential

$$t_{elec,i} = \frac{\mathrm{erf}(a_i \, r_{elec,i})}{r_{elec,i}} \ , \tag{3.9}$$

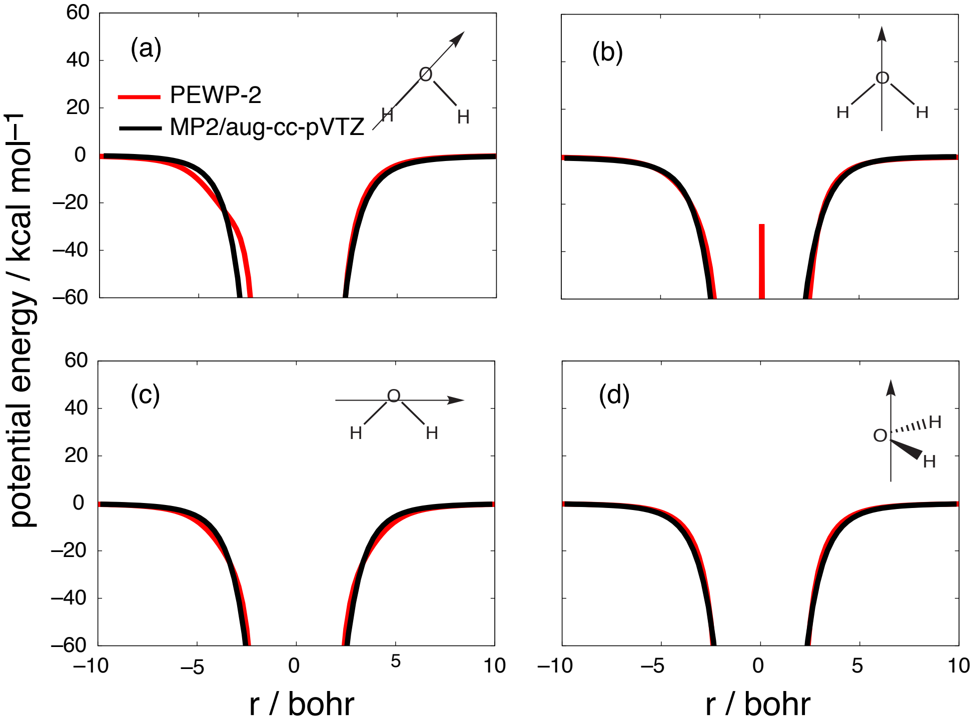

Figure 3.1: Calculated MP2 polarization potential, as compared to the fit that is used to obtain Coulomb damping parameters. The origin of the coordinate system is the H_2O center of mass, except in panel (a), where the origin is the oxygen atom.

where a_i is one of two damping parameters (i = O or H), and $r_{elec,i}$ is the electron–multipole distance. [Technically, $t_{elec,i}$ is the modified Coulomb operator for electron–monopole interactions; analogous quantities for higher-order multipoles are obtained by differentiating $t_{elec,i}$.[3]] This same damped Coulomb operator is used to calculate the wavefunction's contribution to the electric field.

There is no *a priori* reason why the permanent and induced electrostatic interactions should require the same damping parameters a_i, and our model uses different parameters for each. The damping parameters a_O and a_H for the electron/induced dipole interactions ($V_{pol}^{elec-water}$) are obtained from a fit to an *ab initio* polarization potential for H_2O, calculated at the level of second-order Møller-Plesset perturbation theory (MP2), as follows. We first perform an MP2 calculation on isolated H_2O, then use these MOs as the starting point for a calculation that includes a single -1 point charge. The MP2 polarization energy is calculated as a function of the position of this point charge, and includes both the energy decrease that accompanies orbital relaxation in the presence of the point charge, plus the change in the MP2 correlation energy between the isolated H_2O calculation and the calculation in the presence of the point charge. The parameters a_O and a_H are then fit to reproduce this polarization potential along each of the four one-dimensional cuts shown in Fig. 3.1. Since we will ultimately add to this a potential that is quite repulsive in the core molecular region, it is not necessary to obtain an extremely accurate fit for the attractive parts of the potential where r is small; only the region where $r \gtrsim 3$ bohr is relevant. The fits shown in Fig. 3.1 are quite good in the relevant region.

3.2.4 Repulsive potential and fitting parameters

In order to construct a local potential of the form given in Eq. (3.6), we first solve Eq. (3.5) for the nodeless pseudo-wavefunction, $|\phi\rangle$, using an initial guess corresponding to the LUMO of H_2O. Once a self-consistent solution has been determined, we construct a scalar potential for exchange and correlation by setting $\hat{v} = \hat{V}_{xc}$ in Eq. (3.6), using the LRC-μBOP functional[167, 168] to define $\hat{V}_{xc}$. Alternative density functionals such as LRC-ωPBEOP that afford similar VEBEs yield similar results for the exchange-correlation potential, but the pseudopotentials obtained using functionals that strongly overbind the electron (*e.g.*, B3LYP) are notably different.

To this exchange-correlation potential we must add a repulsive potential, whose physical origin is the orthogonality requirement between the excess-electron MO and the core H_2O MOs. In principle, one could construct a repulsive potential using the expression [*cf.* Eq. (3.4)]

$$\hat{V}_{rep} = \sum_{i}^{N_{occ}} (\varepsilon - \varepsilon_i) |\psi_i\rangle\langle\psi_i| \ , \tag{3.10}$$

but our attempts to utilize this expression directly were not successful, as the resulting potential is far too repulsive in the core molecular region. In our view, Eq. (3.10) produces a potential that is much too repulsive for use in conjunction with damped electrostatics, which attenuate the attractive interactions at short range. In parameterizing our previous model, PEWP-1,[3] we drastically scaled down this repulsive potential using a scaling parameter that was fit to reproduce *ab initio* VEBE benchmarks for $(H_2O)_n^-$ clusters; a dramatic scaling of the repulsive potential was also used by Wang and Jordan,[68] to develop a different electron–water potential. Evidently, the Coulomb attenuation in Eq. (3.9) can compensate for this scaling, because PEWP-1 affords fairly accurate VEBEs across a wide range of energies.[3] When applied to the condensed phase, however, PEWP-1 fails to localize the electron into a cavity and predicts a diffusion coefficient that is too large by at least a factor of two. We interpret these observations evidence that the repulsive potential has been reduced too much.

As an alternative to Eq. (3.10), we fit a repulsive potential, as well as damping parameters a_{O} and a_{H} for the interaction between the electron and the H_2O permanent multipoles ($V_{perm}^{elec-water}$). The two damping parameters are fit in order to reproduce the density maximum of the pseudo-wavefunction confined to the region of the molecule. While we do not directly fit to any VEBEs *per se*, in the final step of this procedure we do reject any fits that do not reproduce *ab initio* VEBEs to within $\sim$0.1 eV.

Calculations to determine the pseudo-wavefunction utilize a Gaussian basis set that we call aug-cc-pVQZ+diff–pol. The "+diff" indicates we have added diffuse s and p functions to each hydrogen atom, with exponents of 0.00295375 and 0.0106 bohr^{-2}, respectively; the "–pol" indicates we have removed all g and higher angular momentum functions. A single water molecule does not bind an extra electron, so "convergence" of the basis set cannot be achieved with respect to the excess-electron distribution, which is ultimately bound only by the compactness of the basis set. However, the aforementioned basis set should give a good representation of the H_2O density, while being diffuse enough to describe the excess electron distribution in the immediate vicinity of the molecule, which is the chemically significant region. Calculation of the pseudo-wavefunction was performed using a locally-modified version of Q-CHEM.[117]

The exchange-correlation potential obtained from Eq. (3.6) is computed on a grid of points and then fit to an analytic form consisting of a sum of Gaussian functions centered on the molecular mechanics (MM) atoms,

$$V_{xc}^{elec-water}(\vec{r}) = \sum_i C_i \, \exp\left(-z_i \, |\vec{r} - \vec{r}_i|^2\right) \, . \tag{3.11}$$

A good fit was obtained using a single Gaussian function on the oxygen atom and

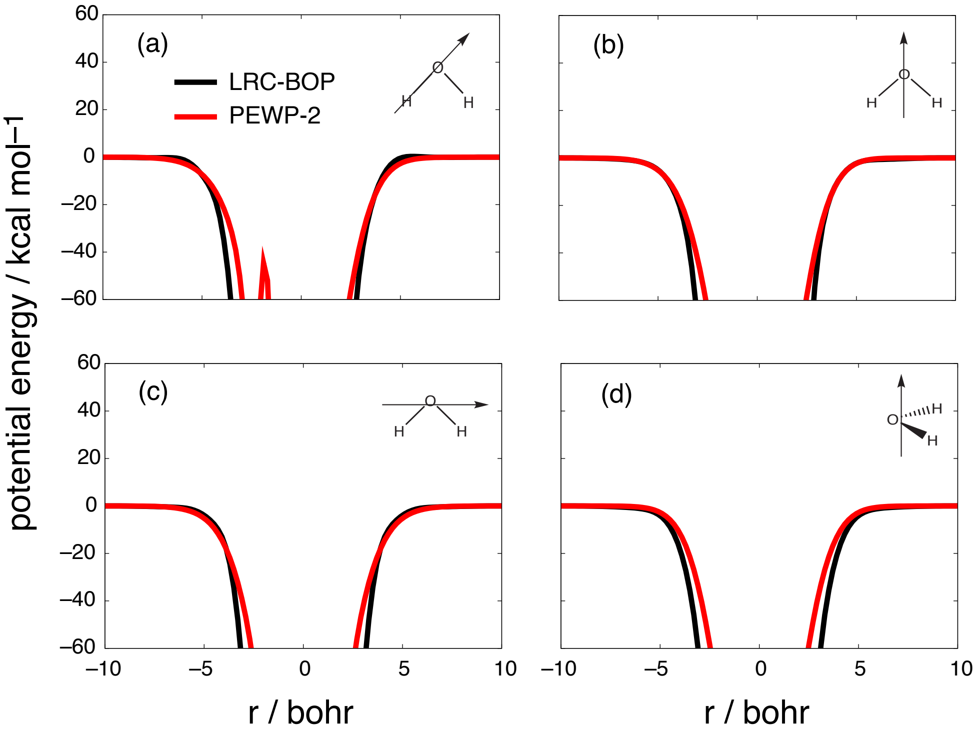

Figure 3.2: The LRC-μBOP exchange-correlation potential, obtained from the pseudo-wavefunction using Eqs. (3.5) and (3.6), along with the fit to this potential that is used to construct the PEWP-2 model potential. The origin of the coordinate system is the H_2O center of mass, except in panel (a), where the origin is the oxygen atom.

three Gaussians on each hydrogen atom. (All fitting parameters are provided in appendix.A) Figure 3.2 plots the fitted potential along four one-dimensional slices. As mentioned above, it is only necessary to obtain a good fit to the attractive parts of the exchange-correlation potential in regions where $r \gtrsim 3$ bohr, and our fit is quite reasonable in these regions.

We construct repulsive potentials centered on each MM atom, of the form

$$V_{rep}^{elec,i}(\vec{r}) = \frac{B_1^i}{r_{elec,i}} \left[\mathrm{erf}(B_2^i \, r_{elec,i}) - \mathrm{erf}(B_3^i, r_{elec,i}) \right] \; , \tag{3.12}$$

where $i = $ O or H, and $r_{elec,i} = |\vec{r} - \vec{r}_i|$. (The total repulsive potential is the sum of the three atom-centered potentials.) Equation (3.12) is the same functional form used by Turi and Borgis[67] to obtain a scalar potential that reproduces the SE pseudo-wavefunction, neglecting exchange and correlation interactions. Following those authors, we apply a confining potential of the form $V_{conf} = k(x^8 + y^8 + z^8)$, with $k = 5$ x 10^{-7} E_h, which keeps the (unbound) excess electron near the core region. This confining potential is only employed in order to fit the pseudo-wavefunction, and not when fitting to the exchange-correlation potential described above. We believe that applying a confining potential is reasonable in that it should mimic the behavior of the excess electron in a high density environment,[169] and hence provide guidance for the fitting of the repulsive potential.

Figure 3.3 shows the density of the excess electron, $|\psi|^2$, calculated using various methods. The H_2O LUMOs computed at both the HF and LRC-μBOP levels are shown, as are the corresponding SE pseudo-wavefunctions. Also shown are the ground-state wavefunctions obtained using the PEWP-1, PEWP-2, and TB model

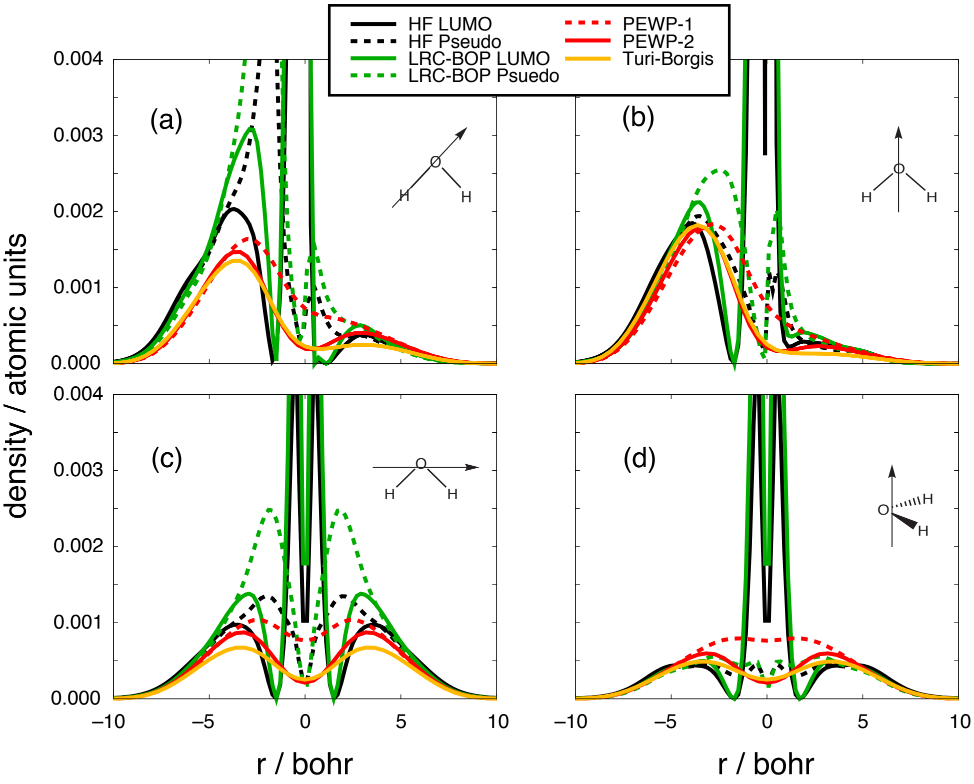

Figure 3.3: Comparison of various plots of $|\psi|^2$ for the excess electron, obtained using a confining potential (see text for details). The origin of the coordinate system is the H_2O center of mass, except for panel (a), where the origin is the oxygen atom.

potentials, the latter having been fit to reproduce the HF pseudo-wavefunction. Several important observations can be made from Fig. 3.3. Comparing the LUMOs to the SE pseudo-wavefunctions, we observe that the latter are indeed asymptotically correct while lacking the large amplitude oscillation in the molecular core. The position of the density maximum in the LUMO, which is similar at both the HF and LRC-μBOP levels of theory, is reproduced best by the HF pseudo-wavefunction, but neither pseudo-wavefunction accurately locates the density maximum along the O–H bond coordinate [see Fig. 3.3(a)]. We feel that this significant discrepancy reflects an inadequacy in the Phillips-Kleinman procedure,[97] such that a pseudopotential that is directly fit to the SE pseudo-wavefunction is likely to afford a one-electron wavefunction that differs substantially from the SOMO in a many-electron calculation.

We chose to fit our potential to reproduce the position of the density maximum of the LUMO, as computed at the LRC-μBOP level. Figure 3.3 shows that we are able to fit to the position of this maximum quite well, even if we cannot fit its precise magnitude; in the end, the PEWP-2 density is quite similar to that obtained using the TB potential.[67] The main differences are that our density maximum is slightly closer to the molecular core, and our potential gives an enhanced amount of density just beyond the oxygen atom, in the plane of the molecule [see Fig. 3.3(c)]. Figure 3.3 also shows why our previous parameterization, PEWP-1, fails to produce a cavity: there is too much density in the core region. In the one-dimensional slices depicted in Figs. 3.3(c) and 3.3(d), for example, the PEWP-1 density achieves nearly its maximum value within the core region. The PEWP-1 repulsive potential is not

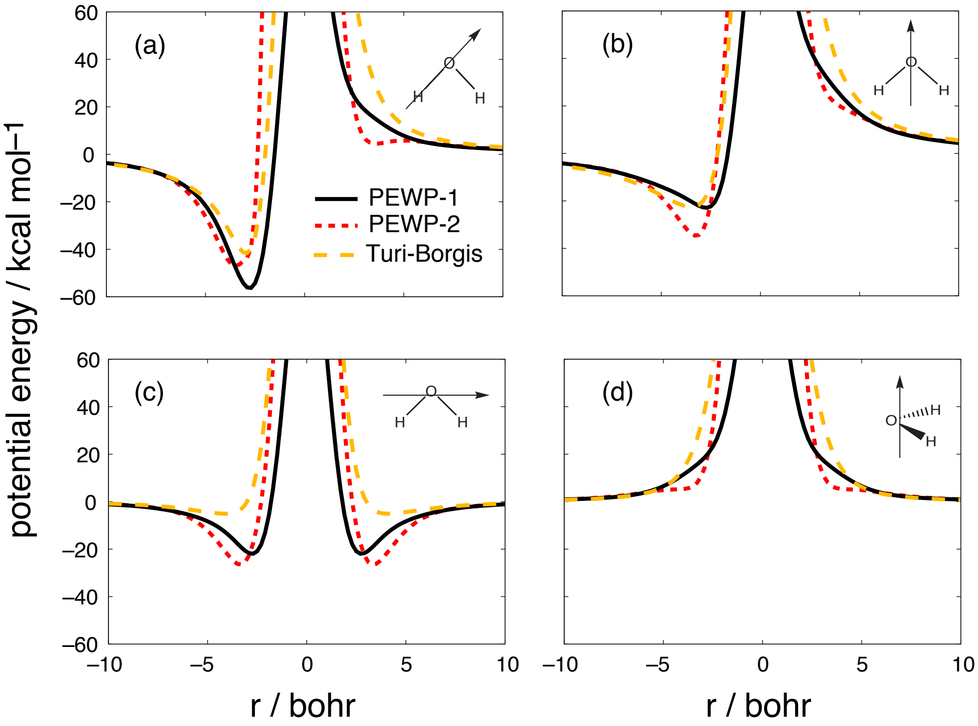

Figure 3.4: Comparison of different electron–water potentials, shown without polarization. The origin of the coordinate system is the H_2O center of mass, except for panel (a), where the origin is the oxygen atom.

nearly repulsive enough, and this allows the electron to penetrate easily into the water network, without the need to form a proper cavity, which accounts for the anomalously large diffusion coefficient predicted by this model. This should not be the case with our new parameterization.

The full PEWP-2 potential is compared to PEWP-1 and to the TB potential in Fig 3.4, where all three potentials are plotted without polarization. It is clear from Fig. 3.4 that PEWP-2 contains a steeper and wider repulsive potential than its predecessor; the maximum value of this potential (not shown in Fig. 3.4) has increased from ~120 kcal/mol (PEWP-1) to ~550 kcal/mol (PEWP-2). This increase leads to a satisfactory reproduction of the LUMO from LRC-μBOP. The new potential is more attractive along the "dipole" coordinate [Fig. 3.4(b)], and also along the perpendicular coordinate in the plane of the water molecule [Fig. 3.4(c)]. These differences largely result from the inclusion of a DFT exchange-correlation potential.

3.3 Computational procedures

Within our model, calculation of energies and wavefunctions requires simultaneous solution of a grid-based Schrödinger equation,

$$\mathbf{H}\mathbf{c}_I = E_I \mathbf{c}_I \ , \tag{3.13}$$

along with linear response equations for the inducible dipoles,

$$\vec{\mu}_i^{\,\text{ind}} = \alpha_i \left(\vec{F}_i^{\text{MM}} + \vec{F}_i^{\text{QM}} \right) \ . \tag{3.14}$$

Solution of Eq. (3.13) was accomplished via the Davidson-Liu method,[109] with a convergence threshold of $||(\hat{H} - E)\psi|| < 10^{-8}\ E_h$. For $(\text{H}_2\text{O})_n^-$ clusters with $n < 20$, we use a 60 Å × 60 Å × 60 Å cartesian grid with a spacing $\Delta x = 1.0$ Å, but for larger clusters (where the wavefunction is more localized), we employ a 40 Å × 40 Å × 40 Å grid, also with $\Delta x = 1.0$ Å. These calculations were performed with our home-built code, FURRY (ver. A),[3] which employs a locally-modified version of the TINKER MM package[170] to evaluate the AMOEBA water potential and solve for the induced dipoles.

Bulk e^-_{aq} simulations use a grid spacing of $\Delta x \approx 0.93$ Å. This choice is quite conservative, and numerical experiments suggest that the energy is probably converged already with a grid spacing of $\Delta x \approx 1.1$ Å. (The smooth, slowly-varying nature of the pseudopotential, combined with the small mass of e^-, enables the use of such a coarse grid.) Simulations were intiated from an equilibrated box of neat liquid water, then allowed to equilibrate for at least 5 ps following introduction of the electron. We propagate the dynamics in the canonical (NVT) ensemble, using the velocity Verlet algorithm. The water molecules were flexible and a time step of 1.0 fs was used. A single Nosé-Hoover thermostat chain,[171] of length four, was used to conserve temperature.

Electrostatic interactions for bulk e^-_{aq} are treated by standard Ewald summation with a uniform positive background density.[172] For simulations using the TB hydrated-electron model,[67] which includes an *ad hoc* polarization potential of the form given in Eq. (3.7), the polarization interactions were summed using the minimum-image convention. Non-electrostatic interactions, including TB polarization, were cut off at one-half of the box length, and were smoothly attenuated starting at 0.95 times that value. (For the 200-molecule unit cell described below, $V_{pol} < 0.04$ kcal/mol at the cutoff distance.)

Regarding Ewald summation, Staib and Borgis[152] point out that because the one-electron wavefunction interacts with its periodic replicas, the electron–electron interactions should be determined self-consistently, leading to an iterative procedure that is reportedly numerically unstable,[169] and is used infrequently. For the fixed-charge TB model, however, Ewald summation has been shown to increase the bulk VEBE by 0.8 eV relative to the value that is obtained using the minimum-image convention.[83]

From our point of view, solution of the grid-based Schrödinger equation simply requires knowledge of the potential energy at every grid point, and interactions with the image electrons are artifacts of the use of a finite simulation cell, which vanish as the size of the unit cell increases. Therefore, we will run trajectories at several different periodic box sizes, in order to extrapolate to the infinite-dilution limit. In our simulations, we evaluate the potential at each grid point as if a $-e$ point charge were located at that grid point, but with induced dipoles that are converged using the actual electric field of the MM molecules and the wavefunction. Standard Ewald summation is then used to sum all of the electrostatic interactions. We find this procedure to be free of instabilities.

We run trajectories for cubic unit cells containing $N = 100$, 200, 300 and 600 water molecules, using a water density of 0.997 g/cm^3. (This corresponds to simulation cell lengths $L_{\text{box}} = 14.4192$ Å, 18.1671 Å, 20.7961 Å, and 26.2015 Å.) For each box size, four independent trajectories were performed, with simulation lengths that varied from 7 ps ($N = 600$) to 60 ps ($N = 100$), for total simulation times of between 21 and 240 ps.

For simulations involving $N \leq 300$ water molecules, the grid is approximately the same size as the simulation cell, but for ground-state dynamics with $N = 600$, we use the same grid as for $N = 300$, in order to make the simulation tractable. (Electronic excitation spectra, however, are obtained using grids that fill the entire simulation cell.) Because the electronic energy is not invariant to translation or rotation of the grid, we would like to avoid moving the grid during the simulation, but this is impossible to avoid altogether because the wavefunction diffuses rapidly through the medium, and would eventually reach the edge of the grid. Energy conservation in the non-polarizable TB model appears to be relatively insensitive to small translations of the grid, and other researchers have employed a procedure in which the grid is translated at each time step, such that its origin always coincides with the centroid of the wavefunction.[67, 83] In the context of our polarizable model, however, this procedure leads to a catastrophic failure to conserve energy, even though the discontinuities engendered by grid translation change the VEBE by only $\sim 10^{-3}$ eV. Presumably, this enhanced sensitivity arises because the polarizable model uses the grid to discretize not only the potential but also the electric field due to the wavefunction.

We tested two strategies designed to avoid this problem. The first was to translate the grid to the center of the electron distribution only when $\sim 1\%$ of $|\psi|^2$ resides on the faces of the cubic grid, meaning that the grid is moved as infrequently as possible. A second strategy was to translate the grid by exactly Δx any time that the centroid of ψ is more than Δx away from the origin, so that the new grid exactly coincides with the previous one, albeit shifted by Δx. The first strategy led to good energy conservation until a translation was performed, at which point the system energy dropped discontinuously, by a significant amount ($\sim 0.1\%$). In the smallest simulation cell, translation events occur at least every 10 ps—frequently enough to give us pause. The second strategy conserves energy fairly well in the smallest simulation cell (albeit with a constant drift), but quite well in the largest simulation cell. Using the second strategy, and assuming that the grid is large enough so that the wavefunction is zero at its edges, the system does not know that the grid has been moved, and energy conservation simply reflects how well the wavefunction is converged as a function of grid size. In the simulations reported below, we employ the second strategy exclusively.

3.4 Cluster benchmarks

As in our previous work,[3] we assess the accuracy of our one-electron model against MP2 benchmarks for $(H_2O)_n^-$ clusters, $n = 2$–33. We will compare PEWP-2 to its predecessor, PEWP-1, and also to the TB model.[67] The latter has been used extensively in recent simulations of both $(H_2O)_n^-$ clusters and also bulk e_{aq}^-.[32, 67, 80–83, 153, 159] The TB model employs a non-polarizable force field for the water molecules,[89] an *ad hoc* electron–water polarization potential [see Eq. (3.7)], and an electron–water pseudopotential that is fit in order to reproduce the SE pseudowavefunction computed at the HF level. As such, this model provides an appropriate baseline for the performance of the PEWP models, which (in principle) offer a more detailed description of the relevant interactions.

VEBEs serve as a primary connection between theory and experiment for the hydrated electron, since photo-electron spectra of $(H_2O)_n^-$ have been measured from $n = 2$ to $n = 200$.[4, 30, 34, 85, 130, 131] At the same time, accurate prediction of VEBEs is a challenging test of one-electron models, as this requires an accurate description of both the neutral and anionic potential surfaces. In particular, the neutral cluster's potential surface must be described well in regions where the anion is stable, which often correspond to highly distorted hydrogen-bonding networks that lie far above the global minimum on the $(H_2O)_n$ potential surface.[91] High-energy configurations are not typically used to parameterize or test interaction potentials that are intended to describe neutral water under ambient conditions.

Benchmark VEBEs for 95 different $(H_2O)_n^-$ cluster isomers, ranging in size from $n = 2$ to $n = 33$, were obtained from Ref. [1], where they were computed at the MP2/6-31(1+,3+)G* level. We have previously shown that this level of theory is accurate to within ∼0.02–0.03 eV of coupled-cluster results,[90, 103, 113] and recent quantum Monte Carlo calculations for two different $(H_2O)_6^-$ isomers also agree, within statistical error bars, with both MP2 and coupled-cluster VEBEs.[173] Our VEBE database[1] contains not only gas-phase cluster geometries (optimized using *ab initio* methods), but also clusters that were extracted from a bulk simulations using the TB model, and which are therefore more illustrative of bulk e_{aq}^- structure.

Figure 3.5 compares VEBEs predicted by the various one-electron models to MP2 benchmarks, while Table 3.1 summarizes the statistical deviations with respect to MP2 results. Our new model, PEWP-2, is a clear improvement upon both the TB model and also PEWP-1, despite the fact that the Coulomb damping parameters in

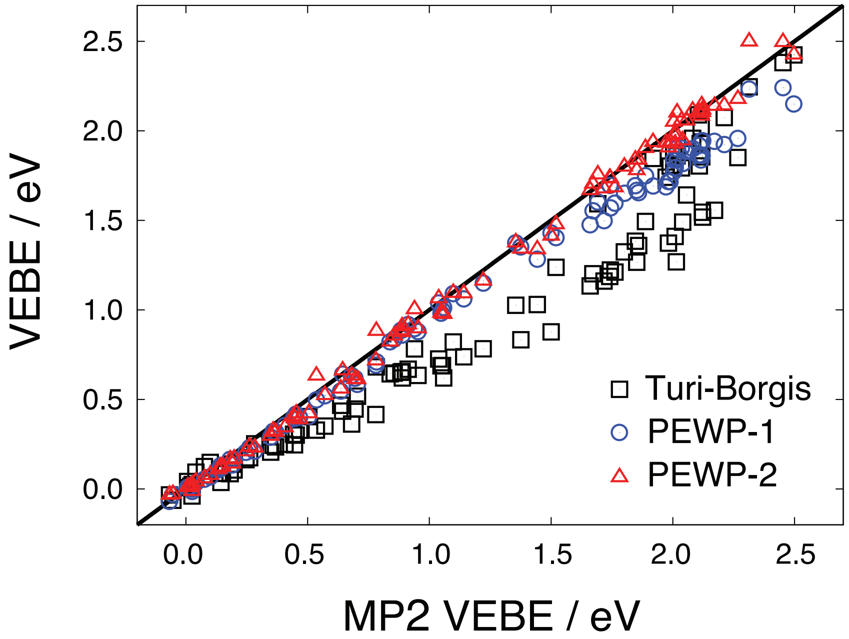

Figure 3.5: VEBEs for 95 different $(\mathrm{H_2O})_n^-$ cluster isomers, n = 2–33, as compared to MP2/6-31(1+,3+)G* benchmarks from Ref. [1].

Method	MUE/eV	MAD/eV
TB	0.253	−0.746
PEWP-1	0.105	−0.348
PEWP-2	0.041	0.184
LRC-μBOP	0.037	0.224

Table 3.1: Mean unsigned errors (MUE) and maximum absolute deviations (MAD) for cluster VEBEs, relative to MP2 benchmarks.

PEWP-1 were fit to reproduce this same set of VEBE benchmarks. Moreover, the PEWP-2 errors do not appear to correlate with cluster size with the magnitude of the VEBE itself, and all of the PEWP-2 VEBEs lie within 0.1 eV of the corresponding MP2 result. The performance of PEWP-2 is similar to that of the LRC-μBOP functional that we used to obtain an exchange-correlation potential.

As in our previous report, we have also evaluated the performance of these models for predicting relative isomer energies in small $(H_2O)_n^-$ clusters, where complete-basis MP2 results are available.[3] The results for our new parameterization are quite good, but do not differ significantly from those obtained for PEWP-1 and discussed in Ref. [3]. These data may be found in appendix A.

3.5 Bulk simulations

The bulk hydrated electron holds an interesting place among aqueous ions, having been deemed, for example, as the "champion structure breaker",[128] owing to its positive entropy of hydration. As summarized in Section 3.1, significant questions remain as to the structure of this species, nevertheless the absorption spectrum,[26, 144, 145, 161–163] fluorescence spectrum,[134] resonance Raman spectrum,[132–136] entropy of solvation,[128] and diffusion coefficient[129] have all been measured, often under a variety of thermodynamic conditions. Several recent measurements of the bulk VEBE are in reasonable agreement with one another.[5–7] In this section, we examine the PEWP-2 predictions for some of these bulk data.

3.5.1 Diffusion coefficient

The diffusion coefficient of e^-_{aq} has been measured over a wide range of temperatures,[129] with a value of $D = 0.51$ Å^2/ps obtained at 300 K. The TB model reproduces the temperature dependence of D, and affords a value of 0.6 Å^2/ps at 298 K.[159] For the PEWP-2 model, we have estimated the diffusion coefficient by fitting the long-time slope of the mean displacement, $\langle|\vec{r}(t) - \vec{r}(0)|^2\rangle$.[172] This average converges quite slowly, as there is only a single solute particle, and because our trajectories are fairly short we have only a crude estimate of D for the PEWP-2 model. At 300 K, we obtain $D = 0.79 \pm 0.16$ Å^2/ps, where the uncertainty represents a 95% confidence interval based on the standard deviation over four different trajectories in our smallest box (100 H_2O molecules). Obviously, this is faster than the experimental value; however, the value of D is quite sensitive to temperature,[129, 159] and $D = 0.79$ Å^2/ps corresponds, experimentally, to $T = 317$ K. Reducing the temperature of our simulation by 18 K (to 282 K), we obtain $D = 0.65 \pm 0.18$ Å^2/ps, similar to the TB value and only slightly higher than experiment, although the uncertainty is considerable. This issue may warrant further investigation in the future, but in any case the agreement with experiment is far more satisfactory than it is for PEWP-1.

3.5.2 Structure

Radial distribution functions (RDFs) for the oxygen and hydrogen atoms, relative to the centroid of the e^-_{aq} wavefunction, are shown in Fig. 3.6 for both the TB and PEWP-2 models. (These RDFs were computed for a unit cell containing 200 water molecules, as we find that structural properties are not strongly affected by the size of the simulation cell.) For both models, integration of the electron–hydrogen RDF up to its first minimum yields a coordination number of four. The cavity size is slightly smaller for our model than for the TB model, with the first hydrogen maximum appearing at 1.7 Å versus 2.0 Å. The average radius of gyration of the electron is also smaller in our model (2.25 Å) than for the TB model (2.45 Å). The first hydrogen (and first oxygen) positions are much more highly correlated with the electron position in our model [$g_{el-\mathrm{H}}(r = 1.7\text{ Å}) \sim 1.5$] than in the TB model [$g_{el-\mathrm{H}}(r = 2.0\text{ Å}) \sim 1.0$]. This is mostly due to the fact that the volume element used to normalize the distributions is smaller in PEWP-2, since the first maximum appears at a smaller distance.

As compared to the TB model, the first oxygen minimum is far shallower and less well-defined for PEWP-2. The RDFs for both models are relatively under-correlated (in comparison to a more typical anion such as Br^- or I^-), and possess rather broad features. This breadth arises from fluctuations in both the size and shape of the cavity. The initial rise of the RDFs is noticeably steeper in PEWP-2 than in the TB model, an effect that was also observed with a very early polarizable model for e^-_{aq}.[63]

As mentioned in Section 3.1, magnetic resonance experiments in alkaline glasses at $T = 77$ K are interpreted in favor of a hexavalent coordination environment for e^-_{aq},[126, 127] which is consistent with some theoretical models of e^-_{aq} in liquid water.[65, 147, 158] An average electron–oxygen distance of ~ 2.0 Å has also been

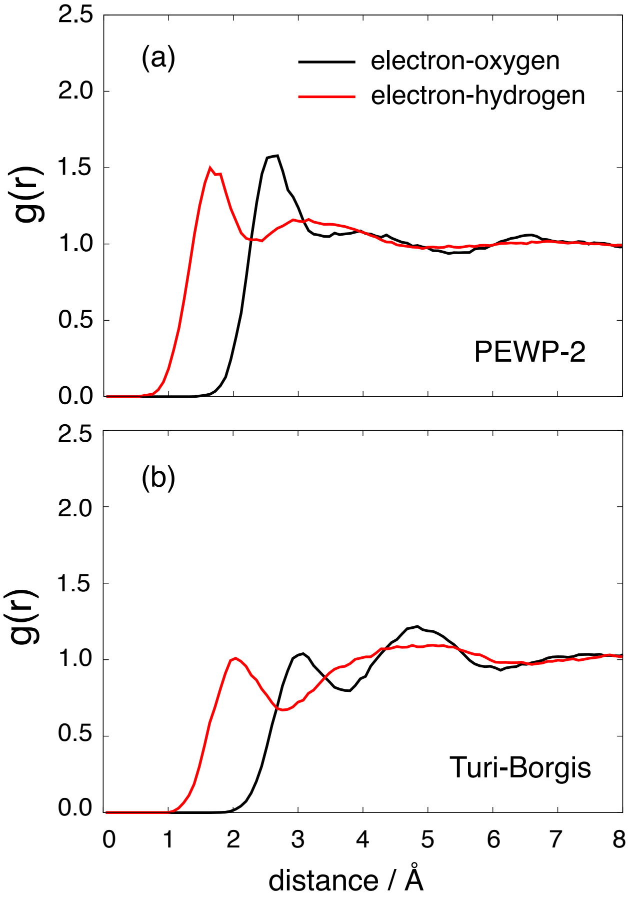

Figure 3.6: Radial distribution functions, $g(r)$, for the PEWP-2 and TB models, with respect to the centroid of the electron's wavefunction.

deduced.[157, 158] If this value is characteristic of e^-_{aq} in liquid water under ambient conditions, then our solvation cavity is ~ 0.3 Å too small, whereas the TB model is about right, although it—like PEWP-2—predicts tetravalent coordination. The notion that the PEWP-2 cavity is ~ 0.3 Å too small is consistent with a radius of gyration (2.25 Å) that is slightly smaller than the experimental estimate of 2.5 Å that is deduced from a moment analysis of the optical absorption spectrum.[86] It appears that our model's cavity structure is qualitatively correct, though not in quantitative agreement with experiment.

Visual inspection of the PEWP-2 trajectories reveals that the electron is typically coordinated to about four water molecules, but that the arrangement of the O–H bonds is usually far from tetrahedral. Five-coordinate structures also exist, albeit transiently. In contrast, the coordination environment in the TB model is almost always tetrahedral. In PEWP-2, we frequently observe a "bridging" water molecule that donates hydrogen bonds to two different first-shell water molecules, such that the positive end of the bridging molecule's permanent dipole moment is oriented towards the wavefunction. This behavior is absent in the TB model, most likely owing this model's expanded cavity size. Using PEWP-2, we find that these bridging H_2O molecules can reside very close to the electron, although they are not coordinated to it, and this feature, together with the fleeting pentavalent structures, effectively "washes out" the first minimum in the electron–oxygen RDF.

Tauber and Mathies[136] have previously invoked the idea of a disrupted H-bonding network in the vicinity of the electron, in order to rationalize the resonance Raman spectrum of e^-_{aq}, but this aspect of e^-_{aq} solvation does not seem to have been examined with detailed simulations. In order to understand the H-bonding environment nearby the electron, we will examine the average number of hydrogen bonds per water molecule, as a function of the electron–oxygen distance, using two different definitions of what constitutes a hydrogen bond. The first definition, which was used to characterize e^-_{aq} diffusion in a previous study,[159] is that the oxygen–oxygen distance between two H-bonded water molecules is less than 3.5 Å, while at the same time the angle between the covalent O–H bond vector and the O–O vector is less than 30°. We call this the "simple geometric criterion" in the discussion that follows. The second criterion was introduced in Ref. [174], and involves an angle-dependent O–O distance threshold,

$$R(\theta)/\text{Å} = -0.00044(\theta/\text{deg})^2 + 3.3 \ , \tag{3.15}$$

for $-50° \leq \theta \leq 50°$. Here, θ is the aforementioned O–H/O–O angle, and according to this definition, a hydrogen bond exists if the O–O distance is less than or equal to $R(\theta)$. This criterion accounts for the fact that if a particular O–O distance is quite long, then the corresponding angle should be small in order for the two H_2O molecules to be considered H-bonded. Alternatively, if the H-bond angle θ is large, then the O–O distance should be small for H-bonded water molecules. In what follows, we will compare the number of hydrogen bonds predicted by these two definitions; when the simple geometric definition predicts an H-bond but the definition in Eq. (3.15) does not, we infer that the hydrogen bond in question is a weak one. We will furthermore decompose the average number of H-bonds per H_2O molecule into the number of

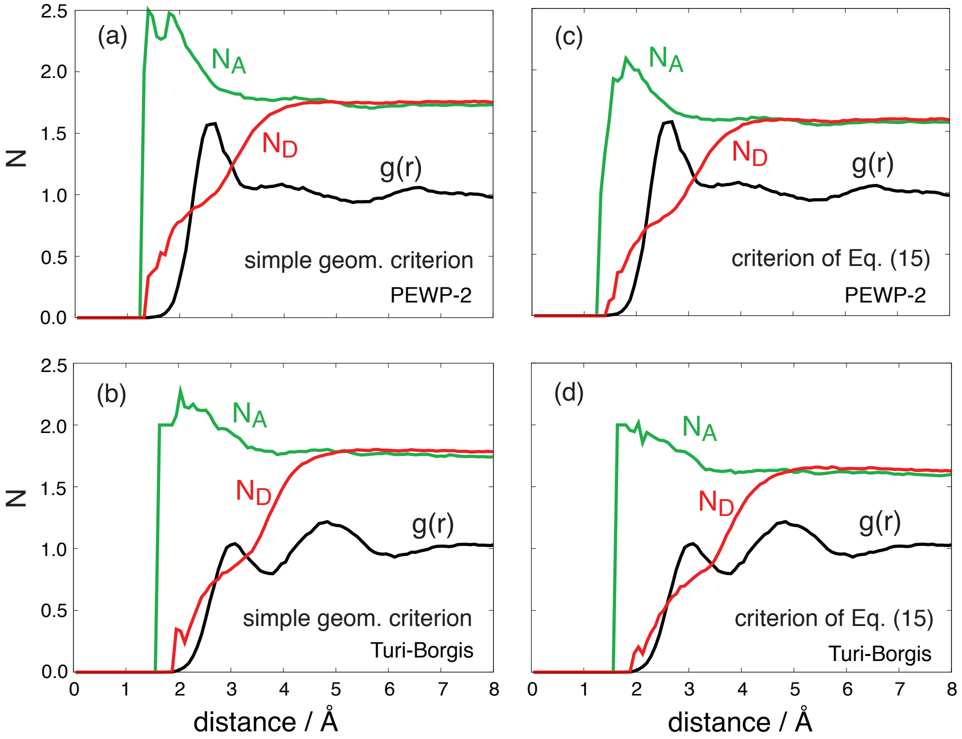

Figure 3.7: Average number of hydrogen bonds donated (N_D) and accepted (N_A) per water molecule, as a function of distance from the electron. Also shown is the electron–oxygen RDF, $g(r)$.

H-bonds donated (N_D) and the number of H-bonds accepted (N_A).

Figure 3.7 shows the results of this analysis, for both the PEWP-2 and TB models. When the electron–oxygen distance is smaller than the first maximum in the electron–oxygen $g(r)$, we find $N_\mathrm{A} \approx 2$ but $N_\mathrm{D} < 1$, whereas bulk behavior ($N_\mathrm{A} \approx N_\mathrm{D}$) is not recovered until $r \approx 5.0$ Å, well into the second solvation shell. These results are independent of which H-bond definition that we choose, and also independent of the particular hydrated-electron model (TB or PEWP-2). At the value of r that corresponds to the first maximum in $g(r)$, the simple geometric criterion affords $N_{\mathrm{D}} \approx 1$, exactly what one would expect for coordination involving one O–H bond per H_2O molecule. The criterion of Eq. (3.15), however, affords a somewhat smaller value of N_{D} in this region, and in either case N_{D} increases rapidly as r decreases. These observations indicate that water molecules in the first solvation shell are relatively poor H-bond donors. Conversely, first-shell water molecules are excellent H-bond acceptors, especially those nearest the electron; in fact, the simple geometric criterion yields $N_{\mathrm{A}} > 2$ for these innermost water molecules. It is tempting to view this as a polarization effect, since strong interaction with the electron could enhance the H_2O dipole moment, making H-bonds with other water molecules even more favorable, and in fact we do see that PEWP-2 affords slightly larger values of N_{A} at small r than does the TB model. Even the TB model, however, predicts $N_{\mathrm{A}} > 2$ at small r. If we substitute the H-bond definition in Eq. (3.15), then the maximum value of N_{A} is reduced to ≈ 2, suggesting that any H-bonds in excess of two per H_2O molecule are fairly weak.

In our view, the weak H-bond-donating capability of first-shell water molecules arises from the diffuse nature of the ion, which provides relatively little restoring force for water librations, as compared to a hydrated halide ion, for example. Thus, we expect H_2O molecules in the first shell to undergo fairly large-amplitude motion, as compared to bulk H_2O, making for poor H-bond donation. This does not necessarily mean that the same first-shell H_2O molecule cannot *accept* hydrogen bonds, however.

In fact, since the electron orients water molecules even in the second solvation shell, this has the effect of enhancing the number accepted H-bonds in the first shell.

3.5.3 Librational dynamics

In the previous section, we hypothesized that water molecules nearby the electron are subject to enhanced librational motions. To substantiate this claim, we next examine the librational dynamics of individual H_2O molecules, as a function of their distance from the centroid of the e^-_{aq} wavefunction. In order to separate librational and vibrational motions as much as possible, we first determine the Eckart frame[175] for each water molecule. We then compute an autocorrelation function

$$C(t) = \left\langle \sum_i \vec{\Omega}_i(0) \cdot \vec{\Omega}_i(t) \right\rangle , \tag{3.16}$$

where $\vec{\Omega}_i$ represents a unit vector along one of the Eckart axes, for the ith water molecule, and the summation runs over a restricted set of water molecules, as detailed below. Angle brackets in Eq. (3.16) indicate an ensemble average. A similar approach has previously been used to characterize librational dynamics in neat liquid water.[176]

In order to analyze the dynamics near the electron, we compute the average in Eq. (3.16) using only those water molecules that, at $t = 0$, lie within a specified distance of the centroid of the electron's wavefunction. Because this distance changes as a function of time, our analysis is limited to the short-time behavior of $C(t)$. We investigate the dynamics in three regions: from $r = 0$ up to the first oxygen minimum ($r = 3.2$ Å for PEWP-2 and $r = 3.8$ Å for TB); from the first oxygen minimum out to $r = 5.0$ Å; and finally, $r > 5.0$ Å. We refer to these regions as the first solvation shell, second solvation shell, and bulk water, respectively.

Figure 3.8 shows $C(t)$ evaluated for a unit vector along the C_2 Eckart axis. (Qualitatively similar results are obtained for all three Eckart axes.) For neat liquid water, $C(t)$ exhibits an ultra-fast inertial response at short times followed by a small recoil prior to the onset of a long-time exponential decay.[176] We are interested in the dynamics prior to the exponential decay.

For neat liquid water, $C(t)$ decays from unity to a value of ~ 0.9 over the first 34 fs, corresponding to a rotation angle of about 25°. Between 34 and 54 fs, the water molecule recoils slightly, as evidenced by a "hump" in $C(t)$ centered around 54 fs. By comparison, the initial Gaussian decay is more pronounced for water molecules in the first shell of e^-_{aq}, and furthermore the average angle prior to recoil increases by 5° and the time period prior to recoil increases by 10 fs, relative to neat liquid water. For the PEWP-2 model, the recoil maximum in $C(t)$ is almost completely absent for first-shell waters, while the TB model shows only a very slow recoil, with a maximum at 80 fs. This is much slower than the 51 fs that is observed for the underlying SPC water model. In contrast, the librational dynamics for first-shell water molecules in aqueous Br^- (as described by the AMOEBA force field) are much faster compared to those in e^-_{aq}, and closely resemble the dynamics of water molecules in the *second* solvation shell around e^-_{aq}.

We interpret the enhanced Gaussian decay and attenuated recoil as evidence of enhanced librations due to smaller restoring forces for hindered rotation near the

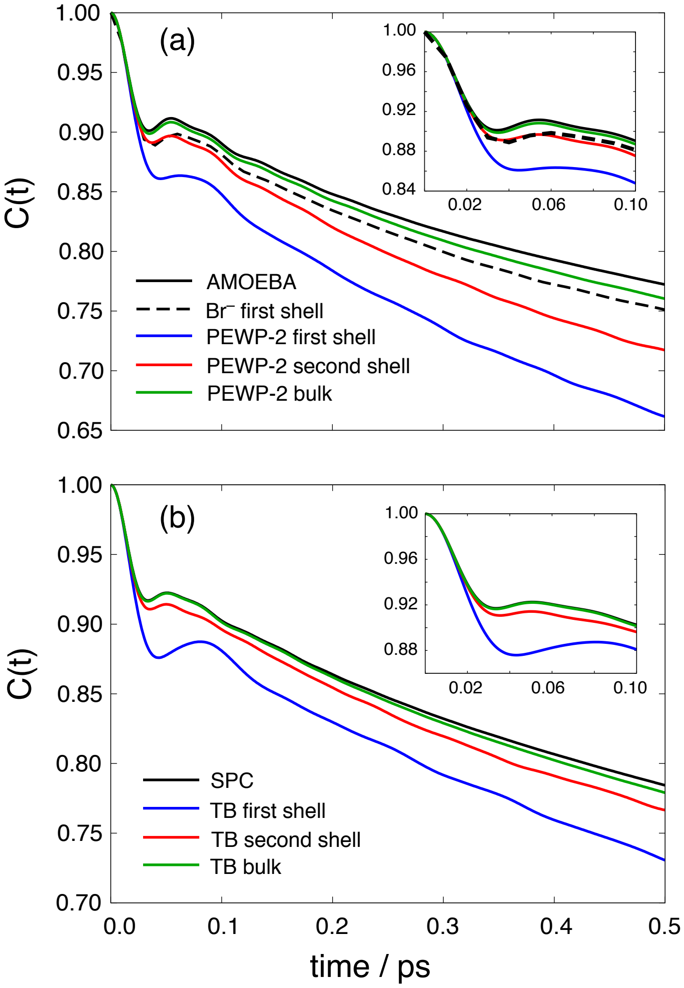

Figure 3.8: Early-time behavior of the orientational time correlation function, $C(t)$ [Eq. (3.16)], for neat liquid water and for e^-_{aq} at various distances from the electron (see text for details). In (a), the neat liquid is described by the AMOEBA force field and e^-_{aq} by the PEWP-2 model; in (b), the SPC model is used for liquid water and the TB model for e^-_{aq}. The correlation function $C(t)$ is computed for a periodic simulation cell containing 200 water molecules.

electron. That is, the inertial decay of $C(t)$, corresponding to quasi-free rotation of H_2O, lasts slightly (~ 10 fs) longer nearby the electron. In addition, the recoil following this event is attenuated. This indicates that librational motion in amplified, and that the restoring forces that lead to recoil are damped. Surprisingly, second-shell water molecules also show enhanced librational dynamics, albeit to a much lesser extent than is observed in the first solvation shell. At distances greater than 5.0 Å, the librational dynamics are essentially identical to those in bulk water. These data support our earlier contention that hydrogen bonding is disrupted by enhanced librational dynamics in the first two solvation shells, but that bulk-like behavior is recovered beyond that.

3.5.4 Vertical electron binding energy

To determine the VEBE of bulk e^-_{aq}, we calculate the average VEBE at each simulation cell size, and then extrapolate to the infinite-dilution ($L_{\text{box}} \to \infty$) limit. For a charged system, the long-range interactions in a Ewald sum converge slowly, and one expects that the VEBE will converge as $1/L_{\text{box}}$,[177, 178] which is precisely what we observe in practice. Extrapolations to $L_{\text{box}} = \infty$ are depicted in Fig. 3.9, where error bars are determined by propagating the statistical error in the mean for each simulated VEBE, and are reported at the 95% confidence level.

For the TB model, the VEBE is (up to a sign) simply the ground-state electronic energy, and extrapolates to a value of 4.79 ± 0.09 eV at infinite dilution. This is considerably larger than all previous reports of this quantity using the TB model; these include a value of 3.12 eV calculated using the minimum-image convention,[67]

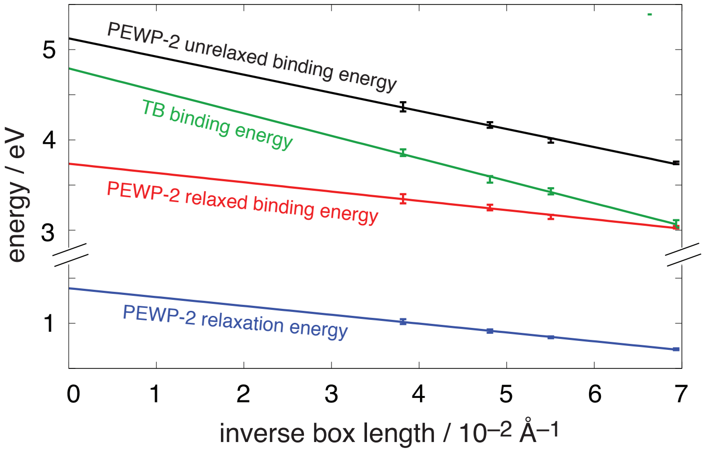

Figure 3.9: Extrapolation of the VEBE as a function of inverse simulation cell length, $1/L_{\text{box}}$.

a value of 3.9 eV determined using Ewald summation (with an unspecified simulation cell size),[153] and a value of 4.4 eV determined by extrapolating cluster VEBEs.[153] That our Ewald-summed value is so much larger than what is reported in Ref. [153] is not altogether surprising, given the sensitivity of the VEBE to L_{box} that is seen in Fig. 3.9, but it is curious that our infinite-dilution value is 0.3–0.4 eV larger than that reported based on cluster extrapolation.

The MM inducible dipoles in our model represent electronic degrees of freedom, albeit coarse-grained ones, and these ought to remain in equilibrium with the electron, relaxing on the same time scale as electronic excitation or electron detachment. Figure 3.9 also shows three separate extrapolations for the PEWP-2 model: a "relaxed" binding energy, an "unrelaxed" binding energy, and the difference between the two, which we call the relaxation energy. The latter is the energy associated with electronic re-organization of the solvent, *i.e.*, changes in the MM inducible dipoles upon electron detachment.

The slope and intercept of the unrelaxed binding energy extrapolation are similar to those obtained for the TB model, where no relaxation is possible, which makes sense because the dielectric constant of the two systems should be quite similar. However, the relaxed binding energy in our model extrapolates to a much smaller value, 3.70 ± 0.071 eV. This value lies between the value of 4.0 eV that is obtained by extrapolating VEBEs for $(H_2O)_n^-$ clusters collected in an ion trap ($T \approx 10$ K),[4] and the value of 3.4 eV that is obtained by extrapolating VEBEs for warmer clusters.[2] Our predicted VEBE is also larger than the value of 3.3 eV obtained in two recent liquid microjet experiments,[5, 6] but is within error bars of a third liquid jet measurement, 3.6 ± 0.1 eV.[7] Considering that the ion trap experiments likely probe ice-like clusters, experimental estimates for the liquid-phase VEBE lie in the range 3.3–3.6 eV; our model's prediction is far closer to these values than is the TB value, when the latter is calculated in a rigorous way.

The relaxation energy extrapolates to a surprisingly large value of 1.37 ± 0.04 eV, which reveals an important fact about non-polarizable solvated-electron models. Specifically, it explains how the TB model can be systematically underbinding in small clusters (Fig. 3.5), yet overbinding in the bulk limit (Fig. 3.9). This does not necessarily imply that the non-polarizable models are inherently flawed, since this relaxation energy does not affect the ground-state forces, and ground-state structure and dynamics may therefore be largely insensitive to the lack of polarization. At the same time, it is clear that some correction needs to be applied to binding energies calculated using non-polarizable models, especially in the bulk limit. We expect this to be the case in any polarizable medium, not just water.

Recently, Madarász *et al.*[153] extrapolated $(H_2O)_n^-$ cluster binding energies for cavity states, calculated using the non-polarizable TB model, and obtained a value of $\sim$4.4 eV. These authors then compare to a Born-like dielectric continuum model developed by Makov and Nitzan,[9] obtaining VEBEs that are surprisingly consistent with those obtained from atomistic simulations. Madarász *et al.* employ the Makov-Nitzan model with an optical (infinite-frequency) dielectric constant $\epsilon_\infty = 1$, consistent with a non-polarizable model. Here, we calculate the relaxation energy predicted by this same continuum model, using water's actual optical dielectric constant, $\epsilon_\infty = 1.8$.[9] Instead of using this model to predict VEBEs of spherical clusters, we will investigate a situation where the electron is embedded in an infinite dielectric. We compare VEBEs obtained for $\epsilon_\infty = 1.0$ versus $\epsilon_\infty = 1.8$, and take the difference to be a continuum approximation for the relaxation energy.

The parameters required for the continuum model are the electronic kinetic energy, a cavity radius for the ion (which we take to be the electron's radius of gyration, r_g), and the static and optical dielectric constants.[9] We use the average electronic kinetic and radius of gyration determined from simulation, and a static dielectric constant of $\epsilon = 78$. The results (Table 3.2) are a relaxation energy of 1.3 eV for the TB model and 1.4 eV for PEWP-2, in excellent agreement with the value extrapolated from

Property	One-electron model	
	TB	PEWP-2
r_g/Å	2.45	2.25
$\langle\hat{T}\rangle$/eV	1.6	1.7
VEBE($\epsilon_\infty = 1.0$)/eV	4.2	4.6
VEBE($\epsilon_\infty = 1.8$)/eV	2.9	3.2
Relaxation energy/eV	1.3	1.4

Table 3.2: Input parameters and results from application of the dielectric continuum model developed in Ref. [9].

simulations with explicit many-body polarization. If the extrapolated TB binding energy from Fig. 3.9 is reduced by 1.3 eV, we obtain a bulk VEBE of 3.5 eV. This modified value is in good agreement with the value of 3.7 eV that is extrapolated for PEWP-2 (see Fig 3.9), especially considering that cluster benchmarks indicate that the TB model is underbinding, relative to PEWP-2, by ~0.25 eV.

3.5.5 Optical absorption spectrum

Whereas VEBEs are important experimental handles for $(\mathrm{H_2O})_n^-$ clusters, optical absorption spectroscopy is the primary means of detecting and characterizing e_{aq}^- in bulk liquids. The absorption spectrum of e_{aq}^- in bulk water is broad and featureless, peaked at 1.72 eV with a Gaussian rise on the low-energy side of the spectrum and a Lorentzian decay on the blue edge (see Fig. 3.10).[2] Of the one-electron models that have been brought to bear on this problem, the TB model affords the best estimate of the absorption maximum, with a prediction of 1.92 eV,[67] whereas other one-electron models put this maximum at still higher excitation energies. Turi and Borgis[67] claim that a self-consistent treatment of solvent electronic polarization in the excited state should bring the absorption maximum into good agreement with experiment, an assertion that will be tested here. Perhaps more importantly, the Lorentzian tail in the spectrum has not been reproduced by any computational means,[154] prior to a recent preliminary account of our PEWP-2 results,[160] which are discussed in more detail here.

Here, we simulate the absorption spectrum by computing oscillator strengths

$$f_{0\to n} = \frac{2m_e}{3\hbar^2}(E_n - E_0) \sum_{\kappa\in\{x,y,z\}} \left|\langle\psi_0|\,\hat{\kappa}\,|\psi_n\rangle\right|^2 \tag{3.17}$$

between the ground state and the lowest 29 excited states ($n \leq 29$), at each of $\sim$1000 snapshots sampled from ground-state molecular dynamics. The absorption spectrum is obtained as a histogram of excitation energies, weighted by the corresponding oscillator strengths. Within our polarizable model, however, the treatment of the excited-state wavefunctions is not entirely straightforward, as we next discuss.

Because the inducible H_2O dipoles represent electronic degrees of freedom, it is physically reasonable that they should remain in equilibrium with the wavefunction upon electronic excitation. In principle, one could imagine a self-consistent procedure to converge the dipoles and wavefunction for each excited state, but we have found that such procedures have serious convergence problems owing to the fact that the polarization energy is quite large in comparison to the small energy gaps between excited states. As such, states may "switch" during the Davidson iterations. As an alternative, we employ a state-specific perturbation theory in order to calculate

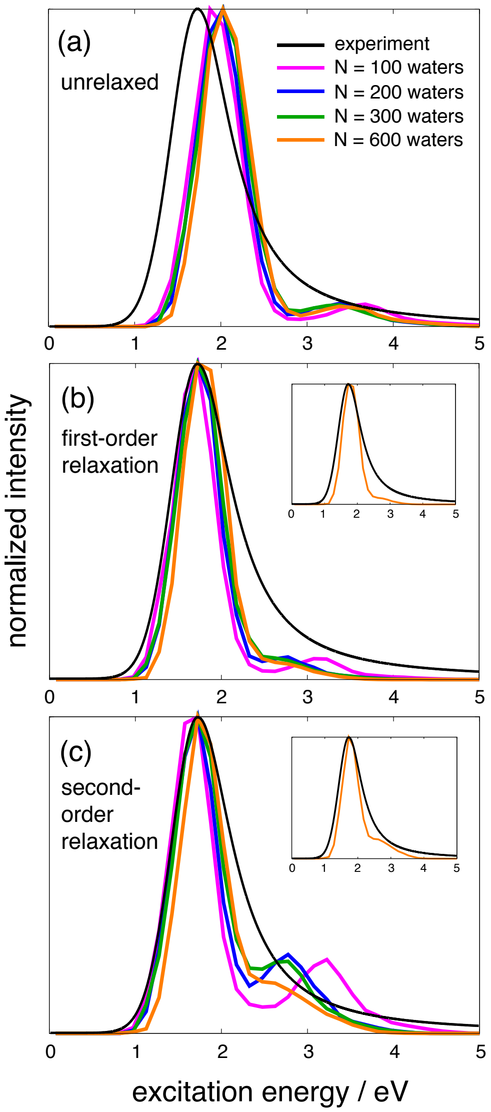

Figure 3.10: Bulk absorption spectra for e^-_{aq}, calculated using various box sizes and various treatments of the solvent's electronic relaxation energy, including (a) neglect of the perturbation $\hat{W}_n$, (b) first-order correction for $\hat{W}_n$, and (c) second-order correction for $\hat{W}_n$. Insets in (b) and (c) compare the experimental spectrum (obtained from line shape parameters in Ref. [2]) to results computed with our largest simulation cell.

"relaxed" excited-state wavefunctions and electronic energies. To obtain the perturbation, we first calculate the ground-state wavefunction, $|\psi_0\rangle$, and an excited-state wavefunction, $|\psi_n\rangle$, using dipoles $\{\vec{\mu}_i^{(0)}\}$ that are converged to $|\psi_0\rangle$. We then obtain new dipoles, $\{\vec{\mu}_i^{(n)}\}$, that are converged to $|\psi_n\rangle$, without relaxing the latter. The quantity

$$\hat{W}_n = \hat{H}\big[\{\vec{\mu}_i^{(n)}\}\big] - \hat{H}\big[\{\vec{\mu}_i^{(0)}\}\big] \tag{3.18}$$

is taken to be the perturbation for state $|\psi_n\rangle$.

One difficulty with the aforementioned procedure is that of orthogonality. Each relaxed excited state is an (approximate) eigenvector of a different Hamiltonian, and therefore these states need not be mutually orthogonal. As such, one might anticipate spurious intensity enhancements due to non-orthogonality. Furthermore, if the quantum states are not orthogonal then the transition dipole matrix elements are not invariant to translation of the coordinate origin. In order to avoid the latter problem, we do not allow the excited states to mix with the ground state in the perturbative expansion of the wavefunction. This at least ensures that $\langle\psi_0|\psi_n\rangle = 0$, even if the excited states are not mutually orthogonal.

Figure 3.10 compares the experimental absorption spectrum to spectra computed using various corrections for the perturbation $\hat{W}_n$. "Unrelaxed" spectra [Fig. 3.10(a)] correspond to a complete neglect of $\hat{W}_n$, *i.e.*, only ground-state dipoles are involved in the calculation. The "relaxed" spectra [Figs. 3.10(b) and 3.10(c)] include corrections for $\hat{W}_n$ based on either first- or second-order perturbation theory. In addition, we also compare spectra computed using different periodic cells. (Since many of the

N	$L_{\text{box}}/$ Å	Unrelaxed		First-order		Second-order	
		E_{max}	σ_G	E_{max}	σ_G	E_{max}	σ_G
100	14.4	1.94	0.27	1.69	0.24	1.65	0.24
200	18.2	1.99	0.26	1.74	0.25	1.70	0.26
300	20.8	2.02	0.29	1.75	0.26	1.73	0.27
600	26.2	2.04	0.25	1.78	0.23	1.77	0.24
Expt.[a]						1.72	0.30

[a] Experimental line shape parameters from Ref. [2].

Table 3.3: Parameters E_{max} and σ_G, both in eV, for fitting the low-energy Gaussian portion of the absorption spectrum [see Eq. (3.19)]. The quantities N and L_{box} specify the number of water molecules and the length of the simulation cell, respectively.

higher-lying states are quite diffuse, for the excited-state calculations we use a grid that fills the entire simulation cell.)

The unrelaxed spectra [Fig. 3.10(a)] are insensitive to the size of the simulation cell, and are quite similar to the spectrum obtained using the non-polarizable TB model.[67, 160] The absorption maximum in these spectra is slightly blue-shifted relative to experiment; upon fitting the low-energy portion of the spectrum to a Gaussian,

$$I(E) = A\ \exp\bigl[-(E - E_{max})^2/2\sigma_G^2\bigr]\ , \tag{3.19}$$

we obtain $E_{max} \approx 2.0$ eV and $\sigma_G \approx 0.25$ eV. (Gaussian fitting parameters are listed in Table 3.3, where they are compared to experimental line shape parameters.) While E_{max} is 0.3 eV higher than experiment, the Gaussian width of the unrelaxed spectrum is reasonably accurate.

A first-order treatment of $\hat{W}_n$ dramatically red-shifts the spectrum [Fig. 3.10(b)], bringing the absorption maximum into excellent agreement with experiment, while changing σ_G by only 0.02 eV. Thus, the Gaussian part of the experimental spectrum is reproduced quantitatively using first-order relaxation, and essentially no further change in the Gaussian feature is observed at second order. The contention of Turi and Borgis,[67] that excited-state electronic polarization would red-shift the spectrum by 0.2–0.3 eV, appears to be correct. What was not anticipated is the effect of polarization on the blue tail.

Figure 3.11 decomposes the computed absorption spectra, for the largest simulation cell, into contributions arising from various categories of excited states. Consistent with the results of previous simulations,[67, 147, 148, 154] we find that most of the absorption intensity is carried by three p-type states that give rise to a broad Gaussian profile. This part of the spectrum is converged even in the smallest simulation cell, and the red edge (up to the absorption maximum) is in quantitative agreement with experiment. At higher excitation energies, however, the unrelaxed spectrum exhibits a gap, with very little spectral intensity, rather than the smooth tail that is observed experimentally. Above this gap is a weak tail comprised of excitations to unbound states, *i.e.*, a photo-electron spectrum. (We categorize states as being bound or unbound based on whether or not the excitation energy exceeds the VEBE. This definition does not preclude the possibility that some of these vertically-bound excitations are *adiabatically* unbound.)

First-order relaxation red-shifts the higher-lying states to a greater extent than

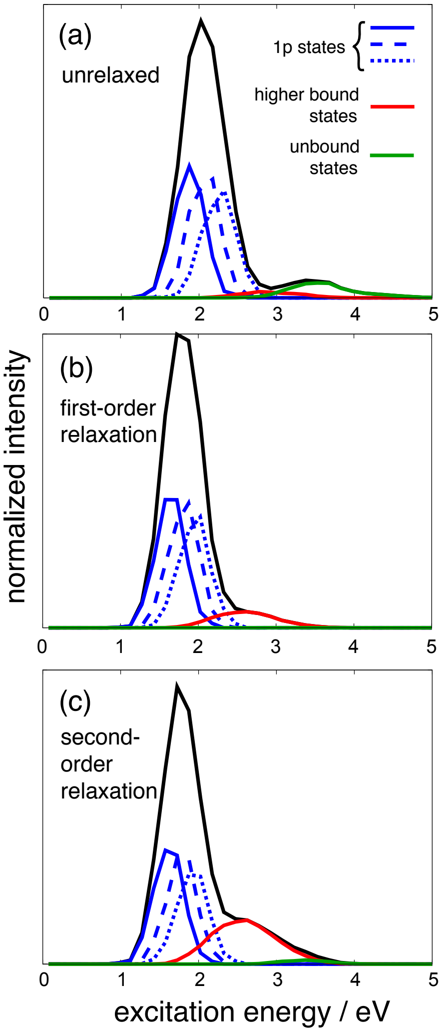

Figure 3.11: Computed absorption spectra for e^-_{aq}, decomposed into various categories of excited states, using our largest simulation cell ($N = 600$ water molecules).

the $1p$ states, resulting in a smoother decay of the spectrum at high energy, without so much of the aforementioned gap in intensity. The distribution of oscillator strengths changes only slightly, however, since first-order relaxation can alter $f_{0\to n}$ only through the excitation energy, $E_n - E_0$ [see Eq. (3.17)]. Whereas the first 29 excited states account for 95% of the total oscillator strength, this figure drops to 80% upon first-order relaxation. This decrease in oscillator strength is understandable, given that first-order relaxation does not alter the transition dipoles, therefore $f_{0\to n}$ must decrease, according to Eq. (3.17).

At second order, one obtains a correction to the wavefunction and therefore the transition dipoles, which allows the unrelaxed excited states to mix with the $1p$ states and thereby acquire oscillator strength. [3.2] The result [Fig. 3.11(c)] is a significant intensity enhancement in the blue tail, relative even to the first-order result. At the same time, the $1p$ states are still clearly responsible for the Gaussian feature in the absorption spectrum. The feature labeled "unbound states" has almost disappeared in the relaxed spectra shown in Fig. 3.11, because relaxation leads to a considerable increase in the number of bound states; of the 29 states that comprise the spectra in Fig. 3.11, an average of 25.6 are bound at second order (collectively accounting for 90% of the total oscillator strength), whereas only 6.9 excited states are bound, on average, when relaxation is neglected. We expect that the "unbound" feature would return if we calculated additional excited states.

[3.2] Within a spherical cavity model, the $1s \to 1p$ transitions carry essentially all of the oscillator strength, since the $1s \to 2s$ and $1s \to 1d$ transitions are dipole-forbidden, while the $2p$ states are quite diffuse and have little overlap with the $1s$ ground state, for cavity radii and binding energies consistent with e^-_{aq}.

Beyond the $1p$ states, the excited states are quite diffuse and are not adequately represented in small simulation cells. (Snapshots of the PEWP-2 excited-state wavefunctions can be found in Ref. [160].) In small unit cells, the second-order relaxation correction (and accompanying intensity borrowing by the higher-lying states) leads to a "hump" on the blue edge of the spectrum, but this feature shifts to lower energy as L_{box} increases, ultimately producing a smooth tail in our largest simulation cell.

Figure 3.12 plots the average excitation energy and radius of gyration, r_g, for each electronic state, as a function of L_{box}. For the ground state and the $1p$ states, r_g is essentially independent of L_{box}, but for the higher-lying excited states, r_g increases steadily as the box (and the grid) are extended. The highest-energy states that we calculate are probably not converged with respect to the size of the unit cell, and a further increase in L_{box} would likely result in a further red-shift of these states that would improve the agreement with experiment around 2.5 eV. Nevertheless, it is clear that the qualitative effect of the solvent's electronic relaxation is to create "polarization-bound" excited states that give rise to a continuous blue tail, without the gap in oscillator strength that is observed in both the unrelaxed spectrum and in the spectra calculated using non-polarizable models.

These observations lead us to the following interpretation of the bulk e^-_{aq} absorption spectrum. The Gaussian feature on the low-energy side of the spectrum arises from three $1s \rightarrow 1p$ excitations, as many previous studies have also concluded.[67, 147, 148, 154, 155, 158, 160] The "blue tail", however, arises from a excitations into diffuse quasi-continuum states that are bound (in a vertical sense) entirely by the

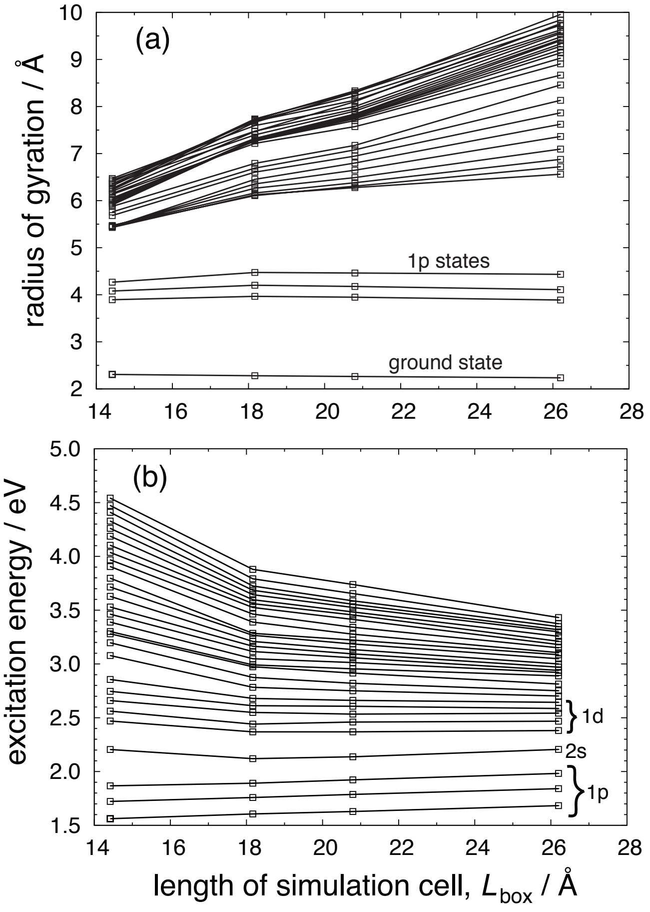

Figure 3.12: Average values of (a) the radius of gyration and (b) the excitation energy, as a function of L_{box}, for each of the lowest 29 electronic states of e^-_{aq}.

instantaneous polarization of the solvent upon excitation of the unpaired electron. These states acquire intensity via solvent-facilitated intensity borrowing from the $1p$ states, which are the only bright states. in a spherical cavity model.

Although the high-energy edge of our computed spectrum is not in quantitative agreement with experiment, it is vastly improved relative to that predicted using non-polarizable models. We note that our calculations do not include any sort of lifetime broadening, which could be important given the high spectral density beyond the $1p$ manifold [see Fig. 3.12(b)], and might be the origin of the Lorentzian line shape that is observed experimentally. Another source of error in the high-energy line shape is that our model includes the solvent's contribution to the oscillator strengths only indirectly, via the response of the electron's wavefunction to changes in the MM dipole parameters. In a fully-QM treatment, the H_2O dipole moments would contribute to the dipole moment operator in Eq. (3.17).

Shkrob *et al.*[158] have reported QM/MM calculations of the e^-_{aq} absorption spectrum, at the level of singles configuration interaction (CIS), but these calculations did not result in a blue tail. These authors acknowledge that the higher-lying states are quite diffuse, and it is unclear whether the QM region in these calculations is sufficient to describe these states. The blue tail is also absent in the Kohn-Sham density of states obtained from a Car-Parrinello simulation of e^-_{aq}.[155] However, we have recently reported time-dependent DFT simulations of the e^-_{aq} absorption spectrum, using a QM/MM formalism in conjunction with the LRC-μBOP density functional, and these calculations *do* result in a substantial blue tail.[160] We find that a sizable

QM region (somewhat larger than that used by Shkrob *et al.*[158]) is required in order to obtain this tail, which we interpret as additional evidence that solvent polarization does indeed facilitates intensity borrowing by higher-lying excited states.

3.5.6 Polarized transient hole-burning

A long-standing discrepancy between experiment and one-electron simulations of e^-_{aq} concerns whether the Gaussian part of the absorption spectrum is primarily homogeneously or inhomogeneously broadened.[179] Most previous simulations suggest inhomogeneous broadening that should be detectable via a polarized transient hole-burning (PTHB) experiment,[108, 151] wherein a polarized pump laser is used to excite a sub-population of the $1s \rightarrow 1p$ band, leading to a bleach in the signal arising from a second, polarized probe laser.[179] Although the first PTHB experiments appeared to confirm this prediction,[180] subsequent experiments failed to detect the anisotropic bleaching dynamics that would indicate of inhomogeneous broadening.[179, 181, 182]

Observation of polarization dependence in the bleaching dynamics requires three properties. First, the three $1p$ sub-populations must be sufficiently well-separated so that the pump pulse can excite primarily a single sub-population; second, the three $1s \rightarrow 1p$ transition dipole moments must be orthogonal, or very nearly so; and third, the re-orientation of these transition dipoles, due to fluctuations in the asymmetry of the cavity, must be slow enough to be detectable via femtosecond spectroscopy. According to the absorption spectrum calculated using our model (Fig. 3.11), electronic relaxation of the solvent causes the three $1s \rightarrow 1p$ sub-bands to overlap more strongly

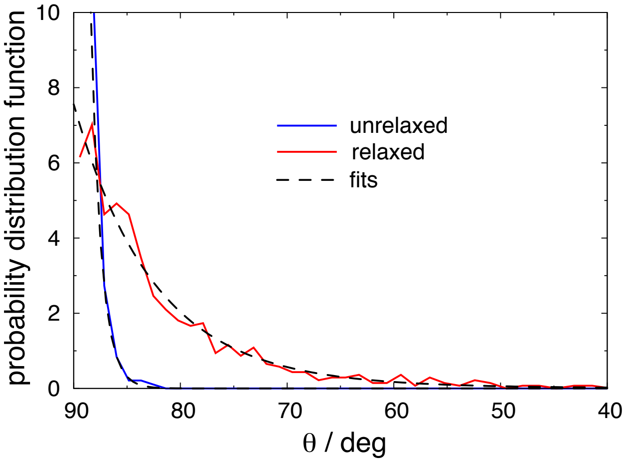

Figure 3.13: Probability distribution functions for the angle between the transition dipole moments of the three $1s \rightarrow 1p$ excitations, along with fits to single-exponential decay curves.

than they do in the absence of relaxation, such that to pump just a single $1s \rightarrow 1p$ transition probably requires excitation at either the red edge or the blue edge of the Gaussian feature. However, our results suggest that the $1s \rightarrow 1p$ excitations near the blue edge are strongly overlapped by quasi-continuum transitions that, as Schwartz and co-workers point out,[179] are unlikely to have sufficient asymmetry in their transition dipoles (if indeed they are polarized at all) to observe polarization-dependent anisotropy. According to our model, then, the only way in which one might expect to observe PTHB dynamics is by exciting on the extreme red edge of the absorption spectrum. Such an experiment has been reported,[179] but no significant polarization dependence was observed in the bleaching dynamics.

Assuming that our model describes the excited states correctly, and assuming that selective excitation of the lowest-lying $1p$ state is indeed feasible, our model suggests that one might still fail to observe PTHB dynamics. To see why, we plot in Fig. 3.13 the probability distribution function for θ, the angle between the $1s \rightarrow 1p$ transition dipole moment vectors. In the absence of electronic relaxation of the solvent, these three vectors are nearly orthogonal, with $\theta > 85°$ in nearly every case. Allowing for second-order relaxation, however, we obtain a much broader distribution in θ, with some amplitude all the way out to at least $\theta = 60°$. Thus, the relaxed transition moments are not strictly perpendicular, even though the excited-state wavefunctions are clearly p-like. Thus, even if it proves feasible to separate the three $1s \rightarrow 1p$ excitations on an energetic basis, one still would still have difficulty distinguishing the populations based upon their orientation. Furthermore, Shkrob[183] has calculated an autocorrelation function for rotation of the $1s \rightarrow 1p$ transition dipole moments, and found that this correlation function decays on a time scale of $\sim$100 fs. Together, these observations indicate that the PEWP-2 model of e^-_{aq} is consistent with the lack of observed PTHB dynamics.

It is worth noting that Larsen *et al.*[44] have used similar arguments to explain the lack of PTHB dynamics in their e^-_{aq} model, which does not form a cavity. Indeed, because earlier, cavity-forming models *did* predict observable PTHB dynamics, this argument was used as evidence in support of the newer model, with its much more diffuse electron.[44] At the very least, the results in this section demonstrate that lack of PTHB dynamics need not be inconsistent with a cavity-bound electron.

3.6 Summary and conclusions

We have described a re-parameterization of a polarizable electron–water interaction potential, PEWP-2, leading to a new hydrated-electron model in which many-body electron–water polarization is included in a self-consistent way. Unlike our previous model (PEWP-1),[3] which afforded promising results for $(H_2O)_n^-$ clusters but failed to localize the electron in the condensed phase, the new parameterization performs at least as well for clusters (as judged by comparison to *ab initio* benchmarks), but also qualitatively reproduces various experimental data for e_{aq}^- in bulk water. As Shkrob *et al.*[157, 158] and others[146, 156] have argued, quantitative reproduction of structural features and experimental parameters may require many-electron quantum mechanics. Nevertheless, the PEWP-2 model affords a VEBE and an optical absorption spectrum that are in far better agreement with experiment than are previous one-electron models, while structural and dynamical features, such as the radius of gyration and diffusion coefficient, are at least qualitatively correct.

For e_{aq}^- in bulk water, we have demonstrated that H_2O molecules in the first solvation shell are poor H-bond donors but good H-bond acceptors, a result that we can also reproduce using a non-polarizable model. This disruption in the H-bonding environment is caused by enhanced librational motions of water molecules nearby the solvated electron, and may be related to the electron's anomalously large entropy of hydration.

By extrapolating the bulk VEBE to the infinite-dilution limit, we predict a bulk binding energy of 3.7 eV, a value that is slightly smaller than the most recent extrapolation of cluster photo-electron data,[4] but is 0.4 eV higher than previous extrapolations.[2] Our value is also 0.4 eV higher than two recent direct measurements of the VEBE using liquid microjets,[5, 6] but is in good agreement with a third liquid microjet experiment.[7] The discrepancy between these various values underscores the need for models such as the one constructed here, which can reproduce both qualitative characteristics of bulk e^-_{aq}, but are also quantitatively accurate for cluster VEBEs.

The importance of self-consistent, many-body electron–water polarization has been demonstrated in two very important ways. First, we have shown that the electronic re-organization energy that accompanies electron detachment is quite large (≈ 1.4 eV) in the bulk limit. This observation indicates that non-polarizable models can dramatically overestimate VEBEs in large systems, while simultaneously underestimating VEBEs in the small $(\mathrm{H_2O})_n^-$ clusters that are often used as benchmarks. A second key effect of self-consistent polarization is a qualitative change in the line shape of the optical absorption spectrum for e^-_{aq}, bringing the predicted spectrum into much closer agreement with experiment than has been seen in any previous one-electron model. Inclusion of electronic relaxation of the solvent upon excitation of the one-electron wavefunction has the effect of red-shifting the absorption maximum by 0.3 eV, placing it in remarkable agreement with experiment. Furthermore, relaxation greatly increases the number of (vertically) bound electronic states, leading to a smooth tail on the blue edge of the absorption spectrum. This "blue tail" has proven elusive in previous simulations,[154] but in our model it arises naturally due to solvent-facilitated intensity borrowing by quasi-continuum excited states.

It is our hope that this potential will ultimately be useful in interpreting photoelectron experiments for $(H_2O)_n^-$ clusters, and for studying the ground- and excited-state dynamics of the solvated electron in bulk water. Work along these lines is in progress.

CHAPTER 4

Comment on "Does the hydrated electron occupy a cavity?"[4.1]

A recent report by Larsen, Glover, and Schwartz [44] (LGS) challenges the long-held view that the "hydrated" (aqueous) electron, e^-_{aq}, consists of a one-electron wavefunction localized within a quasi-spherical solvent cavity, and coordinated to 4–6 water molecules. This has been the dominant paradigm for more than 40 years,[26] and it is supported by numerous atomistic simulations.[67, 73, 184] The challenge by LGS is based upon a new, "rigorously derived" electron–water pseudopotential;[44] simulations using this one-electron pseudopotential model do not afford a well-defined cavity. This model, however, has not yet been tested against reliable benchmarks. Such tests are reported here.

The LGS pseudopotential is derived within the "static exchange" (SE) approximation, which essentially amounts to a Hartree-Fock calculation for H_2O^- using frozen molecular orbitals (MOs) for H_2O. LGS have devised a clever way to obtain a nodeless pseudo-orbital for the unpaired electron, without introducing approximations that are

---

[4.1] This chapter appeared, in a slightly modified form, as a technical comment in *Science*, in 2011, volume 331, page 1387.

typically made in this context.[166] Once the pseudo-orbital is determined, it can be converted into an electron–water pseudopotential for condensed-phase simulations.

The LGS pseudopotential was fit using Mulliken atomic charges $Q_{\mathrm{O}} = -0.862709e$ and $Q_{\mathrm{H}} = +0.431355e$ obtained from a Hartree-Fock calculation, but e^{-}_{aq} simulations were performed using $Q_{\mathrm{O}} = -0.82e$ and $Q_{\mathrm{H}} = +0.41e$, corresponding to the SPC water model.[44] (This corresponds to a reduction in $\mathrm{H_2O}$ dipole moment from 2.39 D to 2.27 D, at the SPC geometry.) LGS augment their model with an approximate polarization potential, which is not included in the SE treatment, and far less attention is paid to this aspect of the model. Polarization parameters from the literature are used, without further comment.

High-level *ab initio* calculations have been reported for $(\mathrm{H_2O})^{-}_{n}$ clusters, $n = 2$–33,[3] but LGS do not report any comparisons to these data. Fig. 4.1 compares benchmark *ab initio* vertical electron binding energies (VEBEs) to results obtained using the LGS pseudopotential. The LGS potential strongly overbinds the electron compared to *ab initio* calculations. By modifying a single parameter in the polarization potential [R_c, in the Supporting Information for Ref. [44]], we obtain a model that we call LGS-mPol that performs reasonably well against this benchmark database, albeit not as well as other hydrated-electron models in the literature.[3, 67, 184] We do not intend LGS-mPol to be a serious e^{-}_{aq} model, but rather to demonstrate that the overbinding exhibited by the LGS model cannot be fixed in a simple way, without deleterious effects on other observable properties.

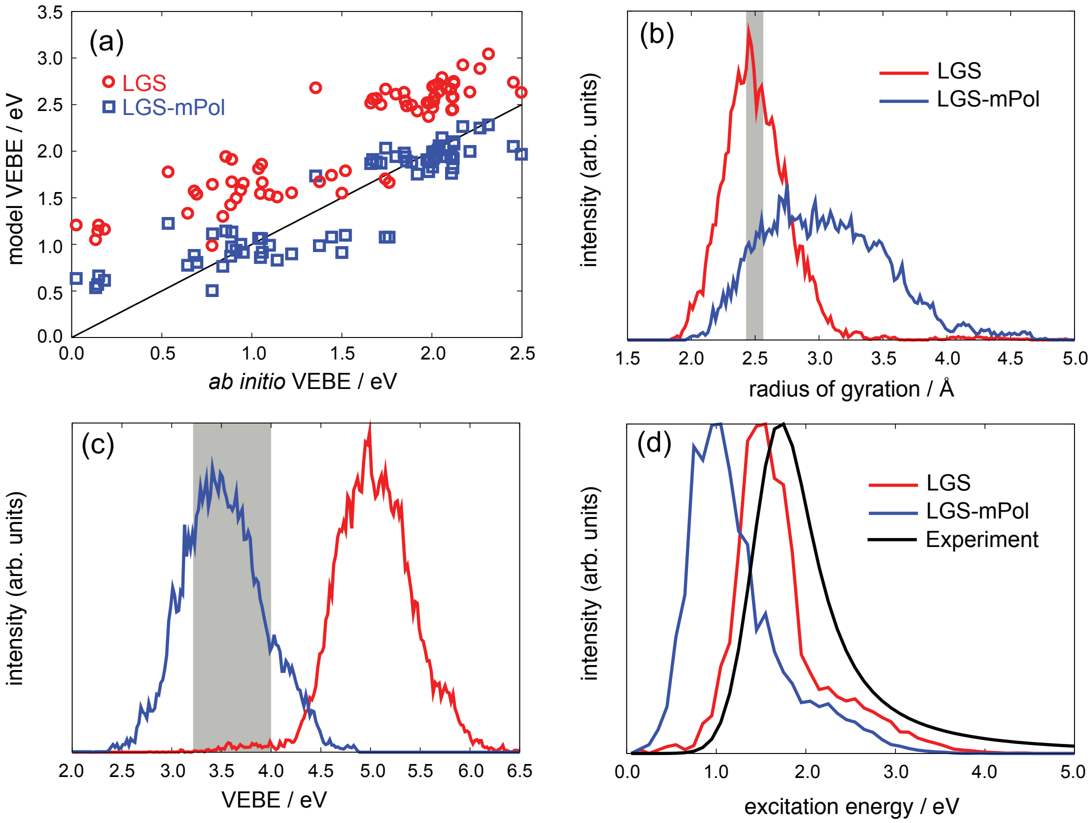

Figure 4.1: Panel (a): Comparison of MP2/6-31(1+,3+)G* benchmark VEBEs [3] to results obtained using LGS-based pseudopotential models, for 71 different $(H_2O)_n^-$ isomers ranging from $n = 12$ to $n = 33$. Panels (b)–(d): Radius of gyration, VEBE, and optical absorption spectrum of e_{aq}^-, obtained from bulk simulations. The gray boxes in (b) and (c) depict the range of the experimental estimates of these quantities. [2, 4–7]

We have performed molecular dynamics simulations of e^-_{aq} using the same simulation procedure reported in Ref. [44]. We find that radial distribution functions and other structural properties reported by LGS are not strongly affected by variation of the polarization potential or the H_2O point charges. Rather, it is the LGS pseudopotential itself that is indisposed toward cavity formation.

Figs. 4.1(b)–(d) shows several properties obtained from our simulations and compares them to experimental estimates. The average radius of gyration for the LGS model is in good agreement with experiment,[2] but the agreement is far less satisfactory for the LGS-mPol variant examined here, which performs much better for VEBEs. The optical absorption spectrum predicted by the LGS model is slightly red-shifted, relative to experiment, and a more rigorous treatment of solvent polarization should further red-shift the spectrum.[184] The attenuated polarization potential in LGS-mPol yields a spectrum that is red-shifted from experiment by 0.7 eV, which makes sense given the larger radius of gyration predicted by this model.

Strikingly, all 29 excited states that we use to generate absorption spectra are vertically bound. In fact, the 29th excited state is bound, in the LGS model, by ~ 1.0 eV. Fig. 4.1(c) plots the distribution of ground-state VEBEs obtained from the simulations. The LGS model overbinds the electron by 1–2 eV, while LGS-mPol predicts a VEBE within the range of experimental estimates for e^-_{aq}.[2, 4–7] This agreement is partly fortuitous, as the binding energy increases by ~ 1 eV if Ewald summation is used to sum the long-range Coulomb interactions,[184] whereas we follow the procedure of LGS [44] and use the minimum-image convention.

In Ref. [44], LGS plot the ground-state e^-_{aq} energy as a function of time. This function oscillates around -5.5 eV, whereas the lowest few excited-state energies oscillate between -3 eV and -4 eV. In contrast, the *ground-state* energy inferred from experiment is 3.4–4.0 eV.[2, 4–7] In view of this tremendous discrepancy, the assertion by LGS that "in every case. . . our predictions are consistent with experiment" appears to be overstated.

Ab initio calculations on $(H_2O)^-_n$ clusters find that orbital relaxation upon electron detachment is fairly minor,[156] hence the Hartree-Fock (HF) singly-occupied MO (SOMO) should offer a qualitatively correct description of the unpaired electron, provided that this orbital is bound. The LGS pseudopotential, in conjunction with an *ad hoc* polarization potential, is intended to mimic the HF SOMO. To examine the extent to which it does so, we carved out a $(H_2O)^-_{31}$ cluster from a cavity-forming model of e^-_{aq},[67] which represents a 5.5 Å radius around the centroid of the cavity-bound wavefunction. The geometry of this cluster was subsequently optimized using HF/6-31++G* theory and, alternatively, the LGS model. Fig. 4.22 shows that HF optimization preserves the cavity-bound nature of the SOMO, but this cavity collapses when optimized using the LGS model. The latter affords a wavefunction that permeates throughout the cluster. At the LGS-optimized geometry, the HF SOMO is unbound and is localized on the surface of the cluster; it has been "squeezed out" by the collapse of the cavity.

Collapse of the solvent cavity arises because the LGS pseudopotential is *far* more attractive near the hydrogen atoms than previous pseudopotentials. This feature

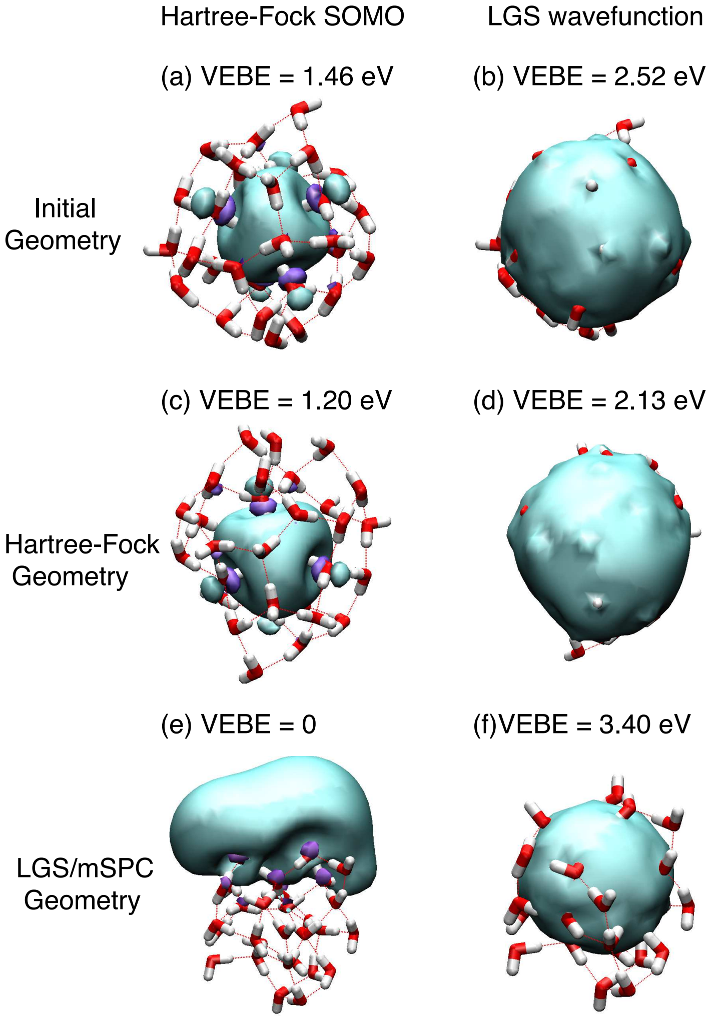

Figure 4.2: Results of optimizing a cavity-bound $(H_2O)_{31}^-$ structure. The initial geometry [panels (a) and (b)] was carved out of a bulk e_{aq}^- simulation and clearly exhibits a compact, cavity-bound wavefunction at the Hartree-Fock level. The cluster geometry in (c) and (d) is the Hartree-Fock minimum-energy geometry, although the wavefunction in (d) is calculated using the LGS model. The cluster geometry in (e) and (f) is the LGS minimum-energy geometry, although the wavefunction in (e) is the Hartree-Fock SOMO. Each isosurface encapsulates $0.9e$.

results from the fact that the density associated with the "exact" pseudo-orbital obtains a maximum over the hydrogen atoms whereas the density of the exact SE wavefunction is at a minimum; see Fig. 1 in Ref. [66] or Fig. 3.3 in this thesis. Any pseudopotential derived from this pseudo-orbital will result in a far too attractive region near the hydrogen atoms. In contrast to the LGS potential, the true HF potential is clearly repulsive in these regions, as evidenced by the "dents" in the HF SOMO around each water molecule (see Fig. 2). In a separate comment Turi and Madarász also argue that the LGS potential is too attractive.[185] These authors show that a minor change in the model can be made (which reproduces the eigenvalue of the pseudo-orbital) which results in cavity formation.

In there response LGS quip that "Jacobson and Herbert's claims of supposed errors in our development reflect a fundamental misunderstanding of pseudopotential theory" and state that "pseudopotentials are based on pseudo-orbitals, not LUMOS".[186] LGS entirely miss our point. The fact that the pseudo-orbital density has a maximum where the LUMO has a minimum implies that the pseudo-orbital does not reproduce the "exact" SE wave function, which is an error. This discrepancy evidently leads to the lack of cavity formation. We do not criticize their fitting procedure, but object to their apparent viewpoint that the model is not approximate, referring to it as "rigorously-derived" and in some instances as "numerically exact".

The structure of e^-_{aq} is intimately quantum-mechanical, and cannot be probed directly by experiment, so there is an acute need for theoretical models to aid in the interpretation of experimental observables. Before new theoretical predictions can be taken seriously, however, such models must be carefully tested against the large body of existing e_{aq}^{-} data. Relative to the current generation of cavity-forming pseudopotential models,[67, 184] the model introduced in Ref. [44] fares poorly in such tests.

CHAPTER 5

Polarization-bound, quasi-continuum states are responsible for the “blue tail” in the optical absorption spectrum of the aqueous electron [5.1]

The notion of a “solvated electron” was introduced more than a century ago, to explain the electrical conductance and optical spectra exhibited by solutions of alkali metals.[22, 187] Owing to the relatively short lifetime of this species in water, however, direct observation of the aqueous electron (e^-_{aq}) was not made until 1962,[124] but since that time it has been recognized that e^-_{aq} is one of the primary radicals formed upon radiolysis of aqueous systems.[25] Nevertheless, important questions persist concerning the structure and dynamics of this diffuse, polarizable, and fundamentally quantum-mechanical solute, especially with regard to its excited electronic states.

Solvated electrons can be generated not only by ionizing radiation, but also by UV irradiation of liquid water, at energies just above the band edge of water’s UV spectrum;[188, 189] the details of this low-energy ionization mechanism remain a matter of debate.[190–193] Moreover, the “pre-hydrated” (or “wet”) electron, a short-lived

---

[5.1] This chapter appeared as a communication in the *Journal of the American Chemical Society* in 2011, volume 132, page 10000.

(< 1 ps), non-equilibrium precursor to the fully solvated electron, whose existence is inferred from ultrafast spectroscopy,[194–196] has only recently been definitively assigned as an excited state of e^-_{aq}.[197] The time scale for internal conversion to the ground state remains controversial, however, with experimental and theoretical estimates ranging from 50–1000 fs.[82] Dissociative electron attachment of the pre-hydrated species by nucleic acids has recently been implicated[27, 198, 199] as a mechanism for DNA damage by ~ 0 eV electrons,[200–202] suggesting that *reductive* chemistry plays a prominent role in biological radiation damage, alongside the more familiar oxidative damage mechanisms involving OH radicals. In contrast to the pre-hydrated electron, however, the equilibrium species e^-_{aq} appears to be relatively ineffective in inducing DNA strand breaks.[203]

Given the importance of excited states of e^-_{aq} in radiation chemistry, and in view of the fact that the optical absorption spectrum of e^-_{aq} is the primary means of detecting and characterizing this species in bulk water, it is significant that no theoretical model or calculation has yet provided a qualitatively satisfactory description of this spectrum. The spectrum (Fig. 1) exhibits a Gaussian line shape on the red edge, with a peak absorption intensity at 1.7 eV (720 nm).[2] The overall shape of this Gaussian feature *is* reproduced by simulations, albeit slightly blue-shifted, and the prevailing view (based upon simulations using one-electron pseudopotential models[147, 148, 154]) is that this feature arises from heterogeneous broadening of three $s \rightarrow p$ excitations of an electron in a cavity. The high-energy side of the spectrum, in contrast, exhibits a Lorentzian line shape[2] that is absent in all previous

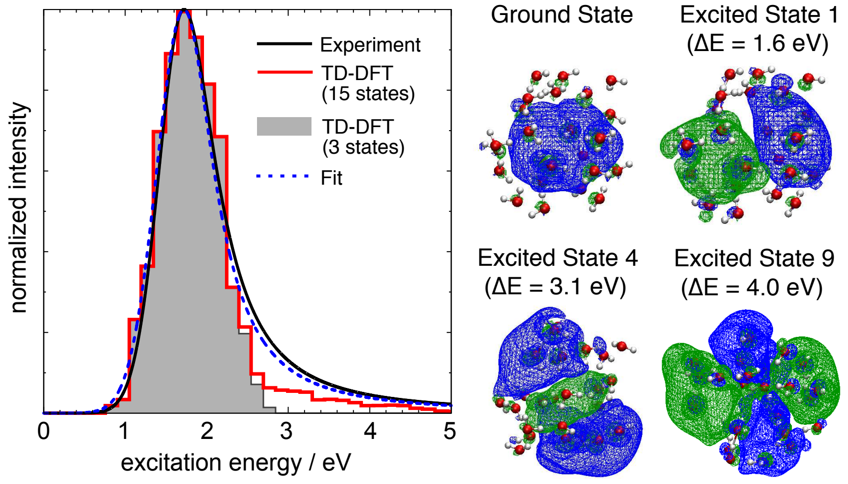

Figure 5.1: Comparison of the experimental absorption spectrum of e^-_{aq} (using line-shape parameters from Ref. [2]) to results obtained from TD-DFT calculations, along with a fit of the TD-DFT data to the line shape function used in Ref. [2]. Also shown are representative examples of the NTOs associated with excitations in various parts of the spectrum. (Only QM water molecules are shown, and these plots represent 90% isoprobability contours.)

simulations of the e^-_{aq} absorption spectrum, including *ab initio* calculations.[155, 158]

Here, we simulate the electronic absorption spectrum of e^-_{aq} in bulk water, using both one-electron and many-electron quantum-mechanical (QM) models. The one-electron model was described in chapters 2 and 3 and incorporates many-body electron–water polarization in a self-consistent way. The many-electron model is time-dependent density functional theory (TD-DFT), using a long-range corrected functional that affords accurate electron binding energies in $(H_2O)^-_n$ clusters,[3, 204] and is free of spurious, low-energy charge-transfer excited states that often plague condensed-phase TD-DFT calculations.[205–207] These are two very different theoretical paradigms, yet the result in both cases is the same: a spectrum that is in far better agreement with experiment than is any previous simulation, both in terms of the peak position and, more importantly, the prediction of significant oscillator strength in the blue tail. The calculations indicate that these higher-energy states (beyond the p manifold) extend deep into the interstices between water molecules, and are bound only by the overall polarization of numerous water molecules with which they interact.

A TD-DFT simulation of the e^-_{aq} absorption spectrum was performed by sampling over snapshots extracted from a simulation of e^-_{aq} in bulk water, obtained using a one-electron model that has been used in many recent e^-_{aq} simulations.[67] Roughly two solvation shells (≈ 28 water molecules) were described using DFT, whereas the remaining bulk solvent was represented by molecular mechanics (MM) point charges. The basis set (6-31+G*) is atom-centered, yet the orbitals shown in Fig. 1 make it clear that this basis is diffuse enough to describe an electron that inhabits the voids between water molecules.

As shown in Fig. 5.1, the TD-DFT simulation exactly reproduces the peak absorption intensity, without adjustable parameters, and also reproduces the width of the Gaussian portion of the spectrum. As in the one-electron models, this feature arises from inhomogeneous broadening of three $s \rightarrow p$ excitations. This is true despite small contributions to the e^- wavefunction from frontier MOs of the water molecules. These small contribution appear to be necessary to explain certain quantitative features of

e^-_{aq} spectroscopy,[146, 156, 157] but do not qualitatively alter the cavity picture of e^-_{aq}, and the low-energy excited states can still be rationalized in terms of a "particle in a spherical box" model. Furthermore, each electronic excitation of e^-_{aq} is well-represented by a single particle/hole pair of natural transition orbitals (NTOs),[208] a few of which are depicted in Fig. 1.

Notably, when only the lowest three excited states are included in the TD-DFT calculation, the spectrum that is obtained is strictly Gaussian. When additional excited states are considered, however, we observe a long tail at higher excitation energies. (In all, 15 excited states are included in these calculations; tests indicate that the next five states support $\lesssim 1\%$ of the total oscillator strength.) The combined oscillator strength of the three $s \rightarrow p$ excitations is extremely sensitive to the size of the QM region in these calculations; somewhat smaller QM regions afford similar excitation energies, but in such calculations, the p states carry essentially all of the oscillator strength. Thus, relaxation of the solvent electron density upon excitation of the cavity-bound electron facilitates intensity borrowing by the higher-energy states, which manifests as the blue tail seen in Fig. 1.

Given that the higher-lying excited states penetrate well beyond the QM region employed here, it will be extremely difficult to reproduce the blue tail *quantitatively* in QM/MM calculations of this sort. To complement this approach, we turn to our polarizable one-electron model, where simulations in bulk water can be performed using periodic boundary conditions.

Our model, which is described in detail in Ref. [184], employs an electron–water

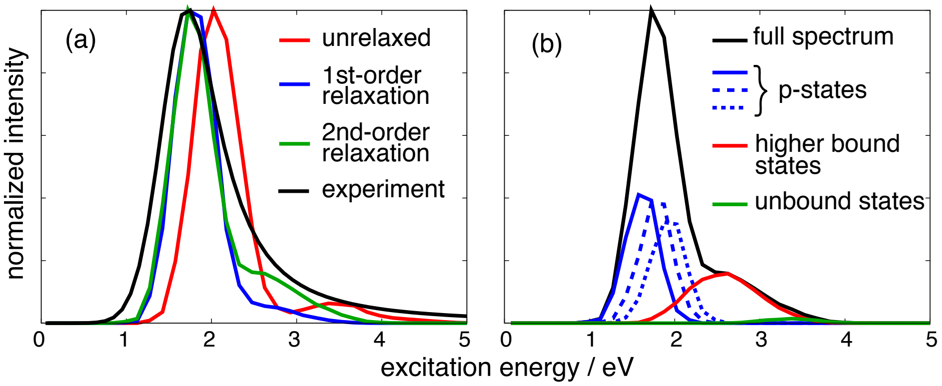

Figure 5.2: (a) Absorption spectra for e^-_{aq} computed from a one-electron model, using various approximations for the dipole relaxation energy. (b) Spectrum computed using second-order relaxation, decomposed into contributions from various excited states.

pseudopotential in conjunction with a polarizable water model, and thereby includes many-body electron–water polarization. This model reproduces numerous *ab initio* benchmarks in $(H_2O)^-_n$ clusters, $n = 2$–33, and provides a vertical electron binding energy (VEBE) for bulk e^-_{aq} that is in far better agreement with experiment than previous (non-polarizable) models, owing to a large ($\approx$ 1.4 eV) dipole relaxation energy, for *vertical* electron detachment.

We calculate the absorption spectrum from this model in several different ways, with results shown in Fig. 5.2. In principle, one should calculate the dipole relaxation energy by converging the H_2O dipoles self-consistently with the excited-state e^- wavefunctions, but this proves difficult because the relaxation energy is large compared to the energy-level splittings. Complete neglect of dipole relaxation (by freezing the

H_2O dipole moments at their ground-state values) affords the "unrelaxed" spectrum in Fig. 5.2(a), which is qualitatively incorrect but is quite similar to results obtained with non-polarizable one-electron models.[67] This spectrum consists of a low-energy Gaussian part arising from the $s \rightarrow p$ excitations, along with a higher-energy feature (above 3 eV) consisting of bound → continuum excitations. In between these features is a conspicuous gap in oscillator strength, not seen experimentally.

To go beyond this crude approximation, we estimate the dipole relaxation energy using perturbation theory, taking the perturbation to be

$$\hat{W} = \hat{H}[\{\mu_{ex}\}] - \hat{H}[\{\mu_{gs}\}] \ . \tag{5.1}$$

Here, $\hat{H}[\{\mu_{gs}\}]$ represents the Hamiltonian determined using dipoles $\{\mu_{gs}\}$ converged self-consistently with the ground-state wavefunction, whereas the dipoles $\{\mu_{ex}\}$ are converged to the excited-state eigenfunctions of $\hat{H}[\{\mu_{gs}\}]$. We do not allow the ground state to mix with the perturbed wavefunctions, so that all of the latter are orthogonal to the ground state, even if they are not quite orthogonal to one another owing to the state-specific nature of the perturbation.

A first-order correction for $\hat{W}$ brings the peak absorption intensity into nearly perfect agreement with experiment, as shown in Fig. 5.2(a). The line shape changes only slightly, however, because first-order perturbation theory alters the line shape only via the excited-state energies, E_n, that appear in the expression for oscillator strength:

$$f_{0\rightarrow n} = \frac{2m_e}{3\hbar^2}(E_n - E_0)\left|\langle\psi_0|\,\hat{\mu}\,|\psi_n\rangle\right|^2 \ . \tag{5.2}$$

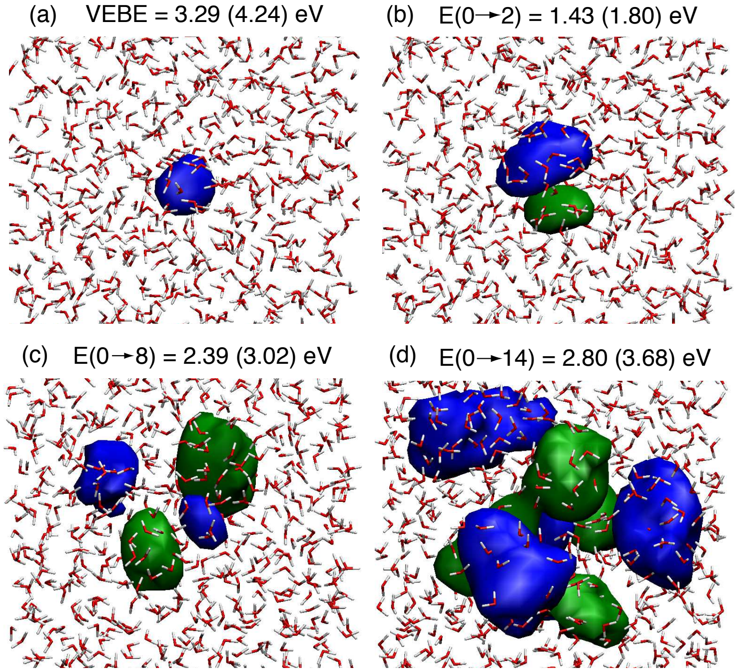

Figure 5.3: Typical examples of (a) the ground-state and (b)–(d) excited-state wavefunctions, obtained from the one-electron model. The VEBE and excitation energies for these particular states are shown as well, with relaxed excitation energies in parentheses. The isosurfaces encapsulate 90% of the probability density, $|\psi|^2$.

Second-order perturbation theory is required to obtain a correction to the transition dipoles, and this correction results in a qualitative change in the distribution of oscillator strengths, leading to significant intensity in the "blue tail" and far better agreement with the experimental line shape. To the best of our knowledge, no other model affords a blue tail with significant oscillator strength.

According to this model, polarization of the water molecules has the effect of binding $\gtrsim 25$ excited states that were unbound in the absence of relaxation. These excited-state wavefunctions are highly diffuse, and penetrate well beyond the cavity occupied by the ground-state wavefunction. Representative examples of these wavefunctions are depicted in Fig. 5.3.

The extremely diffuse nature of these states is consistent with the observation that the blue edge of the e^-_{aq} optical absorption overlaps the red edge of its photoelectron spectrum.[2] In the one-electron simulations, the p-state manifold extends no higher than about 2.5 eV, whereas unbound excitations appear at 3.0–3.5 eV. Within the narrow window in between, the excited states must evolve from compact, hydrogenic wavefunctions [as in Fig. 5.3(b)] into completely delocalized plane waves. Our calculations suggests that this gap is bridged by "quasi-continuum" states [as in Fig. 5.3(d)] that are (vertically) bound, but only via polarization of numerous water molecules that interact with these highly-delocalized electronic wavefunctions.

In summary, we have calculated the absorption spectrum of e^-_{aq} using two completely different methodologies: a many-electron method, in which the water molecules possess explicit MOs that may contribute to the e^- wavefunction; and also a one-electron model where this is not possible, but where the H_2O molecules possess inducible dipoles that respond to excitation of the e^- wavefunction. Qualitatively, both calculations support the same physical picture: that the "blue tail" in the electronic absorption of e^-_{aq} arises from excitations to delocalized, bound states that are stabilized by polarization of water molecules beyond the first solvation shell. Solvent polarization facilitates intensity borrowing from the p states, and while this effect is small, the substantial number of these polarization-bound, quasi-continuum states affords significant intensity in the blue tail.

CHAPTER 6

A simple algorithm for determining orthogonal, self-consistent excited-state wave functions for a state-specific Hamiltonian: Application to the optical spectrum of the aqueous electron [6.1]

6.1 Introduction

First observed directly in 1962,[124] the aqueous (or hydrated) electron, e^-_{aq}, has since that time been the subject of numerous experimental and theoretical investigations.[43, 209] Despite numerous atomistic simulations of this species over the past 25 years,[43] it was not until quite recently that the Lorentzian decay on the high-energy side of the optical absorption spectrum was reproduced even qualitatively.[160, 184]

Due to the highly quantum-mechanical nature of the solute (an electron), the dynamics and bulk structure of e^-_{aq} have mostly been studied using one-electron pseudopotential methods,[39, 43, 64, 66, 210] or in other words, hybrid quantum mechanics/molecular mechanics (QM/MM) procedures with a one-electron QM region. The ostensible simplicity of such models (only one QM electron), combined with the importance of e^-_{aq} in the radiation chemistry of aqueous systems,[25, 209, 211] means

---

[6.1] This chapter appeared as a full article in the *Journal of Chemical Theory and Compuation*, in 2011, volume 7 page 2085.

that these one-electron pseudopotential models have historically been used to test a variety of mixed quantum/classical simulation techniques.

We have recently developed a new one-electron pseudopotential model that incorporates self-consistent polarization between the solvent (water) and the single "excess" electron.[184] Results from this model compare favorably to *ab initio* calculations in $(H_2O)_n^-$ clusters, and various properties of the bulk species, e_{aq}^-, are also reproduced reasonably well.[184] Our model utilizes the AMOEBA water potential,[14] which treats polarization by means of inducible point dipoles located on each MM atom. In our hydrated-electron model,[3, 184] the electric field generated by the QM wave function contributes to the total electric field that polarizes these dipoles.

Because the induced dipoles represent electronic degrees of freedom, they should respond (polarize) on the time scale of electronic excitation. As such, it seems physically reasonable that the calculation of excited states in our polarizable model should require a self-consistent calculation in which the solvent dipoles are converged with respect to each excited-state wave function. Because the QM Hamiltonian depends on the inducible dipoles, the realization of such a procedure effectively renders the Hamiltonian state-specific, *i.e.*, the nature of the Hamiltonian depends upon the particular electronic state that one is attempting to calculate.

In previous work,[184] we encountered difficulties in obtaining self-consistent, excited-state solutions to this effective Hamiltonian, owing to the fact that the energy gaps between states are small ($\sim$0.1 eV) while the electronic relaxation energy of the solvent is large (*e.g.*, 1.4 eV for vertical electron detachment in the bulk limit[184]).

This leads to frequent state-switching during the wave function/dipole optimization. Even if we were able to converge the excited-state wave functions self-consistently with the induced dipoles, the wave functions thus obtained would not be mutually orthogonal, owing to the state-specific nature of the effective Hamiltonian. In view of these difficulties, we have previously resorted to the use of a perturbative correction for the solvent's polarization response upon excitation of the wave function.[160, 184] While this approach allowed us to make progress in understanding the role of solvent polarization, it suffers from a lack of mutual orthogonality amongst the excited-state wave functions, owing to the state-specific nature of the perturbation. As such, one might reasonably be concerned about possible artifacts in the predicted oscillator strengths.

Here, we report a simulated annealing procedure in the space of electronic variables (wave function amplitudes and induced dipoles) by means of which the classical dipoles are converged self-consistently with respect to each wave function. In addition, our algorithm employs Lagrange multipliers to ensure that all of the wave functions are orthonormal, despite the state-specific nature of the Hamiltonian. As a numerical demonstration of this procedure, we calculate the electronic absorption spectrum of the aqueous electron, using our polarizable one-electron model. The orthogonality issue is general to QM/MM methods that employ polarizable force fields, and therefore these ideas may be more broadly applicable. (However, the large polarization energies that we encounter may be unique to charged systems.)

Orthogonality is also an issue in certain self-consistent field (SCF) methods. For example, Gill and co-workers[212, 213] have recently introduced a maximum overlap method (MOM) that attempts to find excited-state solutions to the SCF equations by choosing the occupied orbitals at each SCF iteration, not in the usual *aufbau* way, but rather by selecting those molecular orbitals that have the largest overlap with a set of user-specified guess orbitals. This situation is similar to the problem outlined above in that the effective Hamiltonian (Fock matrix) is state-specific, and the excited-state solutions are not mutually orthogonal. Moreover, there is a direct correspondence between our polarizable QM/MM method and the SCF method. In the QM/MM procedure, we use the one-electron density, $|\psi|^2$, to compute induced dipoles, then use these dipoles to construct an effective Hamiltonian and finally diagonalize this Hamiltonian to obtain a new density. This process is iterated to self-consistency. In the SCF method, one uses the density to compute a new Fock matrix. We believe that our algorithm can be modified for use in the SCF procedure, in a manner that is conceptually (if not computationally) straightforward, and we hope to report on this in the future.

This paper is organized as follows: Section 6.2 provides a brief overview of our one-electron pseudopotential model for e^-_{aq} and introduces the electronic annealing method. Details of the calculations are given in Section 6.3. In Section 6.4, we present results for the optical absorption spectrum of e^-_{aq} and draw a comparison with results obtained previously, using a perturbative treatment of the solvent's polarization response. We discuss certain formal aspects of the method, and some possible generalizations, in Section 6.5. Section 6.6 provides a summary.

6.2 Theory

6.2.1 Polarizable QM/MM model

We will not discuss our hydrated electron model in detail, but will only highlight those aspects that are important to understand the annealing procedure. As in many polarizable QM/MM models, the total Hamiltonian in our model is a function of both the coordinates of the MM atoms, $\{\vec{R}_I\}$, as well as the induced MM dipoles, $\{\vec{\mu}_i\}$. The one-electron Hamiltonian can be written

$$\hat{H}\big(\{\vec{\mu}_i\},\{\vec{R}_I\}\big) = \hat{T} + V_{elec\text{-}water}\big(\{\vec{\mu}_i\},\{\vec{R}_I\}\big) + V_{\text{MM}}\big(\{\vec{\mu}_i\},\{\vec{R}_I\}\big)\ . \tag{6.1}$$

Here, $\hat{T}$ is the one-electron kinetic energy operator, $V_{elec\text{-}water}$ is the electron–water pseudopotential, and V_{MM} is the molecular mechanics (MM) potential energy function for the polarizable water molecules. In our model, V_{MM} is the AMOEBA water force field.[14] The pseudopotential, $V_{elec\text{-}water}$, contains electrostatic interactions between the electron and both the permanent and induced multipole moments of the water molecules. In addition, it contains a repulsive potential that keeps the electron from collapsing into the core molecular region.

The induced dipoles are obtained by solution of the equation[3, 184]

$$\vec{\mu}_i = \alpha_i\big(\vec{F}_i^{\text{MM}} + \vec{F}_i^{\text{QM}}\big)\ , \tag{6.2}$$

in which α_i is an (isotropic) polarizability for site i, $\vec{F}_i^{\text{MM}}$ is the electric field produced by the MM subsystem at site i, and $\vec{F}_i^{\text{QM}}$ is the electric field due to the wave function, also evaluated at site i. It can be shown that the induced dipoles defined by Eq. (6.2) minimize the total energy with respect to variations in $\vec{\mu}_i$.[3, 104] The one-electron wave function is determined by the solution of the Schrödinger equation

$$\hat{H}\big(\{\vec{\mu}_i\},\{\vec{R}_I\}\big)\,|\psi\rangle = E\,|\psi\rangle\ . \tag{6.3}$$

In practice, $|\psi\rangle$ is replaced by $\mathbf{c}$, a vector of amplitudes on a real-space grid. In order to obtain self-consistent polarization, we iterate Eqs. (6.2) and (6.3) to self-consistency. This procedure works well for the ground state but is difficult to converge for more than one or two excited states.

As a result of this difficulty we have, in previous work, computed approximate excited states by means of a simple perturbative scheme.[160, 184] To define the perturbation, we first calculate the ground-state wave function $|\psi_0\rangle$ and some number of excited state wave functions, $|\psi_n\rangle$, using dipoles $\{\vec{\mu}_i^{(0)}\}$ that are converged with respect to $|\psi_0\rangle$. For each excited state, we then obtain new dipoles, $\{\vec{\mu}_i^{(n)}\}$, that are converged with respect to $|\psi_n\rangle$, without relaxing $|\psi_n\rangle$. The quantity

$$\hat{W}_n = \hat{H}\big(\{\vec{\mu}_i^{(n)}\},\{\vec{R}_I\}\big) - \hat{H}\big(\{\vec{\mu}_i^{(0)}\},\{\vec{R}_I\}\big) \tag{6.4}$$

serves as the perturbation.[160, 184]

The perturbatively-corrected wave functions thus obtained are not orthogonal, because the perturbation is state-specific. However, they do turn out to be *approximately* orthogonal, with typical overlaps on the order of $\sim$0.1. Similar overlaps have been reported in MOM-SCF calculations, yet oscillator strengths in these calculations are in reasonable agreement with benchmark results.[212] As such, we believe that the e^-_{aq} spectra computed using the perturbative approach are at least qualitatively correct.

6.2.2 Electronic annealing procedure

We next describe our new algorithm to determine orthogonal excited states for state-specific effective Hamiltonians. The idea is not entirely new, and is inspired by the Car-Parrinello molecular dynamics (CPMD) method,[214, 215] wherein the electronic degrees of freedom are propagated dynamically as classical variables. The CPMD approach can also be used to obtain ground-state, single-determinant wave functions by clamping the nuclei in place and "annealing" a guessed wave function.[214, 216] This amounts to a systematic removal of the fictitious kinetic energy associated with the electronic degrees of freedom. So far as we are aware, however, this technique has not been applied to the annealing of excited states. The main difference here, apart from the obvious difference of having only one QM electron in the present implementation, is that we constrain the wave function of interest to be orthogonal to each previously-determined wave function. Doing this allows one to "march up" the manifold of excited states. Each excited state will then be defined as the lowest energy state that is orthogonal to all previously determined states. In a sense, this is a natural generalization of the linear variation method in elementary quantum mechanics.

Let $\mathbf{c}_0$ denote the vector of wave function amplitudes that we are interested in optimizing, and let $\{\mathbf{c}_i\}_{i=1}^N$ denote a set of previously-determined states. Note that $\mathbf{c}_0$ need not (and probably does not) represent the ground state, but the notation for the equations of motion will be simpler if we adopt a common index for all of the vectors. Only $\mathbf{c}_0$ is propagated in time, whereas $\mathbf{c}_1, \ldots, \mathbf{c}_N$ are fixed. We also find it convenient to define a dot product

$$\mathbf{c}_i \cdot \mathbf{c}_j = \langle \psi_i | \psi_j \rangle = \sum_{\mu=1}^{N_{grid}} c_{i,\mu}\, c_{j,\mu}\, \Delta\tau \qquad (6.5)$$

where the sum runs over grid points and $\Delta\tau$ is the volume element defined by the cubic grid.

We insist that the new state, $\mathbf{c}_0$, must be orthogonal to the previously-determined states $\mathbf{c}_1, \ldots, \mathbf{c}_N$. Our method employs a Lagrangian

$$\mathcal{L} = \tfrac{1}{2}\widetilde{m}_{el}\, \dot{\mathbf{c}}_0 \cdot \dot{\mathbf{c}}_0 + \tfrac{1}{2}\lambda_0\, (\mathbf{c}_0 \cdot \mathbf{c}_0 - 1) + \sum_{i=1}^{N} \lambda_i (\mathbf{c}_i \cdot \mathbf{c}_0) - E[\mathbf{c}_0, \{\vec{\mu}_i\}, \{\vec{R}_i\}]\ , \qquad (6.6)$$

where the λ_i are undetermined multipliers that enforce orthonormality constraints. The parameter $\widetilde{m}_{el}$ is a fictitious electron mass and $E[\mathbf{c}_0, \{\vec{\mu}_i\}, \{\vec{R}_i\}]$ is the energy functional. In principle, one could also propagate the induced dipoles dynamically. Because updating the Hamiltonian is far more expensive than minimizing the energy with respect to the induced dipoles, however, we choose to converge the dipoles each time $\mathbf{c}_0$ is updated.

From the Lagrangian in Eq. (6.6), one obtains the following equations of motion:

$$\widetilde{m}_{el}\, \ddot{\mathbf{c}}_0 = -2\, \mathbf{H}\mathbf{c}_0 + \sum_{i=0}^{N} \lambda_i\, \mathbf{c}_i\ . \qquad (6.7)$$

Here, and in what follows, we use $\mathbf{H}$ to denote the Hamiltonian matrix, and for convenience we omit from our notation the explicit dependence of $\mathbf{H}$ on $\{\vec{\mu}_i\}$ and $\{\vec{R}_I\}$. In deriving Eq. (6.7), we have assumed that all quantities are real-valued.

In the limit that the fictitious kinetic energy goes to zero, minimizing $\mathcal{L}$ with respect to $\mathbf{c}_0$ is equivalent to solving the time-independent Schrödinger equation.

Therefore, if we propagate the electronic degrees of freedom according to Eq. (6.7), and systematically remove kinetic energy, we should eventually find a local minimum where $\partial\mathcal{L}/\partial\mathbf{c}_0 = 0$, although this minimum certainly need not be the global minimum. To remove kinetic energy, we add a velocity-dependent friction term to the equations of motion. Equation (6.7) is thereby modified, affording

$$\widetilde{m}_{el}\,\ddot{\mathbf{c}}_0 = -2\,\mathbf{H}\mathbf{c}_0 + \sum_{i=0}^{N} \lambda_i \mathbf{c}_i - \gamma\,\widetilde{m}_{el}\,\dot{\mathbf{c}}_0\ . \tag{6.8}$$

The friction parameter, γ, has dimensions of reciprocal time. This modified equation of motion is not conservative and does not arise from any Hamiltonian.

We next develop our algorithm for propagating the equations of motion in Eq. (6.8). For this we use a modified form of the velocity Verlet (VV) algorithm,[217] and follow closely the work and the notation of Tuckerman and Parrinello,[218] who developed a VV-type algorithm to integrate the CPMD equations of motion. In the case of no damping ($\gamma = 0$), the appropriate VV equations for our purpose are

$$\mathbf{c}_0(t+\delta t) = \mathbf{c}_0(t) + \delta t\,\dot{\mathbf{c}}_0(t) + \frac{(\delta t)^2}{2\widetilde{m}_{el}}\,\mathbf{f}(t) + \frac{(\delta t)^2}{2\widetilde{m}_{el}} \sum_{i=0}^{N} \lambda_i^{\mathrm{R}}\,\mathbf{c}_i(t) \tag{6.9a}$$

$$\dot{\mathbf{c}}_0(t+\tfrac{1}{2}\delta t) = \dot{\mathbf{c}}_0(t) + \frac{\delta t}{2\widetilde{m}_{el}}\,\mathbf{f}(t) + \frac{\delta t}{2\widetilde{m}_{el}} \sum_{i=0}^{N} \lambda_i^{\mathrm{R}}\,\mathbf{c}_i(t) \tag{6.9b}$$

$$\dot{\mathbf{c}}_0(t+\delta t) = \dot{\mathbf{c}}_0(t+\tfrac{1}{2}\delta t) + \frac{\delta t}{2\widetilde{m}_{el}}\,\mathbf{f}(t+\delta t) + \frac{\delta t}{2\widetilde{m}_{el}} \sum_{i=0}^{N} \lambda_i^{\mathrm{V}}\,\mathbf{c}_i(t+\delta t)\ . \tag{6.9c}$$

Here, δt is the time step and $\mathbf{f}(t) = -2\,\mathbf{H}\,\mathbf{c}_0(t)$ is the force on $\mathbf{c}_0$ at time t. Although we have written all of the vectors $\mathbf{c}_i$ as functions of time (in order to use a common index for $\mathbf{c}_0$ and $\mathbf{c}_i$, which facilitates a compact notation), the vectors $\{\mathbf{c}_i\}_{i=1}^{N}$ are fixed and only $\mathbf{c}_0$ is propagated forward in time. In other words

$$\mathbf{c}_{i\neq 0}(t) = \mathbf{c}_{i\neq 0}(t+\delta t)\ . \tag{6.10}$$

As in the RATTLE method,[219] the undetermined multipliers in Eq. (6.9) are allowed to have two different values, λ_i^{R} and λ_i^{V}, representing coordinate and velocity constraints, respectively. This is similar to the approach used to maintain orthonormality constraints when integrating the CPMD equations of motion.[218]

Upon substituting $\mathbf{f}(t) \rightarrow \mathbf{f}(t) - \gamma\, \widetilde{m}_{el}\, \dot{\mathbf{c}}_0(t)$ in Eq. (6.9), one obtains equations for the case of finite damping. The corresponding VV algorithm can be expressed in three steps. The first step consists of both "coordinate" ($\widetilde{\mathbf{c}}_0$) and half-step "velocity" ($\dot{\widetilde{\mathbf{c}}}_0$) updates:

$$\widetilde{\mathbf{c}}_0(t+\delta t) = \mathbf{c}_0(t) + \delta t\left(1-\tfrac{1}{2}\gamma\delta t\right)\dot{\mathbf{c}}_0(t) + \frac{(\delta t)^2}{2\widetilde{m}_{el}}\mathbf{f}(t) \tag{6.11a}$$

$$\dot{\widetilde{\mathbf{c}}}_0(t+\tfrac{1}{2}\delta t) = \left(1-\tfrac{1}{2}\gamma\,\delta t\right)\dot{\mathbf{c}}_0(t) + \frac{\delta t}{2\widetilde{m}_{el}}\,\mathbf{f}(t)\ . \tag{6.11b}$$

The second step consists of corrections,

$$\mathbf{c}_0(t+\delta t) = \widetilde{\mathbf{c}}_0(t+\delta t) + \sum_{i=0}^{N} X_i\,\mathbf{c}_i(t) \tag{6.12a}$$

$$\dot{\mathbf{c}}_0(t+\tfrac{1}{2}\delta t) = \dot{\widetilde{\mathbf{c}}}_0(t+\tfrac{1}{2}\delta t) + \sum_{i=0}^{N} \frac{X_i}{\delta t}\,\mathbf{c}_i(t)\ , \tag{6.12b}$$

where the intermediate quantities X_i are defined below. The final step is an update and a correction:

$$\dot{\widetilde{\mathbf{c}}}_0(t+\delta t) = \left(1+\tfrac{1}{2}\gamma\delta t\right)^{-1}\left[\dot{\mathbf{c}}_0(t+\tfrac{1}{2}\delta t) + \frac{\delta t}{2\widetilde{m}_{el}}\,\mathbf{f}(t+\delta t)\right] \tag{6.13a}$$

$$\dot{\mathbf{c}}_0(t+\delta t) = \dot{\widetilde{\mathbf{c}}}_0(t+\delta t) + \sum_{i=0}^{N} Y_i\,\mathbf{c}_i(t+\delta t)\ . \tag{6.13b}$$

Equations (6.12) and (6.13) employ the intermediate quantities

$$X_i = \frac{(\delta t)^2}{2\widetilde{m}_{el}}\,\lambda_i^{\mathrm{R}} \tag{6.14}$$

and

$$Y_i = \frac{\delta t}{2\widetilde{m}_{el}}\left(1+\tfrac{1}{2}\gamma\delta t\right)^{-1}\lambda_i^{\mathrm{V}}\ . \tag{6.15}$$

The values of X_i and Y_i are chosen to satisfy the constraint equations

$$\mathbf{c}_0 \cdot \mathbf{c}_0 = 1 \tag{6.16a}$$

$$\mathbf{c}_0 \cdot \mathbf{c}_{i\neq 0} = 0\ . \tag{6.16b}$$

We start by substituting the first update of the second step of the algorithm, Eq. (6.12a), into these constraint equations. The result of this exercise is the following pair of equations:

$$1 = X_0^2 + 2X_0\big[\mathbf{c}_0(t)\cdot\widetilde{\mathbf{c}}_0(t+\delta t)\big] + \big[\widetilde{\mathbf{c}}_0(t+\delta t)\cdot\widetilde{\mathbf{c}}_0(t+\delta t)\big] - \sum_{i=1}^{N} X_i^2 \tag{6.17a}$$

$$X_{i\neq 0} = -\widetilde{\mathbf{c}}_0(t+\delta t)\cdot\mathbf{c}_i\ . \tag{6.17b}$$

Equation (6.17b) can be solved for X_i, for each $i > 0$, and then Eq. (6.17a) affords X_0. To obtain Y_i, we first obtain velocity constraints by differentiating Eq. (6.16) with respect to t, and then substitute the final velocity update, Eq. (6.13), into these velocity constraints. The result is

$$Y_i = -\dot{\widetilde{\mathbf{c}}}_0(t+\delta t)\cdot\mathbf{c}_i(t+\delta t)\ . \tag{6.18}$$

In deriving Eq. (6.17), we have assumed that the constraints are satisfied at time t, and in obtaining Eq. (6.18) we have assumed that the position constraints [Eq. (6.16)] are satisfied at time $t+\delta t$. In practice, this means that the dynamics *cannot* start from a vector $\mathbf{c}_0$ that does not satisfy the constraints in Eq. (6.16). At the beginning of the annealing procedure for a particular state, the guess vector must be orthogonalized against all previously-obtained vectors.

6.3 Computational Details

We compute the optical absorption spectrum of the bulk hydrated electron under periodic boundary conditions, using Ewald summation for the long-range interactions.[184] Two hundred geometries were taken from a ground-state MD run in a periodic box that is 26.2015 Å on a side and contains 600 water molecules, corresponding to a density of 0.997 g/cm^3. We solve the Schrödinger equation on a grid with a spacing of 0.93 Å, for a total of $28^3 = 21952$ grid points. Details of the simulation protocol can be found in Ref. [184].

The zeroth-order states are obtained with the Davidson-Liu method,[109] using a convergence threshold $||(\hat{H} - E)\psi|| < 10^{-8}\ E_h$ as described in Ref. [3]. We use these zeroth-order states to generate a guess for the induced dipoles, $\{\vec{\mu}_i\}$, which we use to construct a Hamiltonian matrix. We then "anneal" the state of interest, subject to the constraint that it remain normalized and orthogonal to the previously-determined states, as described above. Prior to initiation of the MD procedure, we orthogonalize the state of interest against all previous states, using the Gram-Schmidt procedure, so that the constraints are satisfied initially. The initial velocities ($\dot{\mathbf{c}}_0$) are taken to be zero. The electronic degrees of freedom quickly pick up kinetic energy since the guess vector is rarely near a minimum. Annealing proceeds until the change in energy between successive MD steps is less than 10^{-8} E_h. (By that point, the total electronic kinetic energy is also $\sim 10^{-8}$ E_h.) At this point we have an updated wave function that we use to induce new dipoles. This procedure is repeated until the energy change between successive dipole updates is less than 10^{-8} E_h.

In a typical CPMD calculation, one has to choose the fictitious electron mass and time step in such a way that the electronic degrees of freedom are adiabatically decoupled from the nuclear dynamics. (See Refs. [220–222] for an interesting discussion in the context of extended-Lagrangian MD.) This is not an issue here, as we are not propagating the nuclei; rather, we are trying to *find* the Born-Oppenheimer surface, not propagate dynamics along or near it. For this reason, we simply choose a time step and electronic mass such that the annealing is stable. We use $\delta t = 0.1$ fs and $\widetilde{m}_{el} = 400$ a.u., but we have not attempted to optimized these parameters. (We do find that for $\delta t = 0.1$ fs, masses less than 200 a.u. lead to a failure to maintain the constraints.) In our calculations, the position and velocity constraints are typically satisfied to an average absolute error of 10^{-14} and 10^{-16} a.u., respectively.

The friction parameter, γ, is chosen according to the recommendation in Ref. [223], which is based on a three-point fit using energies from successive steepest-decent steps. Since the initial wave function guess may be far from the minimum we found it helpful to generate γ several times during the MD routine; we do this every 50 time steps. We find that the annealing typically converges after 20–300 time steps if the guess is reasonable. However, in cases where the guess is poor, it may take upwards of 2000 steps. The Hamiltonian is not updated during this procedure so the annealing steps are quite inexpensive compared to inducing new dipoles and updating the potential energy at each grid point.

Below, we will compare the e_{aq}^{-} spectrum obtained from the annealing procedure to that calculated using the perturbative scheme that was described in Section 6.2. In the latter scheme, we do not allow the perturbed wave function to mix with the ground state, so that each perturbed state remains orthogonal to the ground state, even though the excited-state wave functions are not mutually orthogonal. (This at least ensures that the transition dipoles are translationally invariant.) An electronic spectrum is constructed from a histogram of oscillator strengths,

$$f_{0\to n} = \frac{2m_e}{3\hbar^2}\left(E_n - E_0\right)\sum_{\kappa\in\{x,y,z\}}\left|\langle\psi_0|\,\hat{\kappa}\,|\psi_n\rangle\right|^2. \qquad (6.19)$$

Wave functions were visualized with the Visual Molecular Dynamics program[118] and isocontour values were generated with OpenCubMan.[224] Calculations were performed with a simulation code that is described in Refs. [184] and [3].

6.4 Results

6.4.1 Benchmark tests using fixed dipoles

Prior to applying our procedure to determine the fully-relaxed excited states of the aqueous electron, we would first like to demonstrate the method's effectiveness in the case that the induced dipoles are not updated. That is, we will first verify that the annealing procedure reproduces the lowest few eigenstates of a Hamiltonian where the induced dipoles are converged to the ground-state wave function (only), in which

	Davidson-Liu diagonalization		Electronic annealing	
n	$E_n - E_0$	$f_{0\to n}$	$E_n - E_0$	$f_{0\to n}$
1	2.13004	0.294897	2.13009	0.294889
2	2.22616	0.306758	2.22618	0.306793
3	2.45889	0.271951	2.45890	0.272044
4	2.89899	0.002009	2.89901	0.001878
5	3.35058	0.007256	3.35084	0.007513
6	3.36738	0.001328	3.36724	0.001038
7	3.42538	0.000995	3.42542	0.001048
8	3.47247	0.010379	3.47247	0.010336
9	3.57655	0.000950	3.57662	0.000979
10	3.62341	0.006859	3.62349	0.006142

Table 6.1: Excitation energies (in eV) and oscillator strengths, in the absence of dipole relaxation, computed using two different algorithms.

case there is no orthogonality problem. For this test, we first determine the ground state wave function and induced dipoles with our standard method,[3, 184] then solve for the lowest 30 eigenstates of $\hat{H}$ with fixed dipoles. Next, we take a set of vectors composed of random numbers and use these as initial guess vectors for the annealing algorithm, fixing the induced dipoles at the values previously determined for the ground-state wave function.

Table 6.1 shows that the annealing procedure reproduces—with high accuracy—both the excitation energies and the oscillator strengths that are obtained by a straightforward Davidson-Liu procedure. In this particular case, where the dipoles are fixed, the states emerge from the annealing procedure in ascending order of energy, indicating that the procedure does not become trapped in any local minima and most likely locates *global* minima of the constrained optimization problem. (Of course, there is no guarantee that this will be the case once we allow the dipoles to relax.) Using the convergence thresholds specified in Section 6.3, we can reproduce excitation energies to within $\sim 10^{-4}$ eV, which is far smaller than the error intrinsic to the pseudopotential model. Due to the completely random nature of the initial guesses, the annealing procedure takes $\sim$1500 steps to converge in this example.

Because the annealing procedure employs a larger number of constraints for higher-energy states as compared to lower-energy states, one might question whether the accuracy of the computed energies degrades as one marches up the manifold of states, adding more and more constraints as the calculation proceeds. The data in Table 6.1 suggest that this is not the case. For example, the $n = 8$ excitation energy computed by means of the annealing algorithm is closer to the Davidson-Liu result than is the $n = 1$ excitation energy. The accuracy is not degraded because the annealing algorithm does not introduce any *new* constraints beyond those imposed by linear algebra. For a fixed set of dipoles, the exact (non-degenerate) eigenvectors of the Hamiltonian are necessarily orthogonal, and obtaining them via diagonalization or via Davidson's procedure is equivalent to minimizing the Rayleigh-Ritz quotient

$$R[\psi] = \frac{\langle\psi|\hat{H}|\psi\rangle}{\langle\psi|\psi\rangle} \ , \tag{6.20}$$

subject to the constraint that $|\psi_n\rangle$ must be orthogonal to all lower-lying states, $|\psi_0\rangle, \ldots, |\psi_{n-1}\rangle$. Our annealing algorithm simply provides an alternative means to enforce these constraints, and to carry out the Rayleigh-Ritz variational procedure in a robust way.

Unlike this benchmark test involving fixed dipoles, the “right” answer is no longer well-defined once we let the MM dipoles relax. However, the very close agreement between the annealing results and the Davidson-Liu results in this test gives us confidence that our approach is a reasonable one, if one insists (as we do here) that the relaxed wave functions should be orthogonal to one another.

The excited states need not emerge in energetic order once we allow the induced dipoles to relax. They would do so only if the annealing procedure managed to find the global minimum of the effective potential (with constraints) on each annealing cycle. The presence of inducible dipoles appears to make this quite challenging, as the states do not come out of the calculations in ascending order. This gives us some pause, and calls into question the nature of our guess. We have run additional calculations in which the guess for the annealing procedure is provided by the first-order corrected wave function from the perturbative scheme. Inspection of the energies and oscillator strengths indicate that typically, the first four states are identical and emerge in the same order for either initial guess. Table 6.2 shows a typical case. The first four excitation energies are nearly identical for either initial guess, and emerge in the same order, but the ordering is different starting with $n = 5$. However, both initial guesses do find the same set of excitation energies through at least $n = 11$.

The fact that the states do not come out energetically ordered is worrisome because the constraints placed on a particular state depend upon the order in which it is determined and this should effect the energy. In the latter columns of Table 6.2 we

	ordered by n[a]				ordered by energy[b]				difference[c]	
	Zeroth-order guess		First-order guess		Zeroth-order guess		First-order guess			
n	$E_n - E_0$	$f_{0\to n}$	$E_n - E_0$	$f_{0\to n}$	$E_n - E_0$	$f_{0\to n}$	$E_n - E_0$	$f_{0\to n}$	$E_n - E_0$	$f_{0\to n}$
1	1.73894	0.133993	1.73894	0.133927	1.73894	0.133993	1.73894	0.133927	0.00000	0.000066
2	1.95139	0.237197	1.95140	0.237188	1.93676	0.028331	1.93668	0.028360	0.00008	0.000029
3	1.93676	0.028331	1.93668	0.028360	1.95139	0.237197	1.95140	0.237188	0.00001	0.000029
4	2.10816	0.132911	2.10817	0.132922	2.10816	0.132911	2.10817	0.132922	0.00001	0.000011
5	2.11486	0.001157	2.28370	0.001407	2.11486	0.001157	2.11521	0.001104	0.00035	0.000053
6	2.28397	0.001359	2.11521	0.001104	2.15224	0.000537	2.14726	0.000641	0.00498	0.000104
7	2.46492	0.001676	2.26762	0.004268	2.26925	0.004114	2.26762	0.004268	0.00163	0.000154
8	2.26925	0.004114	2.14726	0.000641	2.28397	0.001359	2.28370	0.001407	0.00027	0.000048
9	2.42928	0.001936	2.43138	0.001780	2.36290	0.003176	2.36278	0.003178	0.00012	0.000002
10	2.15224	0.000537	2.36278	0.003178	2.42928	0.001936	2.43138	0.001780	0.00210	0.000156
11	2.36290	0.003176	2.46681	0.001478	2.46492	0.001676	2.46681	0.001478	0.00189	0.000198

[a] Excitation energies listed in the order that the states are generated by the annealing procedure

[b] Excitation energies listed in ascending order of energy

[c] Difference in energies and oscillator strengths for the energy-ordered states computed using two different initial guesses

Table 6.2: Excitation energies (in eV) and oscillator strengths computed by electronic annealing, using two different initial guesses.

have re-ordered the states energetically, and we have tabulated the differences in excitation energies and oscillator strengths between the two different initial guesses. The largest discrepancy in the energies between the two initial guesses is only 0.005 eV. This is smaller than the typical energy gap between states, and we therefore find this to be a tolerable error. In principle, one could probably ensure energetic ordering by annealing the same state several times, starting from a variety of different guesses, and taking the lowest energy result in an attempt to find the global minimum for each set of constraints. Another possibility would be to perform the annealing, re-order the states energetically, and repeat the entire procedure using the annealed states as guesses. We have not done so here, owing to the smallness of the discrepancies between energies obtained using different initial guesses.

6.4.2 Aqueous electron absorption spectrum

Figure 6.1(a) compares the absorption spectrum obtained using perturbative techniques[184] to that obtained using the annealing algorithm that is described here. The experimental spectrum (reproduced from the line shape parameters in Ref. [2]) is also shown. With the exception of the annealed spectrum, which is new, these spectra have been described in detail in our previous work,[43, 160, 184] but for completeness we briefly summarize these results here. At zeroth-order in the perturbation, the peak intensity is blue-shifted relative to experiment, and although this zeroth-order spectrum does reproduce the main, Gaussian feature in the experimental spectrum, it exhibits a gap in intensity just below 3 eV, which is followed by a "hump" centered around 3.5 eV that is essentially a photo-electron spectrum. The first-order correction for $\hat{W}_n$ shifts the maxima into quantitative agreement with experiment and also binds states that were (vertically) unbound at zeroth order, meaning that the excitation energies were greater than the vertical detachment energy. A second-order treatment of $\hat{W}_n$ affords a correction to the wave function and hence the transition dipoles, and this has the effect of increasing intensity in the "blue tail".

The spectrum obtained from electronic annealing agrees quantitatively with the second-order perturbation theory spectrum in the Gaussian region, but the annealing procedure shifts even more oscillator strength into the higher-lying bound states that comprise the blue tail. (All of the spectra in Fig. 6.1 are normalized to unit intensity at their respective absorption maxima.) If anything, the blue tail in the annealed spectrum is in better agreement with experiment than is the second-order perturbation theory result.

Figure 6.1(b) decomposes the annealed spectrum into contributions from $1s \rightarrow 1p$ transitions versus excitations into higher-lying bound states. The $1p$ states are the only bright states, for an aqueous electron modeled as a particle in a spherical box,[43] and indeed the $1s \rightarrow 1p$ excitations carry much of the oscillator strength in the annealed spectrum. However, the $1p$ band has significant energetic overlap with the higher-lying bound states, which borrow intensity from the $1p$ states and give rise to a significant "blue tail". The states that comprise this tail are unbound in the zeroth-order treatment, and we have previously referred to them as "quasi-continuum, polarization-bound" excited states.[160] These states have very little oscillator strength at zeroth order, but relaxation of the solvent dipoles allows them to

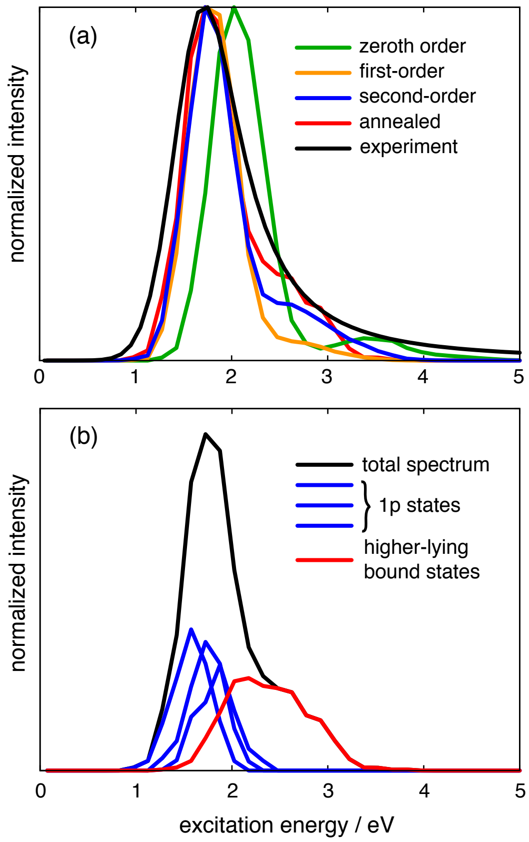

Figure 6.1: Absorption spectra for e_{aq}^{-} in bulk water: (a) comparison of spectra computed using zeroth-, first-, and second-order perturbative treatments of the $\hat{W}_n$ [Eq. (6.4)] to the spectrum computed using the annealing procedure proposed here; (b) decomposition of the annealed spectrum into contributions from various types of excited states.

mix with (and borrow intensity from) the $1p$ states. For the annealed spectrum, all 30 states that we calculate are vertically bound. (The average vertical binding energy for the simulation cell used in this work is 3.35 eV,[184] well into the blue tail in the spectra shown in Fig. 6.1.)

At zeroth-order in $\hat{W}_n$ (what we have previously called the "unrelaxed" approximation[43, 160, 184]), the states are ordered as follows. The ground state is spherical ($1s$) and resides in a roughly spherical solvent cavity, while the first three excited states are p-like ($1p$). The fourth excited state is typically more diffuse and can be identified as the $2s$ state by virtue of a radial node. Above the $2s$ state are several states that resemble $1d$ states, but above this it becomes difficult to assign particle-in-a-cavity quantum numbers to the excited states, whose wave functions are quite diffuse and contain many different lobes. The qualitative nature of these states is not altered significantly by application of second-order perturbation theory.

The annealing procedure, on the other hand, sometimes *does* alter the initial guess wave functions in a qualitative way. In particular, the annealing procedure appears to have the ability to localize diffuse electronic states composed of largely disjoint lobes, and in some cases may enhance the oscillator strength associated with these states, relative to the nominal bright states. In cases where we observe such localization, the nodal character of the state appears to be preserved, although this is only evident if the wave function is plotted using an isosurface that encapsulates nearly all of the electron density.

As an example, Fig. 6.2 depicts the unrelaxed $n = 2$ and $n = 4$ wave functions

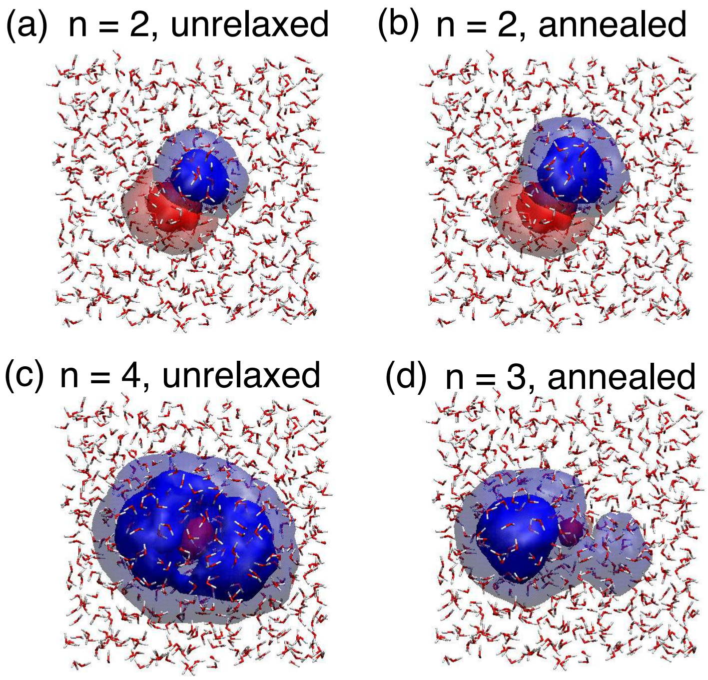

Figure 6.2: Examples of $1p$- and $2s$-like excited states of the aqueous electron. Panels (a) and (c) depict the "unrelaxed" states (zeroth order in $\hat{W}_n$), while panels (b) and (d) depict the wave functions that are obtained by electronic annealing. The opaque and translucent isosurfaces encapsulate 70% and 95% of $|\psi|^2$, respectively.

from the calculation reported in Table 6.1, as well as the corresponding annealed wave functions from the calculation reported in Table 6.2. (The states are labeled in the order that they are calculated by the annealing procedure, which need not be in energetic order.) The unrelaxed $1p$ state shown in Fig. 6.2(a) is not altered by the annealing process in any substantive way and is nearly identical to the $n = 2$ state in the manifold of annealed excited states [Fig. 6.2(b)]. However, the annealed analogue [Fig. 6.2(d)] of the $n = 4$ zeroth order wave function [Fig. 6.2(c)] is more localized than its counterpart. The annealed function appears p-like rather than s-like, if a large isosurface contour value is used to plot the wave function. However, a smaller contour that encapsulates more of the wave function reveals s-like character. The transition from the unrelaxed to the annealed wave function [*i.e.*, Fig. 6.2(c) → Fig. 6.2(d)] enhances the transition dipole, $f_{0\to n}$, of the state in question, because the localized, annealed state has better overlap with the ground state and furthermore sheds some of the pseudo-s-type symmetry that causes the unrelaxed state in Fig. 6.2(c) to exhibit a rather small oscillator strength.

Comparison of Tables 6.1 and 6.2 seems to indicate that the $n = 3$ state loses significant oscillator strength upon annealing, but an inspection of the wave functions reveals that the state that emerges as $n = 3$ from the annealing procedure actually corresponds to the *fourth* excited state at zeroth-order. The latter acquires significant oscillator strength upon annealing, and drops below a state with p-type character to become $n = 3$. While this sort of re-ordering does not occur in the majority of the cases, it is also not entirely uncommon.

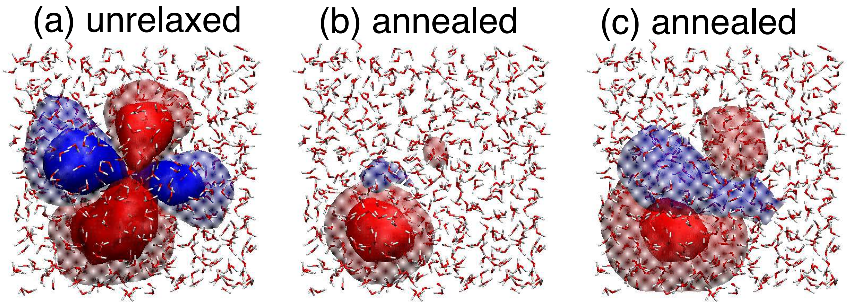

Figure 6.3: An excited electronic state of the aqueous electron with d-type character. Panels (a) and (b) depict the zeroth-order (unrelaxed) and annealed wave functions, respectively, using opaque and translucent isosurfaces that encapsulate 70% and 95% of $|\psi|^2$, respectively. Panel (c) depicts the same annealed wave function as in (b), but plotted using isosurfaces that encapsulate 70% and 99% of $|\psi|^2$.

From the spectrum in Fig. 6.1(b), it appears that the highest-lying $1p$ state carries somewhat less intensity than the two lower-lying $1p$ states. This is partly an artifact of the manner in which we analyzed the data, namely, we assumed in constructing Fig. 6.1(b) that the first three states are the $1p$ states, which is always true in the perturbative approach but is occasionally *not* true following annealing. Despite this occasional re-ordering of states, the $1p$ states still carry the vast majority of the oscillator strength and are still responsible for the Gaussian feature in the absorption spectrum.

Figure 6.3 shows the zeroth-order and the annealed wave functions for a d-type state. Using an isosurface that encapsulates 90% of $|\psi|^2$ [Fig. 6.3(b)], it appears as though the annealed state is effectively a "charge hop", in which the electron is transferred a sizable distance away from the cavity in which the ground-state wave function is localized. However, Fig. 6.3(c) depicts the same annealed wave function, plotted using an isosurface that encapsulates 99% of $|\psi|^2$. In the latter depiction, it is clear that the wave function remains d-like but the electron has largely localized into one of the lobes. In this example, the annealed state has very little overlap with the ground state, which results in a very small transition dipole. States that have localized to such an extent as to exhibit charge-transfer or charge-hopping character exibit very small oscillator strengths, and thus do not contribute greatly to the absorption spectrum. These states are most likely not accessed in experiments that probe vertically excited states. The "blue tail" does not arise from localized charge-hopping states such as that shown in Figs. 6.3(b) and 6.3(c). Rather, it arises due to higher-lying, diffuse excited states that do have reasonable overlaps with the ground-state wave function.[160, 184]

6.5 Discussion

According to the Thomas-Reiche-Kuhn (TRK) sum rule,[225]

$$\sum_{n>0} f_{0\to n} = N_e \tag{6.21}$$

where N_e is the number of electrons. By construction, $N_e = 1$ in our pseudopotential model. In previous work,[184] we observed that $f_{0\to 1} + f_{0\to 2} + \cdots + f_{0\to 29} \approx 0.95$ at zeroth-order, that is, the first 29 excited states account for 95% of the total oscillator strength. A first-order correction for $\hat{W}_n$ reduces the electronic energy gaps ($E_n - E_0$) but does not affect the wave functions, and as a result, the total oscillator strength carried by the first 29 excited states is reduced to ≈ 0.8. At second order, the wave function *is* corrected, and the total oscillator strength recovers, to ≈ 0.9. In the present treatment, however, we find that $f_{0\to 1} + \cdots + f_{0\to 29} \approx 0.65$.

The question then arises as to whether the TRK sum rule is preserved in the case of a state-dependent Hamiltonian and whether or not the expression for $f_{0\to n}$ in Eq. (6.19) is even valid in such a case. Here, we address these questions in the context of the proposed annealing procedure.

In principle, the annealing procedure provides a way to obtain an infinite number of mutually orthogonal states, each of which is an eigenfunction of a different Hamiltonian. For the purpose of analyzing the sum rule in Eq. (6.21), let us make the (perhaps dubious) assumption that this set of eigenfunctions forms a complete orthonormal basis. Then to derive Eq. (6.21), one employs the identity

$$[\hat{H}, \hat{x}] = -\frac{i\hbar}{m}\,\hat{p}_x \; . \tag{6.22}$$

In principle, $\hat{H}$ could be any of the aforementioned Hamiltonians. Inserting Eq. (6.22) into the expression

$$\frac{1}{i\hbar}\big\langle 0\big|[\hat{x}, \hat{p}_x]\big|0\big\rangle = 1 \tag{6.23}$$

and using a resolution of the identity, one obtains

$$\frac{m}{\hbar^2}\sum_n \Big[\langle 0|\hat{x}|n\rangle\langle n|[\hat{H},\hat{x}]|0\rangle - \langle 0|[\hat{H},\hat{x}]|n\rangle\langle n|\hat{x}|0\rangle\Big] = 1 \; . \tag{6.24}$$

This equation is valid for any Hamiltonian and any complete orthonormal basis. However, in order to obtain the sum rule in Eq. (6.21) from Eq. (6.24), the basis states $|n\rangle$ must in addition be eigenstates of the *same* Hamiltonian. In the present case, however, each state is a solution to a different Hamiltonian so the sum rule is not preserved by the annealing procedure. (As such, nothing rests upon our dubious assumption that the states $|n\rangle$ form a complete basis; the sum rule is not preserved, whether or not this is in fact the case.)

Next, we address the question of whether or not Eq. (6.19) is a valid formula for computing absorption intensities. In what follows, we assume that the nuclei are clamped, and we consider the electronic dynamics. The oscillator strength formula in Eq. (6.19) follows from time-dependent perturbation theory.[225] If the system is in state $|n\rangle$ at time $t = 0$, then it seems reasonable that the system evolves under the influence of the Hamiltonian for state $|n\rangle$, $\hat{H}_n$. That is,

$$|\Psi(t)\rangle = e^{-i\hat{H}_n t/\hbar}|n\rangle = e^{-iE_n t/\hbar}|n\rangle \ , \tag{6.25}$$

where we have used the fact that $\hat{H}_n|n\rangle = E_n|n\rangle$.

We now investigate the time evolution in the presence of a time-dependent perturbation. We assume that the time-dependent wave function can be written

$$|\Psi(t)\rangle = \sum_n c_n(t)\ e^{-iE_n t/\hbar}|n\rangle \ . \tag{6.26}$$

This expansion may seem suspicious in light of questions regarding whether the basis $\{|n\rangle\}$ is complete. However, we assume below that the system is initially in the ground state, and we are only interested in the dynamics within the finite subset of states that we have determined by means of annealing. In other words, this basis constitutes the region of interest in Hilbert space. To derive a formula for the transition probabilities, the *ansatz* in Eq. (6.26) should next be inserted into the time-dependent Schrödinger equation, but with which Hamiltonian? In the weak-field limit, the traditional assumption is that the system occupies the ground state at $t = 0$, $c_n(0) = \delta_{n,0}$. It therefore seems reasonable to assume that the dynamics is governed by the ground-state Hamiltonian, so that

$$i\hbar\,|\dot{\Psi}(t)\rangle = \left(\hat{H}_0 + V(t)\right)|\Psi(t)\rangle\ . \tag{6.27}$$

These assumptions, together with the fact that the basis is orthonormal, leads to the textbook[225] dynamical equations for the expansion coefficients $c_n(t)$. For this reason, we would argue that Eq. (6.19) is still valid, even though the TRK sum rule is not.

The ambiguity regarding which Hamiltonian guides the dynamics of the system is clearly an artifact of the model. The inducible dipoles represent electronic degrees of freedom and should respond on the time scale of electronic motion, *i.e.*, these degrees of freedom participate in the short-time dynamics that results in absorption of radiation, and they ought to be included in the quantum-mechanical description of the system. Our decision to treat some of the electronic variables (solvent dipoles) classically leads to some ambiguity (multiple Hamiltonians) since we do not have information regarding the short-time quantum dynamics of these variables. This is to be contrasted with the MOM-SCF technique[212, 213] that was mentioned in Section 6.1. In that method, there is a single Hamiltonian but multiple stationary points (solutions to the SCF equations). Since the SCF energy, at least in Hartree-Fock theory, is the expectation value of the true Hamiltonian, there is no ambiguity as to the quantum dynamics.

In the case of the methodology pursued here, one way around these difficulties would be to use a linear-response formalism, which has been explored in the context of time-dependent density functional theory (TD-DFT) in the presence of a polarizable medium.[226, 227] Here, however, we were interested in a self-consistent, non-perturbative approach. In the future, it might be interesting to compare results obtained from linear-response theory to those obtained from our electronic annealing procedure.

Finally, we would like to speculate that this annealing procedure might be useful for MOM-SCF calculations. The MOM-SCF method appears quite promising, and avoids some problems associated with TD-DFT. However, the excited-state wave functions obtained in MOM-SCF calculations are not orthogonal, although preliminary results do not seem to exhibit any adverse effects on oscillator strengths, possibly because the deviations from orthogonality are small in cases examined so far.[212] In any case, it is possible that the sort of electronic annealing that is introduced here could eliminate any concern over oscillator strengths. This technique might also be useful in the context of excited-state Kohn-Sham simulations,[228] non-adiabatic (surface hopping) simulations utilizing CPMD,[229] or "constrained" DFT calculations,[230, 231] each of which is potentially subject to nonorthogonality problems. Extensions to many-electron QM/MM methods using polarizable force fields are also worth exploring.

6.6 Summary

We have introduced a novel "electronic annealing" procedure that is capable of finding orthogonal solutions to a state-dependent Hamiltonian. This procedure appears to be robust and is capable of finding many such solutions. When applied to a polarizable QM/MM model of the aqueous electron in bulk water,[184] the electronic absorption spectrum computed by means of electronic annealing is in reasonable agreement with results obtained previously[160, 184] based on a perturbative treatment of the MM polarization response following excitation of the QM region. In fact, the annealed spectrum is in slightly better agreement with experiment, as compared to perturbative results. In any case, these computed spectra all support the hypothesis that electronic polarization (as described theoretically via atom-centered inducible dipoles) binds additional excited states of the aqueous electron and facilitates intensity borrowing from the $1p$ states that carry most of the oscillator strength. The "blue tail" in the optical spectrum of e^-_{aq} arises from what we have termed "polarization-bound quasi-continuum states".[160] Here, we find that electronic re-organization of the solvent can also cause diffuse excited states of the electron to localize into "charge-hopping" states. These excitations, however, carry very little oscillator strength and do not make a substantial contribution to the optical absorption spectrum.

In the future, we plan to explore generalizations of this electronic annealing algorithm that are suitable for many-electron QM calculations.

CHAPTER 7

An efficient, fragment-based electronic structure method for molecular systems: Self-consistent polarization with perturbative two-body exchange and dispersion [7.1]

7.1 Introduction

It is well-established that wavefunction-based quantum chemistry using Gaussian basis sets can provide accurate ground-state properties for molecular systems. Application of these same robust methods to condensed-phase systems—be they periodic (crystalline solids) or non-periodic (liquids or amorphous solids)—represents a tremendous challenge, given that the cost of wavefunction methods scales incredibly poorly with system size. In fact, such methods scale *unphysically* with system size,[46] as a result of the use of delocalized molecular orbitals, and the distance dependence of different intermolecular interactions *must* be exploited if we are to apply these methods to condensed phases.[47] From this point of view, Gaussian basis sets possess an inherent advantage over plane-wave basis sets, in that the basis functions are highly localized and the length scale between different basis functions can be assigned

---

[7.1] This chapter appeared as an article in the *Journal of Chemical Physics* in 2011, volume 134, page 94118 in a straightforward way.[232] At present, however, most condensed-phase electronic structure calculations are performed using delocalized plane-wave basis sets, which is appealing for periodic systems because the basis functions are periodic, but may be less advantageous for non-periodic systems. Moreover, despite many advances in the development of "linear scaling" electronic structure methods,[233, 234] routine application of wavefunction-based quantum chemistry remains limited to systems no larger than $\sim$100 atoms.[235]

In the past decade, a variety of fragment-based methods have been introduced, whose goal is to reduce the cost of quantum chemistry calculations in large systems. Such techniques include methods based upon a many-body expansion of the supersystem energy,[51–56, 236] the most sophisticated of which is the "fragment molecular orbital" (FMO) method;[237–239] divide-and-conquer approaches;[240] the "self-consistent field for molecular interactions" (SCF-MI) technique;[48, 49] the "natural linear scaling" coupled-cluster approach;[241, 242] the effective fragment potential (EFP) method;[243–245] and the "explicit polarization" (XPol) method.[57–59, 246] A complete discussion of the strengths and weaknesses of each of these methods is beyond the scope of the present article. Here, it suffices to note that each one—save for EFP, which is an automated way to parameterize polarizable force fields using *ab initio* calculations—requires iterative construction of Fock matrices for dimers of fragments, or sometimes the supersystem itself, or else requires additional, empirical parameters. The present article reports a method that avoids these requirements.

For maximum versatility, a fragment-based quantum chemistry method should allow for the possibility of fragmenting the system across covalent bonds, and several of the aforementioned methods do facilitate this possibility.[58, 247–249] In the present work, however, we exclude fragmentation across covalent bonds, with the aim of developing an accurate and efficient method for molecular clusters, liquids, and solids that are composed of relatively small monomers, each of which constitutes one fragment.

To construct a low-scaling quantum chemistry method, one can imagine at least two (rather disparate) strategies. One strategy is to make well-defined approximations to an existing *ab initio* method, then examine the extent to which the approximate method is faithful to the original one. Examples of this approach include local correlation methods,[233, 250–257] dual basis procedures,[258, 259] and density fitting or resolution-of-identity techniques.[260–264] Alternatively, one might construct a method that is promising in its efficiency, and is based upon either well-defined approximations or else some observations about the physical nature of interactions. The latter approach, which is the one pursued here, does not seek to reproduce or approximate the energetics of any existing quantum chemistry method.

The method that we propose herein was motivated in part by the electrostatically-embedded, many-body expansion method introduced recently by Dahlke and Truhlar.[51–54] In a simple many-body expansion, the energy of N interacting molecules is decomposed into a sum of one-body terms, two-body terms, etc.: $V = V_1 + V_2 + V_3 + \cdots$. For example, V_2 is the sum of the energies of all $N(N-1)/2$ dimers, minus the sum of the N monomer energies to avoid double-counting. Application to water clusters at the level of second-order Møller-Plesset perturbation theory (MP2) demonstrates that four-body terms must be retained in order to obtain accurate results.[265, 266] However, Dahlke *et al.*[51–54] demonstrated that convergence of the many-body expansion is greatly accelerated if low-order n-body calculations are computed in the presence of a set of point charges that approximate the electrostatic potential due to the other monomers. The best results, as compared to supersystem MP2, were obtained using a supersystem Hartree-Fock (HF) calculation followed by a two-body expansion of the MP2 correlation energy.[52, 53] Alternatively, accurate results for hydrogen-bonded clusters have been obtained by computing V_1 and V_2 at the MP2 level while using a polarizable force field to evaluate V_3 and V_4, without the need to perform a supersystem HF calculation.[55, 56, 236]

We glean two important conclusions from these observations. First, it is crucial to include the electrostatic effects of the environment in the one-body (monomer) calculations. Second, although polarization (induction) is an inherently many-body phenomenon, intermolecular electron correlation is largely a two-body effect. These observations suggest that if one can efficiently incorporate many-body induction in a fragment-based scheme, then it may be possible to approximate intermolecular electron correlation in a pairwise fashion, without resorting to supersystem calculations or high-order terms in the many-body expansion.

To accomplish this, we will use the XPol method of Xie *et al.*[59] to perform electrostatically-embedded one-body calculations in a variational, self-consistent manner. The XPol method, which is detailed in Section 7.2, involves solving single-fragment SCF equations in the presence of point charges that represent the electrostatic potential due to the other fragments. These point charges are derived from the fragment wavefunctions, but unlike both the FMO method[267, 268] and the electrostatic embedding method of Dahlke and Truhlar,[51–54] variation of the point charges is included (exactly) within the single-fragment Fock matrices. Operationally, the method is a "dual SCF" procedure, with an outer loop over fragments and an inner loop to solve the single-fragment Roothaan equations. As such, the XPol method incorporates many-body induction (albeit in an approximate way), but ignores electron exchange between fragments. The original XPol method developed by Xie *et al.*[57–59, 246] accounts for dispersion and exchange-repulsion interactions using empirical parameters Lennard-Jones potentials. Our goal is to replace these empirical corrections with *ab initio*, post-XPol corrections based on a two-body form of symmetry-adapted perturbation theory (SAPT).[20, 269]

Traditionally, SAPT has been used as a benchmark method for computing dimer binding energies and for decomposing intermolecular interactions into induction, exchange-repulsion, dispersion, and other components.[20, 269] SAPT calculations can be quite expensive, although reduced-cost variants based on density functional theory (DFT) have recently shown great promise.[270–275] Here, we use the variant known as SAPT(0), which employs HF orbitals for the monomers and does not include monomer electron correlation. We also explore SAPT(KS),[270] which is analogous to SAPT(0) but substitutes Kohn-Sham (KS) orbitals in place of HF orbitals.

Our proposed method incorporates self-consistent many-body induction, but assumes that other interactions, such as exchange-repulsion and dispersion, are pairwise additive. Calculation of non-additive three-body interactions within the SAPT formalism requires computationally-expensive triple excitations,[276–278] but SAPT results for $OH^-(H_2O)_2$ indicate that the two-body terms are about an order of magnitude larger than the three-body terms. Furthermore, the three-body terms are dominated by the induction correction,[279] that is, by the change in electrostatics due to the presence of other molecules. In addition, energy decomposition analysis of $(H_2O)_6$ isomers reveals that electrostatic, exchange-repulsion, and dispersion interactions *are* pairwise additive (or nearly so), whereas polarization exhibits many-body effects of ~ 10 kcal/mol.[280] In our proposed scheme, many-body polarization is mostly captured within the zeroth-order wavefunctions generated by the XPol procedure, and electrostatic embedding serves to reduce the magnitude of the intermolecular perturbation. The fact that the MP2 correlation energy is approximated to high accuracy with only a two-body expansion[53] suggests that we need only extend SAPT to pairwise fragment interactions, which will make the method highly efficient for applications to molecular liquids.

7.2 Theory

The method introduced here is essentially an amalgam of two existing methods, XPol and SAPT, so we call the new method XPol/SAPT or XPS. In what follows, we will use indices A and B to label fragments; i and j to label electrons; $a \in A$ and $b \in B$ to label occupied MOs belonging to fragments A and B, respectively; $r \in A$ and $s \in B$ to label virtual orbitals; Greek letters $(\mu, \nu, \lambda, \sigma)$ to label atomic orbital (AO) basis functions; and $I, J, K, \ldots$ to label nuclei. We restrict our attention to closed-shell spin-restricted calculations. Atomic units are used throughout this section.

7.2.1 XPol

XPol is an approximate, fragment-based molecular orbital method that was developed to be a "next-generation" force field.[57, 58] This method starts from an *ansatz* in which the supersystem wavefunction is written as a direct product of fragment wavefunctions,[59, 281]

$$|\Psi\rangle = \prod_{A}^{N_{frag}} |\Psi_A\rangle \ , \tag{7.1}$$

where N_{frag} is the number of fragments. We assume here that the fragments are molecules and that covalent bonds remain intact, although XPol has been extended to fragmentation of the system across covalent bonds.[58, 59] The fragment wavefunctions are antisymmetric with respect to exchange of electrons within a fragment, but not to exchange between fragments. As such, exchange interactions between fragments are neglected. In the original version of XPol, Lennard-Jones potentials are used to model exchange-repulsion and dispersion interactions,[59] but our aim is to replace these empirical interaction terms with perturbation theory. Very recently, Gao and co-workers extended XPol to include interfragment exchange within the SCF iterations,[60] in a manner highly analogous to the SCF-MI approach.[49] In contrast, our method treats exchange as a post-SCF correction.

For closed-shell fragments, the XPol energy is[59]

$$E_{\mathrm{XPol}} = \sum_A \left[2 \sum_a \mathbf{c}_a^\dagger \left(\mathbf{h}^A + \mathbf{J}^A - \tfrac{1}{2}\mathbf{K}^A \right) \mathbf{c}_a + E_{nuc}^A \right] + E_{embed} \ . \tag{7.2}$$

The term in square brackets is the ordinary HF energy expression,[12] for fragment A. Thus, $\mathbf{c}_a$ is a vector of occupied MO expansion coefficients (in the AO basis) for the occupied MO $a \in A$; $\mathbf{h}^A$ consists of the one-electron integrals; and $\mathbf{J}^A$ and $\mathbf{K}^A$ are the Coulomb and exchange matrices, respectively, constructed from the density matrix for fragment A. The additional terms in Eq. (7.2),

$$E_{embed} = \tfrac{1}{2} \sum_A \sum_{B \neq A} \sum_{J \in B} \left(-2 \sum_a \mathbf{c}_a^\dagger \mathbf{I}_J \mathbf{c}_a + \sum_{I \in A} L_{IJ} \right) q_J \ , \tag{7.3}$$

arise from the electrostatic embedding. The matrix $\mathbf{I}_J$ is defined by its AO matrix elements,

$$(\mathbf{I}_J)_{\mu\nu} = \left\langle \mu \left| \frac{1}{\left| \vec{r} - \vec{R}_J \right|} \right| \nu \right\rangle \ , \tag{7.4}$$

and L_{IJ} is given by

$$L_{IJ} = \frac{Z_I}{\left| \vec{R}_I - \vec{R}_J \right|} \ . \tag{7.5}$$

According to Eqs. (7.2) and (7.3), each fragment is embedded in the electrostatic potential arising from a set of point charges, $\{q_J\}$, on all of the other fragments; the factor of 1/2 in Eq. (7.3) avoids double-counting. Exchange interactions between fragments are ignored, and the electrostatic interactions between fragments are approximated by interactions between the charge density of one fragment and point charges on the other fragments.

Crucially, the vectors $\mathbf{c}_a$ are constructed within the absolutely-localized MO (ALMO) *ansatz*,[49] meaning that the MOs for each fragment are represented in terms of only those AOs that are centered on atoms in the same fragment. This partition of the AO basis leads to significant computational savings, and affords a method whose cost grows linearly with respect to N_{frag}. The ALMO *ansatz* also excludes basis set superposition error (BSSE) by construction, and in compact basis sets it excludes interfragment charge transfer as well.[49]

The original XPol method of Xie *et al.*[57–59, 246] uses Mulliken charges for the q_J in Eq. (7.3), though other charge schemes could be envisaged. In addition to Mulliken charges, we will examine Löwdin charges[12] and charges derived from the electrostatic potential (CHELPG).[282] This aspect of the method is discussed in Section 7.2.2, with additional details given in appendix C.

Derivation of the XPol working equations follows closely that of the HF equations. We require the energy expression in Eq. (7.2) to be stationary with respect to variation of the MO coefficients, subject to the constraint that MOs *within* each fragment are orthonormal. This leads to the XPol SCF equations,[59]

$$\mathbf{F}^A\mathbf{C}^A = \mathbf{S}^A\mathbf{C}^A\boldsymbol{\epsilon}^A \ . \tag{7.6}$$

Here, $\mathbf{F}^A$, $\mathbf{C}^A$, $\mathbf{S}^A$ and $\boldsymbol{\epsilon}^A$ are the fragment Fock matrix, MO coefficient matrix, AO overlap matrix, and Lagrange multiplier matrix, respectively. The dimension of these matrices equals the number of AOs centered on fragment A. Upon diagonalizing $\boldsymbol{\epsilon}^A = \left(\mathbf{C}^A\right)^\dagger \mathbf{F}^A\mathbf{C}^A$, the diagonal elements of $\boldsymbol{\epsilon}^A$ are the eigenvalues of the fragment

Fock matrix, $\mathbf{F}^A$. In the AO basis, $\mathbf{F}^A$ has matrix elements

$$F^A_{\mu\nu} = f^A_{\mu\nu} - \tfrac{1}{2}\sum_{J\notin A}(I_J)_{\mu\nu}q_J + \sum_{J\in A} M_J(\Lambda_J)_{\mu\nu} \tag{7.7}$$

where $\mathbf{f}^A = \mathbf{h}^A + 2\mathbf{J}^A - \mathbf{K}^A$ is the Fock matrix for fragment A in isolation. The additional XPol terms consist of an "M-vector" defined by

$$\begin{aligned} M_J &= \frac{\partial E_{embed}}{\partial q_J} \\ &= \tfrac{1}{2}\sum_{\substack{B \\ (J\notin B)}}\left(-2\sum_b \mathbf{c}_b^\dagger \mathbf{I}_J \mathbf{c}_b + \sum_{I\in B} L_{IJ}\right) \ , \end{aligned} \tag{7.8}$$

and also

$$(\Lambda_J)_{\mu\nu} = \frac{\partial q_J}{\partial P_{\mu\nu}} \ . \tag{7.9}$$

Here, $\mathbf{P}$ represents the one-electron density matrix, which is block diagonal in the fragment index.

Our notation differs slightly from that used by Xie *et al.*,[59] though we believe that ours is more transparent. We have written Eq. (7.7) in a general form that is valid for any charge scheme, and explicit formulas for the charge derivatives, $(\Lambda_J)_{\mu\nu}$, will be presented below. As pointed out by Xie *et al.*,[59] Eq. (7.7) indicates that each fragment is polarized by the rest of the system, with half of this polarization stemming from point charges on the other fragments and half from the true charge density of the rest of the system, which is contained in the M-vector. In principle, the electrostatic embedding could be systematically improved, by using higher-order multipoles or the fragment densities themselves, but we will not explore this possibility here.

Solution of the XPol equations requires a dual SCF procedure, since each fragment Fock matrix depends upon the electron density of the other fragments. Implementation of the dual SCF is straightforward and will be discussed only briefly, in Section 7.3.

7.2.2 Charge schemes

We investigate three different charge schemes: Mulliken, Löwdin and CHELPG. In this section we will derive formulas necessary to incorporate Mulliken charges into the XPS method. Details pertaining to the use of Löwdin and CHELPG charges are given in the appendix C.

The Mulliken charges stem from a simple partitioning of the electron density,[12]

$$q_J^{\text{Mull}} = Z_J - \sum_{\substack{\mu \in J \\ \nu}} S_{\mu\nu} P_{\nu\mu} \ . \tag{7.10}$$

The derivative with respect to a density matrix element is quite simple and can be written as

$$(\Lambda_J^{\text{Mull}})_{\mu\nu} = -\tfrac{1}{2} \left(S_{\mu\nu} \delta_{\mu \in J} + S_{\nu\mu} \delta_{\nu \in J} \right) \ , \tag{7.11}$$

where $\delta_{\mu \in J} = 1$ if the basis function μ is centered on atom J, and $\delta_{\mu \in J} = 0$ otherwise.

In what follows, we will require an operator, $\hat{\Lambda}_J$, whose matrix elements are equal to $(\Lambda_J)_{\mu\nu}$ as given by Eq. (7.11). It can be verified that a reasonable choice is

$$\hat{\Lambda}_J^{\text{Mull}} = -\tfrac{1}{2} \sum_{\mu,\nu \in J} \Big(|\mu\rangle (\mathbf{S}_J^{-1})_{\mu\nu} \langle \nu| + |\nu\rangle (\mathbf{S}_J^{-1})_{\nu\mu} \langle \mu| \Big) \ . \tag{7.12}$$

The quantity $\mathbf{S}_J^{-1}$ in this equation refers to the inverse of the *fragment* overlap matrix, for the fragment that contains atom J. At no point is it necessary to invert the supersystem's overlap matrix.

7.2.3 Symmetry-adapted perturbation theory

Two issues prevent us from applying perturbation theory to the XPol wavefunction, Eq. (7.1), in a straightforward manner. First, the fragment wavefunctions (and ALMOs) are not mutually orthogonal amongst the fragments. Second, while the fragment wavefunctions are properly antisymmetric with respect to exchange of electrons *within* a fragment, the direct product *ansatz* in Eq. (7.1) is not antisymmetric with respect to exchanges *between* fragments. Symmetry-adapted perturbation theory (SAPT) was developed to overcome precisely these two problems. Here, we review only the most relevant details of SAPT; see Refs. [20] and [269] for a complete introduction to the method.

In SAPT, the Hamiltonian for the A $\cdots$ B dimer is written as[20, 283]

$$\hat{H} = \hat{F}^A + \hat{F}^B + \xi\hat{W}^A + \eta\hat{W}^B + \zeta\hat{V} \ , \tag{7.13}$$

where $\hat{W}^A$ and $\hat{W}^B$ are Møller-Plesset fluctuation operators for fragments A and B, and the intermolecular perturbation, $\hat{V}$, is conveniently written as

$$\hat{V} = \sum_{i\in A}\sum_{j\in B}\hat{v}(ij) \tag{7.14}$$

with

$$\hat{v}(ij) = \frac{1}{\left|\vec{r}_i - \vec{r}_j\right|} + \frac{\hat{v}_A(j)}{N_A} + \frac{\hat{v}_B(i)}{N_B} + \frac{V_0}{N_A N_B} \ . \tag{7.15}$$

The quantity V_0 is the nuclear interaction energy between the two fragments, and

$$\hat{v}_A(j) = -\sum_{I\in A} \frac{Z_I}{|\vec{r}_j - \vec{R}_I|} \tag{7.16}$$

describes the interaction of electron $j \in B$ with nuclei $I \in A$. In what one might call "traditional" SAPT, the interaction energy is expanded in a triple perturbation series in the parameters ξ, η, and ζ.[20, 284]

Here, we expand only with respect to ζ. When the zeroth-order monomer wavefunctions come from HF theory, this is usually termed SAPT(0), where the "(0)" means zeroth-order in the monomer fluctuation potentials.[20] Within this formalism, the interaction energy is given by a symmetrized Rayleigh-Schrödinger perturbation expansion,[269, 284–286]

$$E_{int}(\zeta) = \frac{\langle\Psi_0|\zeta\hat{V}\hat{\mathcal{A}}_{AB}|\Psi(\zeta)\rangle}{\langle\Psi_0|\hat{\mathcal{A}}_{AB}|\Psi(\zeta)\rangle}\ , \tag{7.17}$$

where $\hat{\mathcal{A}}_{AB}$ is an antisymmetrizer for the A $\cdots$ B supersystem that projects out the Pauli-forbidden components of the supersystem wavefunction, $|\Psi(\zeta)\rangle$. The zeroth-order wavefunction, $|\Psi_0\rangle$, is taken to be a direct product of the monomer wavefunctions, and the interaction energy is expanded with respect to ζ. At every order in the perturbative expansion of Eq. (7.17), there is a polarization term analogous to what would be obtained in ordinary Rayleigh-Schrödinger perturbation theory, along with an exchange term.[269] Here, we consider the expansion through second order, in which case the interaction energy can be decomposed as[270]

$$E_{int} = E^{(1)}_{elst} + E^{(1)}_{exch} + E^{(2)}_{pol} + E^{(2)}_{exch}\ . \tag{7.18}$$

The various terms in this expression are discussed below.

The antisymmetrizer in Eq. (7.17) can be written as[20, 284]

$$\hat{\mathcal{A}}_{AB} = \frac{N_A!N_B!}{(N_A+N_B)!}\,\hat{\mathcal{A}}_A\hat{\mathcal{A}}_B\big(\hat{1} + \hat{\mathcal{P}}^{AB} + \hat{\mathcal{P}}'\big)\ , \tag{7.19}$$

where $\hat{\mathcal{A}}_A$ and $\hat{\mathcal{A}}_B$ are antisymmetrizers for the two monomers, and $\hat{\mathcal{P}}^{AB}$ is a sum of all one-electron exchange operators between the two monomers. The operator $\hat{\mathcal{P}}'$ in Eq. (7.19) denotes all of the three-electron and higher-order exchanges. This operator is neglected in what is known as the "single-exchange" approximation.[20, 269, 277] This approximation is expected to be quite accurate at typical van der Waals distances,[269] and we invoke it here.

The electrostatic part of the first-order energy correction is denoted $E^{(1)}_{elst}$ in Eq. (7.18), and represents the Coulomb interaction between the two monomer electron densities.[269] The quantity $E^{(1)}_{exch}$ in Eq. (7.18) is the corresponding first-order (Hartree-Fock) exchange correction. Explicit formulas for these corrections can be found in the literature.[20, 269, 284, 287]

The second-order polarization correction in Eq. (7.18), $E^{(2)}_{pol}$, can be further decomposed into induction and dispersion contributions. The induction correction can be written as

$$E^{(2)}_{ind} = E^{(2)}_{ind}(A \leftarrow B) + E^{(2)}_{ind}(B \leftarrow A)\ , \tag{7.20}$$

where the notation $(A \leftarrow B)$ indicates that the frozen charge density of B polarizes the density of A. In detail,[20]

$$E^{(2)}_{ind}(A \leftarrow B) = 2\sum_{ar} t_{ar}(w_B)_{ra} \tag{7.21}$$

where

$$(w_B)_{ar} = (\hat{v}_B)_{ar} + \sum_b (ar|bb) \tag{7.22}$$

and $t_{ar} = (w_B)_{ar}/(\epsilon_a - \epsilon_r)$. The second term in Eq. (7.20), in which A polarizes B, is obtained from Eqs. (7.21) and (7.22) by interchanging the following labels: $A \leftrightarrow B$, $a \leftrightarrow b$, and $r \leftrightarrow s$.[20] Finally, the dispersion correction is

$$E^{(2)}_{disp} = 4 \sum_{abrs} \frac{(ar|bs)(ra|sb)}{\epsilon_a + \epsilon_b - \epsilon_r - \epsilon_s} \ . \tag{7.23}$$

The induction and dispersion corrections both have accompanying exchange corrections (termed exchange-induction and exchange-dispersion) which are quite lengthy and can be found in the literature.[20, 275]

Although an exact first-order exchange correction that avoids the single-exchange approximation has been derived,[288] to the best of our knowledge the exchange-induction and exchange-dispersion formulas have only been derived within the single-exchange approximation. We have tested this exact formula for $E^{(1)}_{exch}$, and we find that the single-exchange approximation is quite robust. Moreover, the single-exchange approximation does not require inversion of the dimer overlap matrix, which *is* required in the exact formula for $E^{(1)}_{exch}$. For this reason, and in the interest of consistency, we invoke the single-exchange approximation for all of the exchange interaction terms.

It is quite common to replace $E^{(2)}_{ind}$ and $E^{(2)}_{exch\text{-}ind}$ with their "response" analogues, $E^{(2)}_{ind,resp}$ and $E^{(2)}_{exch\text{-}ind,resp}$, which afford the infinite-order correction for polarization arising from a frozen partner density.[20] Operationally, this substitution involves replacing the second-order induction amplitudes, t_{ar} in Eq. (7.21), with amplitudes obtained from solution of the coupled-perturbed Hartree-Fock equations.[289] (The perturbation is simply the electrostatic potential of the other monomer.) In addition, it is common to correct the SAPT(0) binding energy for "higher-order" polarization effects, by adding a correction term

$$\delta E_{int}^{\mathrm{HF}} = E_{int}^{\mathrm{HF}} - \left(E_{elst}^{(1)} + E_{exch}^{(1)} + E_{ind,resp}^{(2)} + E_{exch\text{-}ind,resp}^{(2)} \right) \tag{7.24}$$

to the interaction energy.[20] Here, E_{int}^{HF} is the counterpoise-corrected HF binding energy for $\mathrm{A} \cdots \mathrm{B}$.

If one simply replaces the MOs and eigenvalues of the SAPT(0) corrections with KS MOs and eigenvalues, then the energy expressions above define the method known as SAPT(KS).[270] [This approach was originally termed SAPT(DFT)[270] but the latter term is now reserved for an alternative DFT-based SAPT method.[272–275]] Initially, the SAPT(KS) approach was not deemed very successful, as the electrostatic and induction energies failed to reproduce (traditional) benchmark SAPT values.[271] However, these discrepancies were ultimately determined to result from the incorrect asymptotic behavior of common exchange-correlation (XC) functionals used in DFT. Applying an asymptotic correction to the XC potential improved the agreement with benchmark values,[271] though the dispersion correction was still poor. This led to the development of the method that is nowadays called SAPT(DFT),[272–275] in which the sum-over-states formula for the dispersion interaction [Eq. (7.23)] is replaced with a generalized Casimir-Polder-type expression based on frequency-dependent density susceptibilities for the monomers, which are calculated by solving time-dependent coupled HF or KS equations.[272–275] We have not yet implemented SAPT(DFT), but the SAPT(KS) approach will be considered here, in addition to SAPT(0).

7.2.4 XPol/SAPT

There are two difficulties in combining XPol with SAPT. First, the perturbation in SAPT is not appropriate when XPol is used to obtain zeroth-order wavefunctions and energies, due to the fact that some intermolecular interactions have already been included, albeit approximately, by means of electrostatic embedding. In addition, SAPT(0) must be extended to incorporate an arbitrary number of monomers.

Taking the zeroth-order Hamiltonian to be the sum of the fragment Fock operators defined in Eq. (7.7), we can write

$$\hat{H}_0 = \sum_A \sum_{i \in A} \hat{f}^A(i) - \sum_A \sum_{i \in A} \left[\tfrac{1}{2} \sum_{J \notin A} q_J \hat{I}_J(i) - \sum_{J \in A} M_J \hat{\Lambda}_J(i) \right] , \tag{7.25}$$

where $\hat{f}^A(i)$ is the gas-phase (isolated fragment) Fock operator for electron i in fragment A. Equation (7.25) can be rewritten as

$$\begin{aligned} \hat{H}_0 = {} & \sum_A \sum_{i \in A} \hat{f}^A(i) \qquad (7.26) \\ & - \sum_A \sum_{B > A} \left[\sum_{i \in A} \left(\tfrac{1}{2} \sum_{J \in B} q_J \hat{I}_J(i) - \sum_{I \in A} M_I^B \hat{\Lambda}_I(i) \right) \right. \\ & \left. + \sum_{j \in B} \left(\tfrac{1}{2} \sum_{I \in A} \hat{I}_I(j) q_I - \sum_{J \in B} M_J^A \hat{\Lambda}_J(j) \right) \right] , \end{aligned}$$

where M_J^A is the Jth element of an M-vector that contains only contributions from fragment A. This partitioning of $\hat{H}_0$ suggests that we replace $\hat{v}_A$ and $\hat{v}_B$ in Eq. (7.15) with

$$\hat{v}_A(j) = - \sum_{I \in A} \left(Z_I - \tfrac{1}{2} q_I \right) \hat{I}_I(j) - \sum_{J \in B} M_J^A \hat{\Lambda}_J(j) \tag{7.27a}$$

$$\hat{v}_B(i) = - \sum_{J \in B} \left(Z_J - \tfrac{1}{2} q_J \right) \hat{I}_J(i) - \sum_{I \in A} M_I^B \hat{\Lambda}_I(i) \; . \tag{7.27b}$$

Once these substitutions have been made, we use the standard SAPT(0) corrections, in a pairwise manner, to calculate all dimer interaction energies, E^{AB}_{int}, using Eq. (7.18) in conjunction with the perturbation defined in Eq. (7.27). The total energy within the XPS *ansatz* is then given by

$$E_{\text{XPS}} = \sum_A \left(\sum_a \left[2\, \epsilon^A_a - \mathbf{c}^\dagger_a (\mathbf{J}^A - \tfrac{1}{2}\mathbf{K}^A)\mathbf{c}_a \right] + E^A_{nuc} + \sum_{B>A} E^{AB}_{int} \right) \ . \tag{7.28}$$

In this expression, we have removed the over-counting of two-electron interactions present in HF theory, effectively taking the *intrafragment* perturbation to first order. The generalization from a HF to a KS description of the monomers is straightforward.

To better understand what we have just done, let us first generalize the SAPT Hamiltonian, Eq. (7.13), to an arbitrary number of fragments by writing

$$\hat{H} = \sum_A \left(\hat{F}^A + \xi_A \hat{W}^A \right) + \sum_A \sum_{B>A} \zeta_{AB} \hat{V}_{AB} \ . \tag{7.29}$$

In this expression, there are N_{frag} intramolecular perturbations ($\xi_A \hat{W}^A$) and $N_{dimer} = N_{\mathit{frag}}(N_{\mathit{frag}} - 1)/2$ intermolecular perturbations ($\zeta_{AB}\hat{V}_{AB}$). In principle, one should therefore employ a ($N_{\mathit{frag}} \times N_{dimer}$)-tuple perturbative expansion for this Hamiltonian, analogous to the triple perturbation expansion that is applied to Eq. (7.13). However, we neglect intrafragment electron correlation, analogous to SAPT(0) for dimers. In addition, we neglect second-order terms arising from coupling between first-order perturbations on different dimers.

We have also made a third (and somewhat more subtle) approximation. Neglecting monomer electron correlation ($\hat{W}^A$) in the Hamiltonian of Eq. (7.29), the first-order (intermolecular) energy correction is [*cf.* Eq. (7.17)]

$$E^{(1)} = \frac{\left\langle \Psi_0 \left| \left(\sum_A \sum_{B>A} \hat{V}_{AB} \right) \hat{\mathcal{A}} \right| \Psi_0 \right\rangle}{\left\langle \Psi_0 \middle| \hat{\mathcal{A}} \middle| \Psi_0 \right\rangle} \; . \tag{7.30}$$

Here, $|\Psi_0\rangle$ is the zeroth-order, direct-product wavefunction for the supersystem. Note that $\hat{\mathcal{A}}$ is a supersystem antisymmetrizer and is not pairwise additive. This operator can be expressed as

$$\hat{\mathcal{A}} = \frac{\left(\prod_A N_A! \hat{\mathcal{A}}_A \right)}{(\sum_A N_A)!} \left(1 + \sum_A \sum_{B>A} \hat{\mathcal{P}}^{AB} + \hat{\mathcal{P}}' \right) \; , \tag{7.31}$$

where the operator $\hat{\mathcal{P}}^{AB}$ generates all pairwise electron exchanges between fragments A and B. Higher-order exchange terms contained in $\hat{\mathcal{P}}'$ are neglected within the single-exchange SAPT approximation that was introduced in Section 7.2.3. In XPS, however, there are multiple dimers of fragments, and in developing this method we have tacitly introduced a further approximation in which only "diagonal" terms such as $\langle \Psi_0 | \hat{V}_{AB} (\hat{1} + \hat{\mathcal{P}}^{AB}) | \Psi_0 \rangle$ are retained in the numerator of Eq. (7.30). This approximation neglects some single-exchange terms involving three or more fragments. For example, in trimers A $\cdots$ B $\cdots$ C, fragments A and B can be coupled by $\hat{\mathcal{P}}^{AB}$ while B and C are coupled by $\hat{V}_{BC}$, but such terms are neglected in the present formulation of XPS. The impact of neglecting these terms is unclear, although such terms are only likely to be important when all three fragments are in very close proximity. In future work, we plan to reformulate our XPS procedure in a more rigorous and systematic manner based on Eqs. (7.29)–(7.31), which includes coupling between first-order perturbations and also all single-exchange terms.

At present, we have provided an *ad hoc* physical motivation for the XPS method, rather than a rigorous derivation starting from Eq. (7.29). For this reason, we refer to XPS as a *parameter-free* quantum-chemical model, rather than an *ab initio* model. Our aim for the time being is to replace the Lennard-Jones terms used in the XPol calculations of Xie *et al.*[57–59, 246] with pairwise SAPT corrections. To this end, we have assumed that the leading many-body effect is induction, and we incorporate this effect within the zeroth-order Hamiltonian in an efficient (albeit approximate) manner. We assume that the remaining induction corrections, as well as all intermolecular exchange and dispersion interactions, can be described in a pairwise fashion. To the extent that the method is successful, it succeeds by reducing the size of the many-body perturbation, to the point where low-order, pairwise perturbation theory provides sufficient accuracy.

The inclusion of many-body induction within the zeroth-order Hamiltonian makes the subsequent SAPT corrections less meaningful in terms of energy decomposition analysis. For instance, the first-order electrostatic correction in XPS is *not* the total electrostatic energy, since the former corrects for errors in the approximate electrostatic treatment at zeroth order (*i.e.*, the electrostatic embedding). The dispersion correction may be less contaminated, since all of the XPS modifications to the traditional SAPT perturbation are one-electron operators [see Eq. (7.27)], and therefore the pairwise dispersion correction differs from its traditional SAPT analogue only insofar as the MOs are perturbed by the electrostatic embedding. As such, we will continue to interpret this as a true dispersion correction.

Finally, some discussion of basis sets is warranted. Typically, SAPT calculations are performed in the so-called dimer-centered basis set (DCBS),[290] which means that the combined A + B basis set is used to calculate the zeroth-order wavefunctions for both A and B. This leads to the unusual situation that there are more MOs than basis functions: one set of occupied and virtual MOs for each monomer, both expanded in the same (dimer) AO basis. As an alternative to the DCBS, one might calculate $|\Psi_A\rangle$ using only A's basis functions (similarly for B), in which case the SAPT calculation is said to employ the monomer-centered basis set (MCBS).[290] Because XPol derives its efficiency by restricting MOs on fragment A to be built from AOs on fragment A, we consider only the MCBS for the purpose of converging the fragment wavefunctions. (In Section 7.4.2, however, we will introduce a post-XPol pseudo-canonicalization in the DCBS, in order to recover intermolecular charge transfer.) Use of the MCBS means that our SAPT(0) corrections are most likely *not* converged with respect to basis-set expansion,[290] and thus rely on a cancellation of errors to provide meaningful results. As stated above, we intend XPS not as a benchmark method but rather as an efficient, parameter-free method to study molecular clusters and liquids. As such, we see no problem with relying on error cancellation, provided that the accuracy and robustness of the cancellation are established by thorough comparisons to benchmark calculations. Such comparisons are reported in Sections 7.4 and 7.5.

7.3 Computational details

We have implemented the XPol, SAPT(0), and XPS methods within a locally modified version of the Q-CHEM software package.[117] The XPol SCF equations are solved by means of a dual SCF procedure similar to that described by Xie *et al.*[59] In brief, we iterate Eq. (7.6) to convergence for each fragment A, using a fixed set of point charges derived from the previous SCF solutions for the other fragments. Once all N_{frag} sets of SCF equations have been converged in this manner, we evaluate the supersystem SCF error as the average of fragment errors, each of which is defined as the root mean square of the off-diagonal Fock matrix elements in the ALMO basis. The dual SCF is considered to be converged when this error is $< 10^{-8}$ a.u. The integral threshold is set to 10^{-14} a.u. for all calculations reported here, and all SAPT calculations employ Cartesian Gaussian basis functions.

To generate the CHELPG charges, we evaluate the electrostatic potential on a cubic grid, with a grid spacing of 1.0 Å. We discard grid points that lie within the van der Waals radius of any nucleus, using the van der Waals radii suggested by Bondi.[291, 292] The grid edges extend 3.0 Å from the nearest atomic surface, as defined by these radii.

As we have not yet implemented the analytic gradient for the XPS method, geometry optimizations are performed using a three-point finite difference of the total energy, with atomic displacements of 10^{-3} bohr. For calculations using CHELPG charges,[282] the number of grid points used to evaluate the electrostatic potential may change as the nuclei are displaced. To avoid discontinuities in the potential energy surface, we therefore use a modified CHELPG procedure based upon a weighted least-squares fit to the electrostatic potential. Details of this procedure can be found in appendix C.

In this report, we use the standard density functionals B3LYP,[293, 294] BOP,[167] and PBE0.[295–297] We also employ several "long-range corrected" (LRC) functionals including LRC-ωPBEh[298, 299] and LRC-μBOP.[168, 300] The LRC-μBOP functional uses Coulomb attenuation parameter ($\mu = 0.47$ bohr^{-1}) recommended in Ref. [300], while the LRC-ωPBEh functional uses the parameters recommended in Ref. [299] ($\omega = 0.2$ bohr^{-1} and 20% short-range HF exchange).

7.4 Dimer Benchmarks

In this section, we evaluate dimer binding energies predicted by the XPS method, in comparison to benchmark values. Cembran *et al.*[60] note that the XPol method is not intended to reproduce HF or DFT energies, but is instead intended as an efficient way to obtain energies and forces for simulations of macromolecules and liquids. Similarly, our XPS method is not intended to reproduce any particular model chemistry but rather to allow efficient, accurate, and parameter-free simulations of molecular systems. As such, we compare to dimer SAPT(0) results not with the expectation of reproducing SAPT(0) binding energies exactly, but simply to demonstrate that our procedure does not significantly degrade the results of a method that is known to perform reasonably well for dimer binding energies. We also compare to complete basis set (CBS) extrapolations of binding energies computed at the MP2 level, and at the coupled-cluster level with single, double, and perturbative triple excitations [CCSD(T)].

The use of large basis sets is not consistent with our goal of fast quantum chemistry, so for XPS we consider only double-ζ and a few Pople-type triple-ζ basis sets. In a sense, one may think of the basis set and point-charge embedding scheme as parameters of the method.

7.4.1 S22 database

The S22 database of dimer binding energies was assembled in Ref. [301], although we use the revised binding energies from Ref. [302] in this work. The data set contains 22 biologically-relevant molecular dimers, including seven hydrogen-bonded dimers, eight dispersion-dominated complexes, and seven complexes where both dispersion and hydrogen-bonding contribute significantly to the binding energy. The benchmark binding energies for these complexes range from $\sim$0.5–20.0 kcal/mol, and are estimates of CCSD(T)/CBS binding energies. (See Ref. [302] for details of the CBS extrapolation procedure.)

We will compare SAPT(0) and SAPT(KS) binding energies with and without inclusion of the XPol procedure. When XPol is used to obtained the zeroth-order wavefunction, and the perturbation is therefore modified according to Eq. (7.27), we will refer to these methods as XPS(0) and XPS(KS). We have neglected the $\delta E_{int}^{\text{HF}}$ correction, as the need for a counterpoise-corrected supersystem binding energy makes this an unattractive option for large systems. We will use the notation SAPT(PBE0)/6-31G*, for example, to indicate a SAPT(KS) calculation using the PBE0 density functional and the 6-31G* basis set, and the notation XPS(PBE0)/6-31G* to denote the corresponding XPS(KS) method. For XPS calculations, the additional symbol "*resp*" will be used to indicate that we have replaced the second-order induction amplitudes with amplitudes obtained from the solution of coupled-perturbed HF or KS equations.[20, 289]

Table 7.1 shows errors for the SAPT(0), SAPT(KS), XPS(0) and XPS(KS) methods, using Mulliken charges for the XPS calculations. (Additional results, for a wider variety of basis sets and density functionals, can be found appendix C.) We note that XPS(0) generally outperforms XPS(KS), and among variants of the latter, the LRC functionals generally outperform their uncorrected counterparts. The XPS(0) procedure typically results in slightly smaller errors than SAPT(0), but this is not always the case. The inclusion of infinite-order induction ("*resp*") universally improves the results when using XPS(0) and SAPT(0), but sometimes degrades the results of SAPT(KS) calculations, especially for the non-LRC functionals.

The fact that traditional generalized gradient approximations (GGAs), such as BOP, and global hybrid functionals, such as B3LYP and PBE0, fare poorly in SAPT(KS) calculations is well-documented.[270, 271, 273–275] In particular, SAPT(KS) has been shown to overestimate dispersion energies, owing to highest occupied/lowest unoccupied MO (HOMO/LUMO) gaps that are too small.[270] Figure 7.1 shows the S22 database errors for SAPT(KS) and XPS(KS) methods in more detail, and the same

Method	SCF method, X =									
	HF		BOP		PBE0		LRC-μBOP		LRC-ωPBEh	
SAPT(X)/6-31G*	0.79	(3.27)	2.02	(9.55)	1.52	(6.47)	1.56	(7.31)	1.45	(6.75)
SAPT(X)-*resp*/6-31G*	0.65	(2.48)	2.50	(9.21)	1.73	(6.50)	1.52	(7.33)	1.51	(7.36)
XPS(X)/6-31G*	0.56	(1.46)	2.00	(9.66)	1.33	(6.24)	1.10	(3.79)	0.99	(3.57)
XPS(X)-*resp*/6-31G*	0.90	(3.16)	1.87	(9.01)	1.28	(5.99)	0.80	(3.14)	0.82	(3.11)
SAPT(X)/cc-pVDZ	1.06	(4.45)	2.45	(9.58)	1.83	(6.27)	1.89	(8.30)	1.81	(7.76)
SAPT(X)-*resp*/cc-pVDZ	0.91	(3.72)	2.92	(9.41)	2.06	(7.46)	1.87	(8.34)	1.88	(8.37)
XPS(X)/cc-pVDZ	0.71	(1.94)	2.58	(10.11)	1.73	(6.81)	1.62	(5.93)	1.59	(5.83)
XPS(X)-*resp*/cc-pVDZ	0.50	(1.81)	2.52	(9.00)	1.66	(5.90)	1.38	(5.43)	1.42	(5.45)

Table 7.1: Mean absolute errors and (in parentheses) maximum absolute errors for the the S22 database, in kcal/mol. A variety of SAPT(X) and XPS(X) variants are considered; note that SAPT(HF) is equivalent to the method that is traditionally called SAPT(0). All XPS methods use Mulliken charges for the electrostatic embedding.

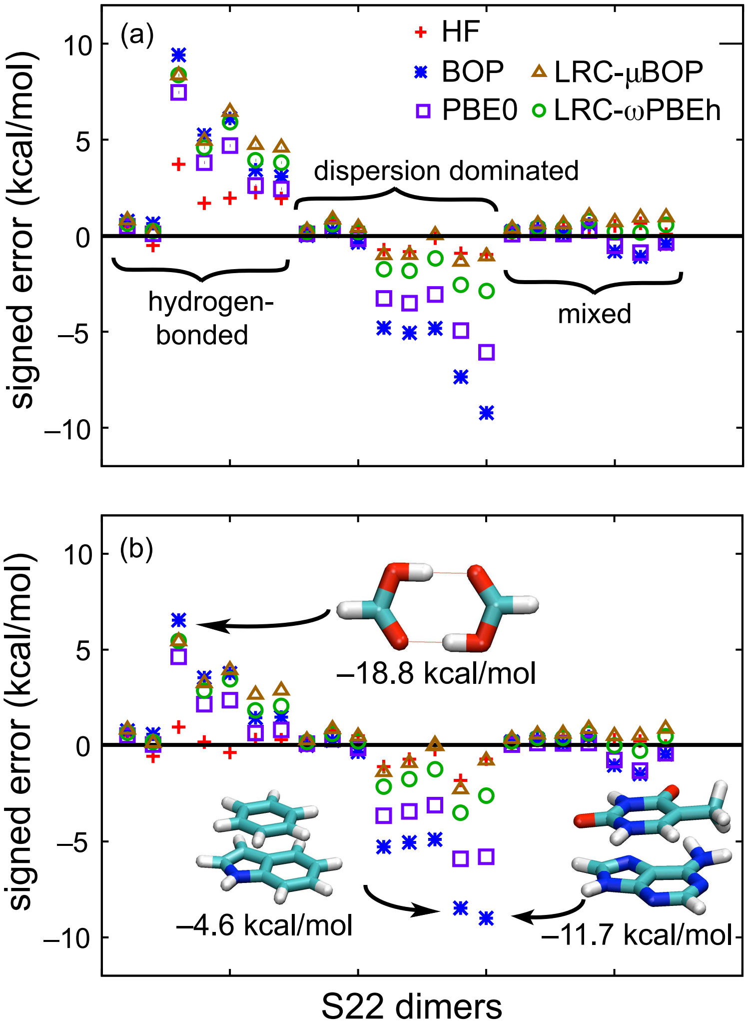

Figure 7.1: Binding energy errors (in kcal/mol) across the S22 database, as computed at (a) the SAPT(X)/cc-pVDZ level and (b) the XPS(X)/cc-pVDZ level (with Mulliken embedding charges), for a variety of different SCF methods, X. A few difficult cases are highlighted in panel (b). Starting at the top and moving clockwise around panel (b), these are formic acid dimer, an indole-benzene π stack, and an adenine-thymine π stack.

trend is evident among traditional (*i.e.*, non-LRC) density functionals. LRC functionals, however, widen the HOMO/LUMO gap,[168] leading to larger energy denominators in Eq. (7.23), and therefore smaller dispersion energies. Although the LRC procedure appears to eliminate the strong overestimation of the dispersion energy, *all* of the density functionals tend to underbind the hydrogen-bonded complexes, often to a considerable extent.

The LRC correction scheme that is employed here differs from the asymptotic correction[303, 304] (AC) that is typically used in SAPT(DFT) and SAPT(KS) calculations.[271, 275] Although the traditional AC guarantees that the KS potential has the correct asymptotic behavior,[303, 304] it has two major drawbacks that, in our view, make it unappealing for XPS calculations. First, construction of the AC requires an accurate ionization potential as input, and second, the AC-KS potential does not correspond to the functional derivative of any known energy functional.[303, 304] (In practice, the AC is applied to correct the asymptotic behavior of the potential, but the energy functional is not modified.) These may not be serious problems for SAPT(KS) calculations, where the binding energy is obtained directly and the total system energy is not needed. However, in XPS some of the interaction energy is wrapped up in the zeroth-order XPol energy. We aim to use this method as an efficient way to perform *ab initio* molecular dynamics simulations in clusters and condensed-phase systems, where the total supersystem energy is obviously an important and meaningful quantity. That said, in the context of SAPT(KS) or SAPT(DFT) calculations, it is unclear to us whether the use of LRC functionals is superior to the AC procedure.

Looking carefully at the errors listed in Table 7.1, it may seem strange that the SAPT(0) and XPS(0) approaches are not equivalent for hydrogen-bonded complexes when the infinite-order induction correction is applied. In fact, XPS(0) outperforms SAPT(0) in many of these cases. This is because the response correction is an infinite-order (non-perturbative) correction for induction *in the presence of a frozen partner density*, whereas XPS treats polarization self-consistently, if not exactly. This means that the XPS procedure attempts to include "higher order" induction effects into the zeroth-order energy. In SAPT(0) calculations, such terms are typically incorporated by means of the $\delta E_{int}^{\mathrm{HF}}$ correction, which is omitted here.

Although these initial tests of XPS appear promising, we are generally unable to converge the XPol procedure when Mulliken embedding charges are used in conjunction with diffuse basis functions. This is perhaps not entirely surprising, given the well-known instability of Mulliken charges with respect to basis-set expansion. (In their work on XPol, Xie *et al.*[57–59, 246] use Mulliken charges exclusively, but have only reported calculations in small basis sets.) For small, compact basis sets, we find that Mulliken, Löwdin, and CHELPG embedding charges all perform similarly, and henceforth we discontinue the use of Mulliken charges in favor of these other two charge schemes.

Having demonstrated that the LRC functionals are superior to traditional GGAs and global hybrid functionals for use with XPS, all remaining calculations focus on HF, LRC-μBOP and LRC-ωPBEh. Table 7.2 displays XPS statistical errors, evaluated over the S22 database, for a larger range of basis sets and charge schemes.

	XPS-Löwdin			XPS-CHELPG			MP2	MP2 (counter-poise)
Basis	HF	LRC-μBOP	LRC-ωPBEh	HF	LRC-	LRC-μBOP	ωPBEh	
6-31G*	0.73 (2.31)	0.91 (3.91)	0.93 (3.86)	0.87 (2.47)	0.87 (3.56)	0.90 (3.53)	1.44 (3.34)	2.09 (4.47)
6-31G*, *resp*	0.75 (2.40)	0.90 (3.88)	0.93 (3.88)	0.87 (2.55)	0.87 (3.54)	0.91 (3.55)	—	—
6-311G*	0.57 (2.76)	1.20 (6.52)	1.38 (6.92)	0.56 (2.32)	1.21(6.20)	1.40 (6.67)	1.54 (4.86)	1.82 (5.81)
6-311G*, *resp*	0.54 (2.55)	1.18 (6.41)	1.37 (6.88)	0.54 (2.18)	1.20 (6.15)	1.40 (6.65)	—	—
cc-pVDZ	0.55 (2.04)	1.46 (6.39)	1.48 (6.30)	0.39 (1.12)	1.35 (5.72)	1.39 (5.68)	1.68 (4.75)	1.98 (4.73)
cc-pVDZ, *resp*	0.51 (1.75)	1.44 (6.26)	1.47 (6.27)	0.38 (1.02)	1.35 (5.70)	1.39 (5.69)	—	—
aug-cc-pVDZ	1.52 (4.48)	2.46 (10.24)	2.71 (9.63)	1.26 (3.38)	2.21 (8.43)	2.49 (7.91)	3.15 (11.15)	1.00 (2.80)
aug-cc-pVDZ, *resp*	1.40 (3.80)	2.39 (9.91)	2.67 (9.52)	1.25 (3.39)	2.23 (8.40)	2.49 (7.91)	—	—
aug-cc-pVDZ$'$	—	—	—	1.31 (3.86)	—	—	1.76 (2.64)	1.02 (2.96)
aug-cc-pVDZ-proj	—	—	—	1.31 (4.42)	1.66 (4.36)	2.05 (6.51)	—	—
aug-cc-pVDZ$'$-proj	—	—	—	0.75 (3.38)	—	—	—	—

Table 7.2: Mean absolute errors and (in parentheses) maximum absolute errors for the S22 database, in kcal/mol. A variety of XPS(X) variants are considered, using either Löwdin or CHELPG embedding charges. For several of the basis sets, the corresponding response ("*resp*") result is also listed. The primed and projected ("proj") basis sets are defined in the text (Section 7.4.2). MP2 results, with and without counterpoise correction, are also listed for comparison.

(Results for some additional basis sets can be found in appendix C.) Also listed in Table 7.2 are statistical errors for binding energies computed using standard supersystem MP2 calculations, both with and without counterpoise correction.

The XPS methods are generally more accurate than MP2 in the smaller basis sets, whereas counterpoise-corrected MP2/aug-cc-pVDZ and MP2/aug-cc-pVDZ′ results both exhibit mean errors of 1.0 kcal/mol, versus a mean error of 1.3 kcal/mol for XPS(0)-CHELPG calculations in the same basis sets. For the MP2 calculations, however, counterpoise correction is essential to obtain errors this low, whereas this correction is unnecessary in XPS calculations. This represents a significant advantage in the context of larger clusters.

As in the case of Mulliken embedding charges, XPS(0) outperforms XPS(KS) for the S22 database. Oddly, inclusion of diffuse basis functions slightly degrades the performance of XPS(0) results but greatly degrades XPS(KS) results. The compact basis sets perform quite well, and the smallest errors are obtained using the cc-pVDZ basis set, CHELPG charges, and HF orbitals. This combination affords a mean unsigned error of only 0.4 kcal/mol and a maximum error of 1.0 kcal/mol. It is interesting to note that the infinite-order induction correction has very little effect on the errors when CHELPG embedding charges are used. We take this as an indication that these charges better reproduce the electrostatic potential outside of the molecular core, which is precisely what CHELPG charges are designed to do.

The large errors observed at the XPS(KS) level, particularly where diffuse basis sets are employed, result from an underestimation of the binding energies in strongly

H-bonded complexes. (The S22 data set contains five H-bonded complexes whose binding energies exceed 15 kcal/mol in magnitude.) In particular, the XPS binding energy of formic acid dimer is almost always underestimated, and often this species affords the largest error. This was also observed by Hohenstein and Sherrill,[305] in both SAPT(0) calculations as well as SAPT calculations that include intramonomer electron correlation. These authors suggest that it is "imperative" to include the $\delta E_{int}^{\mathrm{HF}}$ correction for H-bonded complexes. However, it appears that the XPol procedure recovers some of the higher-order induction effects that the $\delta E_{int}^{\mathrm{HF}}$ correction is intended to incorporate. In fact, the errors reported here are competitive with those reported in Ref. [305], where intramonomer electron correlation was included and the aug-cc-pVDZ/DCBS was used.

Hohenstein and Sherrill[305] report that intramonomer correlation is especially important in the formic acid dimer. It is therefore curious that the XPS(KS) errors are much larger for this species than are the XPS(0) errors, given that XPS(KS) includes some intramolecular electron correlation whereas XPS(0) does not. Where does XPS(KS) go wrong? Rephrasing this question: if we assume that XPS(0) is doing something *right*, then what is so different about XPS(KS)?

To answer this question, we define the total Coulomb and exchange energies for the A $\cdots$ B dimer according to

$$E_{Coul} = E_0^{AB} + E_{elst}^{(1)} + E_{ind}^{(2)} - E_0^A - E_0^B \tag{7.32}$$

and

$$E_{exch} = E_{exch}^{(1)} + E_{exch\text{-}ind}^{(2)} \,, \tag{7.33}$$

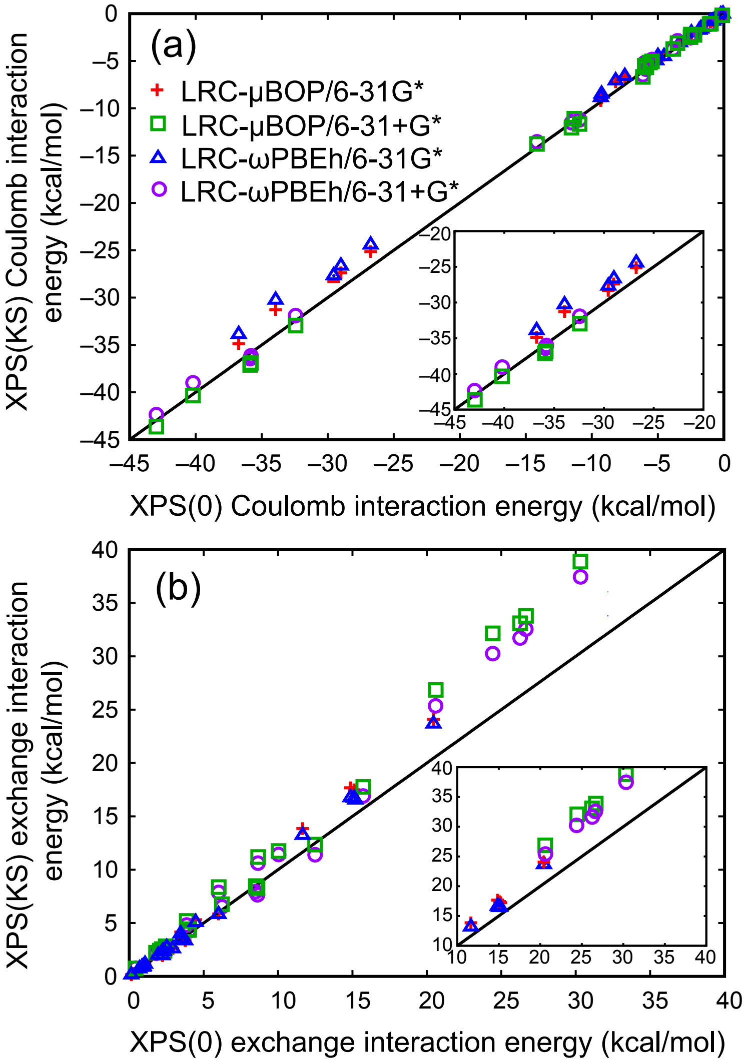

Figure 7.2: Comparison of (a) the total Coulomb and (b) the total exchange interaction energies computed at the XPS(0) and XPS(KS) levels, for the S22 database. CHELPG charges are used in each case. The insets present the data for the five strongly H-bonded complexes whose binding energies exceed 15 kcal/mol).

respectively, where E_0^{AB}, E_0^{A}, and E_0^{B} are the zeroth-order energies of the dimer and the two monomers. Figure 7.2 shows that the XPS(0) and XPS(KS) methods predict nearly identical Coulomb energies, but that the XPS(KS) methods predict much larger exchange energies, especially for dimers that exhibit strong hydrogen bonding. The net result is a less favorable cancellation of errors, and therefore an underestimation of the binding energies, when XPS(KS) methods are applied to these complexes. As the quality of the basis set increases, we expect the total electrostatic energy to become more negative while the exchange energy will become more positive (since an increasingly diffuse basis set will allow the monomer wavefunctions to overlap to a larger extent). When HF orbitals are used, errors in the Coulomb and exchange energies due to basis incompleteness must cancel, approximately, as relatively accurate binding energies are obtained. This is not the case when KS orbitals are used. It is tempting to attribute this to the well-known "delocalization error" in DFT,[306] which might exaggerate the degree of overlap and therefore the exchange energy. This artifact would tend to cancel out in SAPT(DFT) calculations, if the $\delta E_{int}^{\mathrm{HF}}$ correction were used. For this reason, it may come as no surprise that the HF variant of XPS outperforms KS variants.

7.4.2 Potential energy curves

The results of the previous section demonstrate that XPS(0) calculations, with a suitable choice of basis set and point-charge embedding scheme, can approach the accuracy of complete-basis CCSD(T) benchmarks for the S22 database of dimers. The best results are obtained using the cc-pVDZ basis set, which is far from complete, hence our method must benefit from some cancellation of errors. It is important to understand whether that cancellation is robust across potential energy surfaces. In this section, we examine some potential energy curves for $(H_2O)_2$ and $(C_6H_6)_2$. The benzene dimer was selected because it is a stringent test of the accuracy of dispersion interactions, and because CCSD(T)/CBS potential energy curves are available.[8] The water dimer was chosen because in Section 7.5 we will examine the performance of XPS(0) for binding energies in larger water clusters.

Figure 7.3 shows binding energy curves for the "parallel-displaced" benzene dimer at three different values of R_1, the distance between the two C_6H_6 planes. For non-polar molecules, Löwdin and CHELPG charges produce nearly identical results, so only the latter are used here. We observe that 6-311G*, cc-pVDZ and aug-cc-pVDZ qualitatively capture the profile of the binding energy curves (Fig. 7.3), but the 3-21G* and 6-31G* basis sets do not (see appendix C). The latter basis sets exhibit too small of a barrier at $R_2 = 0$. In our view, the cc-pVDZ and 6-311G* basis sets exhibit acceptable errors of $\sim$1 kcal/mol.

The largest basis set that we examine, aug-cc-pVDZ, overbinds the benzene dimer, which is not surprising given that XPS employs an MP2-like dispersion formula, and the MP2 method is known to overestimate the interaction energy of dispersion-bound complexes.[8] The dispersion energy in SAPT(0) generally increases as the size of the basis increases,[290] leading to a fortuitous cancellation of errors in small- to medium-sized basis sets, particularly ones that lack diffuse basis functions. For MP2-like methods, Hohenstein and Sherrill[305, 307] recommend a modified form of

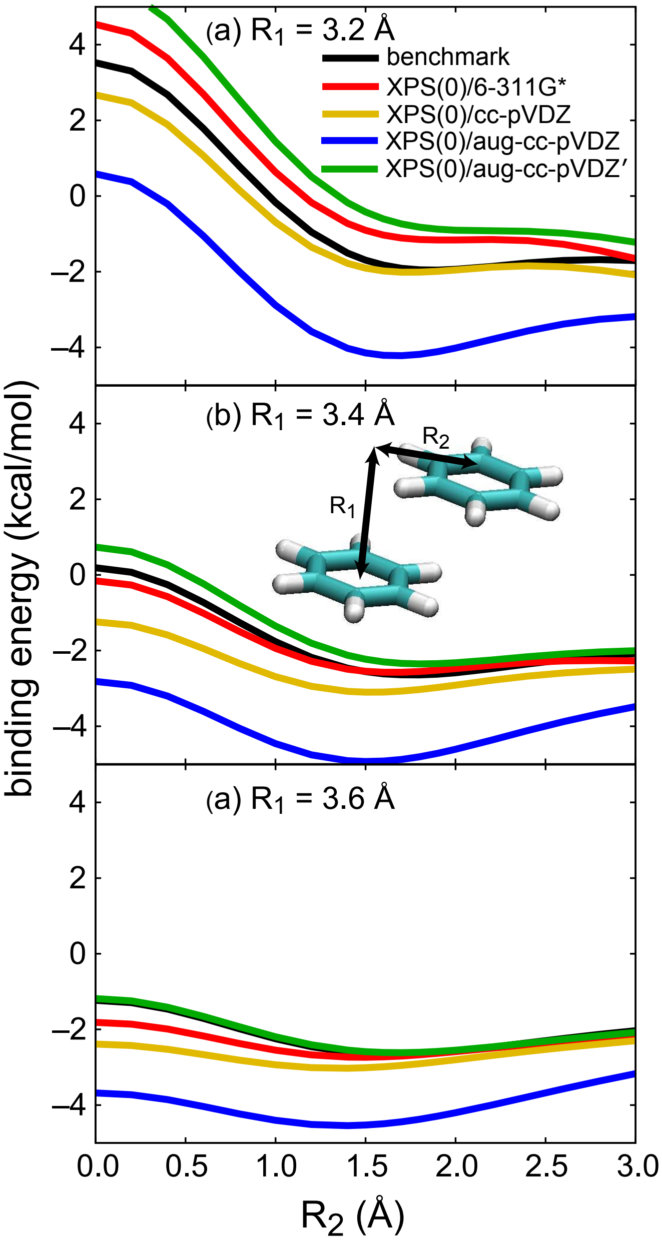

Figure 7.3: Binding energy curves for the parallel-displaced benzene dimer, computed at the XPS(0) level using CHELPG charges. CCSD(T)/CBS benchmarks are taken from Ref. [8].

aug-cc-pVDZ that they call aug-cc-pVDZ′, wherein the diffuse functions on hydrogen atoms are removed along with the diffuse d functions on the carbon atoms. For the parallel-displaced benzene dimer, we find that this basis leads to a remarkably good cancellation of errors, such that for $R_1 = 3.6$ Å the XPS(0) curve is indistinguishable from the benchmark.

A comparison of the potential energy curves for the three different values of R_1 shown in Fig. 7.3 suggests that the XPS exchange repulsion energy decays too rapidly with respect to monomer separation. This is more obvious in the case of the "T-shaped" and "sandwich" isomers of $(C_6H_6)_2$, potential energy curves for which are shown in Fig. 7.4. The aug-cc-pVDZ basis substantially overbinds these isomers at their minimum-energy geometries, although the cc-pVDZ and 6-311G* basis sets perform fairly well, affording errors on the order of ∼1 kcal/mol at the minimum. The aug-cc-pVDZ′ basis set performs extremely well for the sandwich dimer but slightly worse for the T-shaped dimer. For the sandwich configuration all of the basis sets afford a minimum at shorter separations than the benchmark result, except for the aug-cc-pVDZ′, where the entire potential curve is quite accurate. With the exception of XPS(0)/aug-cc-pVDZ′ basis, all of the XPS(0) methods perform better for the T-shaped isomer than they do for the sandwich conformation, which probably results from underestimating the induction interactions while simultaneously overestimating the dispersion energy.

To explore the $(H_2O)_2$ potential surface, we follow Burnham and Xantheas[308] in examining four different $(H_2O)_2$ isomers with distinct point-group symmetries. These

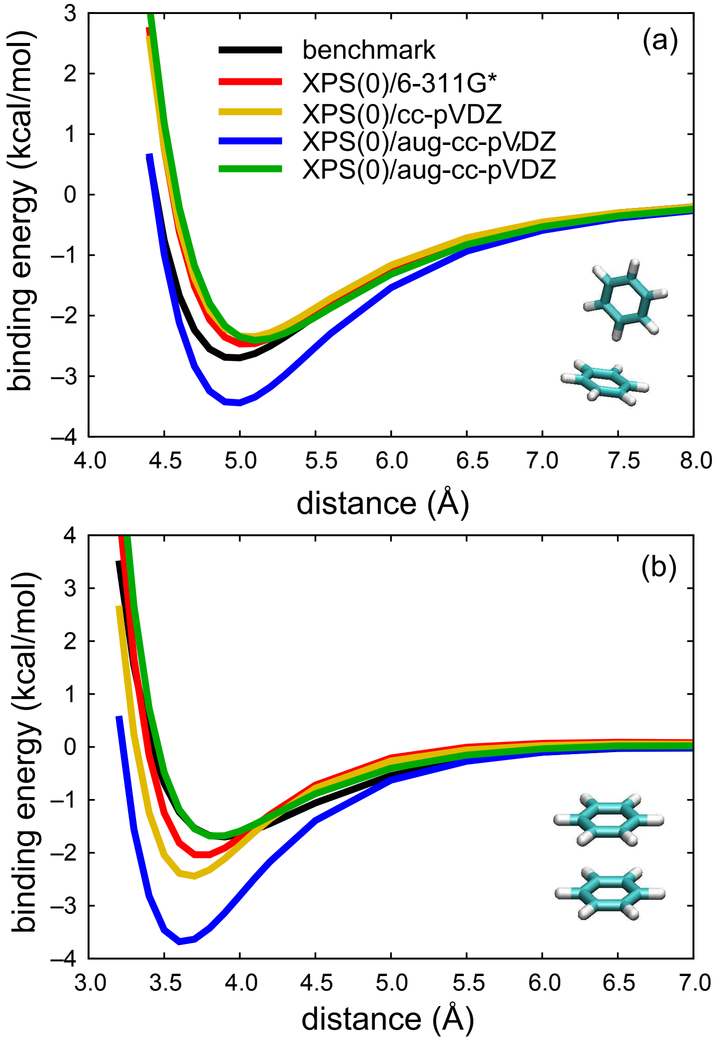

Figure 7.4: Binding energy curves for (a) the T-shaped and (b) the sandwich isomer of the benzene dimer. Benchmark CCSD(T)/CBS values are taken from Ref. [8]. The distance coordinate in both panels is the center-to-center distance between the benzene rings.

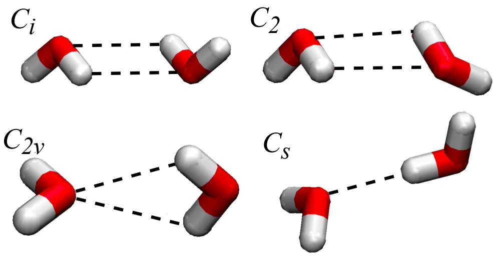

Figure 7.5: $(H_2O)_2$ structures consider in this work.

are pictured in Fig. 7.5. We investigate minimum energy paths (MEPs) along the oxygen–oxygen distance coordinate, relaxing the other degrees of freedom subject to the constraint that point-group symmetry is maintained. To obtain benchmark MEPs, we optimized the geometries at the MP2/aug-cc-pVTZ level and then used counterpoise-corrected MP2/aug-cc-pVXZ calculations (X = D, T, Q) to estimate the MP2/CBS binding energy. The HF energy was extrapolated using the three-point *ansatz*

$$E(X) = E(\infty) + ae^{-bX} \ , \tag{7.34}$$

where a and b are fitting parameters.[115] The correlation energy was extrapolated using a two-point formula (X = T, Q),

$$E(\infty) = E(X) + cX^{-3} \ , \tag{7.35}$$

where c is a fitting parameter.[116]

Figure 7.6 compares these MP2/CBS benchmark MEPs to XPS(0)-CHELPG results, using a variety of basis sets. The salient features of the MP2 benchmarks that we would like to capture with XPS are:

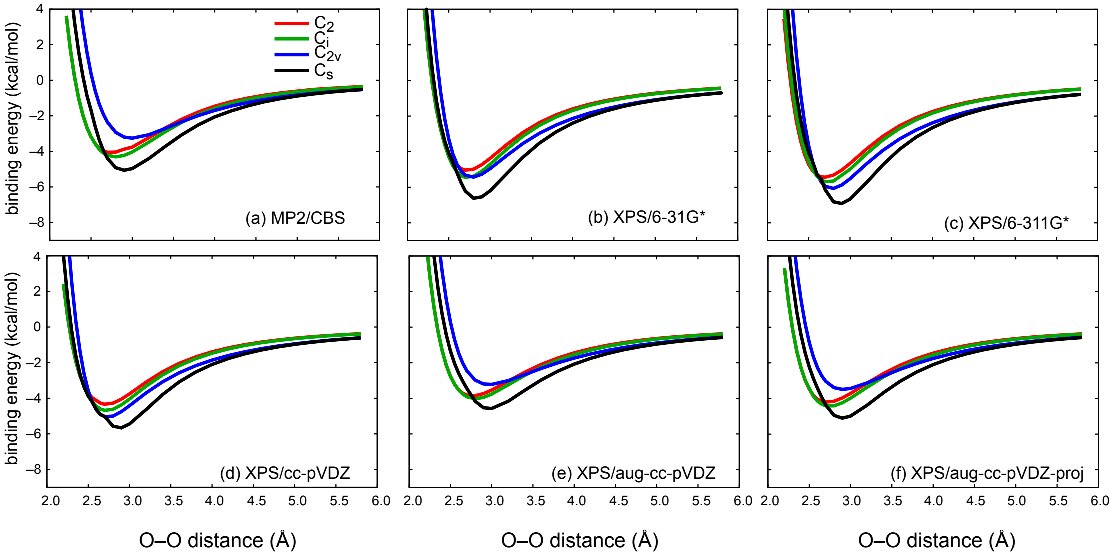

Figure 7.6: Binding energy curves for four symmetry-distinct $(H_2O)_2$ isomers shown in Fig. 7.5: (a) MP2/CBS benchmarks, and (b)–(f) XPS(0) results using a variety of basis sets. Löwdin and CHELPG embedding charges afford essentially identical potential curves, so only the latter are shown.

(*i*) the global minimum along the C_s curve at $R_{\text{O}-\text{O}} \approx 2.9$ Å;

(*ii*) a C_{2v} curve with a minimum at the same value of $R_{\text{O}-\text{O}}$ but higher in energy by ≈ 2 kcal/mol;

(*iii*) C_2 and C_i curves having minima at $R_{\text{O}-\text{O}} \approx 2.75$ Å located about 1 kcal/mol above the C_s minimum; and

(*iv*) C_2 and C_i curves that coalesce at $R_{\text{O}-\text{O}} \approx 2.5$ Å, which results from a collapse to C_{2h} symmetry.[308]

Panels (b)–(e) of Fig. 7.6 show that it is relatively easy to obtain features (*i*), (*iii*), and (*iv*), even if the binding energies are not in agreement with the benchmark values. However, feature (*ii*) is reproduced only if we use an augmented basis set. With the aug-cc-pVDZ basis, the XPS(0) method reproduces the relative energetics of the four MEPs quite well but the curves are slightly (≈ 0.5 kcal/mol) underbound at the C_s minimum, which is pushed out to about 3.0 Å. While the 0.5 kcal/mol underbinding represents only about a 10% error at the minimum, this will add up to fairly significant errors when applied to large water clusters.

Our XPS calculations use the MCBS, in which the MOs of fragment A are expanded in terms of only those AOs that are centered on atoms in fragment A. For this reason, one could argue that we have neglected charge-transfer interactions. (However, some charge-transfer-like interaction must certainly be present, since the basis functions on fragment A do extend over fragment B.) It would be useful to have a basis that mimics the DCBS that is often used in SAPT calculations for dimers,[290] but it is not clear how to generalize this idea to the case of more than two fragments.

As an alternative, we have utilized what we call the projected ("proj") basis set, borrowing an idea from dual-basis MP2 calculations.[259, 309] We first solve the XPol SCF equations and then, for a particular pairwise SAPT(0) correction, we construct the XPol Fock matrices for fragments A and B in the dimer (A + B) basis set. We then separately diagonalize the occupied-occupied and virtual-virtual blocks of these matrices, which is sometimes called "pseudo-canonicalization". This procedure leaves the fragment densities and and zeroth-order fragment energies unchanged, but provides a larger set of virtual orbitals that extend over the partner fragment. We use this larger virtual space to perform the perturbative correction. Because the occupied-virtual block of the Fock matrix is non-zero, the pseudo-canonical MOs are not rigorous eigenfunctions of the fragment Fock matrices. In principle, we could include a perturbative correction to the zeroth-order energies, of the form $\sum_{ar} F_{ar}^{A}/(\epsilon_a - \epsilon_r)$ for fragment A. (In the context of MP2-like methods, this is sometimes called the "non-Brillouin singles" term.[49]) We decline to do so, however, as this would have the effect of re-introducing BSSE. Instead, our aim is to enlarge the virtual space in a manner that can account for interfragment charge transfer.

As compared to SAPT(0) calculations performed with the DCBS, we find that the use of this "projected" basis set (aug-cc-pVDZ-proj) results in about a 10% error in the $(H_2O)_2$ binding energy. However, most of this error is contained in the $E_{exch}^{(1)}$ correction, and the components involving virtual orbitals carry an error of $< 1\%$.

Therefore, if the aim is to increase the virtual space without changing the zeroth-order density, then this is a successful strategy. If the first-order corrections are converged in the MCBS, then this procedure should incur very little additional error.

XPS(0) binding energy curves for $(H_2O)_2$, using the projected basis, are shown in Fig. 7.6(f). They are qualitatively similar to those in the aug-cc-pVDZ basis but now the binding energies are in good agreement with MP2/CBS results. Interestingly, if we take the difference in the binding energies computed in the aug-cc-pVDZ MCBS and in the corresponding projected basis set as an estimate of the charge-transfer interaction energy, then charge transfer accounts for only about 10% of the $(H_2O)_2$ interaction energy, a figure that is substantially smaller than that estimated by energy decomposition analysis in the ALMO basis.[50] In Ref. [50], it was also reported that the charge-transfer component of the interaction energy is significantly larger when DFT is used to compute the ALMOs. In the context of the present work, this observation may indicate that the strong underbinding of hydrogen-bound complexes by XPS(KS) may be an artifact of the use of the MCBS. Use of the projected basis significantly decreases the XPS(KS) errors for the S22 database (see Table 7.2). We plan to explore this issue further in future work.

7.5 Water clusters

We have demonstrated that our method does not degrade the results of SAPT(0) for the S22 database, and furthermore that we can describe binding energy curves of benzene dimer with reasonable accuracy, and those of water dimer with high accuracy.

Our ultimate goal, however, is application to larger clusters and molecular liquids. In this section, we evaluate the binding energies predicted by our method for a set of water clusters, in order to determine whether many-body effects are accurately reproduced by XPS.

We have assembled a database of 19 $(H_2O)_n$ isomers ranging from $n = 2$ to $n = 20$. Structures and benchmark binding energies for these clusters are taken from the work of Xantheas and co-workers.[92, 310–314] The data set includes MP2/CBS binding energies for the dimer; the cyclic trimer, tetramer, and pentamer; the ring, book, cage, and prism isomers of the hexamer; and the S_4 and D_{2d} isomers of the octamer. In addition, it includes binding energies for five different $(H_2O)_{11}$ isomers, computed at the MP2/aug-cc-pVQZ//MP2/aug-cc-pVTZ level. (Following Ref. [313], these isomers are labeled $43'4$, $44'3'$, 515, 551 and $44'12$.) Lastly, we include MP2/CBS binding energies for four $(H_2O)_{20}$ isomers,[92] one from each of the four families of low-lying minima (dodecahedron, fused cubes, face-sharing pentagonal prisms, and edge-sharing pentagonal prisms) exhibited by the 20mer. Binding energies for all of the benchmarks are computed relative to relaxed monomers.

In larger clusters, a meaningful comparison of binding energies between different levels of theory should employ geometries that are optimized, separately, at either level of theory. For XPS calculations, geometries were optimized using a three-point finite-difference algorithm in cartesian coordinates, and were considered to be converged when the change in energy dropped below 10^{-6} hartree. This procedure is quite demanding, computationally, and for the $(H_2O)_{20}$ clusters with the larger basis sets (aug-cc-pVDZ and aug-cc-pVDZ-proj), it was necessary to reduce the convergence threshold to 10^{-4} hartree. Tighter optimization would necessarily increase the binding energies, which (as will become clear in what follows) would improve the agreement between XPS results and benchmark binding energies. However, we expect that the binding energies would increase by no more than a few kcal/mol, for clusters whose binding energies are $\sim$200 kcal/mol. As such, we believe that these $(H_2O)_{20}$ tests are still meaningful.

Figure 7.7(a) shows the correlation between the XPS(0) and the benchmark binding energies. In general, the basis sets that were overbinding for $(H_2O)_2$ are also overbinding in larger clusters. In addition, Löwdin embedding tends to afford lower binding energies than CHELPG embedding, indicating that the Löwdin charge scheme underestimates the dipole moments of the H_2O monomers. As was the case for the S22 benchmarks, the cc-pVDZ basis set affords a superb cancellation of errors and yields results in good agreement with the benchmark values.

Figure 7.7(b) plots the binding energy errors per hydrogen bond, as a function of the number of hydrogen bonds. In all cases, this error grows rapidly from one to five hydrogen bonds, but beyond this it is nearly a constant with respect to the number of hydrogen bonds. We interpret this as evidence that XPS(0) recovers a constant fraction of the many-body interaction energy in large water clusters.

Binding energies computed at the XPS(0)-CHELPG level, as well as percentage errors relative to MP2 benchmarks, are listed in Table 7.3. The best results are

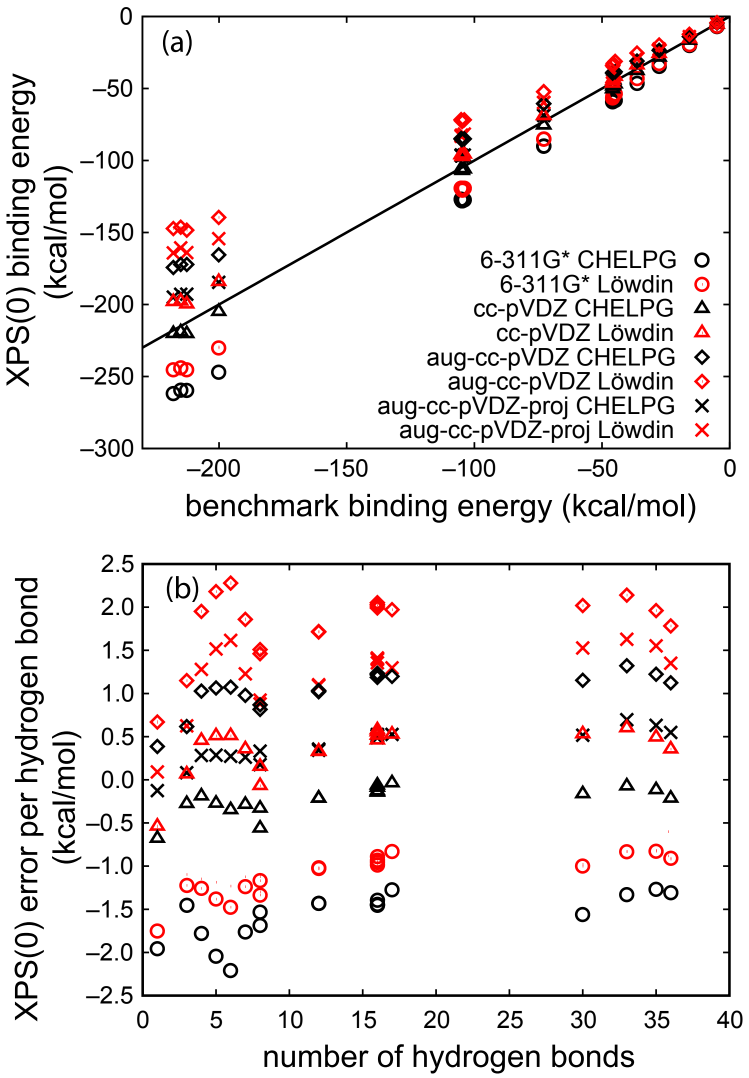

Figure 7.7: (a) Correlation between XPS(0) binding energies and MP2 benchmarks. (b) XPS(0) error per hydrogen bond, as a function of the number of hydrogen bonds.

n	Isomer	XPS(0)-CHELPG								Benchmark
		6-311G*		cc-pVDZ		aug-cc-pVDZ		aug-cc-pVDZ-proj		
2		6.9	(39.4)	5.6	(13.7)	4.6	(7.8)	5.1	(2.5)	4.97
3		20.2	(27.6)	16.6	(5.3)	14.0	(11.7)	15.6	(1.6)	15.82
4		34.8	(25.8)	28.4	(2.7)	23.5	(14.9)	26.5	(4.1)	27.63
5		46.5	(28.1)	37.7	(3.8)	31.0	(14.7)	34.9	(3.9)	36.31
6	book	57.9	(27.0)	47.6	(4.4)	38.8	(15.0)	43.8	(4.0)	45.61
6	cage	58.0	(26.7)	48.4	(5.8)	38.8	(15.2)	43.8	(4.2)	45.79
6	cyclic	58.1	(29.6)	47.0	(4.7)	38.4	(14.3)	43.2	(3.7)	44.86
6	prism	59.4	(29.4)	50.4	(9.8)	39.3	(14.2)	44.5	(3.1)	45.86
8	D_{2d}	90.1	(23.6)	75.5	(3.5)	60.5	(17.0)	68.6	(5.9)	72.88
8	S_4	90.0	(23.6)	75.4	(3.5)	60.6	(16.8)	68.7	(5.6)	72.83
11	$43'4$	126.8	(20.6)	105.8	(0.6)	84.8	(19.4)	96.2	(8.5)	105.16
11	$44'3'$	128.0	(22.2)	107.1	(2.2)	85.3	(18.6)	96.6	(7.8)	104.76
11	515	127.4	(21.2)	106.1	(1.0)	85.4	(18.8)	96.7	(8.0)	105.09
11	551	128.0	(22.0)	106.4	(1.4)	85.5	(18.5)	96.8	(7.8)	104.95
11	$44'12$	127.2	(22.4)	106.0	(2.0)	85.0	(18.3)	96.2	(7.5)	103.97
20	dodecahedron	247.0	(23.4)	205.0	(2.5)	165.5	(17.3)	184.6	(7.7)	200.10
20	edge-sharing	261.8	(20.1)	220.3	(1.1)	174.3	(20.0)	194.9	(10.6)	217.90
20	face-sharing	259.4	(20.6)	219.1	(1.9)	172.2	(19.9)	192.9	(10.3)	215.00
20	fused cubes	259.7	(22.1)	220.4	(3.6)	172.2	(19.0)	192.8	(9.3)	212.60

Table 7.3: Negative binding energies for $(H_2O)_n$ cluster isomers, in kcal/mol. Percent errors in the XPS binding energies, relative to the benchmarks, are listed in parentheses.

Isomer	XPS(0)-Löwdin		XPS(0)-CHELPG		Benchmark
	cc-pVDZ	aug-cc-pVDZ-proj	cc-pVDZ	aug-cc-pVDZ-proj	
dodecahedron	184.2 (7.9)	154.3 (22.9)	220.4 (3.6)	184.6 (7.7)	200.10
edge sharing	198.1 (9.1)	164.2 (24.7)	220.3 (1.1)	192.8 (9.3)	217.90
face sharing	197.8 (8.0)	160.7 (25.3)	219.1 (1.9)	192.9 (10.3)	215.00
fused cubes	199.8 (6.0)	164.0 (22.9)	220.4 (3.6)	192.8 (9.3)	212.60

Table 7.4: Negative binding energies for $(H_2O)_{20}$ clusters, in kcal/mol. Percent errors in the XPS binding energies, relative to the benchmarks, are listed in parentheses.

obtained using the cc-pVDZ and aug-cc-pVDZ-proj basis sets. The cc-pVDZ, aug-cc-pVDZ and aug-cc-pVDZ-proj basis sets all reproduce the correct energetic ordering of the $(H_2O)_6$ isomers, even though the error in the binding energy is greater than the energetic difference between these isomers. The same is not true for the octamers and endecamers, although the energy differences among these isomers amount to only about 1% of the total binding energies. It is difficult to compare the relative energies of the $(H_2O)_{20}$ isomers since our geometries are not fully relaxed, but in all cases the dodecahedron is correctly identified as the highest-energy isomer.

As can be seen in Table 7.3, the water dimer is overbound by 14% using the cc-pVDZ basis while the larger water clusters are overbound by $\sim$2%. In contrast, the aug-cc-pVDZ-proj basis accurately reproduces the dimer binding energy but underestimates the $(H_2O)_{20}$ binding energies by about 10%. Using the aug-cc-pVDZ basis set, the error grows from 8% at $n = 2$ to 20% at $n = 20$. We interpret these findings as an indication that, for a fixed pairwise error, our method recovers $\sim$90% of the interaction energy when used with CHELPG embedding charges. A smaller fraction of the interaction energy is recovered using Löwdin charges, as shown in Table 7.4, and by a similar argument we conclude that the XPS(0)-Löwdin method recovers $\sim$80% of the interaction energy. By performing single-point energy calculations on the $(H_2O)_{20}$ isomers at the optimized XPS(0)-CHELPG geometries, we find that traditional pairwise SAPT(0) in the aug-cc-pVDZ-proj basis recovers $\sim$70% of the binding energy. This indicates that roughly 30% of the binding energy in these clusters comes from many-body effects, and we recover about 2/3 of this using XPS(0) with CHELPG embedding charges.

7.6 Computational expense

We intend XPS as a method for large systems, so let us comment on its computational scaling. The first step in an XPS calculation, solving the XPol SCF equations, scales linearly with N_{frag}, assuming that construction and diagonalization of the fragment Fock matrices is much more demanding than formation of the one-electron integrals needed to compute the electrostatic interactions between the fragment densities and the embedding charges. (Even the latter step can ultimately be made to scale linearly by exploiting fast-multipole techniques.[232]) Increasing the size of the basis set formally scales as $\mathcal{O}(N_{basis}^4)$ for Fock matrix construction and $\mathcal{O}(N_{basis}^3)$ for diagonalization.

In the second step of XPS, we perform $N_{frag}(N_{frag} - 1)/2$ independent, pairwise SAPT(0) corrections, so this step scales as $\mathcal{O}(N_{frag}^2)$ and dominates the total cost in our present, serial implementation. Figure 7.8 shows actual timings for water

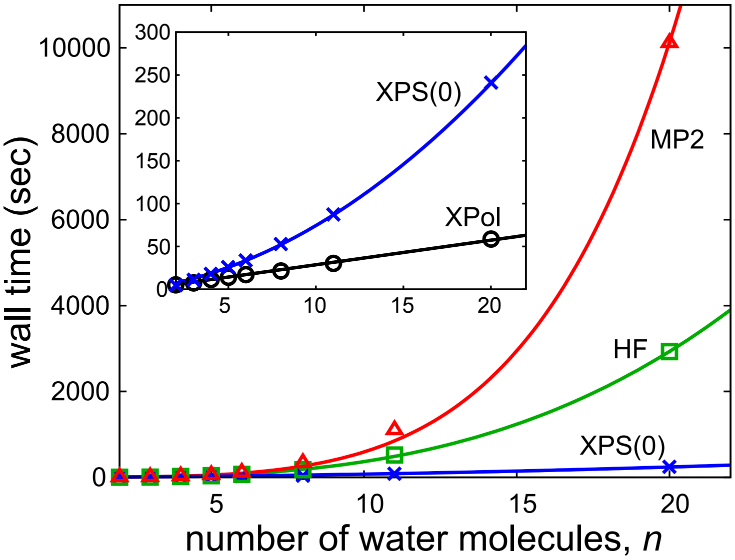

Figure 7.8: Wall time required for XPS(0), HF, and MP2 calculations in $(H_2O)_n$ clusters. The inset shows the XPS(0) and XPol timings in more detail. The solid curves are fits to polynomials representing theoretical scalings: n^5 for MP2, n^3 for HF, n^2 for XPS(0), and n for XPol.

clusters, as compared to timings for supersystem HF and MP2 calculations. Already in its present implementation, XPS can be scaled up to quite large water clusters.

Each pairwise correction in SAPT(0) and XPS(0) requires integrals of the form $(aX|bY)$, where $a \in A$ and $b \in B$ are occupied MOs, whereas X and Y range over all occupied and virtual MOs on both fragments. We compute these integrals by first computing all N_{basis}^4 AO integrals $(\mu\nu|\lambda\sigma)$, which represents some unnecessary overhead in the MCBS. The AO integrals are transformed in four steps that scale as $\mathcal{O}(N_o^A N_{basis}^4)$, $\mathcal{O}(N_o^A N_o^B N_{basis}^3)$, $\mathcal{O}(N_o^A N_o^B N_{MO}^{AB} N_{basis}^2)$ and $\mathcal{O}[N_o^A N_o^B (N_{MO}^{AB})^2 N_{basis}]$, where N_o^A is the number of occupied MOs on fragment A and N_{MO}^{AB} is the total number of MOs (occupied + virtual) on fragments A and B. The most time-consuming contraction step in the SAPT(0) correction is the accumulation of $E^{(2)}_{exch\text{-}disp}$, the bottleneck of which scales as $\mathcal{O}[(N_o^A)^2 N_o^B N_v^A N_v^B]$ where N_v^A is the number of virtual MOs associated with fragment A. [As such, the scaling of this step is usually reported as $\mathcal{O}(o^3v^2)$.[273, 275, 307]] We find that the integral transformation is at least one order of magnitude more expensive than the contractions.

In practice, the SAPT(0) corrections that we use in XPS exhibit a scaling similar to that of dimer MP2 calculations, with respect to either the size of the fragments or the size of the basis set. Stand-alone dimer SAPT(0) calculations are in general less expensive than supersystem MP2 calculations, since the occupied and virtual spaces in SAPT(0) are partitioned into components from fragments A and B, leading to an overall computational expense of $\mathcal{O}(N_o^A N_{basis}^4)$ for SAPT(0) versus $\mathcal{O}[(N_o^A + N_o^B)N_{basis}^4]$ for MP2.[307]

The exchange interactions in SAPT(0) decay rapidly as a function of interfragment distance, which could be exploited to reduce the cost of large XPS calculations by introducing cutoff schemes, such that the exchange corrections are evaluated only for nearby fragments. Thresholds could also be used to avoid accumulating dispersion and induction corrections for distant pairs. At very long range, the electrostatic interactions included at the XPol level may be sufficiently accurate to avoid computing $E^{(1)}_{elst}$ altogether. Parallelization of the $N_{frag}(N_{frag} - 1)/2$ independent SAPT(0) corrections is another obvious way to reduce the cost. We plan to explore such cost-reduction techniques in the future.

7.7 Summary and outlook

We have introduced a new quantum chemistry method for studying intermolecular interactions, which we call XPol/SAPT, or XPS. This method incorporates electronic induction, intermolecular electrostatic interactions, and intramolecular interactions at the SCF level, using a charge embedding scheme whose computational cost grows linearly with the number of monomers. Dispersion, exchange-repulsion, and intermolecular charge-transfer effects, along with corrections to the electrostatic charge embedding, are introduced by means of a pairwise, perturbative post-SCF correction. The monomers are allowed to be fully flexible.

In developing this method, our intention was to replace the need for Lennard-Jones parameters in the XPol procedure,[59] while preserving the favorable scaling of that method with respect to system size. We have demonstrated that the XPS method does not degrade, and in many cases improves upon, the results of traditional SAPT(0) calculations for molecular dimers. Given an appropriate choice of basis set and electrostatic embedding, XPS recovers $\sim 90\%$ of the binding energy of large water clusters, as compared to MP2/CBS benchmarks, whereas traditional pairwise SAPT(0) recovers $\sim 70\%$. In our present implementation, the cost of the post-XPol corrections scales quadratically with the number of monomers. The computational cost is already quite low for large clusters, if the monomers are small, and can ultimately be made to scale linearly with the number of monomers, by introducing appropriate distance-dependent cutoffs. Work along these lines, including an implementation using periodic boundary conditions, is currently in progress.

While the XPS method is promising with respect to both accuracy and efficiency, many future improvements must be explored. The poor scaling [$\mathcal{O}(N^5)$] of the SAPT corrections with respect to fragment size can be improved by using density-fitting techniques that have previously been introduced in the context of traditional SAPT calculations.[273, 275, 305, 307] A method for fragmenting the system across covalent bonds, such as that used in the original XPol method[57, 58] or in the fragment MO method,[247–249] will be needed in order to handle large monomers. These developments are currently being explored in our group.

The XPS method is systematically improvable, which may help to further improve the accuracy. In particular, a more rigorous formulation of the method—which goes beyond the pairwise approximation—is possible, as outlined in Section 7.2.4, and work along these lines is in progress. It may also be possible to incorporate Casimir-Polder-type dispersion formulas, as currently used in SAPT(DFT),[273, 275] in order to obtain better results when DFT is used to describe the monomers. At present, XPS results using KS orbitals are notably inferior to those obtained using HF orbitals.

CHAPTER 8

Future Directions

In this thesis we have argued that explicitly including many-body induction in a potential describing the interactions of an excess electron with water molecules can have large qualitative effects. Our model was applied to the bulk hydrated electron where we demonstrated that accounting for the electronic relaxation of the solvent, upon rapid changes in the solute density, can lead to large effects and new insights. We now have a model that appears to be applicable from small clusters to the bulk limit. This leaves us in a unique position to attempt to reproduce the cluster VDEs observed by photoelectron spectroscopy [4, 30, 34] and provide an interpretation of these experiments. This work is currently in progress.

At the heart of the photoelectron data is a debate over whether or not the excess electron prefers to reside on the surface of the cluster or in the interior. Evaluation of free energy profiles as a function of electron solvation may be insightful. Furthermore, we might conjecture that the isomers observed experimentally are free energy minima. One may be able to explore the energetic relationship of these isomers and estimate free energy barriers for conversion between isomers. The behavior and free energy profiles of an excess electron at the (infinite) air–water interface is also of interest

[315] and could potentially serve as a controlled test case for free energy calculations since the position of the surface is better defined than that of a cluster.

In order to construct a free energy profile for this system one might consider umbrella sampling along some coordinate that is collective; the distance between the center of the electron and the center of mass of the cluster, or perhaps the surface. To do this we must be able to constrain the *centroid* of the electron using a harmonic potential. Unfortunately adding a potential such as

$$U(r) = \frac{1}{2}k\left(\vec{r} - \vec{r}_0\right)^2, \tag{8.1}$$

where $\vec{r}_0$ is the desired position for the electron (which may be a function of the nuclear coordinates) would also constrain the extent of the wave function. If we were to use a CPMD-like algorithm to propagate the dynamics instead of a Born-Oppenheimer dynamics scheme we may be able to constrain the centroid of the electron without effecting its extent.

The algorithm developed in chapter 6 allows for a self-consistent treatment of excited states with our polarizable model. This in turn enables us to evaluate gradients and propagate dynamics on the excited state surfaces. We have argued that solvent induction is important when the density of the solute changes rapidly. This is the case in experiments investigating the relaxation dynamics of the solvated electron where the electron is photo-excited and the relaxation dynamics are followed. The Neumark group has argued that the extrapolation of relaxation dynamics in clusters supports the conclusion that the Isomer I data, measured first by Coe *et al.* are cavity isomers.[29, 139, 140, 142] No theoretical treatment of the relaxation dynamics in clusters has been reported and would be of interest.

The hydrated electron work reported in this thesis improves our understanding of the "blue-tail" of the optical absorption spectrum but our knowledge is still incomplete. We report states as being bound in a vertical sense, that is, they are bound if the excitation energy is lower than the binding energy. In our calculations there is an implicit boundary condition that the wave function go to zero at the edges of the grid. This condition enters through the analytic kinetic energy matrix elements, see appendix A of Ref. [106] for details. The low-lying states are most likely converged with respect to the size of the grid but higher lying states are not. It is not clear whether these states are bound and localized or unbound, free-electron states. It would be interesting to investigate alternative boundary conditions such as Siegert boundary conditions that require the wave function to be proportional to a plane wave at the boundary.[316] This has the added difficulty that the eigenvalues are complex and one may have to solve a Schrödinger equation for numerous wave vectors. However, this would allow one to calculate bound to continuum transitions (resonances) and improve our understanding of the qualitative nature of the highly excited states of the hydrated electron.

The XPS method introduced in chapter 7 is a promising route to extend wave function-based quantum chemistry to the condensed phase. Some improvements have been made since the writing of chapter 7 and many await future work. We have implemented density fitting [260–264] to increase the efficiency of the SAPT corrections and begun work on a parallel implementation. We have also reformulated the theory in a more rigorous manner which includes three-body induction effects, this is done as indicated by Eqs. 7.29, 7.30 and 7.31. The methodology should also be extended to better electrostatic descriptions such as using the fragment electron densities to compute electrostatic interactions as opposed to approximate point charges. In order for XPS to be useful as a means to compute on the fly energies and gradients for dynamics calculations we need to implement periodic boundary conditions for the XPol Fock matrix using either Ewald summation or the continuous fast multipole method.[232] It would also be useful to couple the XPS code to some efficient means of sampling the nuclear configuration space, such as configurationally biased Monte-Carlo algorithms.[172]

A final avenue of research is exploration of the "diagonal exchange" approximation introduced in chapter 7. This approximation appears to be effectively unexplored in electronic structure theory but may be of interest in a few contexts. For weakly interacting systems (molecular liquids and solids) it would be interesting to approximate the Hartree-Fock procedure by

$$\begin{aligned} E_{HF} &= \min_{\{\phi_i\}} \left(\langle \Phi_0^H | \hat{H}_{elec} \mathcal{A} | \Phi_0^H \rangle - \sum_{ij} \epsilon_{ij} (S_{ji} - \delta_{ji}) \right) \qquad (8.2) \\ &\approx \min_{\{\phi_i\}} \left[\langle \Phi_0^H | \hat{H}_{elec} \left(\frac{\prod_A N_A! \hat{\mathcal{A}}_A}{(\sum_A N_A)!} \right) \left(1 + \sum_A \sum_{B>A} \hat{\mathcal{P}}^{AB} \right) | \Phi_0^H \rangle - \sum_{ij} \epsilon_{ij} (S_{ji} - \delta_{ji}) \right] \end{aligned}$$

where $|\Phi_0^H\rangle$ is a Hartree product of spin orbitals and $\mathcal{A}_A$ is the antisymmetrizer for fragment A. This approximation is possible if one utilizes the ALMO *ansatz* for spin orbitals. The computational advantage is that the exchange interactions woule be constructed in a pairwise fashion. It would be interesting to see how closely one can approximate the Hartree-Fock solution with this approximation and would serve as a test of the diagonal exchange approximation.

This line of thinking can be taken further. A similar approximation can be used in a CIS scheme to compute approximate excited states. One could start from gas-phase molecular wave functions and use these to construct an exciton-like model, but one that includes exchange. It would be interesting to compare this to exciton models that neglect exchange. This type of methodology could also have applications in construction of diabats for studies of charge-transfer excitation since the charge on any fragment is easily constrained without relying on atom-centered charges as in constrained DFT calculations.[230, 231]

APPENDIX A

Supporting information for "A one-electron model for the aqueous electron that includes many-body electron–water polarization: Bulk equilibrium structure, vertical electron binding energy, and optical absorption spectrum"

A.1 Fit parameters

The fit parameters that ultimately define the PEWP-2 model are given in Table A.1. The nature of these parameters is described below.

- $a_{\rm ind}$: Coulomb damping parameters for electrostatic interactions between the electron and the inducible dipoles, using the modified Coulomb operator defined in Eq. (7) of the paper. These parameters (one for the H-atom dipoles and one for the O-atom dipoles) are obtained by a fit to the MP2 polarization potential.
- $a_{\rm perm}$: Coulomb damping parameters for electrostatic interactions between the electron and the permanent AMOEBA multipoles. These are fit, in conjunction with the repulsive potential, in order to reproduce the density maximum of the LRC-μBOP pseudo-wavefunction.

Parameter	Atomic site	Value (atomic units)
a_{ind}	oxygen	1.47027
a_{perm}	oxygen	1.077362
a_{ind}	hydrogen	0.514081
a_{perm}	hydrogen	0.840234
B_1	oxygen	1.035565
B_2	oxygen	0.999428
B_3	oxygen	0.40954
B_1	hydrogen	0.4
B_2	hydrogen	1.010174
B_3	hydrogen	0.463554
c_1	oxygen	-0.226083
c_1	hydrogen	-0.7930992
c_2	hydrogen	-0.03180506
c_3	hydrogen	0.892828395
z_1	oxygen	0.18013656
z_1	hydrogen	2.19453033
z_2	hydrogen	0.12620980
z_3	hydrogen	2.76886142

Table A.1: Parameters that define the PEWP-2 model.

- B_i: These are parameters that define the repulsive potential, as defined in Eq. (10) of the paper. There is one set of parameters B_i (i = 1,2,3) for H and one set of O.

- c_i, z_i: These are parameters that are used to fit the exchange-correlation potential to a sum of atom-centered Gaussian functions, as in Eq. (9) of the paper. There is one set of each parameter for the O sites and one set for the H sites.

A.2 Additional cluster benchmarks

A.2.1 Relative isomer energies

While the MP2/6-31(1+,3+)G* method affords accurate VEBEs, due to a lack of strong correlation effects and absence of significant orbital relaxation upon electron detachment,[317] accurate benchmarks for relative conformational energies demand a higher level of theory. To assess how well the model predicts the relative energies of $(H_2O)_n^-$ cluster isomers, we use MP2/CBS benchmarks, where "CBS" indicates extrapolation to the complete-basis limit, as described in our previous work.[3] Geometries for the benchmark clusters ($n = 4, 5, 6$) were optimized on the anion surface at the B3LYP/6-31(1+,3+)G* level, and were then re-optimized using the model potentials, in order to compare the relative energetics. We compare both the relative energies of the anion isomers, and also the relative energies of the neutral clusters at the same geometries, as the latter provides a sense of how well the neutral potential surface is described at typical anion geometries. The full set of isomer geometries is depicted in Ref. [3].

Figures A.1, A.2, and A.3 show the relative energy comparisons for $n = 4$, 5, and 6, respectively. For the tetramers, all of the model potentials reproduce the *ab initio* data surprisingly well, for both the neutral and anionic clusters. For the pentamers, however, only the polarizable models (PEWP-1 and PEWP-2) track the *ab initio* data well. In particular, the TB models gives a relatively poor description of the isomer "pent-5", placing it too high in energy by ∼5 kcal/mol in both the anion and neutral case. This poor description does not arise from any deficiency in the electron-water

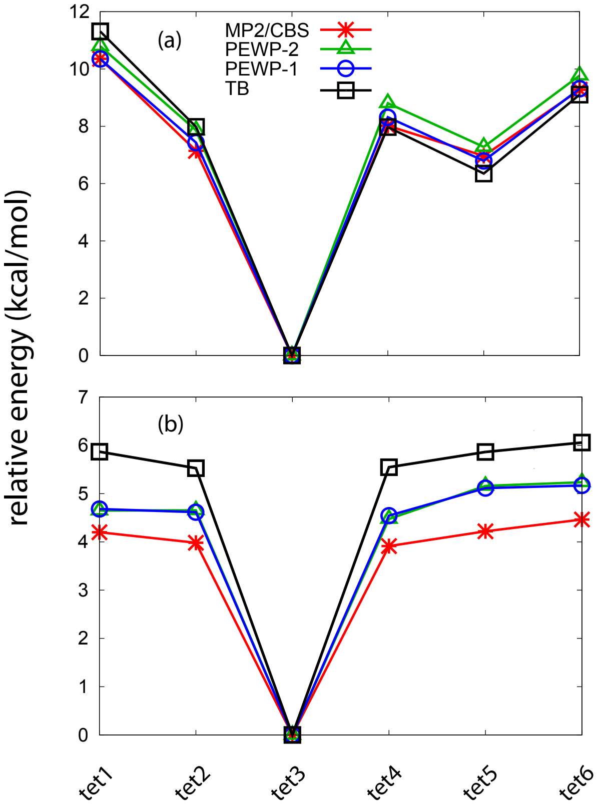

Figure A.1: Relative energies of (a) $(H_2O)_4$ cluster isomers and (b) $(H_2O)_4^-$ isomers at the same geometries, which represent stationary points on the anion potential energy surface. *Ab initio* geometries are from B3LYP/6-31(1+,3+)G*.

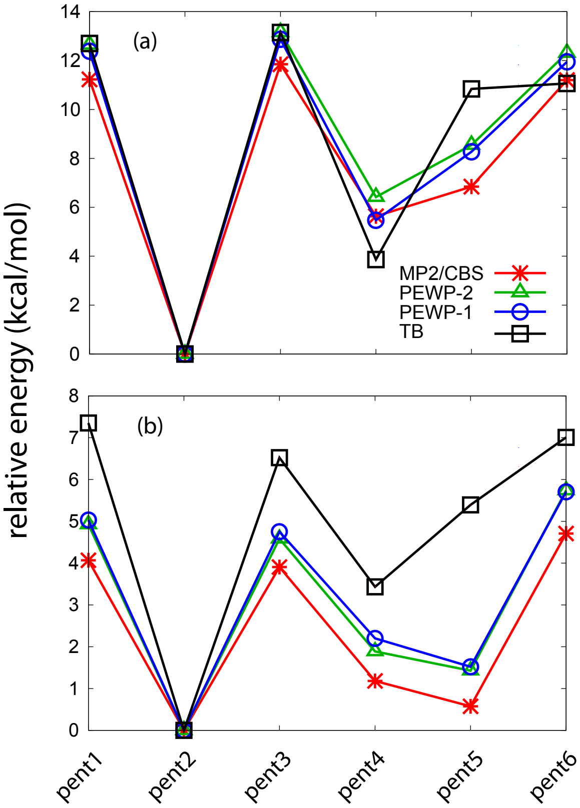

Figure A.2: Relative energies of (a) $(H_2O)_5$ cluster isomers and (b) $(H_2O)_5^-$ isomers at the same geometries, which represent stationary points on the anion potential energy surface. *Ab initio* geometries are from B3LYP/6-31(1+,3+)G*.

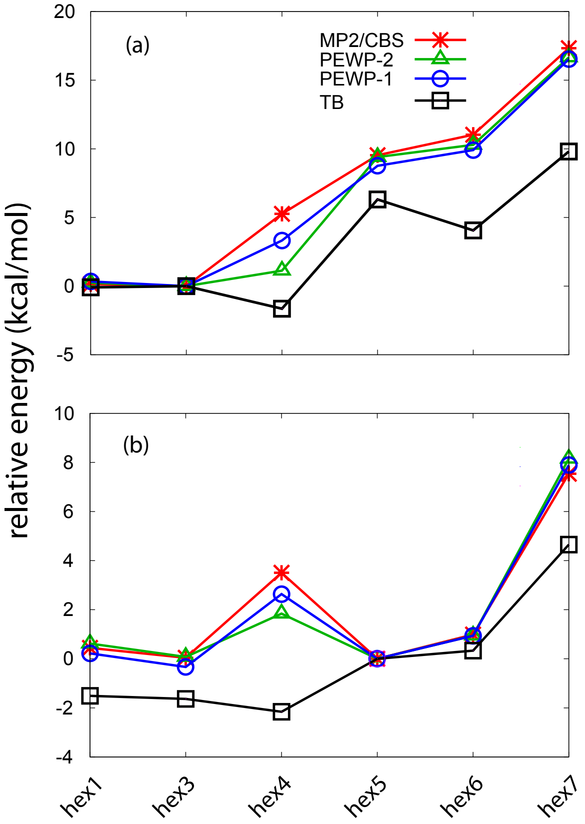

Figure A.3: Relative energies of (a) $(H_2O)_6$ cluster isomers and (b) $(H_2O)_6^-$ isomers at the same geometries, which represent stationary points on the anion potential energy surface. *Ab initio* geometries are from B3LYP/6-31(1+,3+)G*.

interactions, but is due to the underlying water model, SPC, as discussed below.

A comparison is made in Fig. A.4 between the *ab initio* optimized geometries and those obtained using the TB model. Geometries from the PEWP-1 and PEWP-2 models are not shown, as they are nearly identical to the *ab initio* geometries. Optimization on the TB surface tends to rotate non-hydrogen-bonded (dangling) hydrogen atoms such that the water molecules lie in planes. Good examples of this are the isomers "tet-3" where all waters have been rotated into a plane, and "tet-5" where the three-dimensional cage-type structure collapses onto a plane. This rotation into planes seems not to affect the relative energies of the tetramers, although it does effect the pentamer and hexamer energies. In particular, the only geometry in which this rotation does not occur is pent-5. The waters in this geometry are not able to rotate because all of the hydrogen atoms, save for those associated with the "double acceptor" ("AA") water molecule, are involved in hydrogen bonds, and the aforementioned rotation would break these bonds. This apparently leaves this geometry quite high in energy.

As discussed previously,[3] we believe the source of this planarity problem is the lack of out-of-plane electrostatics. Effectively, the point charge water molecules are rotating into planes because they are aligning dipoles which must only have components in the plane of the molecule. This rotation does not occur with the AMOEBA model because it contains quadrupole (and induced dipole) components that do not lie in the plane of the water molecule. The SPC model is missing weaker electrostatic forces that stabilize non-planar configurations in the *ab initio* and PEWP-2

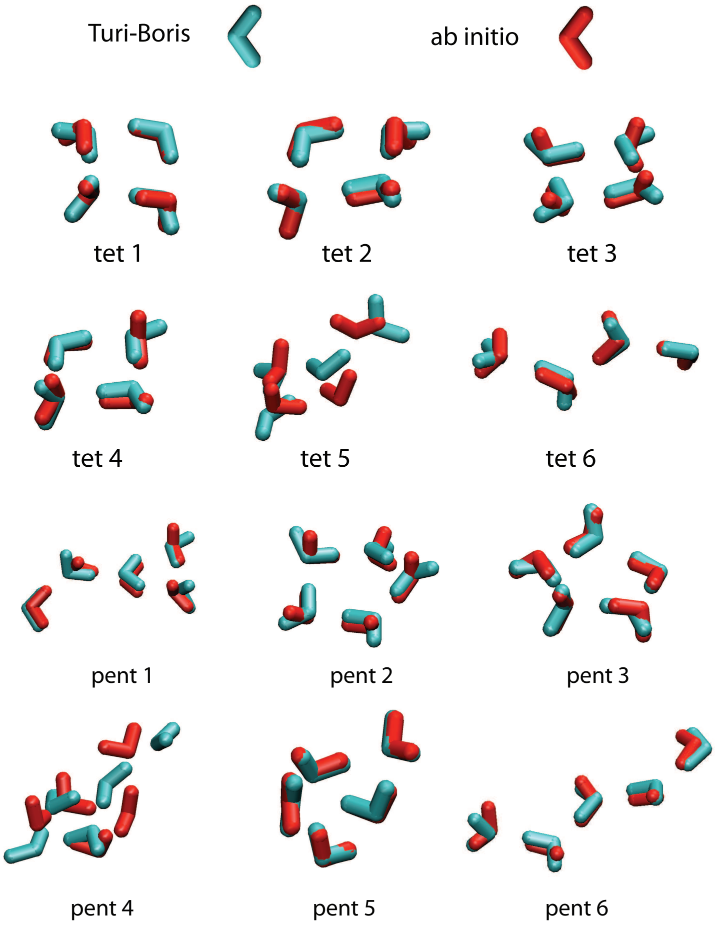

Figure A.4: Comparison of *ab initio* and TB geometries for the tetramer structures studied in this work. Geometries were optimized on the anion potential energy surface, and *ab initio* geometries are from B3LYP/6-31(1+,3+)G*.

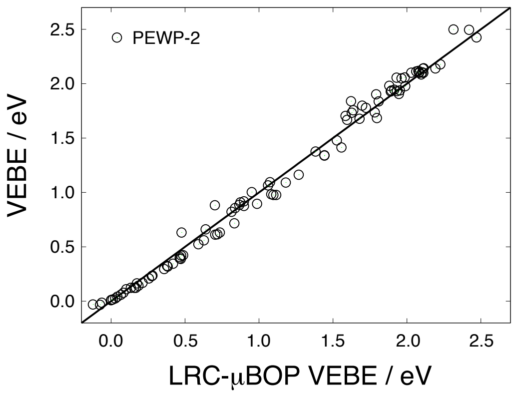

Figure A.5: Correlation of VEBEs computed using PEWP-2 with LRC-μBOP.

geometries.

A.2.2 VEBE of PEWP-2 compared to LRC-μBOP

Finally, we compare VEBEs computed with PEWP-2 to those obtained using LRC-μBOP. This comparison (see Fig. A.5) is made over our full database of 95 cluster geometries. The average absolute error for PEWP-2 compared to LRC-μBOP is 0.059 eV, however the average signed error is only -0.003 eV instead of -0.020 eV when compared to MP2. This indicates that, on average, the binding energies of PEWP-2 are in very good agreement with this density functional. This agreement is ultimately a sort of self-consistency check, since the exchange-correlation potential used to parameterize PEWP-2 was obtained from the LRC-μBOP functional.

APPENDIX B

Supporting information for “Polarization-bound quasi-continuum states are responsible for the ‘blue tail’ in the optical absorption spectrum of the aqueous electron”

This appendix provides additional details regarding the TD-DFT calculations and the calculations utilizing the one-electron model.

B.1 TD-DFT calculations

B.1.1 Functional and basis set

TD-DFT calculations employ a long-range-corrected (LRC) version of the “BOP” density functional, where BOP indicates the combination of the Becke exchange (B88) functional[318] with the “one-parameter progressive” (OP) correlation functional.[167] A short-range version of the B88 functional (μB88) was constructed according to the procedure described in Ref. [168], and the total exchange–correlation functional is

$$E_{xc}^{\mathrm{LRC}\text{-}\mu\mathrm{BOP}} = E_c^{\mathrm{OP}} + E_x^{\mu\mathrm{B88,SR}} + E_x^{\mathrm{HF,LR}} , \tag{B.1}$$

where “SR” and “LR” indicate that only the short-range or long-range parts of the Coulomb operator are used to evaluate certain energy components. Our group has implemented this and other LRC functionals[207, 299, 319] within the Q-Chem electronic structure program.[117] Within Q-Chem, the functional denoted in Eq. (B.1) is known as LRC-μBOP, although the value of the Coulomb attenuation parameter, μ, must be set by the user.

The LRC-μBOP functional with $\mu = 0.33\ a_0^{-1}$ has been shown to afford vertical electron binding energies (VEBEs) for $(H_2O)_n^-$ clusters that are comparable to those obtained at the CCSD(T) level.[3, 204] In addition, we have shown[206, 207] that LRC functionals with comparable values of μ remove the spurious, low-energy charge-transfer excited states that would otherwise be encountered in calculations such as these.[205] Inadvertently, we used a slightly different value for the Coulomb attenuation parameter, $\mu = 0.37\ a_0^{-1}$, for the TD-DFT calculations reported in this work, as opposed to the value $\mu = 0.33\ a_0^{-1}$ that was used in previous VEBE benchmarks. However, a comparison of TD-DFT excitation energies for these two values of μ, at a small number of randomly-chosen solvent configurations, reveals that the excitation energies differ on average by only 0.06 eV, and in no case by more than 0.09 eV.

As in earlier QM/MM calculations of bulk e_{aq}^-, carried out at the CIS level by Skrob *et al.*,[158] we use the 6-31+G* basis set for these calculations. Our own prior work on $(H_2O)_n^-$ clusters[1, 156, 320] has shown that somewhat more diffuse basis sets are necessary to describe weakly-bound isomers, but VEBEs for cavity-like isomers converge much more quickly as a function of the number of diffuse basis functions. Since the energy of the neutral cluster changes very little as additional diffuse shells

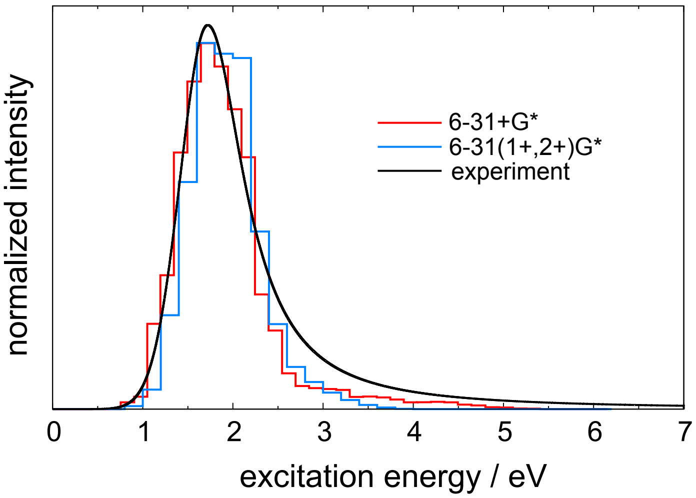

Figure B.1: Comparison of simulated TD-DFT absorption spectra, computed with the LRC-μBOP functional using two different basis sets.

are added, we regard convergence of the VEBE as evidence that the description of the singly-occupied MO (SOMO) has converged. It is worth noting that the most diffuse Gaussian basis function in the 6-31+G* basis set has a full width at half maximum of 4.6 Å, which is large compared to the distance between nearest-neighbor water molecules. The SG-1 quadrature grid[321] is used in all calculations, which has been shown to be adequate even in the presence of highly diffuse basis functions.[320] All TD-DFT calculations were performed using Q-Chem.[117]

As one marches up the manifold of states in the TD-DFT calculation, one expects that these states will become increasingly sensitive to the diffuseness of the basis set. Therefore as a check, we also computed the absorption spectrum using the same functional but a much more diffuse basis set, 6-31(1+,2+)G*, which includes two additional sets of diffuse *s* functions on the hydrogen atoms. (Details of the simulation procedure used to obtain the spectra are discussed in Section B.1.2 of this document.) Figure B.1 shows that the results are quite similar to those obtained with the more compact 6-31+G* basis. In particular, the peak absorption intensity and the width of the Gaussian feature are reproduced essentially quantitatively, while a non-trivial tail is observed at higher excitation energies. This blue tail is somewhat attenuated in the more diffuse basis set, because this basis lowers the energies of the higher-lying states to a much greater extent that for the first few excited states. To obtain significant intensity above $\sim$3.5 eV in the larger basis, we would need to compute a much larger number of excited states, which would make the calculations prohibitively expensive. For this reason, and because we are somewhat wary of having basis functions that extend well into the MM region, we report the 6-31+G* calculations in Fig. 1 of the manuscript.

B.1.2 Simulation procedure

Geometries for the TD-DFT calculations were obtained from a simulation of an excess electron in bulk liquid water. This simulation employed the one-electron pseudopotential model developed by Turi and Borgis,[67] a model that we selected because it has been used extensively in recent hydrated-electron simulations,[32, 67, 80–83, 153, 159] and because it provides a more accurate value for the e^-_{aq} absorption maximum than any other non-polarizable one-electron model. (Our polarizable model is more accurate in this respect, but we used the Turi–Borgis model for these calculations because

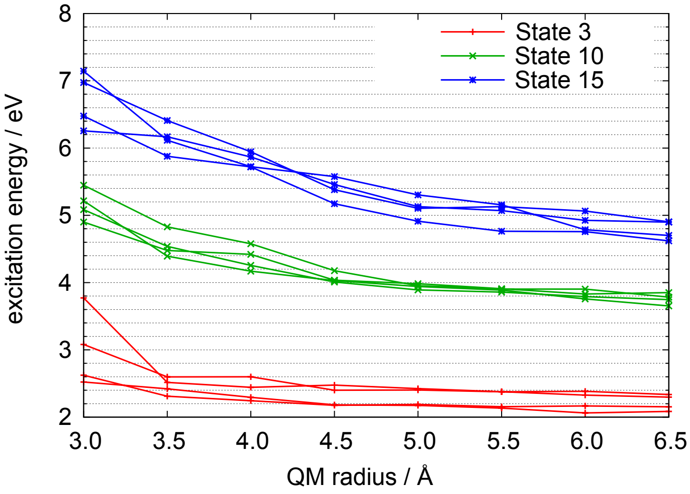

Figure B.2: Convergence of the TD-DFT [LRC-μBOP/6-31+G*] excitation energies as a function of the radius of the QM region, for three different randomly-selected snapshots taken from a bulk e^-_{aq} simulation.

we wanted the TD-DFT calculations to be completely independent of the calculations performed using our own one-electron model, in order to report results from two completely independent computational paradigms.)

Four independent, equilibrated trajectories were propagated at $T = 298$ K, using a simulation code that we have described previously.[3] These simulations were performed in a periodic unit cell, 18.1671 Å on a side, and snapshots were extracted every 0.5 ps. All H_2O molecules having an O or H atom within 5.5 Å of the centroid of the electron's wavefunction were described using DFT (corresponding to an average of 28 water molecules in the QM region), whereas remaining water molecules (out to a distance of 50 Å from the centroid of the wavefunction, or $\sim 18,000$ water molecules) were described using point charges ($q_{\mathrm{O}} = -0.82, q_{\mathrm{H}} = +0.41$). The 5.5 Å radius for the QM region was chosen based upon convergence tests (see Fig. B.2) for a small number of snapshots, which reveal that the first ten excitation energies are converged at this size, and the next five states are nearly converged (to within ∼0.1–0.2 eV).

In all, 124 snapshots were used to construct the histogram that appears in Fig. 1 of the paper. The overall shape of this histogram is unchanged if the number of snapshots is reduced by a factor of two, although somewhat larger bin widths are then required to obtain a smooth spectrum. We take this as an indication that the spectrum is converged with respect to statistical sampling of liquid configurations.

B.2 One-electron model

Our one-electron model is based upon a polarizable electron–water pseudopotential that we have recently developed. For details regarding the construction of this model and its performance relative to various experimental and *ab initio* benchmarks, the reader is referred to Ref. [184]. Previously, we had developed an alternative pseudopotential for $(H_2O)_n^-$ calculations,[3] but subsequent analysis, as documented in Ref. [43], demonstrated that this potential is inappropriate for simulation of e_{aq}^- in bulk water.

In Ref. [184], we also discuss the convergence of the bulk e_{aq}^- calculations with respect to the simulation cell size, which is an important issue for these excited-state calculations. Based upon these tests, the calculations described in this work utilize a cubic simulation cell of length 26.2015 Å that contains 600 water molecules, corresponding to a water density of 0.997 g/cm^3, at $T = 298$ K. This cell size is more than sufficient to converge structural properties and low-lying excitation energies. (The radii of gyration of the p states are essentially independent of simulation cell size, for example.[184]) The higher excited states ($\sim$3 eV and above) are probably not (quite) converged, even in this very large box, hence we list their radii of gyration as simply "$>$ 10 Å", since this value would increase somewhat in a larger simulation cell. A larger simulation cell would likely red-shift the "higher bound states" in Fig. 2(b) of the paper, thus improving the agreement with the experimental line shape. Because the mixed quantum/classical dynamics is rather expensive in these larger cells, we have not done this calculation.

Absorption spectra are computed using several independent, ground-state trajectories for e^-_{aq} in the aforementioned periodic box. Each simulation is $\approx$ 21 ps in length, and is propagated with a time step of 1 fs using flexible water molecules and full Ewald summation (as described in Ref. [184]) for the long-range electrostatics, and a Nosé-Hoover thermostat chain to simulate the NVT ensemble. The wavefunction is represented on a cubic grid with $\Delta x \approx 0.93$ eV. (Excitation energies appear to be converged with respect to Δx.) These simulations were performed with a home-built simulation code that we have described previously.[3] Following the ground-state trajectory calculations, we calculate the lowest 29 excitation energies from each of $\sim$1000 snapshots, and bin these to form an absorption spectrum.

APPENDIX C

Supplementary Material for "An efficient, fragment-based electronic structure method for molecular systems: Self-consistent polarization with perturbative two-body exchange and dispersion"

This appendix provides some additional theoretical details and benchmark calculations. Section C.1 is an expanded version of Section 7.2.2 of Chapter 7, and provides detailed equations for implementing the XPS method with either Mulliken, Löwdin, or CHELPG embedding charges. For CHELPG embedding charges, the original CHELPG algorithm[282] must be modified in order to avoid discontinuities as the nuclei are displaced (since CHELPG uses atom-centered Cartesian grids to discretize the electrostatic potential). The weighted least-squares procedure that is used to ensure continuity is discussed in Section C.2. Finally, in Section C.3, we present expanded versions of some of the figures and tables from the paper. These provide additional benchmark data, using a wider variety of basis sets and density functionals.

C.1 Details of the charge schemes

We investigate three different charge schemes: Mulliken, Löwdin and CHELPG. The Mulliken and Löwdin charges stem from two different partitions of the electron density,[12]

$$q_J^{\text{Mull}} = Z_J - \sum_{\substack{\mu\in J\\ \nu}} S_{\mu\nu} P_{\nu\mu} \tag{C.1a}$$

$$q_J^{\text{Lowd}} = Z_J - \sum_{\substack{\mu\in J\\ \nu,\lambda}} (\mathbf{S}^{1/2})_{\mu\nu} P_{\nu\lambda} (\mathbf{S}^{1/2})_{\lambda\mu} \ . \tag{C.1b}$$

Derivatives of these charges with respect to density matrix elements are quite simple:

$$(\Lambda_J^{\text{Mull}})_{\mu\nu} = -\frac{1}{2}\left(S_{\mu\nu}\delta_{\mu\in J} + S_{\nu\mu}\delta_{\nu\in J}\right) \tag{C.2a}$$

$$(\Lambda_J^{\text{Lowd}})_{\mu\nu} = -\sum_{\lambda\in J} (\mathbf{S}^{1/2})_{\lambda\mu} (\mathbf{S}^{1/2})_{\nu\lambda} \ . \tag{C.2b}$$

The quantity $\delta_{\mu\in J} = 1$ if the basis function μ is centered on atom J, and is zero otherwise.

CHELPG charges[282] are designed to minimize the difference between the electrostatic potential, $\Phi(\vec{r})$, that is generated by the electron density, and the electrostatic potential, $\phi(\vec{r})$, that is generated by a set of atom-centered point charges. This minimization is performed subject to the constraint that the sum of the point charges equals the overall system charge, Q, and the potentials are evaluated at a set of grid points $\vec{R}_k$. The CHELPG charges are defined as those that minimize the quantity

$$\mathcal{L} = \sum_{k}^{N_{grid}} \left(\Phi_k - \phi_k\right)^2 + \lambda \left(\sum_{J}^{N_{atoms}} q_J - Q \right) \ , \tag{C.3}$$

where λ is a Lagrange multiplier. The true electrostatic potential at the ith grid point, $\Phi_k = \Phi(\vec{R}_k)$, is

$$\Phi_k = \sum_J^{N_{atoms}} \frac{Z_J}{\left|\vec{R}_k - \vec{R}_J\right|} - \sum_{\mu\nu} \left(I_k\right)_{\mu\nu} P_{\mu\nu} \ . \tag{C.4}$$

The electrostatic potential $\phi_k = \phi(\vec{R}_k)$ that is generated by the point charges is

$$\phi_k = \sum_J^{N_{atoms}} \frac{q_J}{\left|\vec{R}_k - \vec{R}_J\right|} \ . \tag{C.5}$$

Minimization of $\mathcal{L}$ with respect to variation of q_J defines the CHELPG charges:

$$q_J^{\text{CHELPG}} = (\mathbf{G}^{-1}\mathbf{e})_J - \left(\frac{\operatorname{tr}(\mathbf{G}^{-1}\mathbf{e}) - Q}{\operatorname{tr}(\mathbf{G}^{-1})}\right) \sum_K (\mathbf{G}^{-1})_{JK} \ . \tag{C.6}$$

Here, the matrix $\mathbf{G}$ is defined by

$$G_{IJ} = \sum_k^{N_{grid}} \left|\vec{R}_I - \vec{R}_k\right|^{-1} \left|\vec{R}_k - \vec{R}_J\right|^{-1} \tag{C.7}$$

and the vector $\mathbf{e}$ has elements

$$e_J = \sum_k^{N_{grid}} \frac{\Phi_k}{\left|\vec{R}_k - \vec{R}_J\right|} \ . \tag{C.8}$$

It is straightforward to take the derivative of Eq. (C.6) to obtain

$$\begin{aligned}(\Lambda_J^{\text{CHELPG}})_{\mu\nu} = &- \sum_K (\mathbf{G}^{-1})_{JK} \sum_k^{N_{grid}} \frac{(I_k)_{\mu\nu}}{\left|\vec{R}_k - \vec{R}_K\right|} \\ &+ \left(\frac{\sum_{KL} (\mathbf{G}^{-1})_{KL} \sum_k^{N_{grid}} (I_k)_{\mu\nu}^{-1} \left|\vec{R}_k - \vec{R}_K\right|^{-1}}{\operatorname{tr}(\mathbf{G}^{-1})}\right) \sum_K (\mathbf{G}^{-1})_{JK}\end{aligned} \tag{C.9}$$

In what follows, we will require an operator, $\hat{\Lambda}_J$, whose matrix elements are equal to $(\Lambda_J)_{\mu\nu}$ as given by Eq. (C.2) or Eq. (C.9). For CHELPG charges, this operator is trivially constructed by making the replacement $\mathbf{I}_k \rightarrow \hat{I}_k$ in Eq. (C.9). The operators corresponding to the matrices in Eq. (C.2) are less obvious, but it can be verified that the appropriate choice is

$$\hat{\Lambda}_J^{\text{Mull}} = -\tfrac{1}{2} \sum_{\mu,\nu \in J} \Big(|\mu\rangle (\mathbf{S}_J^{-1})_{\mu\nu} \langle \nu| + |\nu\rangle (\mathbf{S}_J^{-1})_{\nu\mu} \langle \mu| \Big) \tag{C.10a}$$

$$\hat{\Lambda}_J^{\text{Lowd}} = \sum_{\mu,\lambda,\sigma \in J} |\lambda\rangle (\mathbf{S}_J^{-1/2})_{\lambda\mu} (\mathbf{S}_J^{-1/2})_{\mu\sigma} \langle \sigma| \; . \tag{C.10b}$$

The quantities $\mathbf{S}_J^{-1}$ and $\mathbf{S}_J^{-1/2}$ in this equation refer to the inverse and inverse square-root of the *fragment* overlap matrix, for the fragment that contains atom J. At no point is it necessary to invert the supersystem's overlap matrix.

C.2 Weighted Least Squares CHELPG Charges

We have not yet implemented analytic gradients for the XPS method, so the geometry optimizations reported here were performed using a three-point finite difference of the total energy, with atomic displacements of 10^{-3} bohr. The number of CHELPG grid points may change as the nuclei are displaced, so to avoid discontinuities we replace the Lagrangian in Eq. (C.3) with a weighted Lagrangian,

$$\mathcal{L} = \sum_k^{N_{grid}} w_k \left(\Phi_k - \phi_k\right)^2 + \lambda \left(\sum_J^{N_{atoms}} q_J - Q \right) . \tag{C.11}$$

The weight w_k for grid point k is taken to be a product of short- and long-range weighting functions, $w_k = w_k^{short} w_k^{long}$. The short-range weight is itself a product over atomic weights, $w_k^{short} = \Pi_J A_k^J$, where

$$A_k^J = \begin{cases} 0 & \text{if } |\vec{R}_k - \vec{R}_J| < R_{cut,J}^{short} \\ \tau(|\vec{R}_k - \vec{R}_J|, R_{cut,J}^{short}, R_{on,J}) & \text{if } R_{cut,J}^{short} \leq |\vec{R}_k - \vec{R}_J| < R_{on,J} \\ 1 & \text{otherwise} \end{cases} \; . \tag{C.12}$$

The cutoff parameters $R^{short}_{cut,J}$ and $R_{on,J}$ are given below. The tapering function, τ, is taken from Ref. [322]:

$$\tau(R, R_{cut}, R_{\mathit{off}}) = \frac{(R - R_{cut})^2(3R_{\mathit{off}} - R_{cut} - 2R)}{(R_{\mathit{off}} - R_{cut})^3} \; . \tag{C.13}$$

To determine the long-range weight, we first find the minimum distance from the grid point $\vec{R}_k$ to any nucleus,

$$R^{min}_k = \min_J |\vec{R}_k - \vec{R}_J| \; . \tag{C.14}$$

Then

$$w^{long}_k = \begin{cases} 1 & \text{if } R^{min}_k < R^{long}_{cut} \\ 0 & \text{if } R^{min}_k > R_{\mathit{off}} \\ 1 - \tau(R^{min}_k, R^{long}_{cut}, R_{\mathit{off}}) & \text{otherwise} \end{cases} \tag{C.15}$$

To evaluate the weights, we set $R^{short}_{cut,J}$ equal to the Bondi radius for atom J. We set $R_{\mathit{off}} = 3.0$ Å, $R_{on,J} = R^{short}_{cut,J} + \Delta r$, and $R^{long}_{cut} = R_{\mathit{off}} - \Delta r$, where the quantity Δr controls how rapidly a grid point's weight is scaled to zero by the tapering function. We use a fairly small value, $\Delta r = 0.1$ bohr, because we were concerned about possible discontinuities arising on the length scale of the finite-difference steps. Although it may be necessary to increase this to ensure smoothness in molecular dynamics applications, we have not encountered difficulties in geometry optimizations.

C.3 Expanded Versions of Data Tables and Figures

Table C.1 is an expanded version of Table I from the paper, and provides a statistical summary of how XPS performs for the S22 database, when Mulliken embedding charges are employed. Table C.2 is an expanded version of Table II from the paper, and shows the XPS results for the S22 database using either Löwdin or CHELPG embedding charges. Figure C.1 expands upon Fig. 1 from the paper, and shows errors over the S22 database for several other density functionals, including B3LYP. (B3LYP results were not discussed in the paper because, in the context of XPS, they tend to be similar to—but of slightly lower quality than—PBE0 results.) Figures C.2 and C.3 are analogous to Figs. 3 and 4 in the paper, and show benzene dimer potential energy curves computed at the XPS(0) level, but for a wider variety of basis sets than were considered in the paper. Figure C.4 expands upon Fig. 7 from the paper and shows the performance of XPS(0) for water clusters, using a wider variety of basis sets. Numerical results for this wider variety of basis sets are provided in Table C.3.

Method	SCF method, X =											
	HF		B3LYP		BOP		PBE0		LRC-μBOP		LRC-ωPBEh	
SAPT(X)/3-21G*	0.84	(2.25)	0.97	(2.92)	1.32	(4.96)	1.01	(2.86)	0.82	(4.24)	0.68	(3.62)
SAPT(X)-*resp*/3-21G*	0.91	(2.72)	1.04	(5.23)	1.41	(5.67)	0.98	(3.89)	0.87	(4.61)	0.74	(4.53)
XPS(X)/3-21G*	1.04	(3.06)	0.92	(3.76)	1.31	(4.70)	0.84	(2.43)	0.81	(3.14)	0.65	(2.97)
XPS(X)-*resp*/3-21G*	1.10	(3.43)	0.91	(3.71)	1.28	(4.61)	0.84	(2.38)	0.80	(2.95)	0.65	(2.83)
SAPT(X)/6-31G*	0.79	(3.27)	1.76	(6.82)	2.02	(9.55)	1.52	(6.47)	1.56	(7.31)	1.45	(6.75)
SAPT(X)-*resp*/6-31G*	0.65	(2.48)	2.03	(7.88)	2.50	(9.21)	1.73	(6.50)	1.52	(7.33)	1.51	(7.36)
XPS(X)/6-31G*	0.56	(1.46)	1.43	(6.70)	2.00	(9.66)	1.33	(6.24)	1.10	(3.79)	0.99	(3.57)
XPS(X)-*resp*/6-31G*	0.90	(3.16)	1.39	(6.37)	1.87	(9.01)	1.28	(5.99)	0.80	(3.14)	0.82	(3.11)
SAPT(X)/6-311G*	1.24	(6.40)	2.27	(8.43)	2.58	(9.80)	2.07	(7.48)	1.88	(9.63)	1.90	(9.51)
SAPT(X)-*resp*/6-311G*	1.09	(5.51)	2.54	(10.44)	3.05	(11.19)	2.26	(9.20)	1.83	(9.55)	1.96	(10.04)
XPS(X)/6-311G*	1.11	(4.91)	2.20	(8.15)	2.99	(12.76)	1.98	(7.39)	1.71	(6.70)	1.72	(6.95)
XPS(X)-*resp*/6-311G*	0.57	(2.22)	2.05	(6.82)	2.54	(8.14)	1.81	(5.65)	1.16	(5.91)	1.41	(6.37)
SAPT(X)/cc-pVDZ	1.06	(4.45)	2.14	(6.79)	2.45	(9.58)	1.83	(6.27)	1.89	(8.30)	1.81	(7.76)
SAPT(X)-*resp*/cc-pVDZ	0.91	(3.72)	2.41	(8.75)	2.92	(9.41)	2.06	(7.46)	1.87	(8.34)	1.88	(8.37)
XPS(X)/cc-pVDZ	0.71	(1.94)	2.09	(7.44)	2.58	(10.11)	1.73	(6.81)	1.62	(5.93)	1.59	(5.83)
XPS(X)-*resp*/cc-pVDZ	0.50	(1.81)	2.02	(6.45)	2.52	(9.00)	1.66	(5.90)	1.38	(5.43)	1.42	(5.45)

Table C.1: Mean absolute errors and (in parentheses) maximum absolute errors for the the S22 database, in kcal/mol. A variety of SAPT(X) and XPS(X) variants are considered; note that SAPT(HF) is equivalent to the method that is traditionally called SAPT(0). All XPS methods use Mulliken charges for the electrostatic embedding.

Basis	XPS-Löwdin						XPS-CHELPG					
	HF		LRC-μBOP		LRC-ωPBEh		HF		LRC-μBOP		LRC-ωPBEh	
3-21G*	1.09	(3.52)	0.81	(3.01)	0.66	(2.87)	1.17	(3.95)	0.79	(2.57)	0.67	(2.46)
resp	1.11	(3.61)	0.81	(2.98)	0.66	(2.87)	1.17	(3.98)	0.79	(2.56)	0.67	(2.45)
6-31G*	0.73	(2.31)	0.91	(3.91)	0.93	(3.86)	0.87	(2.47)	0.87	(3.56)	0.90	(3.53)
resp	0.75	(2.40)	0.90	(3.88)	0.93	(3.88)	0.87	(2.55)	0.87	(3.54)	0.91	(3.55)
6-31+G*	0.90	(2.08)	2.52	(9.06)	1.94	(8.32)	0.89	(1.99)	2.56	(9.03)	1.98	(8.26)
resp	0.89	(1.99)	2.55	(9.12)	1.96	(8.40)	0.90	(2.10)	2.60	(9.05)	2.00	(8.32)
6-31+G**	1.11	(3.94)	2.76	(10.85)	2.22	(9.98)	1.03	(3.22)	2.73	(10.29)	2.20	(9.40)
resp	1.08	(3.75)	2.77	(10.84)	2.24	(10.03)	1.03	(3.08)	2.77	(10.30)	2.21	(9.46)
6-311G*	0.57	(2.76)	1.20	(6.52)	1.38	(6.92)	0.56	(2.32)	1.21	(6.20)	1.40	(6.67)
resp	0.54	(2.55)	1.18	(6.41)	1.37	(6.88)	0.54	(2.18)	1.20	(6.15)	1.40	(6.65)
6-311+G*	1.13	(6.63)	2.21	(12.31)	2.24	(12.25)	1.20	(6.73)	2.31	(12.55)	2.34	(12.48)
resp	1.11	(6.48)	2.22	(12.30)	2.25	(12.28)	1.20	(6.59)	2.34	(12.54)	2.37	(12.50)
6-311+G**	1.23	(7.12)	2.37	(12.75)	2.39	(12.54)	1.19	(6.60)	2.37	(12.39)	2.41	(12.20)
resp	1.18	(6.81)	2.36	(12.65)	2.39	(12.53)	1.19	(6.47)	2.39	(12.38)	2.43	(12.23)
cc-pVDZ	0.55	(2.04)	1.46	(6.39)	1.48	(6.30)	0.39	(1.12)	1.35	(5.72)	1.39	(5.68)
resp	0.51	(1.75)	1.44	(6.26)	1.47	(6.27)	0.38	(1.02)	1.35	(5.70)	1.39	(5.69)
aug-cc-pVDZ	1.52	(4.48)	2.46	(10.24)	2.71	(9.63)	1.26	(3.38)	2.21	(8.43)	2.49	(7.91)
resp	1.40	(3.80)	2.39	(9.91)	2.67	(9.52)	1.25	(3.39)	2.23	(8.40)	2.49	(7.91)
aug-cc-pVDZ′	—		—		—		1.31	(3.86)	—		—	
aug-cc-pVDZ-proj	—		—		—		1.31	(4.42)	1.66	(4.36)	2.05	(6.51)
aug-cc-pVDZ′-proj	—		—		—		0.75	(3.38)	—		—	

Table C.2: Mean absolute errors and (in parentheses) maximum absolute errors for the S22 database, in kcal/mol. A variety of XPS(X) variants are considered, using either Löwdin or CHELPG embedding charges. For several of the basis sets, the corresponding response (“*resp*”) result is also listed. The primed and projected (“proj”) basis sets are defined in the paper.

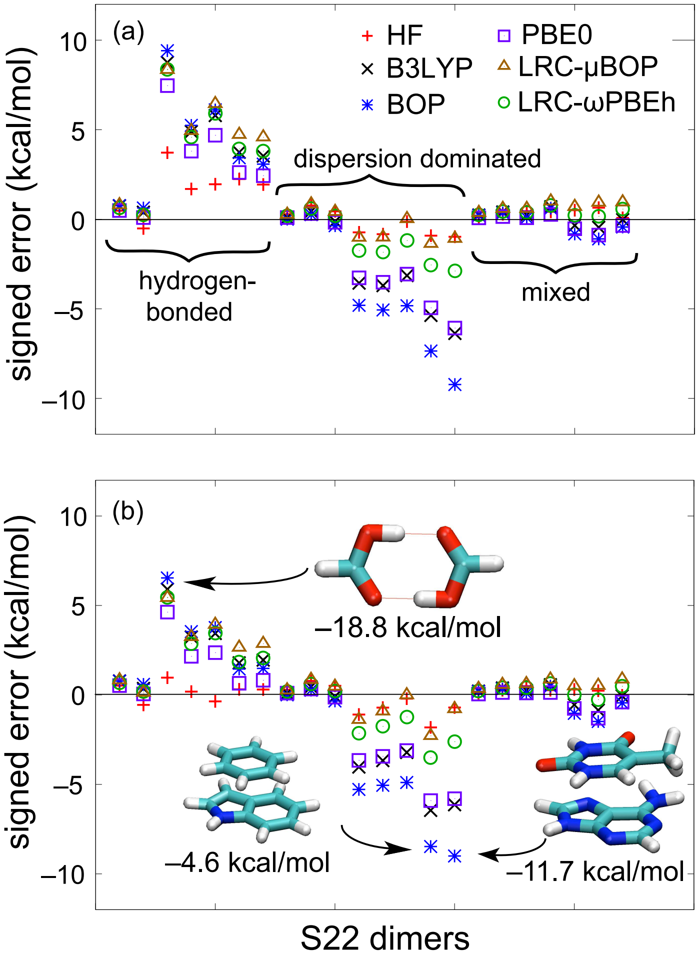

Figure C.1: Binding energy errors (in kcal/mol) across the S22 database, as computed at (a) the SAPT(X)/cc-pVDZ level (for various SCF methods, X) and (b) the XPS(X)/cc-pVDZ level, for a variety of different density functionals, X. A few difficult cases are highlighted in panel (b). Starting at the top and moving clockwise around panel (b), these are formic acid dimer, an indole-benzene π stack, and an adenine-thymine π stack.

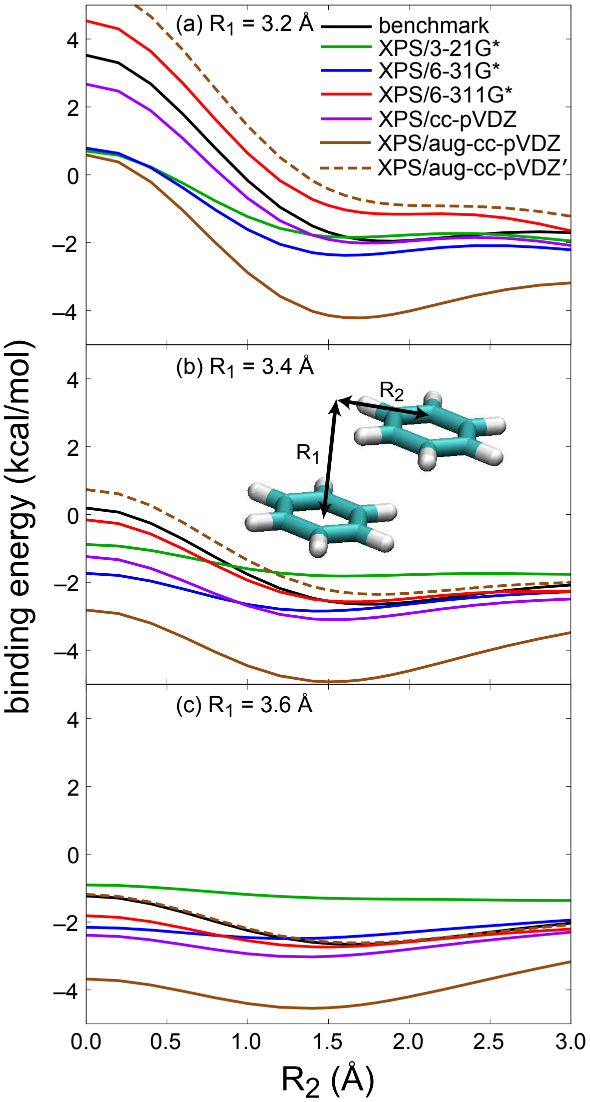

Figure C.2: Benchmark and XPS(0) binding energy curves for the parallel-displaced benzene dimer, computed at the XPS(0) level using CHELPG charges. CCSD(T)/CBS benchmarks are taken from Ref. [8].

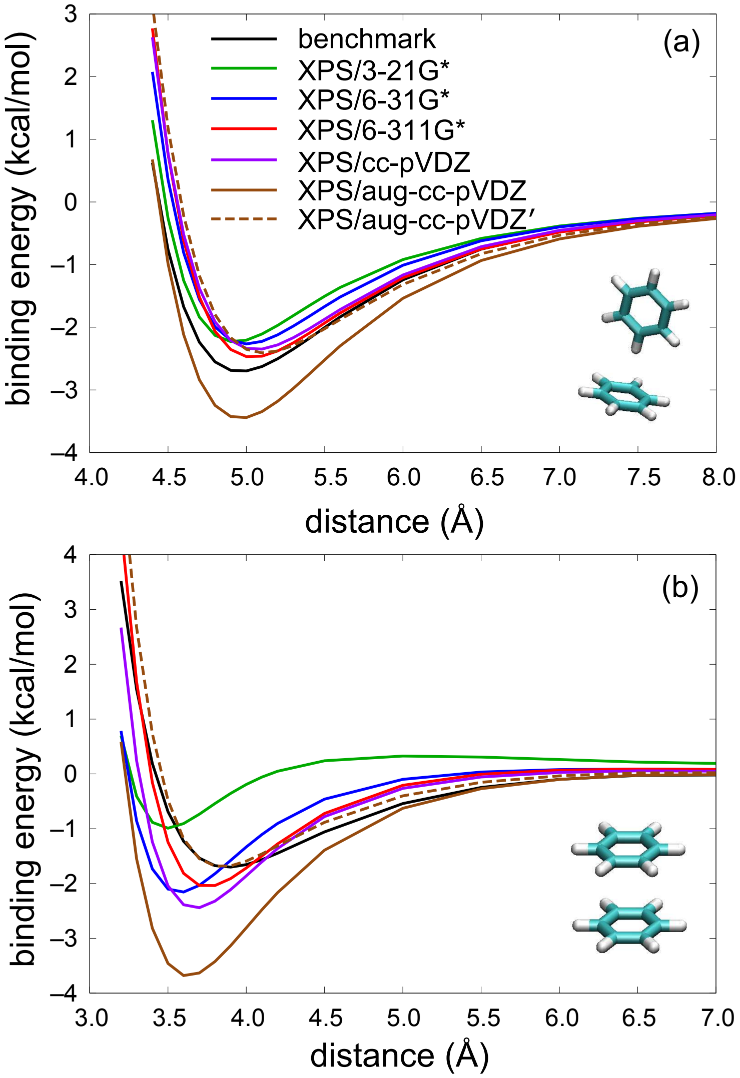

Figure C.3: Benchmark and XPS(0) binding energy curves for (a) the T-shaped and (b) the "sandwich" isomers of the benzene dimer. Benchmark CCSD(T)/CBS values are taken from Ref. [8]. The distance coordinate in both panels is the center-to-center distance between the benzene rings.

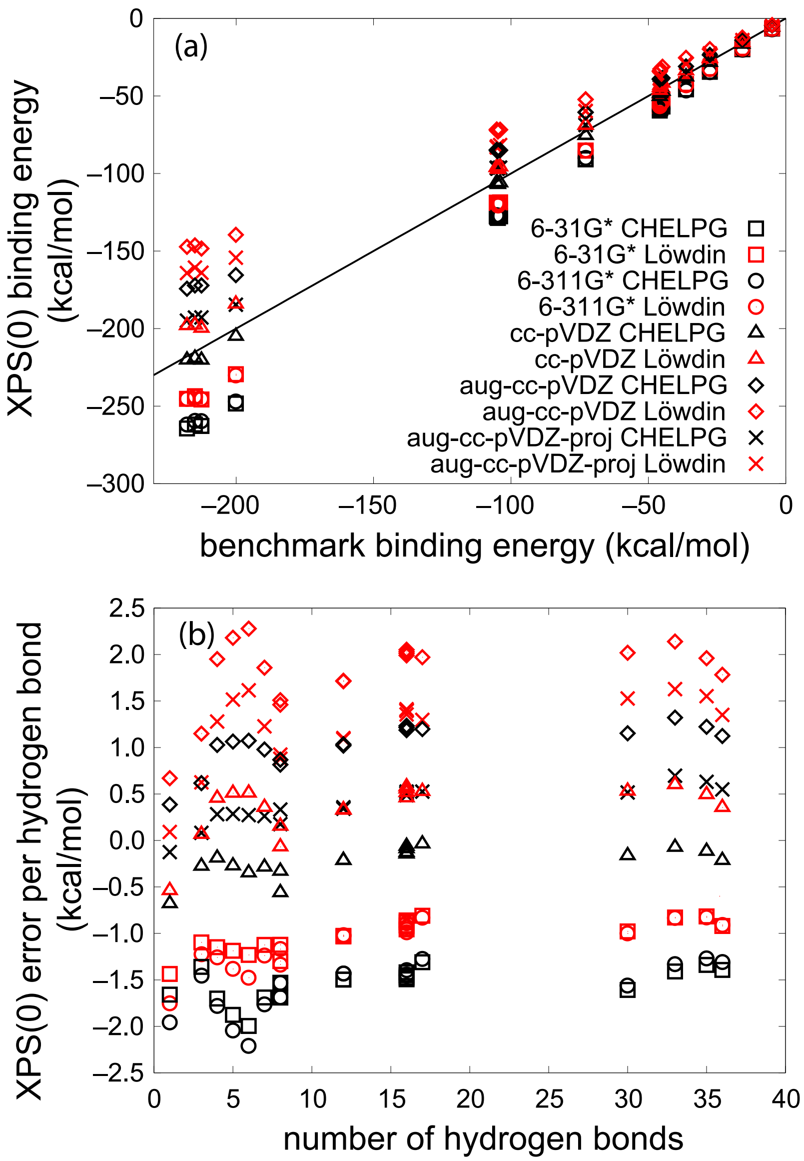

Figure C.4: (a) Correlation between XPS binding energies and MP2 benchmarks. (b) XPS error per hydrogen bond, as a function of the number of hydrogen bonds.

n	Isomer	XPS(0)-CHELPG										Benchmark
		6-31G*		6-311G*		cc-pVDZ		aug-cc-pVDZ		aug-cc-pVDZ-proj		
2		6.6	(33.4)	6.9	(39.4)	5.6	(13.7)	4.6	(7.8)	5.1	(2.5)	4.97
3		19.9	(25.8)	20.2	(27.6)	16.6	(5.3)	14.0	(11.7)	15.6	(1.6)	15.82
4		34.4	(24.6)	34.8	(25.8)	28.4	(2.7)	23.5	(14.9)	26.5	(4.1)	27.63
5		45.7	(25.8)	46.5	(28.1)	37.7	(3.8)	31.0	(14.7)	34.9	(3.9)	36.31
6	book	57.4	(25.9)	57.9	(27.0)	47.6	(4.4)	38.8	(15.0)	43.8	(4.0)	45.61
6	cage	58.0	(26.7)	58.0	(26.7)	48.4	(5.8)	38.8	(15.2)	43.8	(4.2)	45.79
6	cyclic	56.8	(26.7)	58.1	(29.6)	47.0	(4.7)	38.4	(14.3)	43.2	(3.7)	44.86
6	prism	59.4	(29.5)	59.4	(29.4)	50.4	(9.8)	39.3	(14.2)	44.5	(3.1)	45.86
8	D_{2d}	90.8	(24.6)	90.1	(23.6)	75.5	(3.5)	60.5	(17.0)	68.6	(5.9)	72.88
8	S_4	90.8	(24.7)	90.0	(23.6)	75.4	(3.5)	60.6	(16.8)	68.7	(5.6)	72.83
11	$43'4$	127.4	(21.2)	126.8	(20.6)	105.8	(0.6)	84.8	(19.4)	96.2	(8.5)	105.16
11	$44'3'$	128.7	(22.8)	128.0	(22.2)	107.1	(2.2)	85.3	(18.6)	96.6	(7.8)	104.76
11	515	127.8	(21.6)	127.4	(21.2)	106.1	(1.0)	85.4	(18.8)	96.7	(8.0)	105.09
11	551	128.2	(22.1)	128.0	(22.0)	106.4	(1.4)	85.5	(18.5)	96.8	(7.8)	104.95
11	$44'12$	127.6	(22.7)	127.2	(22.4)	106.0	(2.0)	85.0	(18.3)	96.2	(7.5)	103.97
20	dodecahedron	248.4	(24.1)	247.0	(23.4)	205.0	(2.5)	165.5	(17.3)	184.6	(7.7)	200.10
20	edge-sharing	264.4	(21.3)	261.8	(20.1)	220.3	(1.1)	174.3	(20.0)	194.9	(10.6)	217.90
20	face-sharing	261.9	(21.8)	259.4	(20.6)	219.1	(1.9)	172.2	(19.9)	192.9	(10.3)	215.00
20	fused cubes	262.8	(23.6)	259.7	(22.1)	220.4	(3.6)	172.2	(19.0)	192.8	(9.3)	212.60

Table C.3: Negative binding energies for $(H_2O)_n$ cluster isomers, in kcal/mol. Percent errors in the XPS binding energies, relative to the benchmarks, are listed in parentheses.

Bibliography

[1] C. F. Williams and J. M. Herbert, J. Phys. Chem. A **112**, 6171 (2008).

[2] J. V. Coe, S. M. Williams, and K. H. Bowen, Int. Rev. Phys. Chem. **27**, 27 (2008).

[3] L. D. Jacobson, C. F. Williams, and J. M. Herbert, J. Chem. Phys. **130**, 124115 (2009).

[4] L. Ma, K. Majer, F. Chirot, and B. von Issendorff, J. Chem. Phys. **131**, 144303 (2009).

[5] Y. Tang et al., Phys. Chem. Chem. Phys. (2010).

[6] K. R. Siefermann et al., Nature Chemistry **2**, 274 (2010).

[7] A. T. Shreve, T. A. Yen, and D. M. Neumark, Chem. Phys. Lett **493**, 216 (2010).

[8] C. D. Sherrill, T. Takatani, and E. G. Hohenstein, J. Phys. Chem. A **113**, 10146 (2009).

[9] G. Makov and A. Nitzan, J. Phys. Chem. **98**, 3459 (1994).

[10] M. Born and J. R. Oppenheimer, Ann. Physik **84**, 457 (1927).

[11] A. Nitzan, *Chemical Dynamics in Condensed Phases*, Oxford University Press, 2006.

[12] A. Szabo and N. S. Ostlund, *Modern Quantum Chemistry*, Dover Publications Inc., 1982.

[13] T. D. Crawford and H. F. Schaefer III, Rev. Comp. Chem. **14**, 33 (2000).

[14] P. Ren and J. W. Ponder, J. Phys. Chem. B **107**, 5933 (2003).

[15] A. J. Stone, *the Theory of Intermolecular Forces*, Oxford University Press, 1996.

[16] D. J. Griffiths, *Introduction to Electrodynamics*, Pearson Education, Inc., 1999.

[17] C. J. F. Bottcher, O. V. Belle, P. Bordewijk, and A. Rip, *Theory of Electric Polarization*, volume 1 of *Dielectrics in Static Fields*, Elsevier, 1973.

[18] J. Applequist, Chem. Phys. **85**, 279 (1984).

[19] H. Berendsen, J. Grigera, and T. Straatsma, J. Phys. Chem. **91**, 6269 (1987).

[20] B. Jeziorski et al., SAPT: A program for many-body symmetry-adapted perturbation theory calculations of intermolecular interaction energies, in *Methods and Techniques in Computational Chemistry: METECC-94*, edited by E. Clementi, volume B, chapter 3, pages 79–129, STEF, Cagliari, 1993.

[21] C. A. Kraus, J. Am. Chem. Soc. **30**, 1323 (1908).

[22] G. E. Gibson and W. L. Argo, J. Am. Chem. Soc. **40**, 1327 (1918).

[23] F. P. Sargent and E. M. Gardy, Chem. Phys. Lett **39**, 188 (1976).

[24] E. J. Hart, *Solvated Electron*, American Chemical Society Publications, 1965.

[25] B. C. Garrett et al., Chem. Rev. **105**, 355 (2005).

[26] E. J. Hart and M. Anbar, *The Hydrated Electron*, Wiley, 1970.

[27] C.-R. Wang, J. Nguyen, and Q.-B. Lu, J. Am. Chem. Soc. **131**, 11320 (2009).

[28] K. D. Jordan and F. Wang, Annu. Rev. Phys. Chem. **54**, 367 (2003).

[29] D. M. Neumark, Mol. Phys. **106**, 2183 (2008).

[30] J. V. Coe et al., J. Chem. Phys. **92**, 3960 (1990).

[31] R. N. Barnett, U. Landman, C. L. Cleveland, and J. Jortner, J. Chem. Phys. **88**, 4429 (1988).

[32] L. Turi, W.-S. Sheu, and P. J. Rossky, Science **309**, 914 (2005).

[33] L. Turi, W.-S. Sheu, and P. J. Rossky, Science **310**, 1769 (2005).

[34] J. R. R. Verlet, A. E. Bragg, A. Kammrath, O. Cheshnovsky, and D. M. Neumark, Science **307**, 93 (2005).

[35] J. R. R. Verlet, A. E. Bragg, A. Kammrath, O. Cheshnovsky, and D. M. Neumark, Science **310**, 1769 (2005).

[36] H. Haberland, H. Langosch, H. Schindler, and D. R. Worsnop, J. Phys. Chem. **88**, 3903 (1984).

[37] M. Armbruster, H. Haberland, and H. Schindler, Phys. Rev. Lett. **47**, 323 (1981).

[38] R. N. Barnett, U. Landman, and C. L. Cleveland, Phys. Rev. Lett. **59**, 811 (1987).

[39] R. N. Barnett, U. Landman, C. L. Cleveland, and J. Jortner, J. Chem. Phys. **88**, 4421 (1988).

[40] R. N. Barnett, U. Landman, G. Makov, and A. Nitzan, J. Chem. Phys. **93**, 6226 (1990).

[41] P. Ayotte and M. A. Johnson, J. Chem. Phys. **106**, 811 (1997).

[42] L. Turi, W.-S. Sheu, and P. J. Rossky, Science **309**, 914 (2005).

[43] J. M. Herbert and L. D. Jacobson, Int. Rev. Phys. Chem **30**, 1 (2011).

[44] R. E. Larsen, W. J. Glover, and B. J. Schwartz, Science **329**, 65 (2010).

[45] M. Head-Gordon, J. Phys. Chem. **100**, 13213 (1996).

[46] P. Pulay, Chem. Phys. Lett. **100**, 151 (1983).

[47] S. Hirata, Phys. Chem. Chem. Phys. **11**, 8397 (2009).

[48] H. Stoll, G. Wagenblast, and H. Preuß, Theor. Chim. Acta. **57**, 169 (1980).

[49] R. Khaliullin, M. Head-Gordon, and A. T. Bell, J. Chem. Phys. **124**, 204105/1 (2006).

[50] R. Z. Khalliulin, E. A. Cobar, R. C. Lochan, A. T. Bell, and M. Head-Gordon, J. Phys. Chem. A **111**, 8753 (2007).

[51] E. E. Dahlke, H. R. Leverentz, and D. G. Truhlar, J. Chem. Theor. Comp. **4**, 33 (2008).

[52] E. E. Dahlke and D. G. Truhlar, J. Chem. Theor. Comp. **3**, 46 (2007).

[53] E. E. Dahlke and D. G. Truhlar, J. Chem. Theor. Comp. **3**, 1342 (2007).

[54] E. E. Dahlke and D. G. Truhlar, J. Chem. Theor. Comp. **4**, 1 (2008).

[55] G. J. O. Beran, J. Chem. Phys. **130**, 164115 (2009).

[56] G. J. O. Beran and K. Nanda, J. Phys. Chem. Lett. **1**, 3480 (2010).

[57] W. Xie and J. Gao, J. Chem. Theor. Comp. **3**, 1890 (2007).

[58] W. Xie, M. Orozco, D. G. Truhlar, and J. Gao, J. Chem. Theor. Comp. **5**, 459 (2009).

[59] W. Xie, L. Song, D. G. Truhlar, and J. Gao, J. Chem. Phys. **128**, 234108/1 (2008).

[60] A. Cembran et al., J. Chem. Theor. Comp. **6**, 2469 (2010).

[61] C. D. Jonah, C. Romero, and A. Rahman, Chem. Phys. Lett. **123**, 209 (1986).

[62] A. Wallqvist, D. Thirumalai, and B. J. Berne, J. Chem. Phys. **85**, 1583 (1986).

[63] A. Wallqvist, D. Thirumalai, and B. J. Berne, J. Chem. Phys. **86**, 6404 (1987).

[64] J. Schnitker and P. J. Rossky, J. Chem. Phys. **86**, 3462 (1987).

[65] I. Park, K. Cho, S. Lee, K. S. Kim, and J. D. Joannopoulos, Comp. Mat. Sci. **21**, 291 (2001).

[66] L. Turi, M.-P. Gaigeot, N. Levy, and D. Borgis, J. Chem. Phys. **114**, 7805 (2001).

[67] L. Turi and D. Borgis, J. Chem. Phys. **117**, 6186 (2002).

[68] F. Wang and K. D. Jordan, J. Chem. Phys. **116**, 6973 (2002).

[69] T. Sommerfeld and K. D. Jordan, J. Phys. Chem. A **109**, 11531 (2005).

[70] A. DeFusco, T. Sommerfeld, and K. D. Jordan, Chem. Phys. Lett. **455**, 135 (2008).

[71] J. E. Aremu-Cole, *Mixed quantum-classical study of a hydrated electron and investigation of temperature-control algorithms*, PhD thesis, Clemson University, 2007.

[72] A. Wallqvist, G. Martyna, and B. J. Berne, J. Phys. Chem. **92**, 1721 (1988).

[73] J. Schnitker and P. J. Rossky, J. Chem. Phys. **86**, 3471 (1987).

[74] R. N. Barnett, U. Landman, D. Scharf, and J. Jortner, Acc. Chem. Rev. **22**, 350 (1989).

[75] M. Skorobogatiy, I. J. Park, and J. D. Joannopoulos, Comp. Mat. Sci. **32**, 96 (2005).

[76] C. Nicolas, A. Boutin, B. Levy, and D. Borgis, J. Chem. Phys. **118**, 9689 (2003).

[77] F. Wang and K. D. Jordan, J. Chem. Phys. **119**, 11645 (2003).

[78] T. Sommerfeld and K. D. Jordan, J. Am. Chem. Soc. **128**, 5828 (2006).

[79] T. Sommerfeld, S. D. Gardner, A. DeFusco, and K. D. Jordan, J. Chem. Phys. **125**, 174301 (2006).

[80] L. Turi, Á. Madarász, and P. J. Rossky, J. Chem. Phys. **125**, 014308 (2006).

[81] D. Borgis, P. J. Rossky, and L. Turi, J. Chem. Phys. **125**, 064501 (2006).

[82] D. Borgis, P. J. Rossky, and L. Turi, J. Chem. Phys. **127**, 174508 (2007).

[83] Á. Madarász, P. J. Rossky, and L. Turi, J. Chem. Phys. **126**, 234707 (2007).

[84] J. V. Coe, Int. Rev. Phys. Chem **20**, 33 (2001).

[85] J. V. Coe, S. T. Arnold, J. G. Eaton, G. H. Lee, and K. H. Bowen, J. Chem. Phys. **125**, 014315 (2006).

[86] D. M. Bartels, J. Chem. Phys. **115**, 4404 (2001).

[87] T. Frigato, J. VandeVondele, B. Schmidt, C. Schütte, and P. Jungwirth, J. Phys. Chem. A **112**, 6125 (2008).

[88] H. J. C. Berendsen, J. P. M. Postma, W. F. van Gunsteren, and J. Hermans, in *Intermolecular Forces*, edited by B. Pullman, page 331, Holland, 1981, Dordrecht.

[89] K. Toukan and A. Rahman, Phys. Rev.B **31**, 2643 (1985).

[90] J. M. Herbert and M. Head-Gordon, Proc. Nat. Acad. Sci. **103**, 14282 (2006).

[91] J. M. Herbert, L. D. Jacobson, and C. F. Williams, The role of the *neutral* water potential in determining the properties of *anionic* water clusters, in *Molecular Potential Energy Surfaces in Many Dimensions*, edited by M. M. Law and A. Ernesti, pages 28–38, Collaborative Computational Project on Molecular Quantum Dynamics (CCP6), Daresbury, United Kingdom, 2009.

[92] G. S. Fanourgakis, E. Aprà, and S. S. Xantheas, J. Chem. Phys. **121**, 2655 (2004).

[93] F. Webster, P. J. Rossky, and R. A. Friesner, Comp. Phys. Comm. **63**, 494 (1991).

[94] M. A. Morrison and L. A. Collins, Phys. Rev.B **17**, 918 (1978).

[95] W. Yang and R. G. Parr, *Density Functional Theory of Atoms and Molecules*, Oxford, New York, 1989.

[96] G. G. Kleinman and U. Landman, Phys. Rev. B **8**, 5484 (1973).

[97] J. C. Phillips and L. Kleinman, Phys. Rev. **116**, 287 (1959).

[98] A. Stone, Mol. Phys. **56**, 1047 (1985).

[99] A. Stone, Chem. Phys. Lett. **83**, 233 (1981).

[100] J. Applequist, J. Chem. Phys. **83**, 809 (1985).

[101] B. Thole, Chem. Phys. **59**, 341 (1981).

[102] A. DeFusco, D. P. Schofield, and K. D. Jordan, Mol. Phys. **105**, 2681 (2007).

[103] J. M. Herbert and M. Head-Gordon, J. Phys. Chem. A **109**, 5217 (2005).

[104] M. Dupuis, M. Aida, Y. Kawashima, and K. Hirao, J. Chem. Phys. **117**, 1242 (2002).

[105] D. Kosloff and R. Kosloff, J. Comput. Phys. **52**, 35 (1983).

[106] D. T. Colbert and W. H. Miller, J. Chem. Phys. **96**, 1982 (1992).

[107] J. K. Cullum and R. A. Willoughby, *Lanczos Algorithms for Large Symmetric Eigenvalue Computations*, volume I, Birkhauser, Boston, 1985.

[108] B. J. Schwartz and P. J. Rossky, J. Phys. Chem. **98**, 4489 (1994).

[109] C. W. Murray, S. C. Racine, and E. R. Davidson, J. Comput. Phys. **103**, 382 (1992).

[110] M. L. Leininger, C. D. Sherrill, W. D. Allen, and H. F. Schaefer III, J. Comp. Chem. **22**, 1574 (2001).

[111] R. Kosloff, J. Phys. Chem. **92**, 2087 (1988).

[112] J. Ponder, Tinker.

[113] J. M. Herbert and M. Head-Gordon, Phys. Chem. Chem. Phys. **8**, 68 (2006).

[114] K. Yagi, Y. Okano, Y. Kawashima, T. Tsudeda, and K. Hirao, J. Phys. Chem. A **112**, 9845 (2008).

[115] A. Halkier, P. Jorgensen, W. Klopper, and J. Olsen, Chem. Phys. Lett. **302**, 437 (1999).

[116] T. Helgaker, P. Jorgensen, and J. Olsen, *Molecular Electronic-Structure Theory*, Wiley, 2000.

[117] Y. Shao et al., Phys. Chem. Chem. Phys. **8**, 3172 (2006).

[118] W. Humphrey, A. Dalke, and K. Schulten, J. Molec. Graphics **14**, 33 (1996).

[119] N. I. Hammer, J. R. Roscioli, and M. A. Johnson, J. Phys. Chem. A **109**, 7896 (2005).

[120] N. I. Hammer et al., Science **306**, 675 (2004).

[121] H. M. Lee, S. Lee, and K. S. Kim, J. Chem. Phys. **119**, 187 (2003).

[122] J.-W. Shin, N. I. Hammer, J. M. Headrick, and M. A. Johnson, Chem. Phys. Lett. **399**, 349 (2004).

[123] R. R. Zope and B. I. Dunlap, J. Chem. Theor. Comp. **1**, 1193 (2005).

[124] E. J. Hart and J. W. Boag, J. Am. Chem. Soc. **84**, 4090 (1962).

[125] J. W. Boag and E. J. Hart, Nature **197**, 45 (1963).

[126] L. Kevan, J. Phys. Chem. **85**, 1628 (1981).

[127] L. Kevan, Acc. Chem. Rev. **14**, 138 (1981).

[128] P. Han and D. M. Bartels, J. Phys. Chem. **94**, 7294 (1990).

[129] K. H. Schmidt, P. Han, and D. M. Bartels, J. Phys. Chem. **99**, 10530 (1995).

[130] G. H. Lee et al., Z. Phys. D Atom. Mol. Cl. **20**, 9 (1991).

[131] J. Kim, I. Becker, O. Cheshnovsky, and M. A. Johnson, Chem. Phys. Lett. **297**, 90 (1998).

[132] M. Mizuno and T. Tahara, J. Phys. Chem. A **105**, 8823 (2001).

[133] M. Mizuno and T. Tahara, J. Phys. Chem. A **107**, 2411 (2003).

[134] M. J. Tauber and R. A. Mathies, J. Phys. Chem. A **105**, 10952 (2001).

[135] M. J. Tauber and R. A. Mathies, Chem. Phys. Lett. **354**, 518 (2002).

[136] M. J. Tauber and R. A. Mathies, J. Am. Chem. Soc. **125**, 1394 (2003).

[137] N. I. Hammer, J. R. Roscioli, J. C. Bopp, J. M. Headrick, and M. A. Johnson, J. Chem. Phys. **123**, 244311 (2005).

[138] J. R. Roscioli, N. I. Hammer, M. A. Johnson, K. Diri, and K. D. Jordan, J. Chem. Phys. **128**, 104314 (2008).

[139] A. E. Bragg, J. R. R. Verlet, A. Kammrath, O. Cheshnovsky, and D. M. Neumark, Science **306**, 669 (2004).

[140] A. E. Bragg, J. R. R. Verlet, A. Kammrath, O. Cheshnovsky, and D. M. Neumark, J. Am. Chem. Soc. **127**, 15283 (2005).

[141] K. R. Asmis et al., J. Chem. Phys. **126**, 191105 (2007).

[142] G. B. Griffin, R. M. Young, O. T. Ehrler, and D. M. Neumark, J. Chem. Phys. **131**, 194302 (2009).

[143] D. H. Paik, I. Lee, D. Yang, J. Baskin, and A. H. Zewail, Science **306**, 672 (2004).

[144] D. M. Bartels, K. Takahashi, J. A. Cline, T. W. Marin, and C. D. Jonah, J. Phys. Chem. A **109**, 1299 (2005).

[145] Y. Du, E. Price, and D. M. Bartels, Chem. Phys. Lett. **438**, 234 (2007).

[146] P. M. Hare, E. A. Price, C. M. Stanisky, I. Janik, and D. M. Bartels, J. Phys. Chem. A **114**, 1766 (2010).

[147] P. J. Rossky and J. Schnitker, J. Phys. Chem. **92**, 4277 (1988).

[148] J. Schnitker, K. Motakabbir, P. J. Rossky, and R. A. Friesner, Phys. Rev.Lett. **60**, 456 (1988).

[149] B. J. Schwartz and P. J. Rossky, J. Chem. Phys. **101**, 6902 (1994).

[150] B. J. Schwartz and P. J. Rossky, Phys. Rev. Lett. **72**, 3282 (1994).

[151] B. J. Schwartz and P. J. Rossky, J. Chem. Phys. **101**, 6902 (1994).

[152] A. Staib and D. Borgis, J. Chem. Phys. **103**, 2642 (1995).

[153] A. Madarasz, P. J. Rossky, and L. Turi, J. Chem. Phys. **130**, 124319 (2009).

[154] L. Turi, G. Hantal, P. J. Rossky, and D. Borgis, J. Chem. Phys. **131**, 024119 (2009).

[155] M. Boero, M. Parrinello, K. Terakura, T. Ikeshoji, and C. C. Liew, Phys. Rev.Lett. **90**, 226403 (2003).

[156] J. M. Herbert and M. Head-Gordon, J. Am. Chem. Soc. **128**, 13932 (2006).

[157] I. A. Shkrob, J. Phys. Chem. A **111**, 5223 (2007).

[158] I. A. Shkrob, W. J. Glover, R. E. Larsen, and B. J. Schwartz, J. Phys. Chem. A **111**, 5232 (2007).

[159] K. A. Tay and A. Boutin, J. Phys. Chem. B **113**, 11943 (2009).

[160] L. D. Jacobson and J. M. Herbert, J. Am. Chem. Soc. **132**, 10000 (2010).

[161] R. Lugo and P. Delahay, J. Chem. Phys. **57**, 2122 (1972).

[162] F.-Y. Jou and G. R. Freeman, J. Phys. Chem. **81**, 909 (1977).

[163] F.-Y. Jou and G. R. Freeman, Can. J. Chem. **57**, 591 (1979).

[164] P. Ren and J. W. Ponder, J. Phys. Chem. A **108**, 13427 (2004).

[165] A. Gaathon, G. Czapski, and J. Jortner, J. Chem. Phys. **58**, 2648 (1973).

[166] C. J. Smallwood, R. E. Larsen, W. J. Glover, and B. J. Schwartz, J. Chem. Phys. **125**, 074102 (2006).

[167] T. Tsuneda, T. Suzumura, and K. Hirao, J. Chem. Phys. **110**, 10664 (1999).

[168] H. Iikura, T. Tsuneda, T. Yanai, and K. Hirao, J. Chem. Phys. **115**, 3540 (2001).

[169] L. Mones and L. Turi, J. Chem. Phys. **132**, 154507 (2010).

[170] J. Ponder, Tinker.

[171] G. Martyna, M. Tuckerman, D. Tobias, and M. Klein, Mol. Phys. **87**, 1117 (1996).

[172] D. Frenkel and B. Smit, *Understanding Molecular Simulation: From Algorithms to Applications*, Academic Press, 2002.

[173] J. Xu and K. D. Jordan, J. Phys. Chem. A **114**, 1364 (2010).

[174] P. Wernet et al., Science **304**, 995 (2004).

[175] J. D. Louck and H. W. Galbraith, Rev. Mod. Phys. **48**, 69 (1976).

[176] M. Maroncelli and G. R. Fleming, J. Chem. Phys. **89**, 5044 (1988).

[177] M. Leslie and M. J. Gillan, J. Phys. C **18**, 973 (1985).

[178] G. Makov and M. C. Payne, Phys. Rev. B **51**, 4014 (1995).

[179] M. C. Cavanagh, I. B. Martini, and B. J. Schwartz, Chem. Phys. Lett **396** (2004).

[180] P. J. Reid, C. Silva, P. K. Walhout, and P. F. Barbara, Chem. Phys. Lett. **228**, 658 (1994).

[181] M. Assell, R. Laenen, and A. Laubreau, J. Phys. Chem. A **102**, 2256 (1998).

[182] M. Assell, R. Laenen, and A. Laubreau, J. Chem. Phys. **111**, 6869 (1999).

[183] I. A. Shkrob, Chem. Phys. Lett. **467**, 84 (2008).

[184] L. D. Jacobson and J. M. Herbert, J. Chem. Phys. **133**, 154506 (2010).

[185] L. Turi and A. Madarasz, Science **331**, 1387 (2011).

[186] R. E. Larsen, W. J. Glover, and B. J. Schwartz, Science **331**, 1387 (2011).

[187] C. A. Kraus, J. Am. Chem. Soc. **29**, 1557 (1907).

[188] J. W. Boyle, J. A. Ghormley, C. J. Hochanadel, and J. F. Riley, J. Phys. Chem. **73**, 2886 (1969).

[189] D. N. Nikogosyan, A. A. Oraevsky, and V. I. Rupasov, Chem. Phys. **77**, 131 (1983).

[190] E. Keszei and J.-P. Jay-Gerin, Can. J. Chem. **70**, 21 (1992).

[191] A. Bernas and D. Grand, J. Phys. Chem. **98**, 3440 (1994).

[192] D. M. Bartels and R. A. Crowell, J. Phys. Chem. A **104**, 3349 (2000).

[193] C. G. Elles, I. A. Shkrob, R. A. Crowell, and S. E. Bradforth, J. Chem. Phys. **126**, 164503 (2007).

[194] A. Migus, Y. Gauduel, J. L. Martin, and A. Antonettie, Phys. Rev. Lett. **58**, 1559 (1987).

[195] F. H. Long, H. Lu, and K. B. Eisenthal, Phys. Rev. Lett. **64**, 1469 (1990).

[196] R. Laenen, T. Roth, and A. Laubereau, Phys. Rev. Lett. **85**, 50 (2000).

[197] C.-R. Wang, T. Luo, and Q.-B. Lu, Phys. Chem. Chem. Phys. **10**, 4463 (2008).

[198] Y. Gauduel, Y. Glinec, and V. Malka, J. Phys.: Conf. Ser. **101**, 012004 (2008).

[199] C.-R. Wang and Q.-B. Lu, Angew. Chem. Int. Ed. Engl. **46**, 6316 (2007).

[200] B. Boudaiffa, P. Cloutier, D. Hunting, M. A. Huels, and L. Sanche, Science **287**, 1658 (2000).

[201] M. A. Huels, B. Boudaiffa, P. Cloutier, D. Hunting, and L. Sanche, J. Am. Chem. Soc. **125**, 4467 (2003).

[202] X. Li, M. D. Sevilla, and L. Sanche, J. Am. Chem. Soc. **125**, 13668 (2003).

[203] B. D. Michael and P. O'Neil, Science **287**, 1603 (2000).

[204] K. Yagi et al., J. Phys. Chem. A **112**, 9845 (2008).

[205] A. Lange and J. M. Herbert, J. Chem. Theor. Comp. **3**, 1680 (2007).

[206] A. W. Lange and J. M. Herbert, J. Am. Chem. Soc. **131**, 3913 (2009).

[207] A. W. Lange, M. A. Rohrdanz, and J. M. Herbert, J. Phys. Chem. B **112**, 6304 (2008).

[208] R. Martin, J. Chem. Phys. **118**, 4775 (2003).

[209] M. Mostafavi and I. Lampre, The solvated electron: A singular chemical species, in *Radiation Chemistry*, edited by M. Spotheim-Maurizot, M. Mostafavi, J. Belloni, and T. Douki, chapter 3, pages 33–52, EDP Sciences, 2008.

[210] T. Sommerfeld, A. DeFusco, and K. D. Jordan, J. Phys. Chem. A **112**, 11021 (2008).

[211] G. V. Buxton, An overview of the radiation chemistry of liquids, in *Radiation Chemistry*, edited by M. Spotheim-Maurizot, M. Mostafavi, J. Belloni, and T. Douki, chapter 1, pages 3–16, EDP Sciences, 2008.

[212] A. T. B. Gilbert, N. A. Besley, and P. M. W. Gill, J. Phys. Chem. A **112**, 13164 (2008).

[213] N. A. Besley, A. T. B. Gilbert, and P. M. W. Gill, J. Chem. Phys. **130**, 124308 (2009).

[214] R. Car and M. Parrinello, Phys. Rev. Lett. **55**, 2471 (1985).

[215] D. Marx and J. Hutter, Ab initio molecular dynamics: Theory and implementation, in *Modern Methods and Algorithms in Quantum Chemistry*, edited by J. Grotendorst, volume 1 of *NIC Series*, pages 329–477, John von Neumann Institute for Computing, Jülich, Germany, 2nd edition, 2000.

[216] F. Tassone, F. Mauri, and R. Car, Phys. Rev. B **50**, 10561 (1994).

[217] M. P. Allen and D. J. Tildesley, *Computer Simulations of Liquids*, Oxford, 1992.

[218] M. E. Tuckerman and M. Parrinello, J. Chem. Phys. **101**, 1302 (1994).

[219] H. C. Andersen, J. Comput. Phys. **52**, 24 (1983).

[220] J. M. Herbert and M. Head-Gordon, J. Chem. Phys. **121**, 11542 (2004).

[221] S. S. Iyengar, H. B. Schlegel, G. E. Scuseria, J. M. Millam, and M. J. Frisch, J. Chem. Phys. **123**, 027101:1 (2005).

[222] J. M. Herbert and M. Head-Gordon, J. Chem. Phys. **123**, 027102:1 (2005).

[223] M. I. J. Probert, J. Comput. Phys. **191**, 130 (2003).

[224] M. Haranczyk and M. Gutowski, J. Chem. Theor. Comp. **4**, 689 (2008).

[225] J. L. McHale, *Molecular Spectroscopy*, Prentice Hall, 1998.

[226] S. Yoo, F. Zahariev, S. Sok, and M. S. Gordon, J. Chem. Phys. **129**, 144112:1 (2008).

[227] A. H. Steindal, K. Ruud, L. Frediani, K. Aidas, and J. Kongsted, J. Phys. Chem. B **115**, 3027 (2011).

[228] N. L. Doltsinis and D. Marx, Phys. Rev. Lett. **88**, 166402:1 (2002).

[229] E. Tapavicza, I. Tavernelli, and U. Rothlisberger, Phys. Rev. Lett. **98**, 023001:1 (2007).

[230] Q. Wu and T. Van Voorhis, J. Chem. Theor. Comp. **2**, 765 (2006).

[231] Q. Wu, C.-L. Cheng, and T. Van Voorhis, J. Chem. Phys. **127**, 164119:1 (2007).

[232] C. A. White, B. G. Johnson, P. M. W. Gill, and M. Head-Gordon, Chem. Phys. Lett. **230**, 8 (1994).

[233] S. Saebo, Low-scaling methods for electron correlation, in *Computational Chemistry: Reviews of Current Trends*, edited by J. Leszczynski, volume 7, pages 63–87, World Scientific, 2002.

[234] C. Ochsenfeld, J. Kussmann, and D. S. Lambrecht, Linear-scaling methods in quantum chemistry, in *Reviews in Computational Chemistry*, edited by K. B. Lipkowitz and T. R. Cundari, volume 23, chapter 1, pages 1–82, Wiley-VCH, 2007.

[235] R. A. Friesner, Proc. Nat. Acad. Sci. **102**, 6648 (2005).

[236] A. Sebetci and G. J. O. Beran, J. Chem. Theor. Comp. **6**, 155 (2010).

[237] K. Kitaura, E. Ikeo, T. Asada, T. Nakano, and M. Uebayasi, Chem. Phys. Lett. **313**, 701 (1999).

[238] D. G. Fedorov and K. Kitaura, J. Phys. Chem. A **111**, 6904 (2007).

[239] D. G. Fedorov and K. Kitaura, Theoretical background of the fragment molecular orbital (FMO) method and its implementation in GAMESS, in *The Fragment Molecular Orbital Method: Practical Applications to Large Molecular Systems*, edited by D. G. Fedorov and K. Kitaura, chapter 2, pages 5–36, CRC Press, Boca Rotan, FL, 2009.

[240] W. Yang, Phys. Rev.Lett. **66**, 1438 (1991).

[241] N. Flocke and R. J. Bartlett, J. Chem. Phys. **121**, 10935 (2004).

[242] T. F. Hughes, N. Flocke, and R. J. Bartlett, J. Phys. Chem. A **112**, 5994 (2008).

[243] P. N. Day et al., J. Chem. Phys. **105**, 1968 (1996).

[244] M. S. Gordon et al., J. Phys. Chem. A **105**, 293 (2000).

[245] D. Ghosh et al., J. Phys. Chem. A **114**, 12739 (2010).

[246] L. Song, J. Han, Y.-L. Lin, W. Xie, and J. Gao, J. Phys. Chem. A **113**, 11656 (2009).

[247] T. Nakano et al., Chem. Phys. Lett. **318**, 614 (2000).

[248] D. G. Fedorov, J. H. Jensen, R. C. Deka, and K. Kitaura, J. Phys. Chem. A **112**, 11808 (2008).

[249] Y. Komeiji, Y. Mochizuki, and T. Nakano, Chem. Phys. Lett. **484**, 380 (2010).

[250] S. Saebo and P. Pulay, Ann. Rev. Phys. Chem **44**, 213 (1993).

[251] M. Schütz and H.-J. Werner, J. Chem. Phys. **114**, 661 (2001).

[252] M. Schütz and F. R. Manby, Phys. Chem. Chem. Phys. **5**, 3349 (2003).

[253] H.-J. Werner, F. R. Manby, and P. J. Knowles, J. Chem. Phys. **118**, 8149 (2003).

[254] H.-J. Werner and K. Pflüger, Annu. Rep. Comput. Chem. **2**, 53 (2006).

[255] J. E. Subotnik and M. Head-Gordon, J. Phys.-Condens. Mat. **20**, 294211/1 (2008).

[256] T. S. Chwee, A. B. Szilva, R. Lindh, and E. A. Carter, J. Chem. Phys. **128**, 224106/1 (2008).

[257] W. Li, P. Piecuch, J. R. Gour, and S. Li, J. Chem. Phys. **131**, 114109/1 (2009).

[258] W. Liang and M. Head-Gordon, J. Phys. Chem. A **108**, 3206 (2004).

[259] R. P. Steele, R. A. D. Jr., Y. Shao, J. Kong, and M. Head-Gordon, J. Chem. Phys. **125**, 74108 (2006).

[260] F. Weigend, M. Häser, J. Patzelt, and R. Ahlrichs, Chem. Phys. Lett. **294**, 143 (1998).

[261] F. Weigend, Phys. Chem. Chem. Phys. **4**, 4285 (2002).

[262] A. Sodt, J. E. Subotnik, and M. Head-Gordon, J. Chem. Phys. **125**, 194109/1 (2006).

[263] T. B. Pedersen, F. Aquilante, and R. Lindh, Theor. Chim. Acta. **124**, 1 (2009).

[264] C. D. Sherrill, J. Chem. Phys. **132**, 110902/1 (2010).

[265] R. A. Christie and K. D. Jordan, n-body decomposition approach to the calculation of interaction energies of water clusters, in *Intermolecular Forces and Clusters II*, edited by D. Wales and R. A. Christie, volume 116 of *Structure and Bonding*, pages 27–41, Springer, 2005.

[266] J. Cui, H. Liu, and K. D. Jordan, J. Phys. Chem. B **110**, 18872 (2006).

[267] D. G. Fedorov, P. V. Avramov, J. H. Jensen, and K. Kitaura, Chem. Phys. Lett. **477**, 169 (2009).

[268] T. Nagata, D. G. Fedorov, and K. Kitaura, Chem. Phys. Lett. **492**, 302 (2010).

[269] B. Jeziorski, R. Moszynski, and K. Szalewicz, Chem. Rev. **94**, 1887 (1994).

[270] H. L. Williams and C. F. Chabalowski, J. Phys. Chem. A **105**, 646 (2001).

[271] A. J. Misquitta and K. Szalewicz, Chem. Phys. Lett. **357**, 301 (2002).

[272] A. J. Misquitta, B. Jeziorski, and K. Szalewicz, Phys. Rev.Lett. **91**, 033201 (2003).

[273] A. J. Misquitta, R. Podeszwa, B. Jeziorski, and K. Szalewicz, J. Chem. Phys. **123**, 214103 (2005).

[274] A. Heßelmann and G. Jansen, Chem. Phys. Lett. **367**, 778 (2003).

[275] A. Heßelman, G. Jansen, and M. Schutz, J. Chem. Phys. **122**, 014103 (2005).

[276] V. F. Lotrich and K. Szalewicz, J. Chem. Phys. **106**, 9668 (1997).

[277] V. F. Lotrich and K. Szalewicz, J. Chem. Phys. **112**, 112 (2000).

[278] E. G. Hohenstein and C. D. Sherrill, J. Chem. Phys. **133**, 104107 (2010).

[279] N. Turki et al., J. Chem. Phys. **109**, 7157 (1998).

[280] Y. Chen and H. Li, J. Phys. Chem. A **114**, 11719 (2010).

[281] J. Gao, J. Chem. Phys. **109**, 2346 (1998).

[282] C. M. Breneman and K. B. Wiberg, J. Comp. Chem. **11**, 361 (1990).

[283] K. Patkowski, K. Szalewicz, and B. Jeziorski, J. Chem. Phys. **125**, 154107/1 (2006).

[284] R. Moszynski, B. Jeziorski, and K. Szalewicz, J. Chem. Phys. **100**, 1312 (1994).

[285] B. Jeziorski, K. Szalewicz, and G. Chalasinski, Int. J. Quant. Chem. **14**, 271 (1978).

[286] T. Ćwiok, B. Jeziorski, W. Kołos, R. Moszynski, and K. Szalewicz, J. Chem. Phys. **97**, 7555 (1992).

[287] R. Moszynski, B. Jeziorski, S. Rybak, K. Szalewicz, and H. L. Williams, J. Chem. Phys. **100**, 5080 (1994).

[288] B. Jeziorski, M. Bulski, and L. Piela, Int. J. Quant. Chem. **10**, 281 (1976).

[289] J. A. Pople, R. Krishnan, H. B. Schlegel, and J. S. Binkley, Int. J. Quant. Chem. **13**, 225 (1979).

[290] H. L. Williams, E. M. Mas, and K. Szalewicz, J. Chem. Phys. **103**, 7374 (1995).

[291] A. Bondi, J. Phys. Chem. **68**, 441 (1964).

[292] R. S. Rowland and R. Taylor, J. Phys. Chem. **100**, 7384 (1996).

[293] A. D. Becke, J. Chem. Phys. **98**, 5648 (1993).

[294] P. J. Stephens, F. J. Devlin, C. F. Chabalowski, and M. J. Frisch, J. Phys. Chem. **98**, 11623 (1994).

[295] J. P. Perdew, K. Burke, and M. Ernzerhof, Phys. Rev.Lett. **77**, 3865 (1996).

[296] C. Adamo and V. Barone, J. Chem. Phys. **110**, 6158 (1999).

[297] M. Ernzerhof and G. E. Scuseria, J. Chem. Phys. **110**, 5029 (1999).

[298] T. M. Henderson, B. G. Janesko, and G. E. Scuseria, J. Chem. Phys. **128**, 194105 (2008).

[299] M. A. Rohrdanz, K. M. Martins, and J. M. Herbert, J. Chem. Phys. **130**, 54112 (2009).

[300] J. Song, T. Hirosawa, T. Tsuneda, and K. Hirao, J. Chem. Phys. **126**, 154105 (2007).

[301] P. Jurečka, J. Šponer, J. Černý, and P. Hobza, Phys. Chem. Chem. Phys. **8**, 1985 (2006).

[302] T. Takatani, E. G. Hohenstein, M. Malagoli, M. S. Marshall, and C. D. Sherrill, J. Chem. Phys. **132**, 144104 (2010).

[303] D. J. Tozer and N. C. Handy, J. Chem. Phys. **109**, 10180 (1998).

[304] M. Grüning, V. Gritsenko, S. J. A. van Gisbergen, and E. J. Baerends, J. Chem. Phys. **114**, 652 (2001).

[305] E. G. Hohenstein and C. D. Sherrill, J. Chem. Phys. **133** (2010).

[306] A. J. Cohen, P. Mori-Sánchez, and W. Yang, Science **321**, 792 (2008).

[307] E. G. Hohenstein and C. D. Sherrill, J. Chem. Phys. **132**, 184111 (2010).

[308] C. J. Burnham and S. S. Xantheas, J. Chem. Phys. **116**, 1479 (2002).

[309] K. Wolinski and P. Pulay, J. Chem. Phys. **118**, 9497 (2003).

[310] S. S. Xantheas, J. Chem. Phys. **104**, 8821 (1996).

[311] S. S. Xantheas, C. J. Burnham, and R. J. Harrison, J. Chem. Phys. **116**, 1493 (2002).

[312] S. S. Xantheas and E. Aprà, J. Chem. Phys. **120**, 823 (2004).

[313] S. Bulusu, S. Yoo, E. Aprà, S. S. Xantheas, and X. C. Zeng, J. Phys. Chem. A **110**, 11781 (2006).

[314] S. Yoo, E. Aprà, X. C. Zeng, and S. S. Xantheas, J. Phys. Chem. Lett. **1**, 3122 (2010).

[315] D. M. Sagar, C. D. Bain, and J. R. R. Verlet, J. Am. Chem. Soc. **132**, 6917 (2010).

[316] R. Santra, J. M. Shainline, and C. H. Green, Phys. Rev. A **71**, 32703 (2005).

[317] J. M. Herbert and M. Head-Gordon, Phys. Chem. Chem. Phys. **8**, 68 (2005).

[318] A. D. Becke, Phys. Rev. A **38**, 3098 (1988).

[319] M. A. Rohrdanz and J. M. Herbert, J. Chem. Phys. **129**, 34172 (2008).

[320] J. M. Herbert and M. Head-Gordon, J. Phys. Chem. A **109**, 5217 (2005).

[321] P. M. W. Gill, B. G. Johnson, and J. A. Pople, Chem. Phys. Lett. **209**, 506 (1993).

[322] O. Steinhauser, Mol. Phys. **45**, 335 (1982).